MULTI-MODAL DIAGNOSTIC AND PROGNOSTIC TECHNIQUES FOR NDE APPLICATIONS

Ву

Portia Banerjee

A DISSERTATION

Submitted to
Michigan State University
in partial fulfillment of the requirements
for the degree of

Electrical and Computer Engineering–Doctor of Philosophy

ABSTRACT

MULTI-MODAL DIAGNOSTIC AND PROGNOSTIC TECHNIQUES FOR NDE APPLICATIONS

By

Portia Banerjee

With rapid technological breakthroughs, role of non-destructive evaluation (NDE) has shifted from assessing structural integrity to building complex systems with reliable defect classification and decision making capabilities. Widespread use of NDE in industries such as aviation, nuclear, construction and automotive, have resulted in increased amount of NDE data which is beyond capacity for human analysts and demands automated signal classification (ASC) systems for accurate and consistent signal interpretation. A typical ASC system processes NDE signals and classifies signal categories based on appropriate features. Despite striking benefits of ASC systems, classification results are often affected due to inherent ambiguity of non-discriminative features, inadequate training samples or noisy measurements. As a result, uncertainty quantification in defect classification is critical in NDE applications where the performance of a structure depends on the reliability of the ASC results. A reliability measure that accounts for system uncertainties can help in monitoring its performance and automatically flagging indications where operator intervention is required. In addition to diagnosis, i.e., reliable characterization of current health status, damage prognosis or prediction of system's remaining-useful-life (RUL) is another essential aspect of NDE. Accurate health prognosis ensures system reliability and aids in estimating residual serviceability of a component which in turn reduces repair or replacement costs. Moreover, combining information from multiple sensors in multi-modal NDE systems can effectively improve damage growth modeling and prediction of system's RUL. This dissertation presents three major

contributions to the field of NDE diagnosis and prognosis:

- 1. Uncertainty in ASC systems is quantified in a statistical framework to develop a confidence metric (CM) associated with ASC results. By bootstrapping and weighting Bayes posterior probability with estimated noise distribution, effect of measurement noise is embedded into the proposed CM. Effectiveness of the CM is demonstrated on experimental data from eddy current inspection of steam generator tubes. Further, the benefit of CM in improving classification performance is explored using a confidence-rated-classification technique.
- 2. Particle filtering (PF) framework is developed for prediction of impact damage propagation in composite materials which utilizes both physical model based on modified Paris' law and inspection data obtained from NDE system.
- 3. Joint likelihood updation is proposed in existing PF algorithm which enables optimization of damage model parameters at every time step by discarding noisy or biased measurements from multiple sources. Prognosis results on a composite specimen subjected to fatigue testing and inspected using two NDE modalities, validate the benefit of multi-sensor prognosis approach over single-sensor methods. Additional advantage of multi-sensor prediction in reduction of particle count within the PF algorithm is demonstrated, thereby reducing the total computation time and resources.

Overall, a reliability metric and prognosis methodology is discussed for a multi-sensor system that can be extended to multiple applications.

To my family, for their unconditional love and support.

ACKNOWLEDGMENTS

This PhD journey is a culmination of perseverance, blessings, support and guidance from several well-wishers in my life, to whom I am and will remain grateful forever.

Firstly, a very special gratitude goes out to my advisors Dr. Lalita Udpa and Dr. Yiming Deng, who laid the foundation of research ethics in me. I am thankful to Dr. Udpa for trusting me with opportunities during my earlier days of PhD, for providing timely advice on career plans and aiding me in technical writing. I am grateful to Dr. Deng for establishing the basic knowledge about prognostic methods, providing technical suggestions when I was stuck with failed experiments and introducing me to the reliability community. His constant words of encouragement has been a major stress-deterrent and motivated me to adopt a career in post-doctoral research.

I owe my acknowledgment to other advisors in my committee, especially Dr. Mahmoodul Haq and Dr. Satish Udpa. To Dr. Haq, I am thankful for his critical insights and technical know-how in the field of composites and structural engineering. Despite having a background of Electrical Engineering, I was able to conduct a major part of my research on damage progression in composites owing to his invaluable guidance. I would like to thank Dr. Satish Udpa for his important and thought-provoking questions regarding practical applicability of this research at its multiple stages which shaped the final outcome. The rich legacy created by him and Dr. Lalita Udpa in the NDE community, will continue to inspire me and my colleagues throughout our careers.

I am immensely grateful to my past and current colleagues of NDE lab who have been friends as well as a source of good advice and collaboration, particularly Morteza, Pavel, Rajendra, Suhail and Zhiyi for assisting me with several time-intensive experiments and coding. Thank you for creating a positive, motivating and collaborative work environment, ideal for inter-disciplinary research. I extend my gratitude to fellow students at the Composite Vehicle Research Center who manufactured composite specimens required for this research.

This journey would not have been complete without the unconditional love and blessings from my parents and sister. Their sacrifice, enthusiasm and constant support has been and will always be a key reason behind my achievements. I would also take this opportunity to acknowledge my grandfather, Dr. Asit Kr. Mukherjee, who himself being a doctorate in the family has been one of my earliest inspirations. His commitment, zeal and remarkable professional experiences, instilled in me the passion towards "knowing the unknown".

I owe my heartfelt gratitude to friends and family who supported me during the tough years in the Ph.D. pursuit.

Finally, thank you Saptarshi, for being a constant witness, colleague, friend and critic throughout these years. Your commitment towards work is contagious and encourages me to reach out for my goals.

TABLE OF CONTENTS

LIST (OF TA	ABLES
LIST (OF FI	GURES
Chapte	er 1	Introduction
1.1		vation & Objective
1.2	Scope	e and Organization of the dissertation
Chapt	er 2	Diagnostics in NDE
2.1	Intro	duction
2.2	Auto	mated Signal Classification in NDE
2.3		stical measures in NDE
	2.3.1	Hit/Miss response
	2.3.2	Probability of Detection (POD) and Probability of False Alarm (PFA)
	2.3.3	a vs \hat{a} Model
	2.3.4	a90/95 Confidence Bounds on POD curve
	2.3.5	Receiver Operating Characteristics (ROC)
	2.3.6	Confidence Metric
2.4		ing confidence metrics
	2.4.1	Confidence in binary form
	2.4.2	Confidence in terms of probability
	2.4.3	Similarity Ratio in Clustering
	2.4.4	Membership Functions in Neural Networks
	2.4.5	Posterior Probability in Density Estimation techniques
2.5		s Confidence
	0	
Chapte		Comprehensive Confidence Metric in NDE
3.1		duction
3.2		ors Affecting Reliability in NDE Signal Classification
	3.2.1	Quantity and representativeness of training data
	3.2.2	Quality of features
	3.2.3	Noise statistics of test data
3.3	-	orehensive (Boosted) Bayes Confidence
	3.3.1	Bootstrapping
	3.3.2	Incorporation of noise factor
3.4	Simul	lation Results
Chapt	e r 4	Confidence Metric Evaluation: Eddy Current inspection of
		Steam Generator tubes
4.1		duction
4.2	Princ	iple of Eddy Current Testing

4.3	Automated Analysis of SG Tube Inspection data	44
	4.3.1 Signal Pre-processing	45
	4.3.2 ROI Detection	46
	4.3.3 Feature Extraction and Classification	47
4.4	Noise Analysis in Field Data from Eddy Current Inspection	48
4.5	Confidence of Classification with Noise Consideration	52
4.0	Confidence of Classification with Noise Consideration	J2
C 1 4	CCl D-t-1 Cl'Ct' '- NDE	۳,
Chapt		56
5.1	Introduction	56
5.2	Background	58
	5.2.1 ADABOOST	58
5.3	Confidence rated classification :proposed method	59
5.4	Results	62
	5.4.1 Simulation Results	62
	5.4.2 Experimental Results	64
	r	-
Chapte	er 6 Prognosis in NDE	68
6.1	Introduction	68
6.2	Theory of Reliability	68
0.2	6.2.1 Remaining Useful Life (RUL)	71
6.3	Literature Review on RUL Prognosis	74
0.5		
	6.3.1 Model-based methods	74
	6.3.2 Data-based methods	74
	6.3.3 Integrated methods	75
	6.3.3.1 Regression based models	76
	6.3.3.2 Markovian based models	77
	6.3.3.3 Stochastic Filtering	79
6.4	Theory of Bayesian Updating	80
	6.4.1 Bayes update of model parameters using synthetic data	83
6.5	Bayesian Updating based on Particle Filtering(PF) Approach	85
	6.5.1 PF estimate of model parameters using synthetic data	87
Chapt	er 7 Single Sensor Prognosis in Composites by Direct Condition	
-	Monitoring	92
7.1	Introduction	92
7.2	Condition based Maintenance of GFRP	94
,	7.2.1 Impact Damage in GFRP	94
	7.2.1 Impact Damage in GFR1	95 95
7 9	Proposed Prognostic framework for delamination growth model	90 97
7.3	•	
	7.3.1 Damage Propagation Model	97
	7.3.2 Particle Filtering based Prognosis of Delamination Area in GFRP	100
7.4	Experimental Setup and Results	104
	7.4.1 GFRP Specimen and Experimental Setup	104
	7.4.2 Prognosis Results	106

Chapte	r 8	Single Sensor Prognosis in Composites by Indirect Condition	
		Monitoring	113
8.1	Intro	duction	113
8.2	Expe	rimental Setup	115
	8.2.1	Specimen Geometry and Material	115
	8.2.2	Fatigue testing of GFRP under Mode I failure	116
8.3	NDE	of Fatigue Damage in Composites	118
	8.3.1	Delamination detection using OTS	118
	8.3.2	Delamination detection using GW	122
	8.3.3	Overall Framework of Damage Prognosis	125
8.4	Dama	age Prognosis Results	126
	8.4.1	Prediction of Delamination Area by Logarithmic Regression	127
	8.4.2	Prediction of Delamination Area by Kalman filtering	128
	8.4.3	Prediction of Delamination Area by Particle filtering	131
Chapte	r 9	Multi-sensor Prognosis in Composites	134
9.1	Intro	duction	
9.2	Litera	ature Review of Data Fusion Techniques	139
9.3	Joint	Likelihood Computation in Particle Filtering	141
9.4		rimental set-up	
	9.4.1	Specimen Geometry and Material	145
	9.4.2	Fatigue testing of GFRP under tensile loading	146
9.5	NDE	data acquisition	
	9.5.1	Fatigue damage detection by OTS)	147
	9.5.2	Fatigue damage detection by GW	
9.6	Progr	nosis Results	
	9.6.1	PF prognosis on OTS data	
	9.6.2	PF prognosis on GW data	
	9.6.3	PF prognosis on Average of Two Sensors data	
	9.6.4	PF Prognosis on Two Sensor Data by Joint Likelihood Computation .	161
Chapte	r 10	Conclusion	166
APPEN	NDIC	ES	169
		A Bayesian Networks for multi-sensor fusion	
		B Stiffness of Composite Materials	
BIBLIC)GR /	APHV	176

LIST OF TABLES

Table 4.1:	Confidence of classification of defects in steam generator tubes using RPC probe	54
Table 6.1:	Bayes Updating history of parameter m for synthetic crack growth path	85
Table 7.1:	Cumulative energies of consequtive low velocity imapacts on GFRP sample 1 and 2	04
Table 7.2:	Cumulative energies of consequtive low velocity imapacts on GFRP sample 31	04
Table 7.3:	Cumulative energies of more number of impacts on GFRP sample $S1$ from 150J to 450J	10
Table 8.1:	OTS and GW measurements from Mode I fatigue testing of GFRP at intermediate load cycles	26
Table 9.1:	Military applications of data fusion, from [1]	39
Table 9.2:	Non-military applications of data fusion, from [1]	40
Table 9.3:	Loading cycles for intermediate OTS and GW inspections on test GFRP specimen	55

LIST OF FIGURES

Figure 2.1	: Schematic of forward and inverse problem in NDE	6
Figure 2.2	2: A generic automated data analysis system	8
Figure 2.3	S: Schematic of feature space(from training database) with classification threshold and test data \mathbf{x}	9
Figure 2.4	: (a) Example NDE signal (b)Classification between defect and non-defect (noise) indications from NDE signal	10
Figure 2.5	6: Matrix of four possible outcomes from an NDE procedure for flaw detection	12
Figure 2.6	S: Signal/noise distribution for (a) large flaw (b)medium flaw and (c) small flaw	12
Figure 2.7	7: $a \text{ vs } \hat{a} \text{ model with POD curve generation } ([2])$	13
Figure 2.8	POD curves for example dataset calculated at different threshold parameters (adopted from [3])	15
Figure 2.9	2: (a) Loglikelihood ratio space for regression parameters (b)POD with 95% likely parameters [4]	16
Figure 2.1	0: ROC curves for example dataset having different sized flaws [3]	17
Figure 2.1	1: (a) Self-evaluation in ASC system with confidence metrics (b)Single-pass systems in NDE	19
Figure 2.1	2: 2-means clustering on a synthetic dataset	21
Figure 2.1	3: The probabilistic neural network	22
Figure 2.1	4: A sample feature space with decision boundary (dashed line) separating two classes	24
Figure 2.1	5: Bayesian confidence for one-dimensional case in a two-class classification. (Example: test data is $x=1$)	25
Figure 3.1	: Effect of discriminative quality of features on confidence measure	32

Figure 3.2:	(a)Bootstrappping Bayes confidence, (b) Confidence histogram with $C_{0.95}$ value as the red line	34
Figure 3.3:	Effect of number of training data on confidence histogram and $C_{0.95}$ value for test data X (a) $C_{0.95} = 0.4033$ for n=10 (b) $C_{0.95} = 0.6776$ for n=15 (c) $C_{0.95} = 0.7277$ for n=20	36
Figure 3.4:	Demonstration of confidence computation by weighting with noise	38
Figure 3.5:	(a) 2D scatter plot of training and test data \mathbf{x} with noise distributions.(b) Classification confidence of \mathbf{x} in 'Red' class with respect to varying noise levels of test data	40
Figure 4.1:	(a) Eddy current generation and flow in a conducting specimen (b) Change in impedance of coil in a defect and defect free region (X axis: resistance, Y axis: inductance) [5]	44
Figure 4.2:	(a) RPC configuration (b) Post processed eddy current signal (RPC probe at 300KHz) of a defective SG tube [5]	44
Figure 4.3:	Automtated EC data analysis system with confidence metric computation module	45
Figure 4.4:	Various stages of automated signal processing (a) Raw data, (b) Calibrated data, (c) TSP suppression, (d) thresholding (e) ROI detection [6].	46
Figure 4.5:	Scatter plot for steam-generator tube data showing features from training data from both classes and test data \mathbf{x}	47
Figure 4.6:	(a) Imaginary channel image of a sample eddy current response signal at 300KHz with rectangular ROI box indicating circumferential flaw. (b) Signal with masked tube support and flaw region (c) Noise histogram. (d-f) Repeated for real channel data	49
Figure 4.7:	Experimental noise modelled as a bivariate Gaussian distribution	50
Figure 4.8:	(a) Noise-only signal from ECT of Tube 1 using Pancake and Plus-point probes at 200Hz and 300kHz, (b) Noise histogram of Tube 1 signals, (c) Noise-only signal from ECT of Tube 2 using Pancake and Plus-point probes at 200Hz and 300kHz, (d) Noise histogram of Tube 2 signals	51
Figure 4.9:	Scatter plot for steam-generator tube data showing experimental noise distribution for a test feature x	52

Figure 4.10:	fects and affected by different noise levels	53
Figure 5.1:	Automated analysis system with confidence feedback	56
Figure 5.2:	(a) Training data (b) test data with true class labels of two classes: red and blue	62
Figure 5.3:	Training error rate versus number of weak classifiers in (a) traditional ADABOOST (b) Bayes confidence-rated ADABOOST. Test data classified with ADABOOST model (c) traditional ADABOOST: Error rate on test data= 35% (d) Bayes confidence-rated ADABOOST: Error rate on test data= 35%	63
Figure 5.4:	Comparison of classification performance of traditional ADABOOST and confidence-rated ADABOOST	63
Figure 5.5:	A sample post-processed eddy current signal of defective SG tube. Red rectangular boxes: ROIs containing false indications (classified as non-defect); Green rectangular boxes: ROIs containing true defects	64
Figure 5.6:	(a) Training data (b) test data with true class labels of two classes: red (non-defect) and blue (defect)	65
Figure 5.7:	Training error rate versus number of weak classifiers in (a) traditional ADABOOST (b) Bayes confidence-rated ADABOOST. Test data classified with ADABOOST model (c) traditional ADABOOST: Error rate on test data= 19.40% (d) Bayes confidence-rated ADABOOST: Error rate on test data= 14.93%	66
Figure 5.8:	Eddy current response signal after calibration of 3 defective SG tubes (Imaginary channel, plus point probe, at 300KHz). Green boxes: ROIs (true defects) classified as defects by both traditional and Confidence-based ADABOOST. Red boxes: ROIs (true defects) classified as non-defects by traditional ADABOOST but correctly classified as defects by Confidence-based ADABOOST	66
Figure 6.1:	State variable $X(t)$ and Time to Failure t of a system. [7]	69
Figure 6.2:	Distribution function $F(t)$ and probability density function $f(t)$.[7]	70
Figure 6.3:	Reliability or survivor function $R(t)$. [7]	71
Figure 6 4.	Illustration of damage path prognosis and RIII, prediction [8]	72

Figure 6.5:	(a) 1 degree polynomial fitting on measurement data leading to under estimation of RUL (b)2 degree polynomial fitting on measurement data leading to over estimation of RUL	73
Figure 6.6:	Bayes Updating Process	82
Figure 6.7:	(a) Bayes Updating of parameter m (b) Crack growth example for synthetic dataset with estimated crack growth path	84
Figure 6.8:	Illustration of Bayes estimation using particle filtering technique	86
Figure 6.9:	Illustration of resampling by inverse CDF method [8]	89
Figure 6.10:	(a) Crack growth prediction using PF algorithm (b)Predicted RUL histogram (c) Trace of updating of parameter C (d) Trace of updating of parameter m	91
Figure 7.1:	(a) Healthy GFRP sample (no damage),(b) Delaminated GFRP sample after E=20J impact	95
Figure 7.2:	Experimental setup of optical transmission scanning system with impacted sample under test	96
Figure 7.3:	(a) (top) Healthy (no impact) GFRP sample; $(bottom)$ GFRP sample after E=30J impact (b) OT Scan of (top) healthy; $(bottom)$ impacted sample (c) Segmentation of delaminations in (top) healthy; $(bottom)$ impacted sample.	97
Figure 7.4:	Delamination area propagation with respect to increase in cumulative impact energy	99
Figure 7.5:	(a) Measurement noise collected by photodetector without specimen in absence of laser source (b) Measurement noise histogram : $\mathcal{N}(\mu = 0.2535, \sigma = 0.0091)$	101
Figure 7.6:	OTS scans of GFRP sample (a) healthy (b)-(p) after each consequtive impact from 1 to 15 as mentioned in Table 7.1	105
Figure 7.7:	Growth of delamination area for three samples with increased cumulative impact energies (Solid curve- S1, Dashed curve- S2, Dotted curve- S3).	106
Figure 7.8:	Prediction of delamination area curves based on different number of available measurements (a) n=9, (b) n=10, (c) n=11, (d) n=12. The true measured delamination area curve is plotted in dashed lines	107

Figure 7.9:	Comparison of damage area prognosis by Paris model (dashed line) and Paris-Paris model (solid line) for (a) 1 delamination (b) 2 delaminations (c) 3 delaminations (d) 4+ delaminations	108
Figure 7.10:	Prediction of delamination area curves based on different number of available measurements (a) n=8, Paris model (b) n=7, Paris model (c) n=8, Paris -Paris model (d) n=7, Paris -Paris model. The true measured delamination area curve is plotted in dashed lines	109
Figure 7.11:	OTS scans of GFRP sample (a)-(f) after each consequtive impact from 16 to 21 as mentioned in Table 7.3,(g) Camera image of sample 1 after 450 J impact (H) Enlarged image of delamination reaching the edges and breakage of fibers denoting its end-of-life	111
Figure 7.12:	Growth of delamination area for sample 1 with increased cumulative impact energies upto end-of-life	111
Figure 7.13:	RUL prediction for (a) 1 delamination (b) 2 delaminations (c) 2 delaminations and (d) 4 delaminations	112
Figure 8.1:	Double-cantilever beam (DCB) specimen for Mode I fatigue tests, according to $ASTMD5528$	116
Figure 8.2:	(a) Experimental setup for Mode I GFRP sample subjected to cyclic loading in MTS machine, (b) Enlarged image of GFRP sample under Mode I test	117
Figure 8.3:	(a)GFRP sample under Mode I fatigue tests after 160K load cycles (b) OTS image of GFRP sample with delamination indications	119
Figure 8.4:	OTS images of a GFRP sample (a) Healthy sample and on being subjected to Mode 1 cyclic loading after (b) 20K cycles (c) 40K cycles (d) 60K cycles (e) 80K cycles (f) 100K cycles (g) 120K cycles (h) 140K cycles (i) 160 cycles.	120
Figure 8.5:	(a) Fatigued GFRP sample after 160K load cycles (b) OTS image of delaminated sample (c) Binary image denoting delamination area identified after image processing	121
Figure 8.6:	Plot of number of load cycles versus delamination area from OTS measurements	121
Figure 8.7:	(a) Schematic of GW experimental setup (b)Excited and received signals in healthy sample.	123

Figure 8.8:	(a) Received signal for a healthy sample and sample after 20K-160K cycle (b) TOF between received and excited signal with increase in number of fatigue cycles	124
Figure 8.9:	Correlation between TOF from guided wave signals and delamination area from OTS images	125
Figure 8.10:	Damage prognosis flowchart using guided wave and optical transmission data	126
Figure 8.11:	(a) Predicted delamination area from predcited GW measurements using correlation curve(b) Updation of logarithmic rate ' m' at every estimation step	127
Figure 8.12:	(a) Predicted delamination area from predcited GW measurements using correlation curve(b) Updation of logarithmic rate ' m' at every estimation step	131
Figure 8.13:	(a) Predicted delamination area from predcited GW measurements using correlation curve (b) Updation of logarithmic rate 'm' at every estimation step.	132
Figure 8.14:	Error comparison of prognosis methods for prediction of delamination area from guided wave measurements	133
Figure 9.1:	(a) Reference GFRP specimen failing after 1386 cycles while subjected tension-tension fatigue test under constant load (Max load= 70% of failure load, Stress ratio=0.1,Frequency =3Hz), (b) Test GFRP specimen (identical manufacturing conditions) failing after 2250 cycles subjected to identical fatigue testing conditions (c) Normalized stiffness degradation of reference and test specimen from MTS measurements	135
Figure 9.2:	(a) Digital camera image of GFRP sample with delamination, under Mode I fracture test (b) Low-frequency eddy current inspection usng TR coil at 10MHz(c) Near-field microwave scan at 7.5GHz (d)Optical transmission scan at 2.5mW	136
Figure 9.3:	Bayesian network in multi-sensor particle filtering framework	144
Figure 9.4:	(a) Experimental setup for tensile open-hole GFRP coupon subjected to cyclic loading in MTS machine, (b) Healthy and broken GFRP coupons subjecte to fatigue	146

Figure 9.5:	(a) Stress-strain hysteresis loop of GFRP specimen at different intervals of fatigue cycles (b) Stress-strain slope or stiffness modulus (S) as a function of number of load cycles	148
Figure 9.6:	(a) Healthy open-hole GFRP coupon (b) OTS image of healthy GFRP coupon (c) OTS image of GFRP coupon after 900 fatigue cycles at 70% of failure load and stress ratio of 0.1	149
Figure 9.7:	OTS images of an open-holed GFRP coupon under fatigue loading :(a) Healthy (0 cycles) (b)200 cycles (c)400 cycles (d) 600 cycles (e) 800 cycles (f) 900 cycles (g) 1000 cycles (h) 1100 cycles (i) 1200 cycles (j) Total failure at 1386 cycles	150
Figure 9.8:	(a) Increase in delamination area in open-holed GFRP coupon under fatigue loading, from OTS measurements (b)Correlation between normalized stiffness from MTS measurements and delamination area from OTS images	150
Figure 9.9:	Guided Wave inspection of GFRP specimen (a) Experimental setup (b) Schematic of pressure sensitive skin	152
Figure 9.10:	(a) Time shift in GW signals in progressively damaged GFRP specimen under fatigue cycles (b) Enlarged region in S_0 mode of received GW signals	.153
Figure 9.11:	(a) Increase in ΔTOF in open-holed GFRP coupon under fatigue loading, from GW measurements (b) Correlation between normalized stiffness from MTS measurements and delamination area from GW images	154
Figure 9.12:	Prediction of stiffness degradation curve based on different number of available OTS measurements in Paris-Paris model (a) $n=4$, (b) $n=8$ (c) $n=12$ (d) $n=16$	157
Figure 9.13:	${\rm RUL\ prediction\ for\ varying\ number\ of\ available\ OTS\ measurements\ (NRMSE)}$	E=0.1761).157
	Prediction of stiffness degradation curve based on different number of available GW measurements in Paris-Paris model (a) n=4, (b) n=8 (c) n=712 (d) n=16	159
Figure 9.15:	${\rm RUL\ prediction\ for\ varying\ number\ of\ available\ GW\ measurements\ (NRMSE)}$	=0.1441).159
_	Prediction of stiffness degradation curve based on different number of available AVG measurements in Paris-Paris model (a) n=4, (b) n=8 (c) n=12 (d) n=16	161
Figure 9.17:	RUL prediction for varying number of available AVG measurements (NRMSI	Ξ =0.1507).161

Figure 9.18:	Prediction of stiffness degradation curve based on different number of available measurements using joint likelihood computation in Paris-Paris model (a) n=4, (b) n=8 (c) n=12 (d) n=16	162
Figure 9.19:	RUL prediction for varying number of available OTS and GW measurements using joint likelihood computation (NRMSE= 0.065)	164
Figure 9.20:	(a) Error comparison for varying number of available OTS and GW measurements, (b) Error comparison for varying number of particles in PF algorithm	164
Figure A.1:	Example of Bayesian Network with children nodes $(X_1, X_2,, X_M)$ and their parent node (P)	170
Figure B.1:	Material directions in a specimen $x \equiv 1; y \equiv 2; z \equiv 3. \dots$	173

Chapter 1

Introduction

1.1 Motivation & Objective

With advancement of technology in recent years, the field of nondestructive evaluation (NDE) and testing have shifted its gears from classical approaches to more complex inter-disciplinary operations. Traditional NDE systems have focused mostly on evaluation of mechanical components for the detection and characterization of defects in materials or structures. However with discovery of new scientific methods and imaging systems, the field has grown both in scope and across disciplines. NDE engineering is no longer just restricted to detecting and characterizing defects but extends to analyzing 'risk versus rewards' and 'remaining useful life' of systems and components. Overall, industries have started demanding designers, system integrators and operators to collaborate and develop "cradle-to-grave" evaluation solutions.

Integrated NDE inspection primarily comprises two equally important processes (i) diagnostics of systems' health and (ii) prognostics or prediction of remaining operational lifetime.

NDE diagnostics comprises identification of distinguishing features which are indicators of any anomaly or deterioration of general health of industrial components. Existing and emerging NDE monitoring techniques include mechanical, electrical, electromagnetic or optical methods that can successfully image or indicate presence of flaws without compromising

their usefulness. One of the crucial aspects of NDE diagnostics is maintaining reliability and accuracy of its evaluation performance. With increase in amount of information from numerous NDE applications such as defect characterization in steam generator tubes, natural gas transmission pipelines, aircraft engines and components, artificial heart valves and many more, automated data analysis systems have become necessary. In dealing with such large volumes of data, manual analysis besides being time-consuming is often inconsistent which demands the need for automated signal classification (ASC) systems to identify anomalies with reduced error by applying suitable signal processing algorithms on the acquired NDE response signal. Often, expensive remedial operations are involved based on the classification results requiring more accuracy and consistency in ASC systems. After a defect is detected in a tube, it is either replaced or repaired which is both time-consuming and expensive. On the other hand, detection of potentially harmful anomalies which may be fatal and should not be missed at any cost. Such defects should be identified with greater certainty than those generated from benign discontinuities. Hence design of self-evaluating automated data analysis systems have become the need of the hour where safety and serviceability of structural components can be met while necessary level of operator intervention is minimized.

The second crucial process in modern NDE systems is the prognosis of structural aging over time. Prognosis deals with predicting future health of a system, specifically to predict the time until which the system is deemed to be safe. The diagnostic step feeds vital information to the prognostic arm wherein past and present health indicators are used to predict future health of a structure. By calculating the long-term reliability or prognosis of remaining useful life, failures can be avoided enabling the maximum serviceability of the component. This is extremely beneficial to industries since it ensures maximum usage from the component.

Another important advancement in modern NDE is the practice of multi-modal sensing and inspection techniques for characterizing materials or structures. Rapid development in sensing and computing technologies has enabled the use of more than one sensor for simultaneous condition based maintenance (CBM) of a component. Many times a single measurement technique has limited capabilities for characterizing structural health of a component due to their resolution constraints. Different sensors are sensitive to different stages of degradation and can portray multiple perspectives of the underlying damage growth path, thus providing more information about system health. As a result, fusion of measurements from multiple sensors helps reduce the uncertainty of individual sensor signal and enhances the reliability of prognosis. Data fusion techniques are a promising enhancement in the field of NDE wherein current measurement systems combined with advanced statistical processing can provide more reliable results.

The principle objective of this thesis is to provide a detailed investigation of NDE diagnostics and prognostic tools that aim at enhancing reliability, accuracy and consistency of damage detection and characterization systems. Specifically, sources of uncertainties typically encountered in NDE measurement systems and their effects on the final diagnosis of defects are studied. A confidence metric based on Bayes posterior probability has been proposed which can incorporate several factors of uncertainty to provide a comprehensive metric to the final inspection results. Further, use of statistical estimation and optimization tools such as particle filtering method are employed for prediction of damage growth in composite materials. Results from prognosis of delamination in glass fiber reinforced polymers in association with data fusion from multiple NDE modalities are presented in this thesis.

1.2 Scope and Organization of the dissertation

There are ten chapters in this dissertation. Chapter 1 introduces the motivation and objectives of this study. The remaining of the report can be broadly categorized in two parts. Chapters 2-5 discusses the problem of diagnostics in NDE in which the overall background of existing statistical aspects in NDE diagnostics is discussed in chapter 2. Chapter 3 focuses on the importance of confidence metric in NDE signal classification and describes the proposed method of computing a comprehensive Bayes confidence. Results on applying confidence assessment on real data from eddy current inspection of heat exchange tubes are presented in chapter 4 and improving existing classification algorithms by incorporation of confidence metric is demonstrated in chapter 5.

Chapters 6-9 are devoted to prognostics in NDE. The background review and theory of prognosis is discussed in chapter 6. Chapter 7 describes particle filtering technique for predicting damage propagation model and residual life based on NDE data acquired by direct condition monitoring. Results obtained by applying the proposed method on study of impact-damage growth in composites are presented in the same chapter. Prognosis results on indirect condition monitoring of composite joints subjected to Mode I fatigue mechanism are presented in chapter 8. Chapter 9 discusses the benefit of multi-modal NDE measurements on the prognosis of end-of-life of a component. A joint likelihood update method is proposed to particle filtering framework which enables optimization of damage growth model parameters at every time step by discarding noisy or biased measurements. Prediction results of matrix stiffness degradation in tensile composite coupons subjected to run-to-failure fatigue tests are presented. The overall contribution of this research in the field of NDE and future scope of work are summarized in Chapter 10.

Chapter 2

Diagnostics in NDE

2.1 Introduction

Nondestructive evaluation (NDE) encompasses the study and inspection of objects without compromising their structural integrity. In a typical NDE inspection, a test object is stimulated by an external energy source and the response of the energy interaction with the test material is recorded. A schematic of of a typical NDE system with the associated forward and inverse problems, is depicted in Figure 2.1. Forward problem involves prediction of the defect signal given the material, defect parameters and excitation energy. This can be done via experimental methods using appropriate energy sources or via mathematical models which can simulate underlying governing equations (eg: Finite Element Model). On the other hand, detection and characterization of defects based on NDE measurements forms the inverse problem. This includes processes to realize properties of the structure from the NDE response image/signal. Inversion techniques in industries include development of data analysis and image processing methodologies to interpret NDE measurements for visualization, full profile reconstruction or classification of defects in structures. Full profile reconstruction is required for determining size and shape of defects, whereas classification is applied to distinguish defect indications from measurement noise and decide if a flaw is serious enough to render a component unacceptable or unusable.

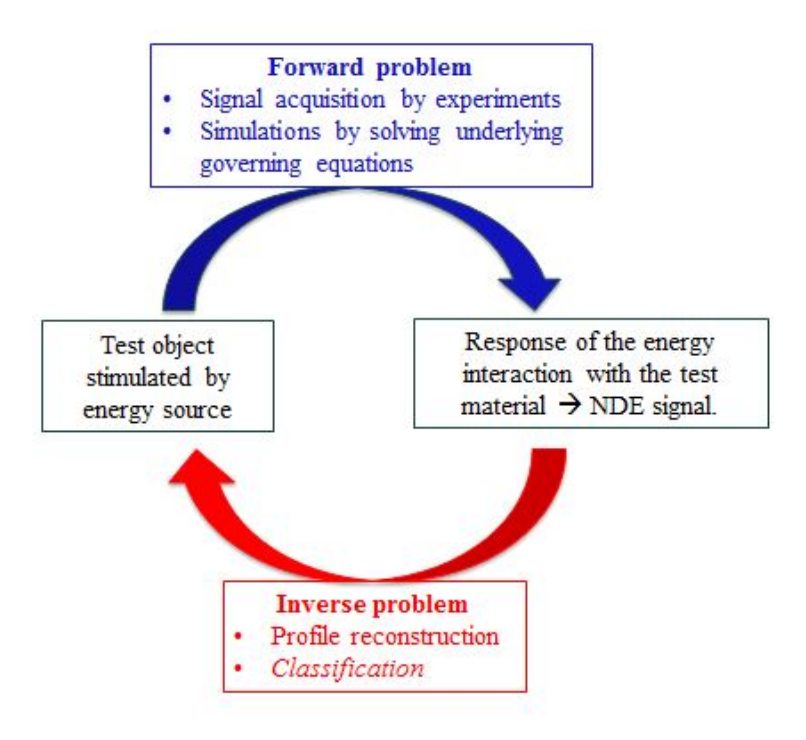


Figure 2.1: Schematic of forward and inverse problem in NDE.

In NDE, automated classification systems are used to analyze large volume of measurement data. For example, defects at rivet sites in aircraft wings is is commonly inspected using electromagnetic NDE methods. Each aircraft wing contains thousands of rivets, with defects in only a few of them. NDE inspection of such structures generate huge amount of information that needs to be processed and classified into defect and non-defect categories. Other NDE applications such as inspection of gas pipelines extending upto hundreds of miles or inspection of thousands of tubes in heat exchange units by multiple probes produce large volumes of data. In such cases, manual analysis of individual measurements take excessive time. Besides, errors due to human fatigue often lead to inconsistent and inaccurate classification results. Performance of manual analysis depends on level of training acquired by the NDE operator which may vary from person to person. Therefore industries are moving towards th use of automated systems that can analyze large volume of NDE measurements faster and with higher accuracy, consistency and reliability [9] [10]. In nuclear industries,

single-pass systems or single-party-analysis is preferred over two-party-analysis whereby NDE signals are analyzed by automated data analysis systems and only a few selected signals are reviewed by review analysts. This reduces cost of human resources as well as down time of the power plant. Moreover, shorter and more accurate inspections by automated systems have a significant economic impact on the overall station's operational cost, since each day of station shutdown can result in millions of dollars in lost revenue. Thus, shorter inspections and prevention of unplanned shutdowns can help the stations save millions of dollars [11].

2.2 Automated Signal Classification in NDE

A schematic of a typical Automated Signal Classification (ASC) system is shown in figure 2.2. It comprises three major components- (1) Signal enhancement, (2) Feature Extraction (3) Classification. Signal enhancement techniques improves the signal-to-noise ratio of input raw signal using methods ranging from simple averaging and low-pass filtering methods [12] to more sophisticated techniques such as wavelet shrinkage de-noising [13] and adaptive noise cancellation. Noise contained in a signal can be attributed to several sources including instrumentation, probe wobble and variations in lift-off or from unwanted reflections caused by the specimen's surface roughness. Depending on the characteristics of noise, different filtering techniques are implemented. Once noise is removed from input signal, regions-of-interest (ROI) or potential defect locations are identified by implementing adaptive thresholds.

After data reduction step, meaningful features are extracted from the ROIs which are able to discriminate defects from noise indications. Feature extraction serves two major functions, namely data compression and invariance. A judiciously selected feature vector contains most of the discriminatory information and yet be substantially smaller in dimension

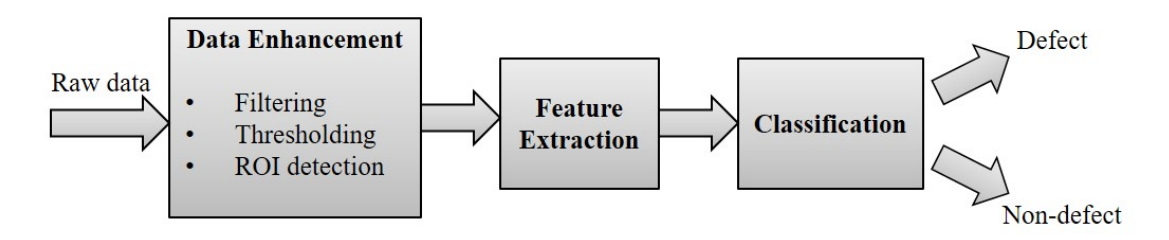


Figure 2.2: A generic automated data analysis system.

relative to the original signal vector. This, in turn, improves the classification accuracy and reduces the overall computational effort. Moreover, NDE signals are often acquired under varying test conditions and their results are sensitive to factors such as variations in probe characteristics, scanning speed, operating frequencies, test object conductivity and permeability values, instrument drift, gain settings, etc. Feature extraction serves as an important step in ASC of NDE signals where features are chosen so that they are invariant to changes in test conditions or test specimen properties.

After feature extraction, the feature vector is sent to the classification module. Signal classification techniques, based on pattern recognition principles, are used to classify signals into one of a known set of classes. Such methods may be employed to discriminate between multiple types of defects or between defects and benign sources. Several classification algorithms have been used in NDE such as K-means clustering [14], neural networks[15], support-vector machine and density estimation techniques. The parameters of the classifier are determined offline using a data bank of signals from known defect types, referred to as the training database. Similar features are extracted from the test ROI and sent as input to the classification algorithm to obtain the output class of the test signal. A schematic of feature space, obtained from training database, with classification threshold and test data is shown in Figure 2.3, indicated by "x". Based on the location of the test feature point, the test data is classified into either of the classes.

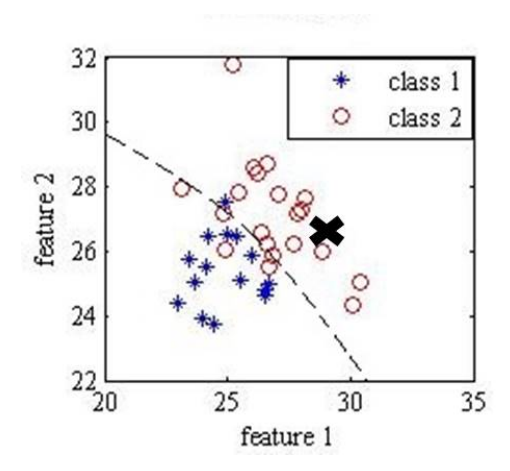


Figure 2.3: Schematic of feature space(from training database) with classification threshold and test data \mathbf{x} .

2.3 Statistical measures in NDE

NDE measurements provide indirect indication of defect locations. For example,eddy current testing generates a complex voltage signal from which relevant features are extracted and classified into positive(defect) and negative(non-defect) indications by human or automated discriminators. Positive signals may be generated from non-defect sources such as surface roughness, grain sructure, variations in geometry and material properties. It is important to note that such signals constitute the application noise inherent to a specific NDE procedure and is different from electronic or measurement noise which can be eliminated by filtering or averaging techniques. Discrimination threshold of NDE signals must be set such that the defect indications exceed the level of application noise. In Figure. 2.4 (a), an example signal/ image obtained from eddy current technique is shown. A histogram of the pixels from the 'defect' and 'non defect or noise' indications typically forms a bimodal distribution and a threshold can be selected to clearly distinguish the defect pixels from the noise indications, as demonstrated in Figure 2.4 (b).

Although control measures are applied to ensure a consistent output, measurements from

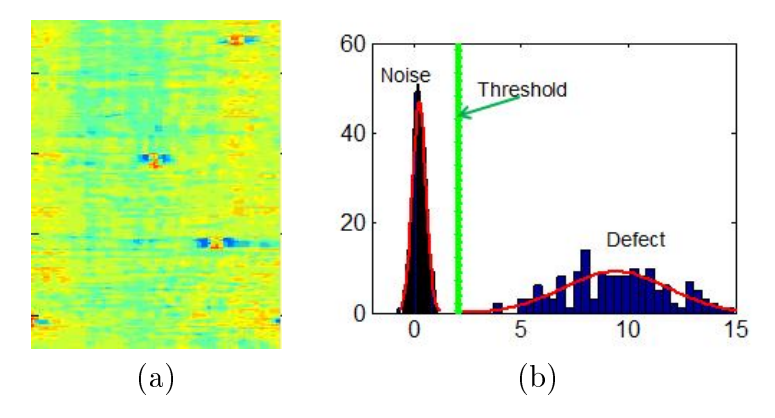


Figure 2.4: (a) Example NDE signal (b) Classification between defect and non-defect (noise) indications from NDE signal.

an NDE system varies within control parameters. Specifically, if the same NDE experiment is repeated multiple times, it is unlikely to obtain the same result every time because of slight variations in hardware, material properties, geometry or surface condition. As a result, a probability distribution of signal is generated at the output instead of a deterministic result. Due to the inherent stochastic nature of any NDE process, several statistical measures such as probability of detection (POD), probability of false alarms (PFA), Receiver-Operating Characteristic (ROC) curve and confidence bounds are defined to characterize detection capability of an NDE procedure. These measures are obtained by using data from experiments. The objective of these measures is solely to characterize inspection capability of the NDE method by providing estimates and confidence bounds for important quantities as described in the following sections.

2.3.1 Hit/Miss response

The name "hit/miss" is derived from the ability of some NDE procedures to detect only the presence or absence of a flaw, providing no quantitative information about flaw characteristics. Binary responses of this type are most common for methods such as the liquidpenetrant imaging and radiography, for which there may be limited ability to measure the flaw size. For a hit/miss data, the response is typically defined as:

$$Y = \begin{cases} 1, & \text{if defect is detected} \\ 0, & \text{if defect is not detected} \end{cases}$$
 (2.1)

2.3.2 Probability of Detection (POD) and Probability of False Alarm (PFA)

When NDE assessment for crack detection is performed, the inspection capability of the procedure cannot be fully characterized by a simple Hit/miss response. As shown in matrix in Figure 2.5 the possible outcomes from a typical inspection system are:

- (a) True positive (TP): A crack exists and is detected, where M(A,a) is the total number of true positives and P(A,a) is the probability of true positive.
- (b) False positive (FP): No crack exists but is identified by the NDE system, where M(A,n) is the total number of false positives and P(A,n) is the probability of false positive.
- (c) False negative (FN): A crack exists but is not detected, where M(N,a) is the total number of false negatives and P(N,a) is the probability of false negative.
- (d) True negative (TN): No crack exists and is not detected, where M(N,n) is the total number of true negatives and P(N,n) is the probability of true negative.

To completely characterize detection capbility of a NDE system, two measures are defined. The probability of detection (POD) or probability for a true positive P(A,a) can be expressed as: $P(A,a) = \frac{M(A,a)}{M(A,a)+M(N,a)}$ or Total true positive calls.

Inspection output Positive, a Negative, n True Positive False Positive (Flaw detected) (False alarm) M(A.a)M(A,n)Positive. A P(A,a) P(A,n)(no error) (Type II error) Ground truth **False Negative** True Negative (Undetected flaw) (No flaw) M(N,a)M(N,n)Negative, N P(N,a) P(N,n)(Type I error) (no error)

Figure 2.5: Matrix of four possible outcomes from an NDE procedure for flaw detection

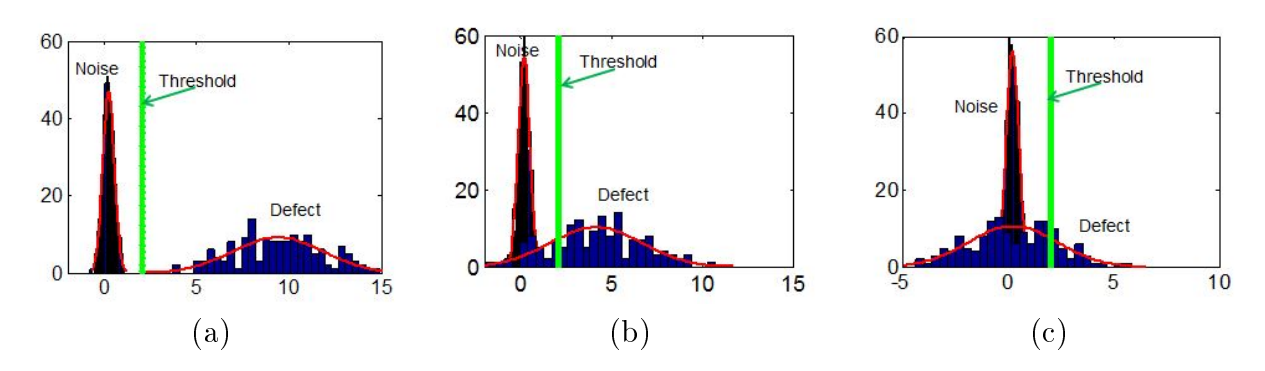


Figure 2.6: Signal/noise distribution for (a) large flaw (b)medium flaw and (c) small flaw.

Similarly, the probability of false alarm (PFA) or probability for a false positive P(A,n) can be expressed as: $P(A,n) = \frac{M(A,n)}{M(A,n)+M(N,n)}$ or $\frac{\text{Total false alarms}}{\text{Total number of non-defects}}$.

For a given flaw size, distributions for application noise and defect signal are depicted in Figure 2.6. The region to the right of the chosen decision threshold corresponds to the POD whereas the region to the left of the threshold represents the PFA. It is obvious that the shaded regions representing POD and PFA depends largely on the distribution of noise and defect signal as well as on the choice of decision threshold.

Under ideal conditions, such as response from a large flaw, the signal and noise distributions are well separated and can be clearly discriminated by the chosen threshold, as shown

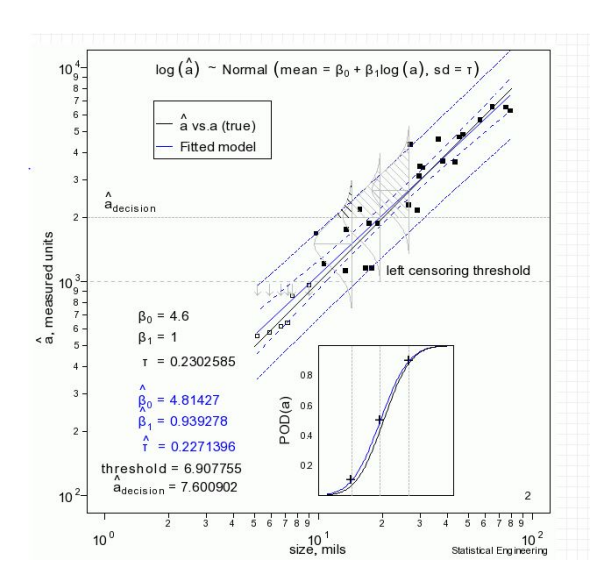


Figure 2.7: a vs \hat{a} model with POD curve generation ([2]).

in Figure 2.6 (a). This corresponds to the most desirable output with high POD and low PFA. For medium flaws as shown in Figure 2.6 (b), there is some overlap between the two distributions. If threshold is the same as the previous case, this NDE inspection will be characterized with lower POD and higher PFA than case (a). Similarly, detection of the smallest flaws is most challenging since the noise and defect signals cannot be separated resulting into lowest POD and highest PFA.

2.3.3 a vs \hat{a} Model

Calculation of POD can be extended to flaws of multiple sizes to generate a POD curve. Suppose a is the true flaw size, the signal response estimated from the output of NDE inspection corresponding to a flaw size a is termed as \hat{a} . Under ideal conditions, measurement \hat{a} is supposed to be exactly equal to true size a and correspond to the black solid line in a versus \hat{a} plot in Figure 2.7. However, in NDE inspections the true size is unknown and relationship between a and \hat{a} is inferred only from the measurement data. According to empirical studies in [16], it was found that a normal-theory regression model, with standard

devaition σ , can be applied to logarithmic transformation on a and \hat{a} such that:

$$Y = \mathcal{N}(\mu = \beta_0 + \beta_1 x_i, \sigma) \tag{2.2}$$

where, $Y = \log \hat{a}$, $X = \log a$, β_0 and β_1 are the regression parameters. For a a versus \hat{a} model in NDE, a threshold a_{th} is set; whenever \hat{a} exceeds the threshold, the ROI is classified as a flaw and the corresponding POD is calculated. The POD is calculated for varying flaw sizes and a POD curve is generated as shown in Figure 2.7. The Probability of Detection (POD) curve is further defined as

$$Pr(\hat{a} > a_{th}|a) = 1 - \phi(\frac{a_{th} - (\beta_0 + \beta_1 \log a)}{\sigma})$$
 (2.3)

where $\phi(Z)$ is the standard normal cdf. Figure 2.8 illustrates the estimated POD curves for a dataset with varying threshold parameters. These curves are useful to examine the trade-off between number of hits versus misses. POD functions can be defined for more general NDE models by including the inspection factors unique to the NDE procedure. Details of POD studies in NDE are available in [17, 18, 19].

2.3.4 a90/95 Confidence Bounds on POD curve

POD curves are critical in assessing the detection capability of any NDE measuring system. However, accuracy of a POD curve is itself dependent on the estimation of the regression parameters β_0 and β_1 . Slight change in these parameters can affect the POD curve greatly and therefore it is necessary to pose confidence bounds on them to allow for discrepancies in the estimated POD values.

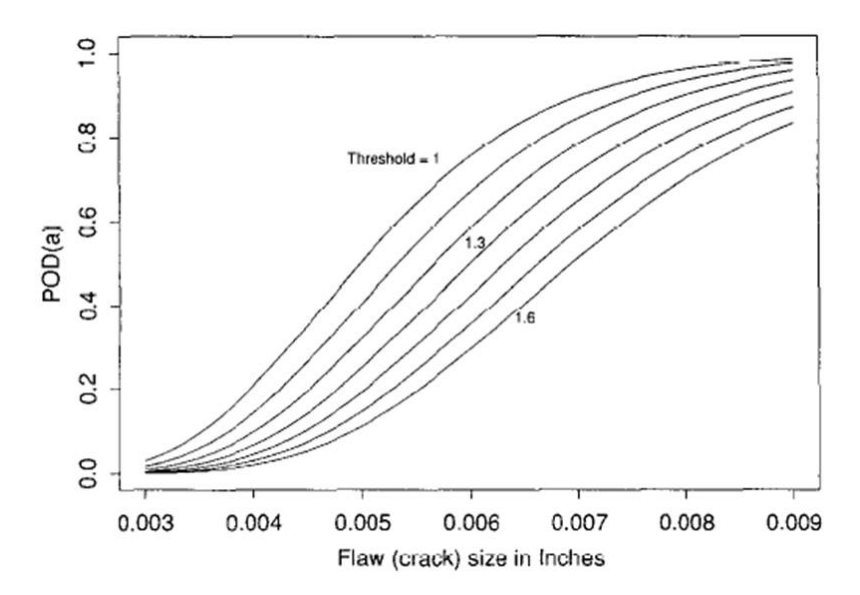


Figure 2.8: POD curves for example dataset calculated at different threshold parameters (adopted from [3]).

Consider a plot of the loglikelihood ratio for different values of μ and σ , as shown in Figure 2.9 (a). According to Knopp et al. [4], if the pair of parameters is moved from their maximum likelihood estimate (MLE) position denoted by +, the loglikelihood changes, as illustrated by the contour lines. One of the contours, shown by the dotted line, is the 95% confidence bound for the parameter estimates based on these data. In other words, the true μ and σ pair is expected to be contained within the confidence ellipse in 95% of future experiments simlar to this one. POD curves are then constructed for all the points along the 95% confidence ellipse as shown in Figure 2.9 (b). The envelope of all these POD(a) curves represents the confidence bounds on the POD(a) curve. The POD curve corresponding to the MLE of parameters is shown as the black solid line in figure 2.9(b). The point where the estimated POD curve intersects POD=0.9, is known as the a90/95 value which represents that in 95 out of 100 similar experiments, the output flaw size having POD of 0.9 will lie within the estimated confidence bounds.

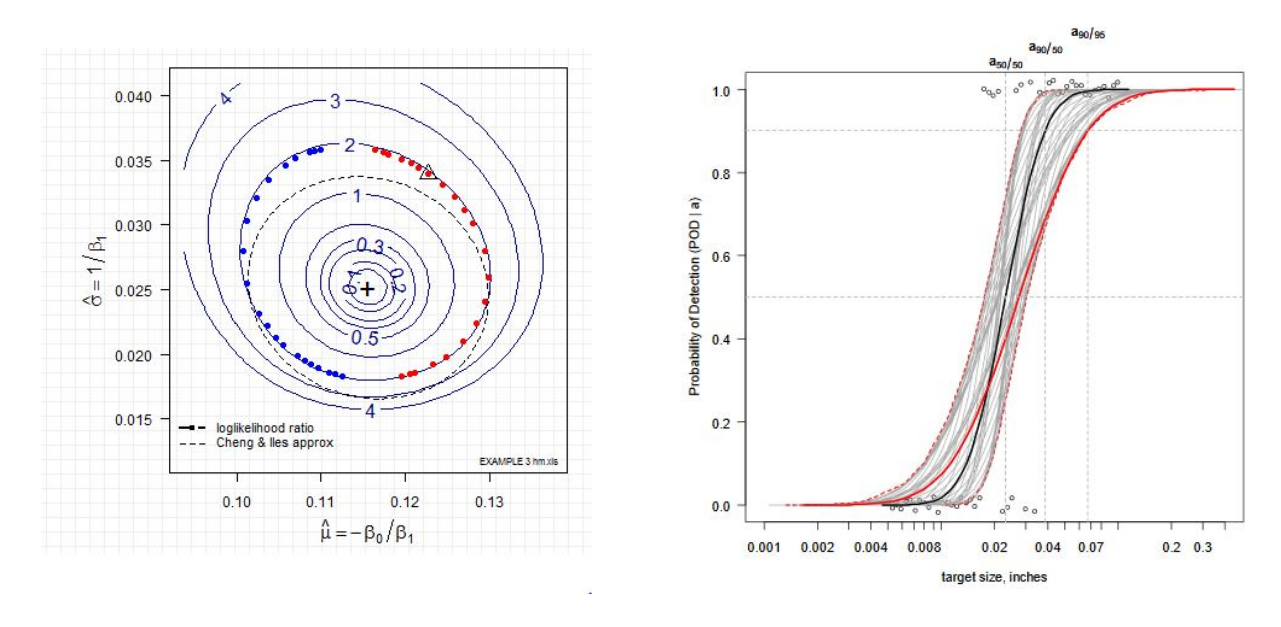


Figure 2.9: (a) Loglikelihood ratio space for regression parameters (b)POD with 95% likely parameters [4].

2.3.5 Receiver Operating Characteristics (ROC)

The ROC curve is a plot of Probability of False Alarm on the horizontal axis and Probability of Detection on the vertical axis, as shown in Figure 2.10. The ROC function is generated by varying detection threshold over all possible values. ROC functions were originally developed to illustrate the effect of choice of threshold on the probability of misclassification in radar applications [20].

If a set of measurements, containing a group of flaws of similar size, is repeatedly assessed, the POD and PFA can be calculated which forms a single point on the ROC curve. This process is repeated by several operators of varying levels of proficiency (denoting varying thresholds) and the ROC curve is generated. A superior discriminating performance of the NDE inspection will result in high POD and low PFA, or the top-left region of the ROC curve is considered as the preferred threshold.

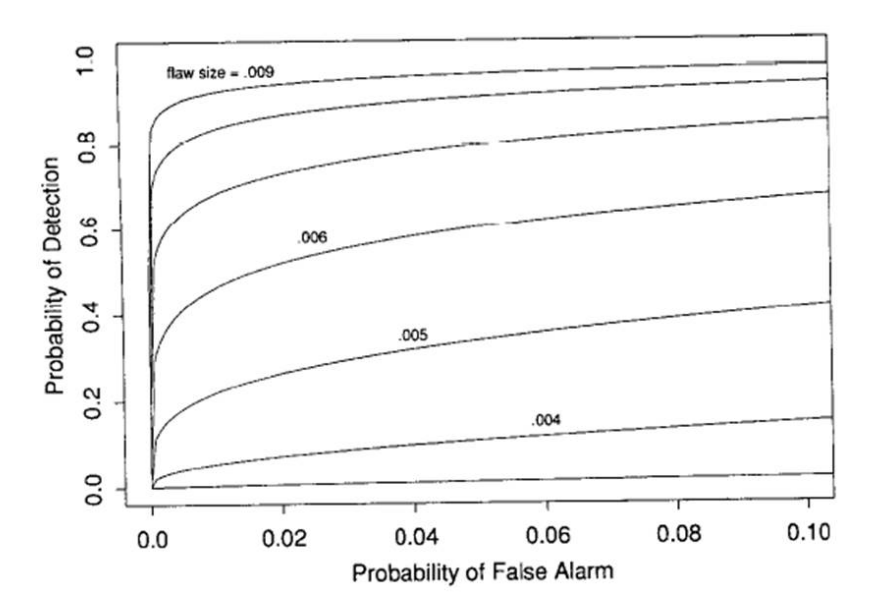


Figure 2.10: ROC curves for example dataset having different sized flaws [3].

2.3.6 Confidence Metric

Statistical measures such as POD and ROC curves with their confidence bounds assesses the inherent detection performance of any NDE measuring system. While ROC curve aids in selecting the optimum threshold for detecting defect of a particular size, POD curve shows the effect of flaw size on detection capability for a fixed threshold. Both these curves are critical for assessing the minimum flaw size that can be accurately detected using the NDE procedure.

However, these measures do not deal with the complete picture of system reliability in NDE. Apart from inherent uncertainties of the measuring system, classification by automated systems are affected by other factors which are not taken into account in either of these measures. An inspection system with high detection capability can still produce inaccurate results if the ASC system is under-trained or sub-optimal signal features are selected. Further, while computing POD and PFA, only application noise is considered which is inherent to the NDE technology. Random noise in measurements which may occur due to

probe lift-off variations, unexpected change in structural geometry or machine fatigue affects classification results which is not captured by either POD or ROC measure.

Most importantly, both POD and ROC curves are generated using experimental data with known flaw sizes, for characterizing the measurement system before applying to field data. On contrary, when field data is inspected by NDE procedure, the ASC system is unaware of defect sizes and the field data can be significantly different from experimental data used to compute POD or ROC curves. The test data of unknown defect profile is processed and the final classification results are based solely on training and selected features. As a result, existing POD and ROC curves cannot quantify reliability of ASC system which is affected by number and distribution of training signals, quality of features and measurement noise in test data. A reliability measure of the ASC system is defined in terms of confidence metric (CM) to quantify uncertainties associated with classification of every ROI. Assessment of CM to individual field data observations is a necessary tool in NDE diagnostics since potentially harmful anomalies are expected to be detected with greater probability than benign discontinuities and an ASC system with such capability can automatically flag indications for which operator intervention is required. As depicted, in Figure 2.11 (a), NDE data 3 and 4 identified with low confidence can be further analyzed before directly replacing or repairing the 'defective' component. By reviewing only selected signals (having low CM), single-pass systems can be reliably used in industries thereby saving both time and cost of human resources.

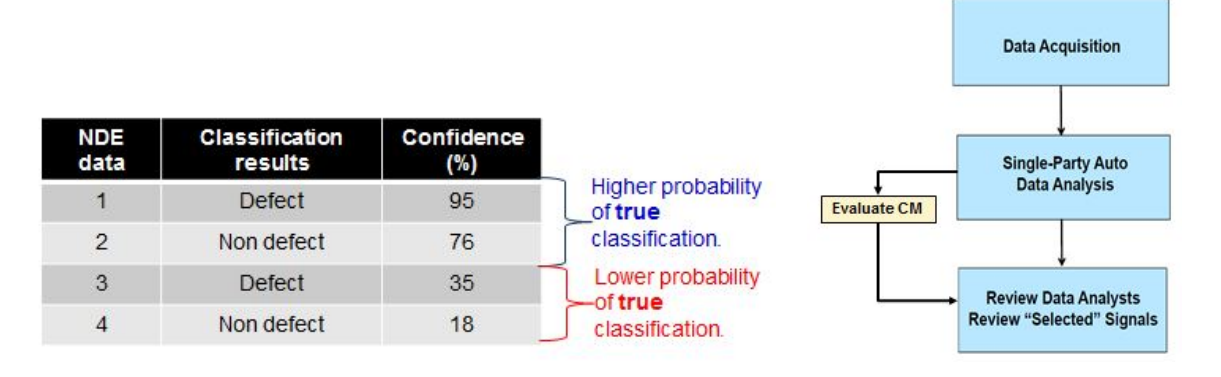


Figure 2.11: (a) Self-evaluation in ASC system with confidence metrics (b) Single-pass systems in NDE.

2.4 Existing confidence metrics

The following section is dedicated to a review of some exising confidence metrics to understand their capabilities and shortcomings in different classifiers.

2.4.1 Confidence in binary form

Initial part of literature on classification algorithms has restricted confidence measure to have a binary form. Grunwald et al.[21] uses high confidence (sure) and low confidence (unsure) as the two labels to denote whether a given indication is correct (C) or incorrect(I). Bailey et al.[22] build on the concept of a rejection region implementing uncertainty envelopes (UE) that are associated with unsure classifications. When tested with a large number of classifiers, the percentage of classifiers that correctly classifies the same exemplar is the level of confidence associated with that exemplar. In such cases, a user-defined threshold is applied to form the UE. Any data falling into the uncertainty envelope is unsure, and any data falling outside the uncertainty envelope is sure. Thus, the confidence measure is essentially a binary indicator, either sure or unsure. Similar concepts have been used by Krzanowski[23] and Jacobsen[24]. Although, these confidence measures give a good estimate

of success-failure analysis of classification, the usage of a user-defined threshold makes these approaches heuristic in nature and do not particularly address the effect of uncertainties in a classification.

2.4.2 Confidence in terms of probability

The most popular method of quantifying uncertainty in classification has been in the form of probability. Due to inherent characteritics of a NDE system, noise and signal conditional distributions overlap and a test data falls under both the classes with different probabilities. Different classification algorithms in literature such as K-nearest neighbor Similarity Ratio [25] provide probability scores which can be defined as confidence metrics. A few other approaches are discussed further.

2.4.3 Similarity Ratio in Clustering

Clustering[14] is an intuitive means of classification that uses the fact that patterns from the same class tend to be similar to each other. Members of a class tend to cluster around a point in feature space. It is a simple algorithm which minimizes the objective function:

$$J = \sum_{i=1}^{k} \sum_{i=1}^{n} \left\| x_i^{(j)} - c_j \right\|^2$$
 (2.4)

where $||x_i^{(j)} - c_j||^2$ is a chosen distance measure between a data point $x_i^{(j)}$ and the cluster centre c_j . n is the total number of data points and k is the number of classes the data is grouped into. The simplest form of clustering is the K-means algorithm which assigns data points to the group that has the closest centroid. Figure 2.12 shows the result of application of 2-means clustering on a synthetic dataset. One possible confidence metric

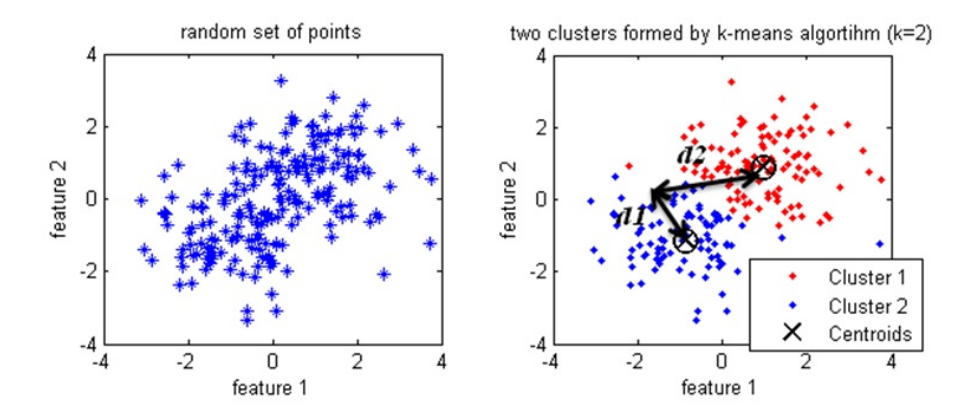


Figure 2.12: 2-means clustering on a synthetic dataset.

in cluster analysis is formulated based on closeness of a data point to the cluster with the closest center. A point which is closer to the centre of its assigned cluster will be associated with higher confidence of classification compared to a point which is far from the cluster. Confidence associated with classification of a datapoint can be computed as:

$$C = 1 - \frac{d_m}{\sum_{i=1}^{k} d_i} \tag{2.5}$$

where d_i is the distance of datapoint i from k cluster centres and d_m is its distance from the cluster to which it is classified to.

2.4.4 Membership Functions in Neural Networks

Neural networks have been used successfully in pattern recognition largely due to their simple learning algorithms and ability to generate complex decision boundaries. They consist of weighted interconnections of simple processing units called neurons. Each weight represents the interconnection strength between two cells. Learning occurs by a process of adapting the weights to reflect mapping of an input to a desired output. Pradeep [26] uses

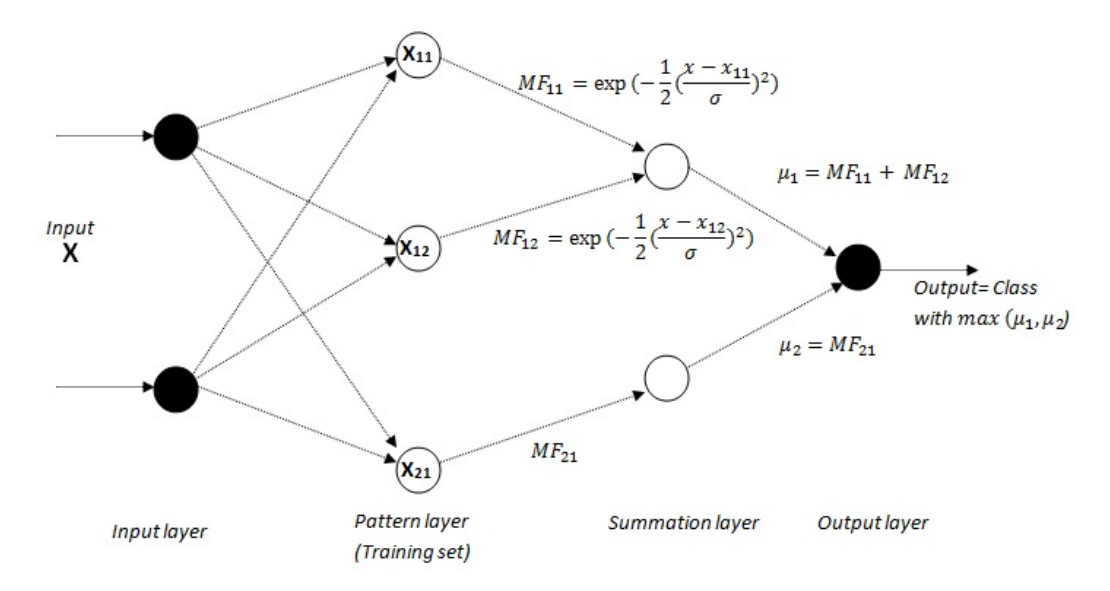


Figure 2.13: The probabilistic neural network.

probabilistic neural network (PNN) as the classification scheme applied on a database of ultrasonic signals obtained from inspection of tubes in nuclear power plants. He further uses membership function to represent the confidence associated with every signal classification. Figure 2.13 shows the architecture of a PNN. The input pattern is multiplied by the interconnection weights and sent to the second layer pattern nodes representing the training dataset. Each pattern unit implements membership function MF defined as:

$$MF = exp\left(-\frac{1}{2}\left(\frac{x-c}{\sigma}\right)^2\right) \tag{2.6}$$

where x is the input and c, σ are the center and spread of the Gaussian membership function of that pattern node. The output of each pattern unit j is the degree t_j to which the rule fires.

$$t_j = MF_j(y_j) \tag{2.7}$$

The outputs of pattern nodes belonging to the same class are sent as input to the summation layer and their corresponding membership values are aggregated. The input pattern is assigned to the class having the maximum output from summation layer. Classification confidence can be interpreted as the aggregated membership values μ_i :

$$\mu_i(x) = \sum_{j \in C_i} t_j \tag{2.8}$$

2.4.5 Posterior Probability in Density Estimation techniques

In classification via density estimation techniques, concept of posterior probability contains relevant information to assess the accuracy of classification result [27, 28, 29]. The datapoints to be classified are assumed to be generated by a underlying probability density function of respective classes. Classification is performed by estimating the density functions for 'defect' and 'non-defect' class and assigning a data to the class having maximum density value. Density estimation techniques include parametric approaches such as Maximum Likelihood Estimate or non-parametric methods such as Parzen window classifier and K-nearest neighbors. A typical confidence metric in density estimation technique is the Bayes posterior probability or the Bayes Confidence.

2.5 Bayes Confidence

During training of the system, features from training data are plotted in a hyper-dimensional feature space and a decision boundary is obtained such that the classification error is minimized as shown in Figure 2.14. This decision boundary partitions the feature space in two categories, defect (class1) and non-defect (class2). Features from test signal are extracted

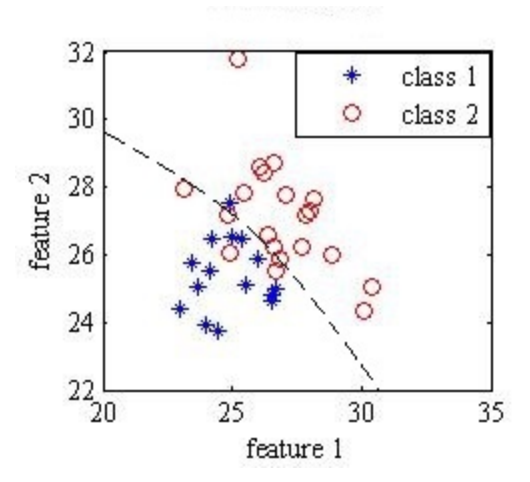


Figure 2.14: A sample feature space with decision boundary (dashed line) separating two classes.

and the signal is classified into the class depending on the location of the test data relative to the decision boundary.

According to Bayes theorem, if x is a pattern vector from a class A_i , the posterior probability of class A_i given x is written as the conditional probability $P(A_i|x)$. Thus, the probability distribution of a class is conditioned on evidence obtained from training data and x is assigned to the class having maximum posterior probability density function.[30]

Confidence in classification can be defined as the probability of making a correct decision. Consequently, the confidence of classifying a test data in class A_i is the posterior probability function, given by the well-known Bayes rule. [31]

$$P(A_i|x) = \frac{p(x|A_i)P(A_i)}{\sum_{i=1}^{c} p(x|A_i)P(A_i)}$$
 (2.9)

where,

 $P(A_i|x)$ is the class-conditional density for a class A_i

 $P(A_i)$ is prior probability of class A_i

 $P(A_i|x)$ is posterior probability of class A_i given the pattern vector x.

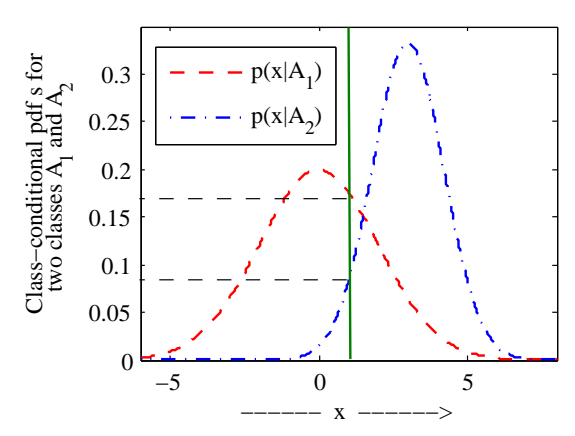


Figure 2.15: Bayesian confidence for one-dimensional case in a two-class classification. (Example: test data is x=1).

If no other information about the classes is available, the prior probabilities can be assumed to be equal. For a 2-class problem (Defect and Non - defect), the equation (2) reduces to

Confidence of x classified as Defect is:

$$P(Defect|x) = \frac{p(x|Defect)}{p(x|Defect) + p(x|Non - Defect)}$$
(2.10)

Hence, for a given test data x, the classification confidence of x as defect can be obtained using the above equation. The conditional probability density functions for the two classes p(x|Defect) and p(x|Non-defect) are estimated from the training set. Figure 2.15 shows the representation of confidence in a 1-dimensional case (where the training set is represented by one feature). Assuming Gaussian distribution for class-conditional density functions of the two classes, the two Gaussian plots represent the estimated distribution of the features from training samples labeled as class A_1 and class A_2 . The confidence of x^* classified as class A_1 is calculated as $C_{A_1} = P(A_1|x^*) = 0.176/(0.176 + 0.0829) = 0.6798$ or 67.98%.

One of the major challenges of using simply the posterior probability directly is that priors are often unknown, as pointed out by Richard et al[32]. Moreover, such a measure

is heavily dependent on correct estimation of density functions. Throughout literature, although confidence measure has been defined in different ways, all approaches deal with a single objective of trying to come up with the best possible way to include the effects of all potential uncertainties encountered in existing NDE classification.

Chapter 3

Comprehensive Confidence Metric in

NDE

3.1 Introduction

Although a wide range of both rule-based and pattern recognition-based classification algorithms have been studied for various NDE applications [33, 34], the estimation of a confidence measure has remained under-emphasized in NDE literature. There are numerous uncertainties involved in NDE systems. Goebel et al. claim that NDE sensor data is often highly noisy and number of training samples available is limited [35]. Although utilizing classifier ensembles improves classification performance for noisy NDE data, the reliability of classification results have not been evaluated. Besides, accuracy of a classifier depends on the discriminative quality of the features used. There has been investigation of noise-invariant features to improve classification performance, for instance in [36], but their effect on reliability is not yet verified. A few quantitative studies on reliability of classification systems have been conducted over the past years [37, 23], but no method of confidence estimation seems to be widely accepted till date. In practice, the sources affecting reliability of signal classification in NDE systems occur simultaneously. While they have been discussed before by NDE specialists, a joint quantification and incorporation of their impact in the

form of a single reliability measure for every decision made remains unsolved.

Much of the current studies [27, 28, 29] use posterior probability or similar measures of confidence. As mentioned in chapter 2, posterior probability of occurrence of an event is representative of inter-class similarities and intra-class distance and thus, may be used as a measure of inherent ambiguity of classes and discriminative quality of features. However the major concern in such approaches lies in the estimation of the parameters of density functions from training set. Bayes confidence takes into account the effect of quality of features extracted from signal assuming that the class-conditional density functions are known a-priori. On the contrary, in practice, lack of adequate training data causes estimated parameters to be significantly different from their true values which affects the calculation of confidence of classifier. To the best of our knowledge, this factor has remained under-emphasized in existing literature on confidence measures. In our study, the difference between true parameters and estimated values is reduced and the effect of size of training data is incorporated in Bayes confidence by applying bootstrap method [38].

The other cause of unreliability in classification decision, irrespective of the classification technique, is the measurement noise. Particularly in NDE, the absolute noise level and absolute strength of a defect signal depends on a number of factors. For example in ultrasound detection, measurement noise depends on probe size and focal properties, probe frequency, inspection path, coupling between transducer and sample, inherent noisiness of the metal microstructure, etc. Similarly in eddy current testing, the major noise sources are temperature variations, probe lift-off, changes in the electromagnetic properties of the material such as electrical conductivity or magnetic permeability and changes in test speed [39]. Researchers in NDE have explored advanced signal processing techniques for detecting different sources of noise and distinguishing signals arising from true defects in presence of

noise [40, 41]. However to the best of author's knowledge, existing confidence assessments do not incorporate noise information. In case of uncertainty analysis, estimation theory suggest that the variance of the estimator depends largely on the variance of noise in observation which therefore affects the confidence of classification result and motivated our study on proposing an updated confidence metric.

In this chapter, the primary sources of uncertainties encountered in a typical ASC system in NDE have been identified. A framework has been developed to incorporate their effect on classification performance into a single quantity. In lieu of the commonly used simplistic assumption of fixed distributions [42], we assume that parameters of the distribution of a class are random variables. We utilize bootstrap method to find empirical distribution of parameters of the class conditional densities based on which a distribution of confidence is obtained [38]. From this distribution, different interpretations of the confidence measure may be provided. Analytical results show how statistical properties of the confidence distribution are representative of the underlying sources of uncertainties in ASC systems.

3.2 Factors Affecting Reliability in NDE Signal Classification

The reliability of classifying a signal as defect is largely affected by the accuracy in estimation of the density functions of the classes. Uncertainties in parametric estimation of the class-conditional densities lead to errors in classification results in terms of missing true defects or causing false alarms. Ideally, a comprehensive confidence measure in ASC systems should be able to quantify the effect of the factors affecting reliability of NDE signal classification and provide self-evaluation of its results. The following factors were identified

and their individual effects were studied.

3.2.1 Quantity and representativeness of training data

Since Bayes confidence relies on parametric statistics, accuracy of estimated confidence heavily depends on the number of training samples used.

According to Chebyshevs Inequality,

$$P(|\overline{x_n} - \mu| \le \varepsilon) \le \frac{\sigma^2}{n\varepsilon^2} \tag{3.1}$$

where, μ is true mean, $\overline{x_n}$ is the expected mean, σ is the variance of the distribution and n is the number of samples. This states that the estimated statistical parameters of class distributions tend to converge to the true distribution as the number of samples increases [43]. Subsequently, the confidence associated with decision of a test signal by an ASC system which is trained with more training samples would be higher, considering that the training data is representative of the class irrespective of its size.

Another desired property of training dataset is that it should be representative of its classes. For instance, an ideal training dataset of defect signals should contain signals obtained from defects of all possible depth, width or any other parameter that affects signal features. If some region of the feature space is under-represented due to lack of enough samples, computation of classification confidence of a test data will be inaccurate.

3.2.2 Quality of features

Features selected to describe the training data should possess discriminative property.

Confidence of a signal being a defect is more when its feature lies closer to the mean of

distribution of class defect and farther from the mean of the other class. Discriminative property of feature ensures that inter-class distance is high and intra-class variance is low which enables separation of two classes in the feature space. A test data which lies farther from the mean of distribution of another class and closer to the mean of its own class is likely to have a higher value of confidence associated with it [44]. This concept can be expressed quantitatively as:

$$Confidence \propto \frac{d_1}{d_2}$$
 (3.2)

d1: Inter-class distance (distance between means of both distributions)

d2: Intra-class distance (variance of each class distribution)

Figure 3.1 shows the case where the same test data is associated with the same classification result but intuitively has different confidence due to difference in discriminative property of feature set chosen. Fig. 3.1 a) indicates higher inter-class distance leading to distinct clusters resulting in higher confidence assigned to a test data. Fig. 3.1 b) uses feature 3 and feature 4 to describe an overlapping feature space and therefore confidence of the same test data (to be in class 1) is low.

3.2.3 Noise statistics of test data

The signal-to-noise ratio (SNR) of the test data affects confidence of its classification. Noise is generated during measurement in NDE systems which may be different for different test samples. A noisy test signal will have inaccuracy in computed features which inherently affects its classification confidence. Hence, to generate a more comprehensive confidence metric, it is important to incorporate noise characteristics into the posterior probabilty measure. The effect of noise statistics on NDE classification confidence and the method of

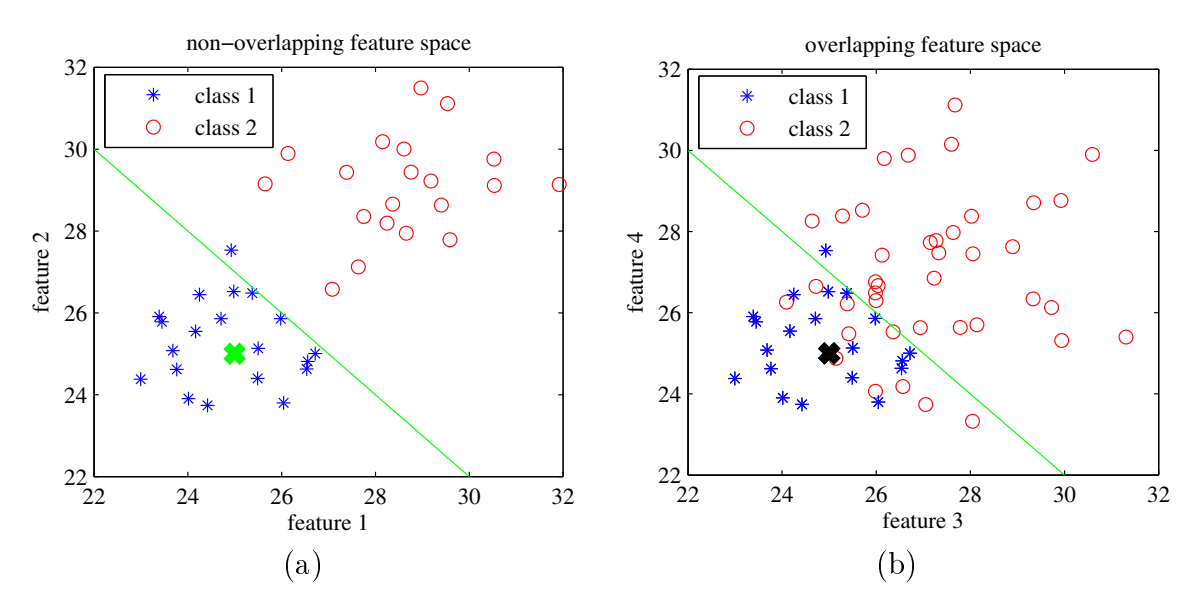


Figure 3.1: Effect of discriminative quality of features on confidence measure.

incorporating it into calculation of confidence are discussed in greater details in later sections.

3.3 Comprehensive (Boosted) Bayes Confidence

Assuming known parameters characterizing the class-conditional density functions, existing Bayes posterior probability sufficiently denotes a possible measure of reliability in classification results. However in NDE applications, density functions are unknown and confidence of signal analysis depends strongly on the accuracy of parametric estimation as well as the noise model. In this thesis, these two issues are addressed. A new metric of reliability is proposed based on traditional Bayes confidence which successfully incorporates effects of uncertainties due to limited number of training data and noise in measurements. A popular sub-sampling technique known as bootstrapping is applied for calculation of posterior probability such that the estimation error is reduced, followed by incorporation of noise statistics from NDE signal into the confidence assessment. The details of the proposed method are described in the following subsections and summarized in Algorithm 1 and 2.

3.3.1 Bootstrapping

Bootstrapping is a technique of sub-sampling with replacement [38]. At every iteration of the algorithm, a subset of the total training dataset (D_t) is selected and maximum likelihood estimators of parameters of the class-conditional density functions are obtained.

A Gaussian mixture model (GMM) is implemented on D_t to model class-conditional pdf for all classes $[\omega_1, ..., \omega_c]$ as:

$$\left(p^{t}(x)\right)_{\omega_{i}} = \left(\sum_{i=1}^{k} \phi_{i} \mathcal{N}\left(\mu_{i}, \Sigma_{i}\right)\right)_{t}$$
(3.3)

where the i^{th} vector component is characterized by normal distributions with weights ϕ_i , means $\vec{\mu_i}$ and covariance matrices Σ_i of k components in GMM [45].

Using estimated values of mean vector and covariance matrix, the Bayes posterior probability is calculated according to Equation 2.9. Repeating the process on other set of samples for a fixed number of iterations provides a deeper insight into the behavior of the entire statistical population. In lieu of deterministic approach, parameters of the distribution of a class are assumed to be random variables under this framework and hence a distribution of confidence is obtained, instead of one-shot confidence calculation. The procedure is illustrated in Figure 3.2.

From the confidence histogram, $C_{0.95}$ measure is calculated to the right of which 95% of the total area under the histogram lies. Classification confidence of $C_{0.95}$ associated with a NDE signal signifies that 95 times out of 100, the ASC ensures that the signal will belong to the reported class with a confidence of $C_{0.95}$. If the histogram of confidence values is denoted as $h = [h_1, \ldots, h_n]$

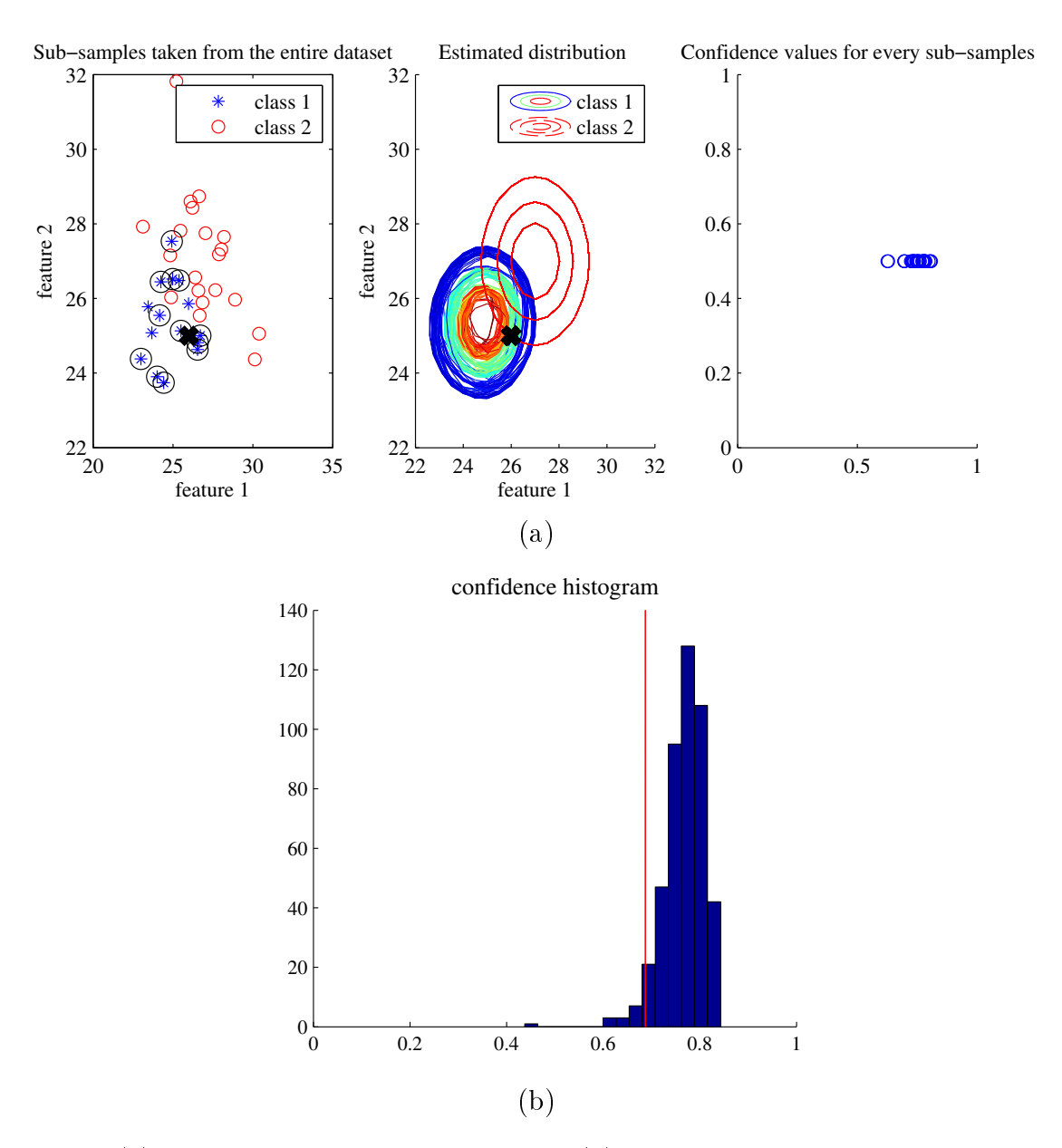


Figure 3.2: (a)Bootstrappping Bayes confidence, (b) Confidence histogram with $C_{0.95}$ value as the red line.

h is defined as:

$$h_n = \sum_{x \in [0,1]} \delta_n(x) \tag{3.4}$$

Where, n:1,2,...,N; N is the total number of bins of histogram and δ_n is an indicator function such that,

$$\delta_n(x) = \begin{cases} 1 & \text{if } \frac{n-1}{N} \le x \le \frac{n}{N} \\ 0 & \text{otherwise} \end{cases}$$
 (3.5)

The metric $C_{0.95}$ is further defined as:

$$C_{0.95} = \frac{\frac{index - 1}{N} + \frac{index}{N}}{2} \tag{3.6}$$

where,

$$index = \max_{j} \left(\sum_{k=j}^{N} h'_{k} \ge 0.95 \right) \tag{3.7}$$

$$h_n' = \frac{h_n}{\sum_{n \in N} h_n} \tag{3.8}$$

As a rule of thumb, at least 75% of the training samples are selected in each iteration to generate unbiased estimates of the parameters. Additionally, bootstrapping reinforces the effect of number of training samples on confidence evaluation, depicted using simulated dataset in Figure 3.3 with training data of size (a) 10, (b) 15 and (c) 20 respectively. Presence of more number of representative training data reduces the variance of the confidence histogram which reflects higher certainty in classification results [46]. It is important to note that training data distribution is unchanged for the three cases, only the number of data varies.

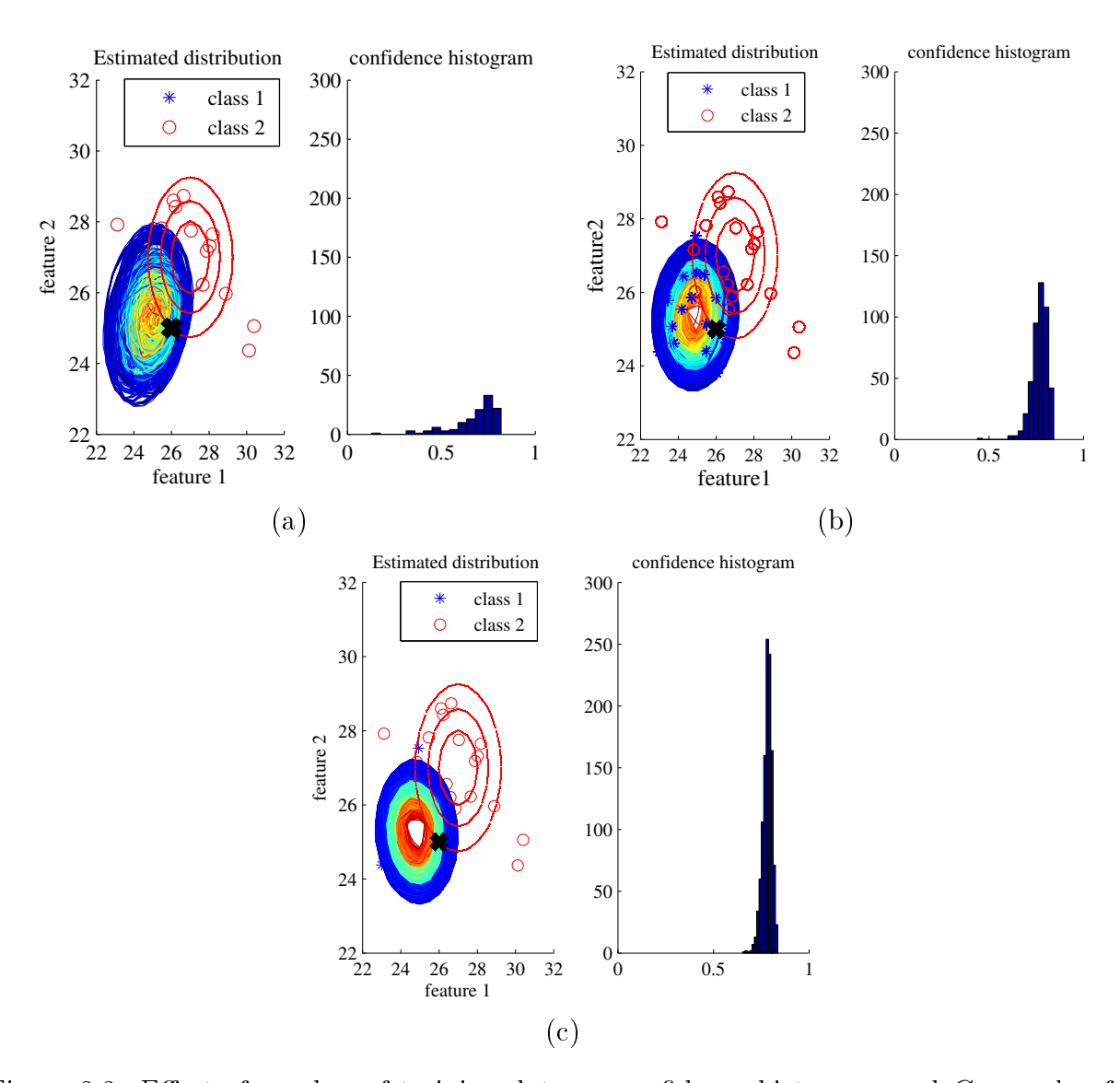


Figure 3.3: Effect of number of training data on confidence histogram and $C_{0.95}$ value for test data **X** (a) $C_{0.95} = 0.4033$ for n=10 (b) $C_{0.95} = 0.6776$ for n=15 (c) $C_{0.95} = 0.7277$ for n=20.

3.3.2 Incorporation of noise factor

As stated by Mann et al. [47], the level of confidence that can be attributed to classification is highly sensitive to prior assumptions regarding the nature of the background noise, as well as the appropriateness of the statistical model for noise. Typical measurements from an NDE experiment contains flaw response affected by different sources of noise. For most cases especially when the flaw size is relatively small, it is very difficult to determine whether an observation arises due to a flaw or measurement noise leading to low confidence in classification. In this work, assuming additive noise we recognize that features from a noisy signal are not deterministic in nature; instead they are random variables whose distribution is affected by the noise pdf. Noise statistics is extracted from the measured NDE signal and characterized by its density function. During training of algorithm, posterior probability function of the feature space is calculated. Subsequently, the Bayes posterior probability function is weighted with the noise density function according to equation 3.3, in order to evaluate corresponding classification confidence [48].

$$(P_W(x))_{\omega} = \frac{\sum_{x \in \mathbf{A}} p_n(x - x^*) \cdot (P_p(x))_{\omega} dx}{\sum_{x \in \mathbf{A}} p_n(x - x^*) dx}$$
(3.9)

where, A is the feature space, $(P_p(x))_{\omega}$ is the calculated posterior probability function of the signal classified into class ω , $p_n(x-x^*)$ is the estimated noise density function of the signal and $(P_W(x))_{\omega}$ is the noise-weighted posterior probability function of the classified signal.

The process of weighting posterior probability with noise distribution is demonstrated in figure 3.4. Bayes confidence of test data x^* without noise is computed as C_1 (value of C(x) at x^*). With effect of noise, the classification confidence is calculated as:

$$C_n = \frac{C_1 n_1 + C_2 n_2 + C_3 n_3 + C_4 n_4 + \dots + C_M n_M}{n_1 + n_2 + n_3 + n_4 + \dots + n_M} \forall n \in N$$
(3.10)

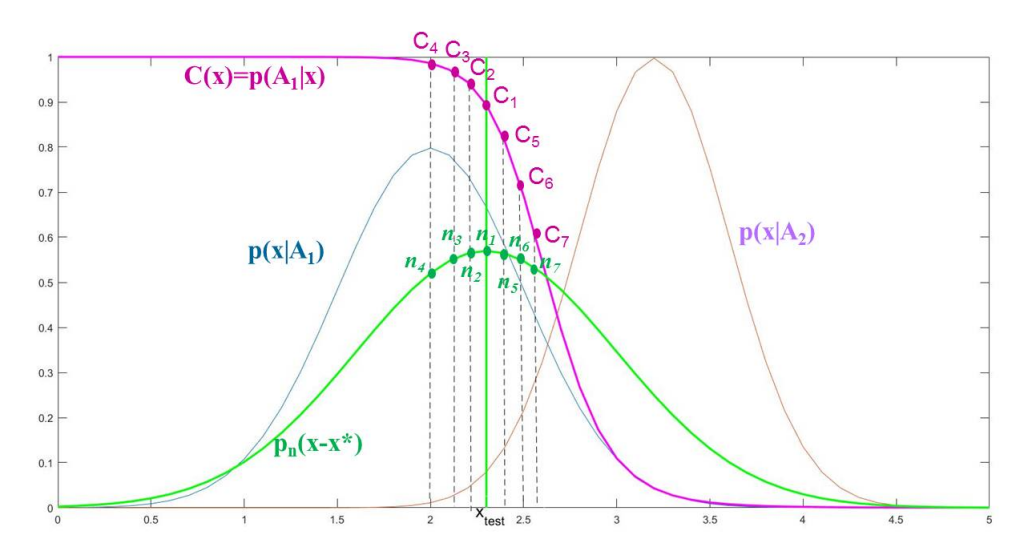


Figure 3.4: Demonstration of confidence computation by weighting with noise.

The proposed method of computing classification confidence of a noisy test data implemented in bootstrap framework is described in Algorithm 1 and 2.

Algorithm 1 Training algorithm

Input: Training data $\mathbf{D} = \{x_i, y_i\}; i \in \{1, 2, ..., N\}$ with true labels $y_i \in \{\omega_j\}; j \in \{1, 2, ..., c\};$

Output: Posterior pdf of the class for which confidence is calculated = $\left(P_{p}^{t}\left(x\right)\right)_{\omega_{j}}$

- 1: Initialize t=1;
- 2: **for** t = 1 to T (Number of iterations) **do**
- 3: Select a training subset D_t containing M samples drawn from \mathbf{D} ;
- 4: Fit GMM to D_t and model class-conditional pdf for all classes $[\omega_1,, \omega_c]$ as : $(p^t(x))_{\omega_i} = (\sum_{i=1}^k \phi_i \mathcal{N}(\mu_i, \Sigma_i))_t$

where the i^{th} vector component is characterized by normal distributions with weights ϕ_i , means $\vec{\mu_i}$ and covariance matrices Σ_i of k components in GMM

- 5: Estimate $(\vec{\boldsymbol{\mu_t}}, \Sigma_t)_{\omega_i}$ for all classes $[\omega_1,, \omega_c]$;
- 6: Calculate the posterior probability for the class for which confidence is obtained (e.g. ω_j):

$$\left(P_{p}^{t}\left(x\right)\right)_{\omega_{j}} = \frac{\left(p^{t}\left(x\right)\right)_{\omega_{j}}}{\sum_{i=1}^{c}\left(p^{t}\left(x\right)\right)_{\omega_{i}}};$$

7: end for

Algorithm 2 Generating confidence of classification of a test data

Input: Test data whose confidence is to be evaluated : x^* ;

Classified label of $x^* = y^*$;

PDF of noise of test data = $p_n(x - x^*)$;

Output: Confidence of test data classified into class $\omega_j = C_{\omega_j}$;

1: for t = 1 to T do

2: Calculate posterior pdf weighted by noise pdf:

$$(P_W^t(x))_{\omega_j} = \frac{\sum_{x \in \mathbf{A}} p_n(x - x^*) \cdot (P_p^t(x))_{\omega_j}}{\sum_{x \in \mathbf{A}} p_n(x - x^*)}$$

where **A** : {feature space}:

- 3: Calculate weighted posterior probability for test data: $(P_W^t(x^*))_{u^*}$;
- 4: end for
- 5: Formulate a histogram of $(P_W(x))_{\omega_j}$ with M bins s.t. $h = [h_1, \ldots, h_M]$;
- 6: Define h_m as:

$$h_m = \sum_{x \in [0,1]} \delta_m(x) \tag{3.11}$$

where,m:1,2,...,M;M is the total number of bins of histogram and δ_m is an indicator function such that,

$$\delta_m(x) = \begin{cases} 1 & \text{if } \frac{m-1}{M} \le x \le \frac{m}{M} \\ 0 & \text{otherwise} \end{cases}$$
 (3.12)

7: Calculate classification confidence of $x^* = C_{\omega_j} = C_{0.95}$;

$$C_{0.95} = \frac{\frac{index-1}{M} + \frac{index}{M}}{2} \tag{3.13}$$

where,

$$index = \max_{j} \left(\sum_{k=j}^{M} h'_{k} \ge 0.95 \right)$$
 (3.14)

$$h_m' = \frac{h_m}{\sum_{m \in M} h_m} \tag{3.15}$$

3.4 Simulation Results

A parametric study showing effect of noise variance on classification confidence is demonstrated in this section. The proposed algorithm is applied on a synthetic example of 2-dimensional feature space classified into two classes-'red' and 'blue'. The 2D feature plot shown in Fig. 2(a) is obtained by random sampling of datapoints from a bivariate distribu-

tion. These points in the feature space signify the features from training dataset and "X" marks the test data (x^*) whose classification confidence is calculated. Simulated noise is modelled by white Gaussian uncorrelated noise model: $p_n(x^*) \sim N(0, \sigma_n^2)$ and is denoted by the elliptical contours around the test data \mathbf{x} in Fig. 2 (a). The noise variance is varied from 0 to 0.05 and corresponding confidence of the test data is computed according to algorithms 1 and 2. It should be noted that the magnitude of σ_n^2 determines the power of the injected noise.

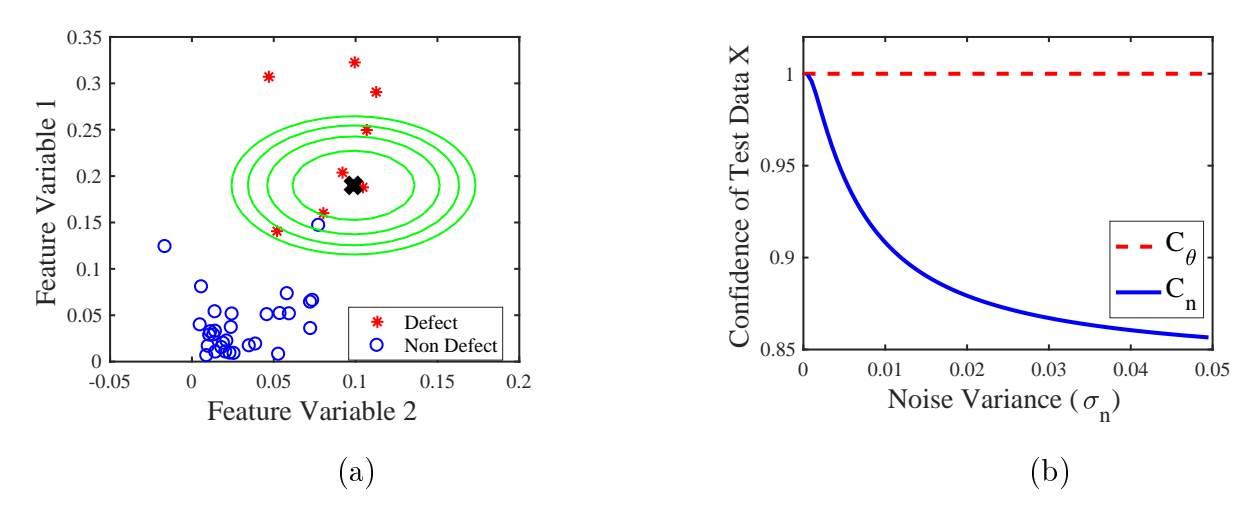


Figure 3.5: (a) 2D scatter plot of training and test data \mathbf{x} with noise distributions.(b) Classification confidence of \mathbf{x} in 'Red' class with respect to varying noise levels of test data.

Fig. 2(b) shows that as variance of noise density function increases, the confidence of classifying the test data reduces, indicated by blue curve C_n . The red dashed line denotes confidence calculated without taking noise into consideration C_{θ} . It is a reasonable argument that if the output measurement from NDE inspection is affected by a high level of noise, corresponding features will be incorrect, leading to less reliable classification decision which is reflected by its low classification confidence. On the other hand, if a flaw-signal is affected by low noise, the contribution of noise weights on the Bayes posterior probability is low and hence the confidence of classification is higher.

Chapter 4

Confidence Metric Evaluation: Eddy

Current inspection of Steam Generator
tubes.

4.1 Introduction

One of the fields where NDE is used extensively since 1950s is the nuclear industry. Steam generators (SG) are heat exchange tubes used in nuclear industries for transferring heat from the primary loop to the hot pressurized water circulating on the outside to produce steam, which is used to run the turbines. These SG tubes are continuously exposed to high temperature, vibrations and corrosive environment often resulting in various types of degradations such as mechanical wear between tube and tube support plates, outer diameter stress corrosion cracking (ODSCC), pitting, volumetric changes, primary water stress corrosion cracking (PWSCC), and inter granular attack (IGA). Tube wall thinning or formation of cracks causes harmful radioactive gases leak from the primary side to the secondary side which may be catastrophic to environment or lead to unscheduled plant shutdowns. Hence there is a strong economic incentive to build NDE systems in order to periodically monitor the general health of SG tubes.

Multi-frequency and multi-coil probe eddy current testing (ECT) has been an effective NDE techniques used for in-service SG tube inspection as they are very well suited for detecting defects in conducting materials [49, 50, 51]. Due to harsh environment faced by the heat exchange units and their complex geometries, often other methods such as ultrasonics, radiography, liquid-penetrants or optical scanning are incapable of producing strong indication of anomalies which makes ECT an obvious choice. Eddy current inspection has proven to be both fast and effective in detecting and sizing most of the degradation mechanisms that occurred in the early generators. By using ECT it is possible to detect and size defects even in the presence of artifacts that usually complicate the analysis procedure. Moreover, collection of data at several test frequencies simultaneously decreases in-service inspection time and human exposure time to radiation. Three major types of multifrequency eddy current probes are used in practice – the bobbin coil, the rotating probe coil (RPC) and the array sensors.

Structural health management of SG tubes and related uncertainty quantification techniques have been an important NDE problem[52]. With rapid increase in the amount of data obtained from heat exchanger tube by EC inspections, there is a high demand of automated signal analysis systems that can provide accurate and consistent signal interpretation and avoid errors by human analysts. The data acquired from SG tube inspection must be analyzed accurately and in near real-time. Generally, the analysis requirement is a classification of the signal into flaw and non-flaw categories. In such scenarios, computation of reliability of each classification becomes critical so that specific classifications with low confidence can be reported to NDE analyst for further investigation. In this chapter, confidence of signal classification has been studied for eddy current data collected using RPC probe from inspection of SG tubes consisting of volumetric flaws. This study was conducted as a part

of a project funded by the Electric Power Research Institute (EPRI), USA. EC data from various tube geometries were collected by EPRI and analysed by an automated analysis software developed by Non Destructive Evaluation Laboratory of Michigan State University [5, 6]. Confidence metrics were assigned to the classification results from this data analysis software.

This chapter briefly reviews the principle of EC technique and existing signal processing methods performed on EC data to enhance flaw indication by increasing signal-to-noise (SNR) ratio. Further, noise from typical eddy current signals obtained from SG tube inspection by RPC probe is studied to extract statistical parameters of the noise distributions. Finally, boosted Bayes Confidence, proposed in chapter 3, was calculated for every flaw indications by taking noise statistics into consideration.

4.2 Principle of Eddy Current Testing

Eddy current (EC) technique works on the principle of electromagnetic induction. When an alternating current source is brought close to an electrically conducting material, an alternating magnetic field is induced in the material which causes current to flow inside the material in the form of closed path like eddies; their direction being opposite to the induced current flow according to Lenz's law. Opposing secondary field generated by the induced current in the sample interacts with the primary field and reduces the characteristic impedance of the excitation coil, as demonstrated in Figure. 4.1. Moreover, presence of a defect in the sample amends the path of the induced eddies which in turn changes the coil impedance substantially. This change in coil impedance forms the NDE signal (containing information about sample defects) recorded by the EC probes [39].

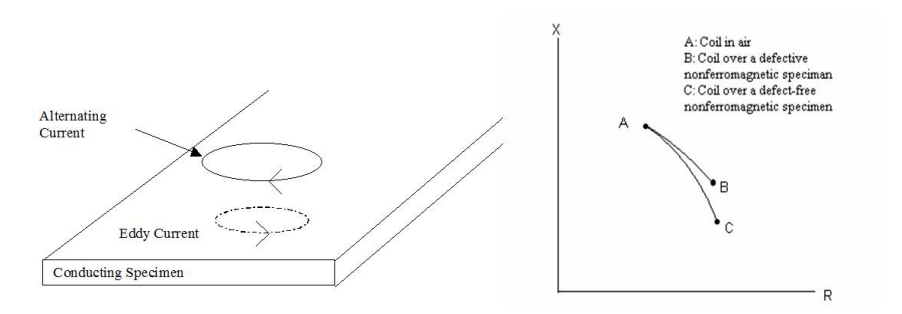


Figure 4.1: (a) Eddy current generation and flow in a conducting specimen (b) Change in impedance of coil in a defect and defect free region (X axis: resistance, Y axis: inductance) [5].

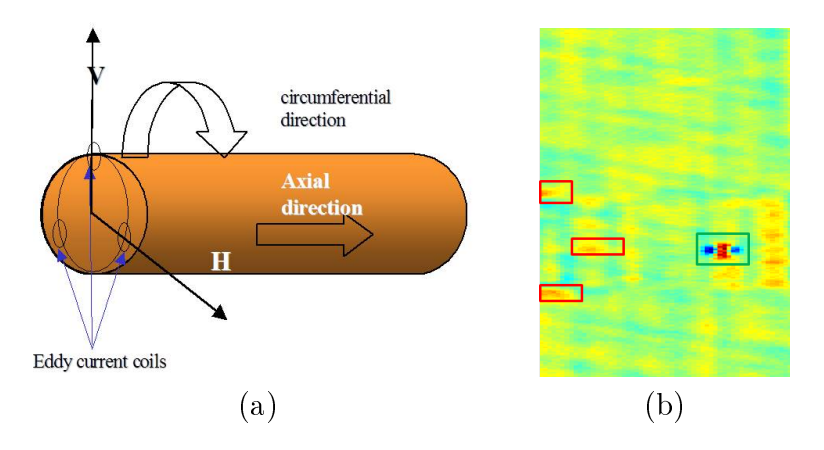


Figure 4.2: (a) RPC configuration (b) Post processed eddy current signal (RPC probe at 300KHz) of a defective SG tube [5].

4.3 Automated Analysis of SG Tube Inspection data

State-of-the art eddy current testing of SG tubes by rotating probe coil (RPC) is demonstrated in Figure 4.2. These probes acquires a two-dimensional data depicting impedance change in the form of a complex voltage which is a function of axial and circumferential position of the probe in the tube structure. Imaginary component of a typical post processed signal from eddy current tube inspection is shown in Figure. 4.2. The abscissa and ordinate denote the circumferential and axial direction of the SG tube respectively. Similar to any NDE data analysis system, eddy current data are first subjected to signal processing followed by identification of regions of interests (ROIs). From the ROIs or the possible location of

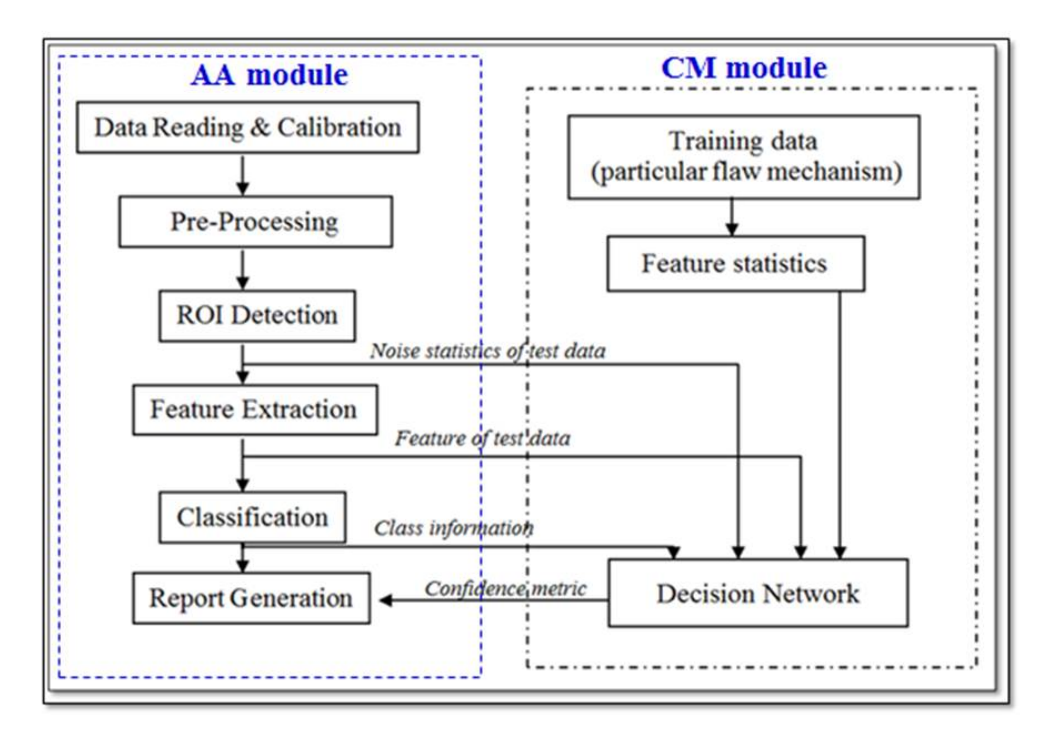


Figure 4.3: Automtated EC data analysis system with confidence metric computation module.

flaws, discriminative features are chosen to eventually classify a ROI into defect or non-defect category.

The flowchart of existing automated eddy current analysis systems along with added confidence metric computation module applicable to inspection data from SG tubes is presented in Figure 8.10.A brief overview of existing methods in EC data analysis is discussed in the following subsections.

4.3.1 Signal Pre-processing

Potential ROIs shown by rectangular boxes in Figure. 4.2 (b) are identified after rigorous signal processing algorithms on the raw signal which includes calibration, tube support signal (TSP) suppression and noise removal. Details of these algorithms are described by Udpa et al. in [6]. Several other signal processing methodologies for analysing EC signals have

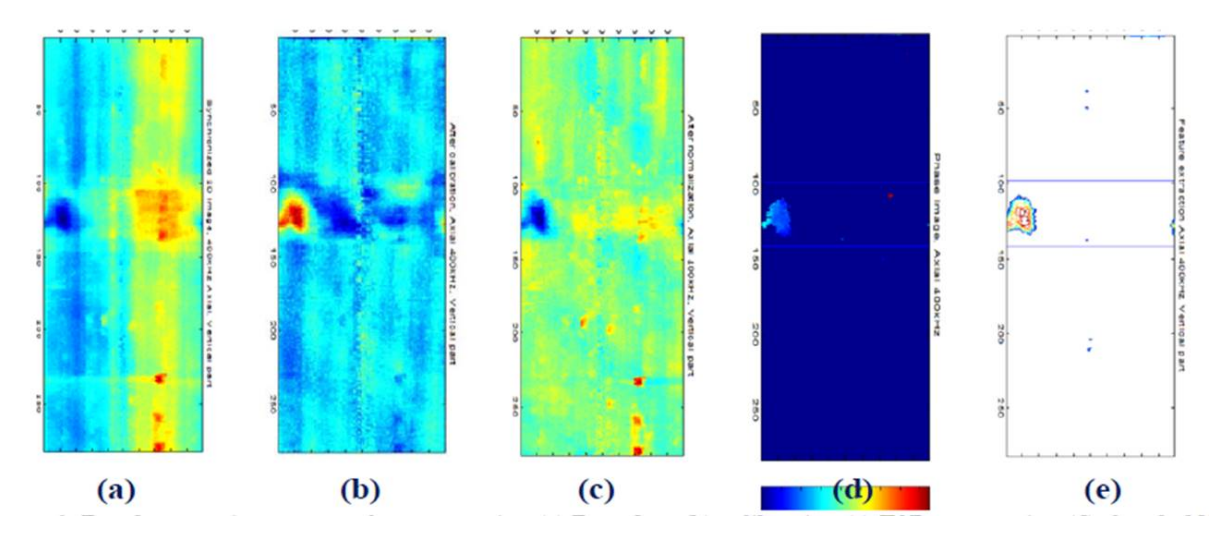


Figure 4.4: Various stages of automated signal processing (a) Raw data, (b) Calibrated data, (c) TSP suppression, (d) thresholding (e) ROI detection [6].

been discussed extensively in literature such as linear and nonlinear mixing [53] and wavelet transforms [54, 40]. Often flaw indications are corrupted by noise and/or nondefect signals due to the probe lift-off and surrounding tube structures which adversely affect detection and characterization of defects. Hence, it becomes necessary to enhance the SNR of the ECT signals by using signal processing methods [55, 56] before implementing the recognition techniques.

4.3.2 ROI Detection

Once the raw signal is cleaned and its SNR is improved, possible flaw locations are identified by selecting peak signals or signals above a pre-defined threshold adaptively [57]. Signals at different frequencies are integrated appropriately to determine the potential defect indications. However, the final result often contain signals from non-flaws as well (for instance, signals from external deposits). The enitre process of adaptive thresolding followed by ROI selection in a typical SG tube inspection signal is demonstrated in Figure. 4.4.

4.3.3 Feature Extraction and Classification

Signal characteristics or salient features are extracted from the ROIs which can distinguish a defect ROI from a non-defect one. Features can be computed using the signal in time domain such as peak-to-peak value of the real and imaginary components of the complex eddy current signal, its phase angle or energy [58]. Transformed features (eg: Fourier descriptors [59]) or statistical features (eg: principal components [60]) have been used as well in existing EC data analysis. These features are calculated from each potential ROI from data obtained at several excitation frequencies. Figure. 4.5 shows the two-dimensional feature space spanned by the real and imaginary components of the complex EC signal acquired at 300kHz by RPC. Each feature point represents an ROI collected from all the training data whose real categories (or ground truth) are known. The red labelled data points are defect ROIs wheras the blue labelled ones are the ROIs which were selected after thresholding step but eventually did not represent a flaw.

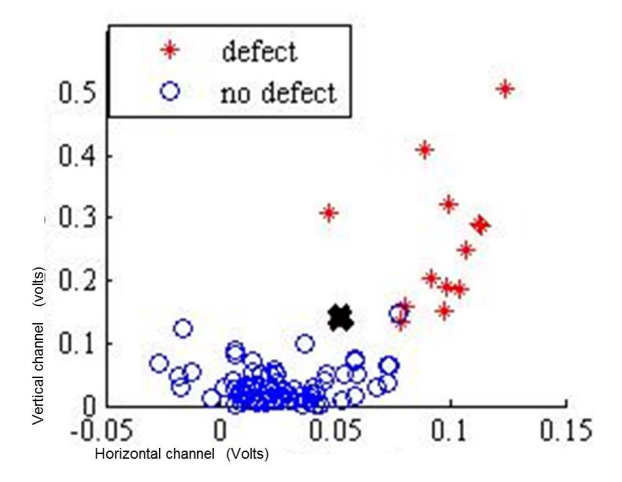


Figure 4.5: Scatter plot for steam-generator tube data showing features from training data from both classes and test data **x**.

Features are fed into a rule-base or neural networks or other machine learning algorithms to classify them into defect or non-defect class. Several classifiers for analysis eddy current signals [9] including impedance plane diagrams [61], inverse analysis [62] and artificial neural networks [15] have been studied in literature. In the example test data shown in Figure. 4.2, red and green boxes denote ROIs in the tube which have been classified as non-defects and defect respectively by rule-based classifier in the automated analysis algorithm.

The subsequent step of an automated signal classifier in NDE is to assess the reliability of its classification results by assigning confidence metrics. Our proposed confidence measure incorporates features, classification results and noise statistics of the acquired EC signal as shown in figure 8.10. Hence, the next section focusses on the study of noise in EC signal obtained from SG tube inspection.

4.4 Noise Analysis in Field Data from Eddy Current Inspection

In our study, noise extracted from EC inspection signals is modelled as a mixture of one or more Gaussian density functions (GMM). The rationale behind this assumption is based on a previous work by Safdarnejad et al. [63] where the authors have not only shown that the experimental noise present in complex ECT signals from SG tube inspection adheres to Gaussian distribution but further reported that GMM along with noise filtering algorithms enhances performance of noisy EC signal analysis. Another important characteristic of the noise is its additive nature. It is known that steam generators consist of several tubes fixed with supports from the outside. Ideally in noise-free scenario, the ECT signal from SG tube inspection contain indications only from the tube supports and from an anomaly if it exists. Signal at the free-span region (in between the tube supports) is assumed to be zero in absence of any noise. However in real experiments, the ECT signal at the free-span is not

zero everywhere but contains some low voltage measurements which originates due to probe wobble, mechanical motion of probe and measurement noise. Therefore, the signal from free-span region is considered as the noise-only measurement which is modeled as additive to the noise-free measurement. This assumption is backed by a previous study where Olin et al. [3] used a sequence of NDE signals at different positions on a unit containing no flaws to provide information about the "noise-only" distribution.

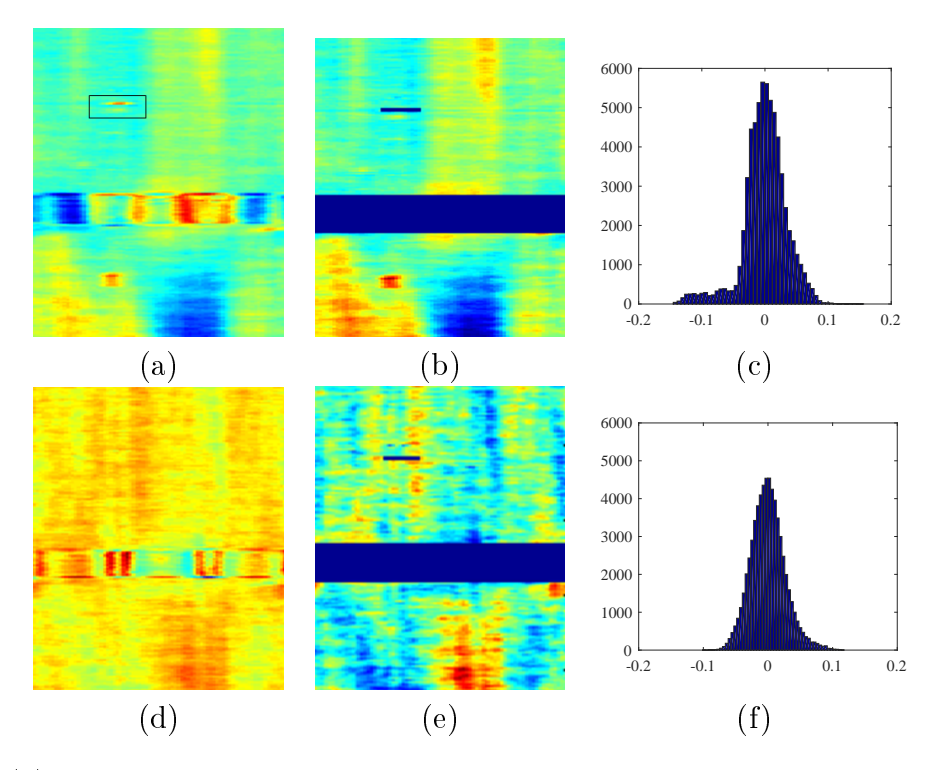


Figure 4.6: (a) Imaginary channel image of a sample eddy current response signal at 300KHz with rectangular ROI box indicating circumferential flaw. (b) Signal with masked tube support and flaw region (c) Noise histogram. (d-f) Repeated for real channel data.

Fig. 4.6 explains the process of estimating noise distribution of a typical eddy current response image. Imaginary and real components of the eddy current inspection image obtained from a defective SG tube at 300KHz are shown in Fig. 4(a) and Fig. 4(d); ROIs containing flaw indications and signal from the tube support are masked, as shown in Fig. 4(b) and Fig. 4(e), and the rest of the signal is used to extract noise-only information represented as

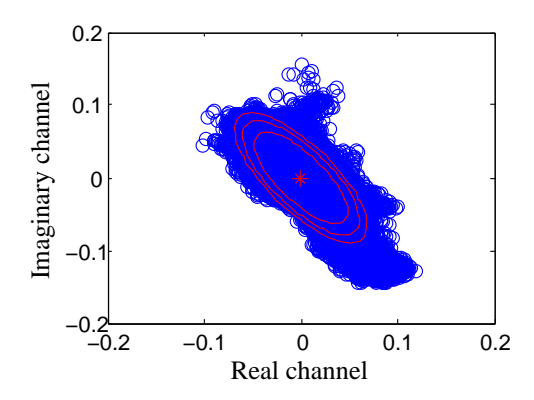


Figure 4.7: Experimental noise modelled as a bivariate Gaussian distribution.

the noise histograms (Fig. 4(c) and Fig. 4(f)). It is important to note that flaw signals in the vicinity of external support structures (such as tube support plates (TSP)) are distorted by the presence of the support structures and hence not included as the noise-only region.

Since, experimental noise is complex with real and imaginary values, the resultant noise is modelled as 2D distribution as shown in Fig. 4.7. In this example, noise distribution has been modelled as a bivariate Gaussian density function whose statistical parameters are estimated by maximizing the likelihood function. The estimated noise distribution is described by the elliptical contours in Fig. 4.7.

It should be noted that experimental noise is specific to tube inspected, probe and the inspection frequency. Fig. 4.8 shows two different tubes that are inspected using two different kinds of RPC probe (pancake and plus-point probe) at 200KHz and 300KHz. Fig. 6(a) and Fig. 6(c) show the noise-only signal obtained from Tube 1 and Tube 2 inspections respectively whereas Fig. 6(b) and Fig. 6(d) show the corresponding noise histograms of the two tubes inspected by two probes at two frequencies-200KHz and 300KHz. Due to such unique nature of experimental noise, it is absolutely imperative to study the nature of inspection noise before computing classification confidence of a ROI present in a particular SG tube.

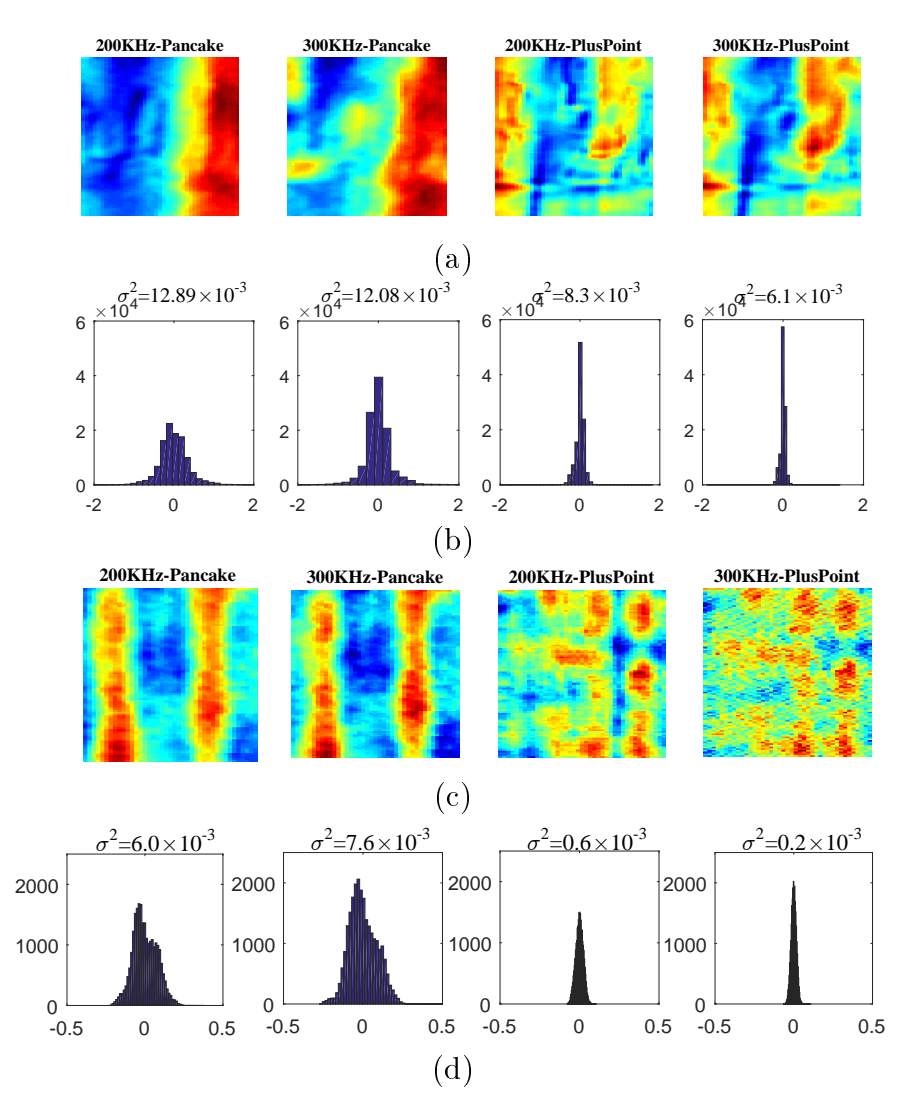


Figure 4.8: (a) Noise-only signal from ECT of Tube 1 using Pancake and Plus-point probes at 200Hz and 300kHz, (b) Noise histogram of Tube 1 signals, (c) Noise-only signal from ECT of Tube 2 using Pancake and Plus-point probes at 200Hz and 300kHz, (d) Noise histogram of Tube 2 signals.

At times when Gaussian function does not serve as the best fitted distribution, other pdfs such as log-normal, exponential, gamma or beta functions can be chosen which has a higher goodness of fit on the noise data. However, the proposed confidence metric evaluation approach can still be applied to those cases with no change applied to the algorithm. As described before, the posterior pdf will be weighted by the noise density function irrespective of its form.

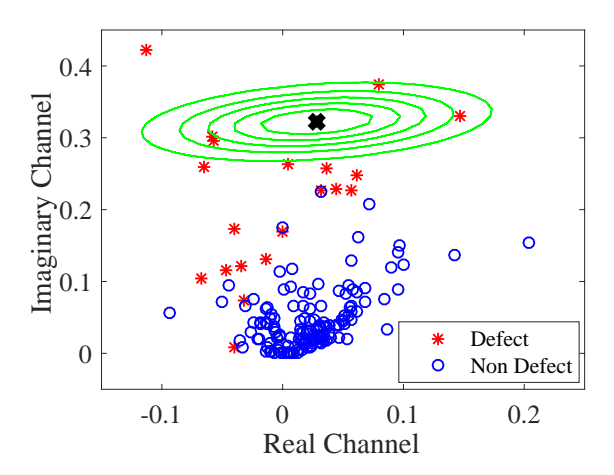


Figure 4.9: Scatter plot for steam-generator tube data showing experimental noise distribution for a test feature \mathbf{x} .

4.5 Confidence of Classification with Noise Consideration.

In eddy current inspection, magnitude and phase based information form crucial features to discriminate signals of a defective sample from a healthy sample [6]. In this thesis, the peak-to-peak value of real and imaginary components of the complex eddy current signal are chosen as suitable features for confidence analysis. Fig.4.9 denotes the feature plot using features extracted from 10 tubes in the training database, each containing one or more flaws. Experimental noise is extracted from one of the test ROIs and modelled as bivariate density function shown by elliptical contours at the test data location. Classification confidence of the test datapoint is calculated according to algorithms 1 and 2 by multiplying Bayes posterior pdf with noise-weights in a bootstrap framework.

In Fig.4.9, confidence of classifying test ROI as 'defect' without taking noise into account is calculated as 90.41%. After incorporating the effect of noise, the confidence reduced to 80.15%. Similarly, all ROIs classified as 'defects' were assessed, noise in their response

signals were extracted and their classification confidence metrics were obtained. The results are recorded in Table 4.1. An important thing to note is that modeling training data with Gaussian pdf may not always be a valid assumption depending on the data and should be chosen carefully before calculating Bayes posterior probability. Statistical tools such as quantile-quantile plots should be computed on the training data to verify the validity of the Gaussian assumption on the training dataset. If data does not fit a normal distribution, other pdfs should be considered or non-parametric (kernel based) approaches may be availed.

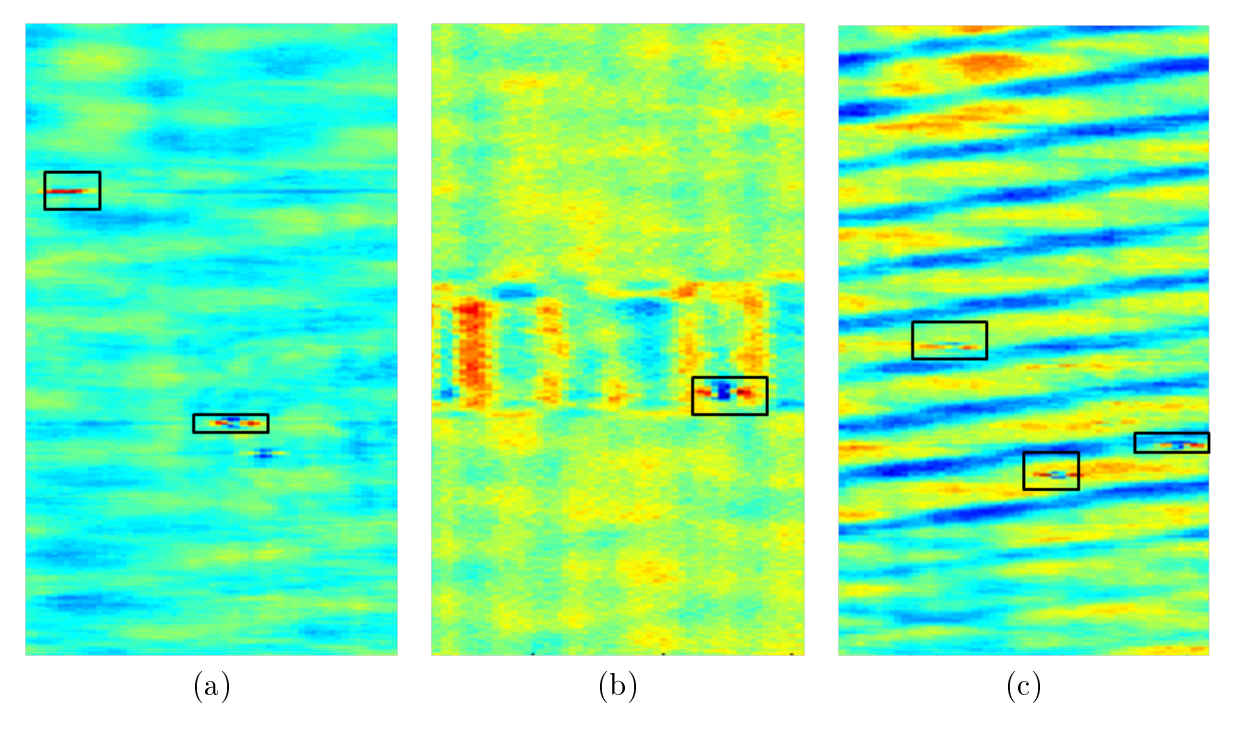


Figure 4.10: Eddy current response signal of three SG tubes with ROIs consisting ofdefects and affected by different noise levels.

In Fig. 4.10, eddy current signals from three SG tubes are shown. The ROIs were identified by automated data analysis software and confidence of classifying each of them as defects was calculated. It can be seen that as the eddy current response image gets noisier, classification of the defect ROIs becomes more difficult. Hence certainty of the auto analysis results decreases with higher noise level which corresponds to lower classification confidence.

Table 4.1: Confidence of classification of defects in steam generator tubes using RPC probe.

Tube-ID	No. of flaws	Noise-mean $(\mu_n) \times 10^{-4}$	Noise-cov $(\Sigma_n) \times 10^{-3}$	$\begin{array}{c} \textbf{Noise-free} \\ \textbf{Confidence} \\ C_0 \end{array}$	Confidence with noise C_n
1	4	$\left[\begin{array}{c} -1.6 \\ -4.2 \end{array}\right]$	$ \begin{bmatrix} 2.9 & 0.5 \\ 0.5 & 2.7 \end{bmatrix} $	0.99 1 0.95 0.59	0.98 0.99 0.65 0.55
2	1	$\left[\begin{array}{c} 0.18\\1.2\end{array}\right]$	$ \left[\begin{array}{cc} 5.8 & 0.6 \\ 0.6 & 0.8 \end{array} \right] $	[0.98]	[0.82]
3	2	$\left[\begin{array}{c} -0.043\\ 0.025 \end{array}\right]$	$ \left[\begin{array}{cc} 1.7 & 0.09 \\ 0.09 & 2.7 \end{array} \right] $	$\left[\begin{array}{c}1\\1\end{array}\right]$	$\left[\begin{array}{c} 0.99 \\ 0.99 \end{array}\right]$
4	2	$\left[\begin{array}{c} -0.022\\ 0.026 \end{array}\right]$	$ \begin{bmatrix} 0.9 & 0.5 \\ 0.5 & 0.9 \end{bmatrix} $	$\left[\begin{array}{c} 0.99\\1\end{array}\right]$	$\left[\begin{array}{c} 0.98 \\ 0.99 \end{array}\right]$
5	1	$\left[\begin{array}{c} 0.19 \\ -0.23 \end{array}\right]$	$\begin{bmatrix} 1.5 & -0.75 \\ -0.75 & 0.8 \end{bmatrix}$] [0.99]	[0.94]
6	3	$\left[\begin{array}{c} 4.5 \\ -0.5 \end{array}\right]$	$ \begin{bmatrix} 2.2 & -1.1 \\ -1.1 & 1.2 \end{bmatrix} $	$\left[\begin{array}{c} 0.99\\1\\0.90\end{array}\right]$	$\left[\begin{array}{c} 0.86 \\ 0.99 \\ 0.61 \end{array} \right]$
7	3	$\left[\begin{array}{c} 0.16 \\ -0.34 \end{array}\right]$		$\left[\begin{array}{c} 0.98 \\ 0.99 \\ 0.96 \end{array} \right]$	$ \begin{bmatrix} 0.58 \\ 0.86 \\ 0.67 \end{bmatrix} $
8	1	$\left[\begin{array}{c} 0.12\\ -0.002 \end{array}\right]$	$\begin{bmatrix} 3.4 & -0.17 \\ -0.17 & 2.8 \end{bmatrix}$] [0.90]	[0.80]
9	3	$\left[\begin{array}{c} 4.6 \\ -2.9 \end{array}\right]$	$\begin{bmatrix} 1.8 & -0.59 \\ -0.59 & 1.3 \end{bmatrix}$	$ \left] \left[\begin{array}{c} 0.63\\1\\0.99 \end{array} \right] $	$\left[\begin{array}{c} 0.61\\ 0.99\\ 0.95 \end{array}\right]$
10	1	$\left[\begin{array}{c} 0.96\\0.38\end{array}\right]$	$ \begin{bmatrix} 1.5 & 4.7 \\ 4.7 & 3.04 \end{bmatrix} $	[0.99]	[0.85]

SG tubes depicted in Fig. 8(a), (b) and (c) correspond to tube ID 4,5 and 7 in Table 4.1 and are affected by low, medium and high noise level respectively. The classification confidence of these ROIs are recorded as a) 99.8%,98.03% (b) 94.23% and (c) 58.36%,86.86%,67.82%. This it can be concluded that the proposed confidence metric is well representative of noise

in NDE response signal.

Another interesting observation to deduce from these results is that a low confidence metric can serve as an indicator of smaller flaws which are more difficult to be diagnosed. For example, the two flaws in Tube ID 1 and 9 were two of the smallest flaws in the database used for this study and they were associated with confidence values of 0.59 and 0.63 respectively even before their experimental noise was considered. In such cases, it might be useful to segregate the study into classes of 'larger flaw' and 'smaller flaw' before evaluating the confidence metrics. This shall be looked into in more detail as a future extension of this research.

Chapter 5

Confidence-Rated Classification in NDE

5.1 Introduction

After identifying the underlying factors of uncertainties in a typical NDE data classification system and generating a suitable confidence metric for classification of NDE signal, the next idea was to study the possibility of improving performance of ASC systems by incorporating knowledge of its classification confidence. The basic idea is to use the confidence metric as a feedback to the classifier as shown in the schematically in figure 5.1. The benefit of such a system is that it not only generates a self-evaluating metric of reliability, but also utilizes it as a feedback and retrains the system to achieve a lower error rate on blind testing.

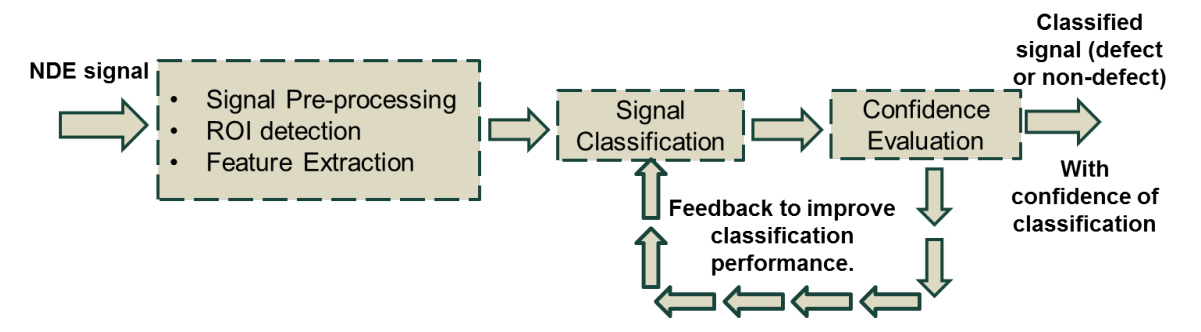


Figure 5.1: Automated analysis system with confidence feedback.

This chapter describes the development of a confidence-rated-classifier ensemble approach is developed to classify eddy current data into 'defect' and 'non defect' class which incorporates underlying statistical characteristics of data. Reliability measure defined by Bayes confidence, in the previous chapters, is fed into the automated data analysis system such that final classification of NDE signals is enhanced. Our work is inspired from Shapire's ADABOOST (traditional boosting)[64] algorithm with the modification of maximizing confidence of classification at every iteration of the classifier ensemble in addition to minimizing the misclassification error. Such an approach helps to detect defects with weaker indications which are missed otherwise.

One of the latest contributions in the field of machine learning is the development of ensemble classifiers known as boosting or mixture of experts. In a broader sense, an ensemble system is a combination of outputs from many individual classifiers such that the combined classifier performs better than all the individual ones. There are several advantages of using ensemble systems, one of them being its ability of statistical learning from limited amount of training data which is particularly relevant for analysing NDE data. In 1990, Schapire [64] proved that a strong classifier can be generated through a weighted combination of several weak classifiers and developed ADABOOST algorithm which was followed by extensive empirical and theoretical study [65] [66] [67]. Other versions of ensemble based decision systems include mixture of experts [68], classifier fusion [69] and committees of neural networks [70]. Benefits of ensemble based systems in automated decision making applications have also been recently discovered by computational intelligence community and NDE researchers. Polikar et al. [71] developed Learn++ algorithm, based on ensemble classifiers, which achieves incremental learning on data from ultrasonic weld inspection wherein the classifier is able to learn new information without forgetting previously acquired knowledge.

5.2 Background

5.2.1 ADABOOST

Boosting is a technique of combining a group of weak learners into a strong classifier with much lower error rate. A weak learner is a simple classifier which produces prediction results of an instance just better than random-guessing. Boosting creates an ensemble of classifiers by strategically resampling the data. The final classification is then obtained by combining prediction results of weak classifiers using majority voting. In 1997, Freund and Schapire introduced ADABOOST algorithm which generates hypotheses by training weak learners on instances drawn from an iteratively updated distribution of the training data [72]. This update ensures that instances which are misclassified in previous classifier are more likely to be included in training data of the next classifier. The pseudocode for the original ADABOOST algorithm is provided in Algorithm 3.

Let $S = \{(x_1, y_1), ..., (x_m, y_m)\}$ be a sequence of m training samples where each instance $x_i \in X$ represents a feature vector and each label $y_i \in Y$ represents the true class of x_i . Although ADABOOST can be exended to multiclass problems, in this paper we limit our discussion to a binary classification scheme such that $Y = \{-1, +1\}$.

For a defined set of T iterations, a weak classifier is trained on the training sequence S. The distribution $D_1(i)$ is initialized to be uniform which signifies that at t = 1, all instances (x_i) are equally likely to be selected for training the first weak classifier.

$$D_1(i) = 1/m; (5.1)$$

With every iteration, the weight distribution is updated according to the equation 5.2 and

a weak hypothesis h_t is generated for every instance $h_t(x_i) \forall i$ such that $h_t(x_i) \in H_t, H_t = [-1, +1].$

$$D_{t+1}(i) = \frac{D_t(i)e^{\left(-\alpha_t y_i h_t(x_i)\right)}}{Z_t}$$
(5.2)

$$\alpha_t = \frac{1}{2} \ln \left(\frac{-1 + r_t}{1 - r_t} \right) \tag{5.3}$$

where $r_t = \sum_i D_t(i) y_i h_t(x_i)$

Whenever there is mismatch in sign of h_t and y_t , it signifies misclassification of that instance and its weight is increased. Correctly classified instances have their weights unchanged. The parameter α controls the influence of each of the weak hypothesis and is defined by equation 5.3. The final output of the classifier ensemble H(x) is the signed summation of all the weak hypotheses given by equation 5.4. During testing of blind data x, the final hypothesis H(x) is calculated and its class is predicted based on its sign $\{-1, +1\}$.

$$H(x) = sign(\sum_{t=1}^{T} \alpha_t h_t(x))$$
(5.4)

5.3 Confidence rated classification :proposed method

In confidence-rated boosting proposed by Schapire and Singer [73], the chosen confidence measure is heuristic in nature and does not quantify the sources of uncertainties. In this thesis, typical uncertainties present in NDE data analysis are quantified in terms of confidence measure which includes effect of quantity of training data, quality of features and noise in test data. Therefore it is a more comprehensive measure of reliability which can be used as feedback to classification algorithm to increase the classification accuracy.

Algorithm 3 ADABOOST

Input: Training data $S = \{(x_i, y_i)\}, i = 1, 2,, m$ with correct labels $y_i \in Y, Y = [-1, +1];$

1: Initialize

$$D_1(i) = 1/m; (5.5)$$

and

$$t = 1; (5.6)$$

2: T =Total no. of iterations in classifier ensemble;

Output: Final hypothesis H(x)

- 3: for $t \leq T$ do
- 4: Train Weaklearner using distribution D_t ;
- 5: Get weak hypothesis $h_t(x_i) \forall i$ such that $h_t(x_i) \in H_t, H_t = [-1, +1]$;
- 6: Calculate

$$\alpha_t = \frac{1}{2} \ln \left(\frac{-1 + r_t}{1 - r_t} \right) \tag{5.7}$$

where $r_t = \sum_i D_t(i) y_i h_t(x_i)$

7: Update

$$D_{t+1}(i) = \frac{D_t(i)e^{\left(-\alpha_t y_i h_t(x_i)\right)}}{Z_t}$$
(5.8)

where Z_t is a normalization factor chosen to have D_{t+1} as a distribution function;

- 8: end for
- 9: Final hypothesis

$$H(x) = sign(\sum_{t=1}^{T} \alpha_t h_t(x))$$
(5.9)

The pseudocode of proposed confidence-rated ADABOOST is shown in Algorithm 4. The primary difference from traditional ADABOOST is that the prediction of every instance by each weak hypothesis is multiplied with its associated Bayes confidence.

$$h_t(x_i) = C_{t,i}(x_i)H_t, H_t = \{-1, +1\}$$
 (5.10)

where,

$$C_{t,i} = \left(p_{pos}^{t}(x)\right)_{y_{j}} = \frac{\left(p^{t}(x)\right)_{y_{j}}}{\sum_{i=1}^{2} \left(p^{t}(x)\right)_{y_{i}}}$$
(5.11)

By weighting the hypothesis of every weak learner with the confidence metric, the samples

which are classified with a higher confidence but to the wrong class are associated with lower weights. Hence, the objective function is modified such that for every iteration classification confidence is maximized along with minimizing the error rate.

Algorithm 4 Bayes confidence-rated ADABOOST

Input: Training data $S = \{(x_i, y_i), i = 1, 2,, m \text{ with true labels } y_i \in Y, Y = \{-1, +1\};$ **Output:** Final hypothesis H(x)

1: Initialize

$$D_1(i) = 1/m (5.12)$$

and

$$t = 1 \tag{5.13}$$

- 2: T =Total no. of iterations in classifier ensemble;
- 3: for $t \leq T$ do
- 4: Estimate $(\mu_t, \sigma_t)_{y_i}$ for all classes y_i
- 5: Calculate class-conditional pdf $(p^t(x))_{y_i}$ for all classes $y_i \in Y$, $Y = \{-1, +1\}$ using estimated $(\mu_t, \sigma_t)_{y_i}$
- 6: Calculate the posterior probability for the class for which confidence is calculated (say y_i):

$$C_{t,i} = \left(p_{pos}^{t}(x)\right)_{y_{j}} = \frac{\left(p^{t}(x)\right)_{y_{j}}}{\sum_{i=1}^{2} \left(p^{t}(x)\right)_{y_{i}}}$$
(5.14)

- 7: Train Weaklearner using distribution D_t ;
- 8: Get weak hypothesis $h_t(x_i) \forall i$ such that

$$h_t(x_i) = C_{t,i}(x_i)H_t, H_t = \{-1, +1\}$$
 (5.15)

9: Obtain

$$\alpha_t = \frac{1}{2} \ln \left(\frac{-1 + r_t}{1 - r_t} \right) \tag{5.16}$$

where $r_t = \sum_i D_t(i) y_i h_t(x_i)$;

10: Update:

$$D_{t+1}(i) = \frac{D_t(i)e^{\left(-\alpha_t y_i h_t(x_i)\right)}}{Z_t} \tag{5.17}$$

where Z_t is a normalization factor chosen to have D_{t+1} as a distribution function;

- 11: end for
- 12: Final hypothesis

$$H(x) = sign(\sum_{t=1}^{T} \alpha_t h_t(x))$$
(5.18)

5.4 Results

5.4.1 Simulation Results

The proposed method of confidence-rated ADABOOST is applied on classification of synthetic data into two classes- red and blue and its performance is compared with traditional ADABOOST performance. Dataset used for training and validation testing of the two methods are shown in figure 5.2.

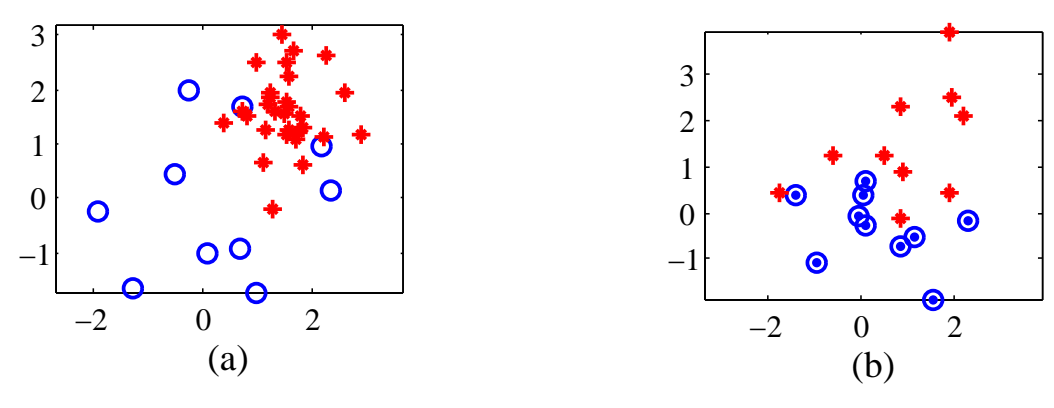


Figure 5.2: (a) Training data (b) test data with true class labels of two classes: red and blue.

Figure 5.3 illustrates the classification results of the two methods. It is found that after 16 iterations, the error rate on training data has reached to zero in traditional ADABOOST classifier, but is at 5% for confidence-rated ADABOOST. However, the error rate on the test data classification is calculated as 35% and 25% for traditional ADABOOST and confidence-rated ADABOOST respectively. This is due to the fact that the principal objective of ADABOOST is to minimize training error which often leads to overfitting of the model. It results in misclassifications on a blind test set which is reflected from the error in the test dataset. When confidence-rated ADABOOST is applied, it increases the generalization property of the classifier by classifying test data with lower error.

Figure 5.4 shows that in both the approaches of classifier ensemble, the error rate on

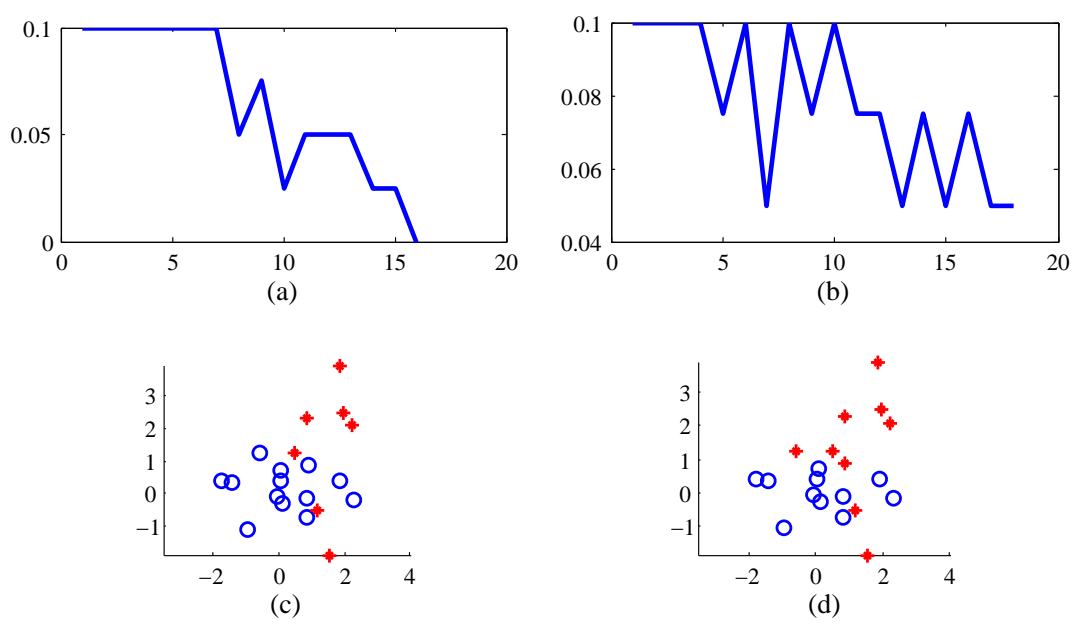


Figure 5.3: Training error rate versus number of weak classifiers in (a) traditional AD-ABOOST (b) Bayes confidence-rated ADABOOST. Test data classified with ADABOOST model (c) traditional ADABOOST: Error rate on test data= 35% (d) Bayes confidence-rated ADABOOST: Error rate on test data= 35%

test data decreases with increase in number of training samples, although confidence-rated ADABOOST poses approximately 5% lower error rate than the other.

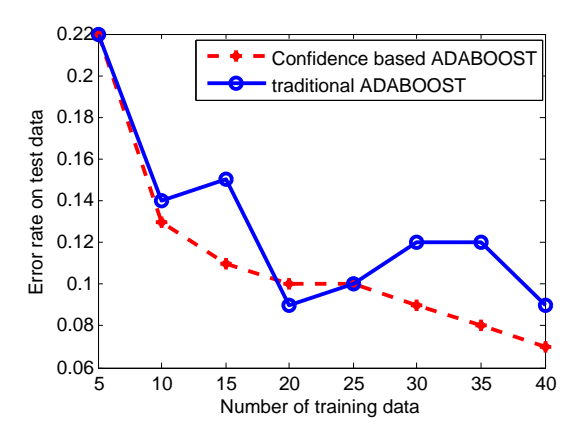


Figure 5.4: Comparison of classification performance of traditional ADABOOST and confidence-rated ADABOOST.

5.4.2 Experimental Results

As described in NDE application presented in chapter 4, confidence-rated classifier ensemble is utilized to classify experimental data obtained from eddy current inspection of steam generator(SG) tubes. SG tubes which are continuously exposed to harsh environmental conditions are affected by various types of degradations. There is demand from industry for the development of automated signal classification systems that can provide accurate and consistent signal interpretation with capability of computing its reliability. A typical post-processed signal from eddy current tube inspection is shown in figure 6. The regions Of interest (ROIs) denoting the possible locations of the flaws are identified by the ASC system as shown by the rectangular boxes.

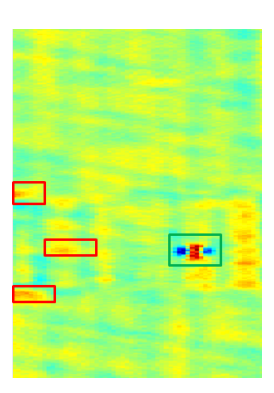


Figure 5.5: A sample post-processed eddy current signal of defective SG tube. Red rectangular boxes: ROIs containing false indications (classified as *non-defect*); Green rectangular boxes: ROIs containing true defects.

Discriminatory features are extracted from these ROIs of training data and used to develop the classifier model. In this experiment, peak values of real and imaginary signal from each ROI are used as features for classification. As in the case of synthetic dataset, the total available training data from experiments was divided into two sets: one to train the classifier model and the other to validate the performance of the classifier. Both methods of classifier ensemble were compared. The feature plots of the training and test dataset are

shown in figure 5.6.

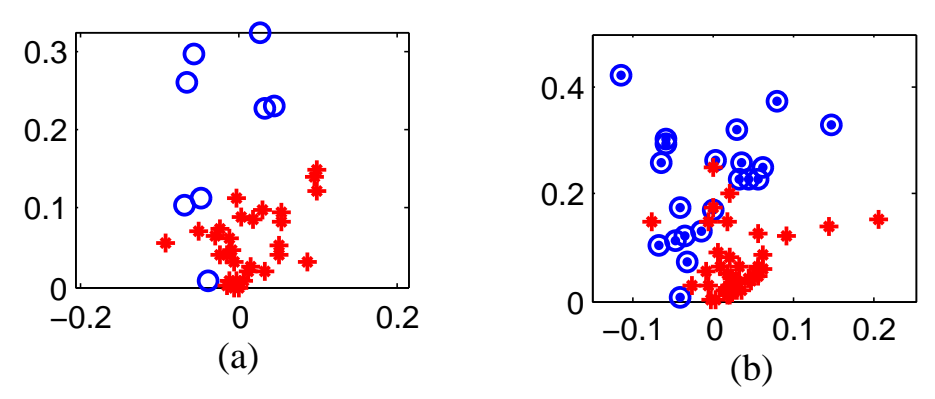


Figure 5.6: (a) Training data (b) test data with true class labels of two classes: red (non-defect) and blue (defect).

Confidence of classification of every training sample is calculated by the comprehensive Bayes posterior probability as stated in algorithm 2 and then implemented into the confidence-rated-classification framework. Classification results by the two ADABOOST methods are shown in figure 5.7. As in synthetic dataset, confidence-rated ADABOOST is able to correctly classify more test instances relative to the traditional ADABOOST. A few flaws, as indicated in Figure 5.8, are detected correctly by applying confidence-feedback to classifier ensemble that were missed by traditional ADABOOST. Three eddy current images of defective steam generator tubes are depicted having ROIs identified by the ASC system. The green boxes indicate defects which are correctly identified by both the classification methods. The red rectangular ROI boxes indicate more subtle flaws and are the ones which are classified as non-defects by traditional ADABOOST, but correctly identified as defects by the confidence-rated ADABOOST. As a result, error rate reduced from 19.40% to 14.93% in the proposed ASC system having confidence feedback.

In this thesis, confidence-based ADABOOST has been validated on a two-class classification problem. This approach not only emphasizes the importance of a self-evaluation

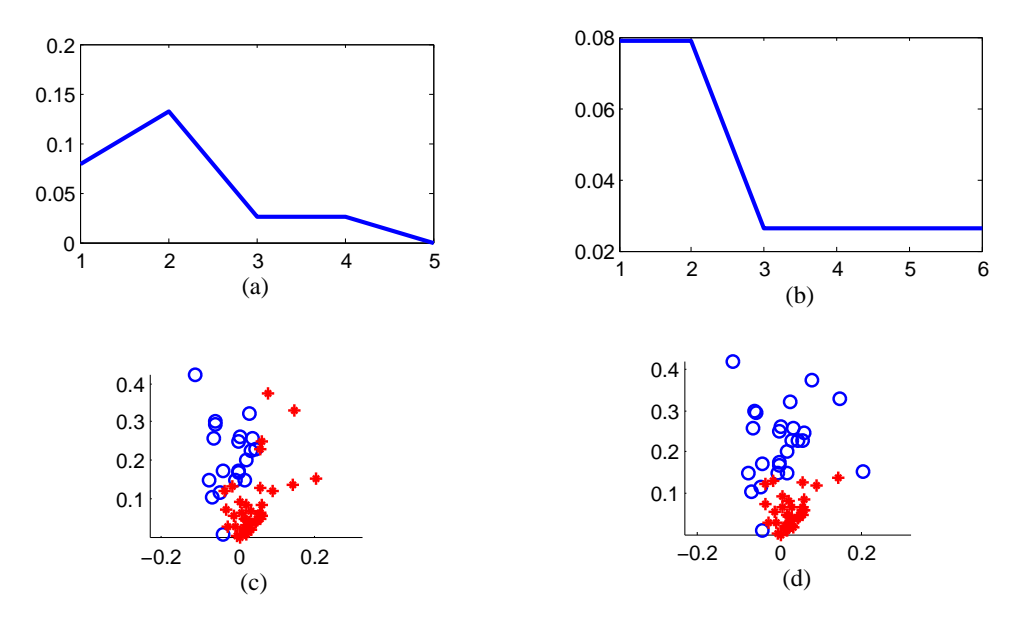


Figure 5.7: Training error rate versus number of weak classifiers in (a) traditional AD-ABOOST (b) Bayes confidence-rated ADABOOST. Test data classified with ADABOOST model (c) traditional ADABOOST: Error rate on test data= 19.40% (d) Bayes confidence-rated ADABOOST: Error rate on test data= 14.93%

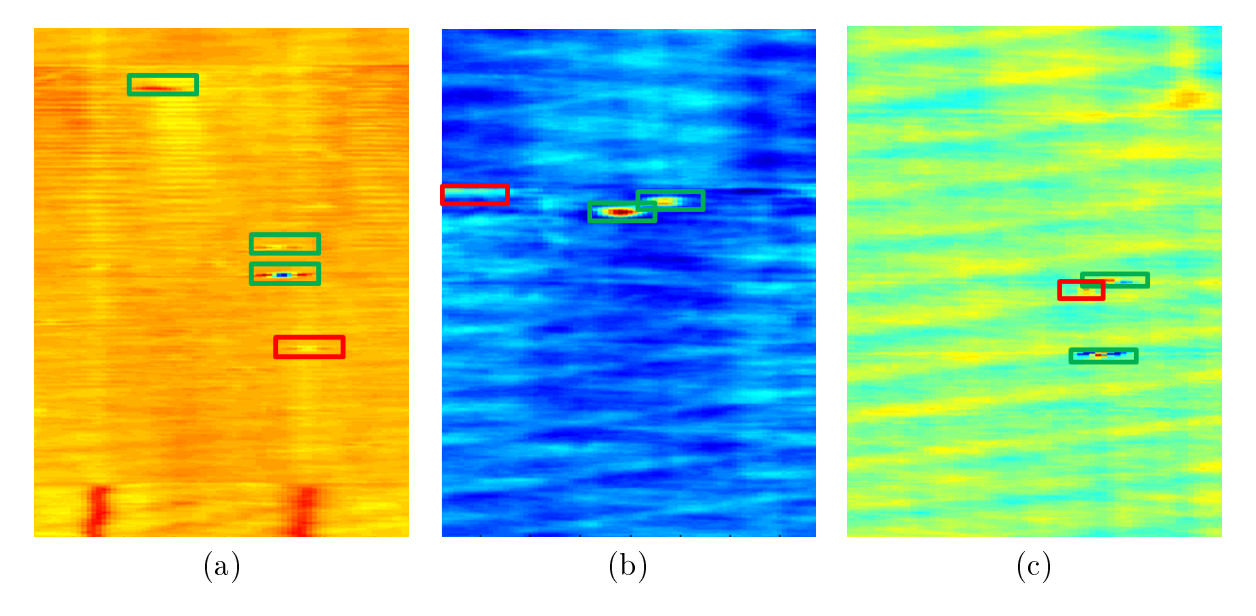


Figure 5.8: Eddy current response signal after calibration of 3 defective SG tubes (Imaginary channel, plus point probe, at 300KHz). Green boxes: ROIs (true defects) classified as defects by both traditional and Confidence-based ADABOOST. Red boxes: ROIs (true defects) classified as non-defects by traditional ADABOOST but correctly classified as defects by Confidence-based ADABOOST.

measure in ASC systems, but further utilizes it for improving classification of NDE signals. The proposed classifier exploits the advantages of a boosting algorithm while avoiding the problem of over-fitting. Weaker indications of tube defects from an eddy current response signal which are misclassified by traditional ADABOOST, are correctly classified with a confidence-based ensemble system.

Chapter 6

Prognosis in NDE

6.1 Introduction

In addition to assessing classification confidence of NDE data obtained from periodic monitoring of structures and industrial components, study of structural reliability based on the acquired data is an equally critical task to achieve. The primary objective of long-term reliability analysis in NDE is defect growth prediction or damage prognosis. As cited by Farrar et al. [74], damage prognosis (DP) is defined as "the estimation of the remaining useful life (RUL) of equipment by taking into consideration the information gathered from monitoring systems, design information, past operation experience and operating environment of the system or equipment". Accurate and dynamic RUL prediction enables industries to maximize usage of a component before it encounters a catastrophic failure. Integrated structural health monitoring and damage prognosis (SHM-DP) strategies [1]–[3], coupled with nondestructive evaluation (NDE) techniques [4]–[6], are becoming fundamental engineering tools for near-real-time structural integrity assessment and predictive maintenance.

6.2 Theory of Reliability

According to International Organization for Standardization (ISO), reliability is defined as " the ability of an item to perform a required function, under given environmental and op-

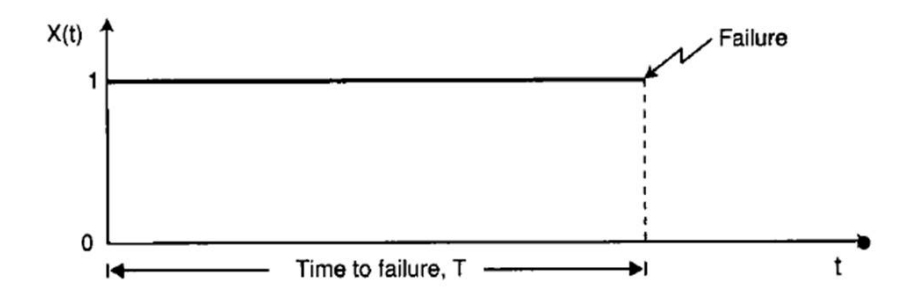


Figure 6.1: State variable X(t) and Time to Failure t of a system. [7]

erational conditions and for a stated period of time (ISO8402)". In simpler terms, reliability is calculated as the probability that a given component or entity can operate satisfactorily for a specified time period in the actual application for which it is intended without experiencing a failure.

The state of an system at time t may be described by the state variable X(t). X(t) is defined as:

$$X_{t} = \begin{cases} 1, & \text{if system is functioning at time t} \\ 0, & \text{if system is not functioning at time t} \end{cases}$$

$$(6.1)$$

Suppose the system starts operating at time t = 0. The time elapsing from its start time to the instant it encounters a failure is termed as the time to failure (T). The relation between X(t) and (T) is demonstrated in Figure 6.1.

It is quite obvious that due to presence of several uncertainties during the operation of the system, time to failure (T) cannot be interpreted as a fixed value but as a random variable with a probability density function f(t) and distribution function:

$$F(t) = Pr(T \le t) = \int_0^t f(u)du \text{for } t > 0$$
(6.2)

where F(t) denotes the probability that the item fails within the time interval (0,t]. The

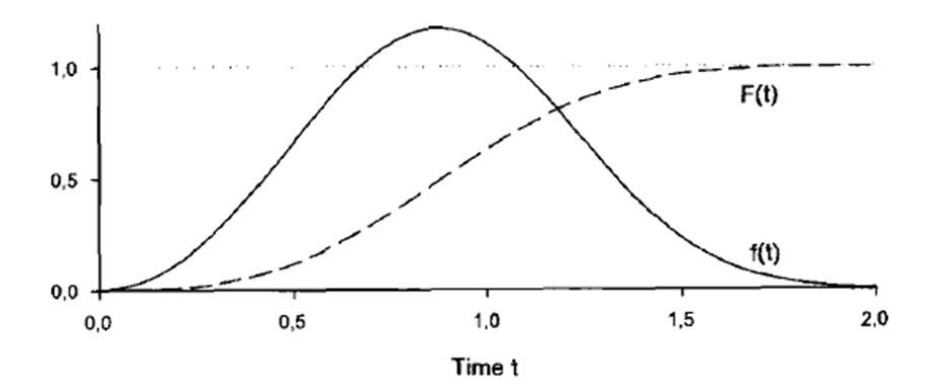


Figure 6.2: Distribution function F(t) and probability density function f(t).[7] pdf f(t) and CDF F(t) are illustrated in Figure 6.2.

It should be noted that the operation time t does not indicate the clock time. It can include any other metrics which counts the age or usage of the system such as number of loading cycles of a mechanical part, number of kilometers a car has been driven, number of rotations of a bearing etc.

The reliability function of a system can be defined as R(t) where:

$$R(t) = 1 - F(t) = Pr(T > t) fort > 0$$
 (6.3)

or equivalently

$$R(t) = 1 - \int_0^t f(u) \, du = \int_t^{\inf} f(u) \, du \tag{6.4}$$

Hence R(t) is the probability that the item does not fail in the time interval (0, t], or, in other words, the probability that the item survives the time interval (0, t] and is still functioning at time t. The reliability function R(t) is also called the survivor function and is illustrated in Figure 6.3. There are several other statistical measures and functions which are useful in study of reliability theory such as Failure Rate function or Mean Time to Failure etc. which are outside the scope of this research and hence not discussed in this thesis. Readers

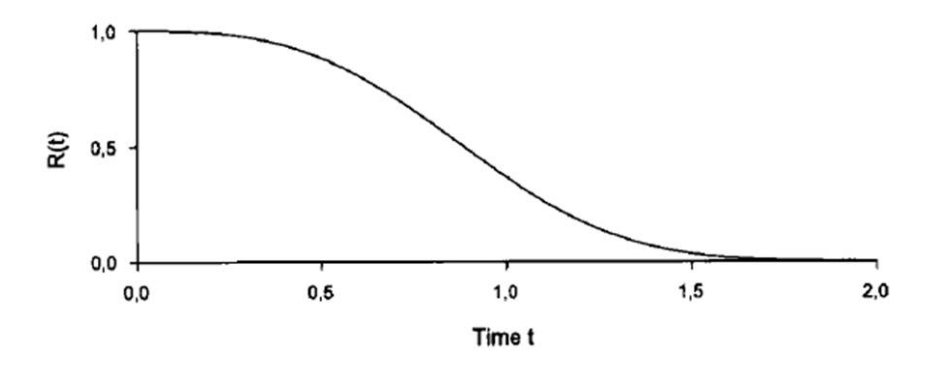


Figure 6.3: Reliability or survivor function R(t). [7]

interested in such topics can find the definitions and explanations in the book by Rausand and Arnljot [7].

6.2.1 Remaining Useful Life (RUL)

Among the broader definition of reliability measure R(t), the metric most commonly used in damage prognosis is remaining useful life (RUL) of a system under operation. RUL of any system can be defined by a random variable which depends on system's current age, its operation environment and health information acquired from periodic NDE of the system. If the history of inspection data acquired upto time t is denoted by Y(t), the primary goal of prognosis is to estimate expectation of the RUL pdf : $E(R_t|Y_t)$.

The process of damage prognosis followed by RUL calculation is demonstrated in figure 6.4. Firstly a health index (HI) is defined which characterizes the damage level of a system or structure at a given time instant t. After regular time intervals (or loading cycles), measurements are recorded and HI is calculated at every time step upto the current time (say k). These constitute the measurement data shown by the black dots in figure 6.4. The objective of damage prognosis is to construct the damage propagation path up to the current time using the measurement HI values as well as predict HI for future time ($\hat{\tau}$) till the system

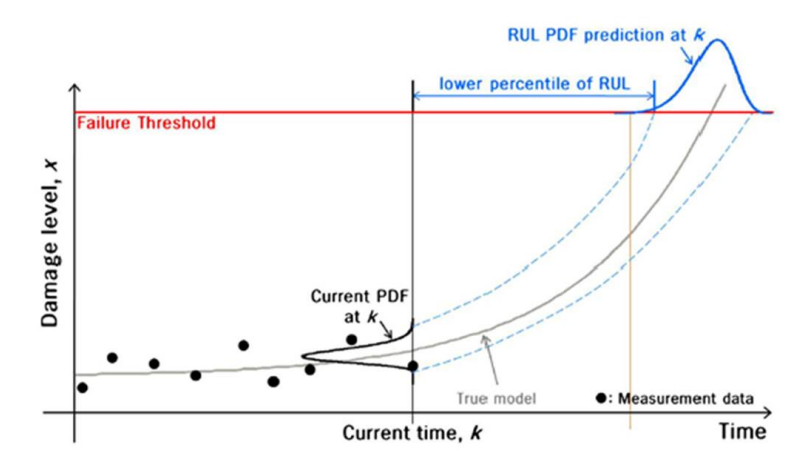
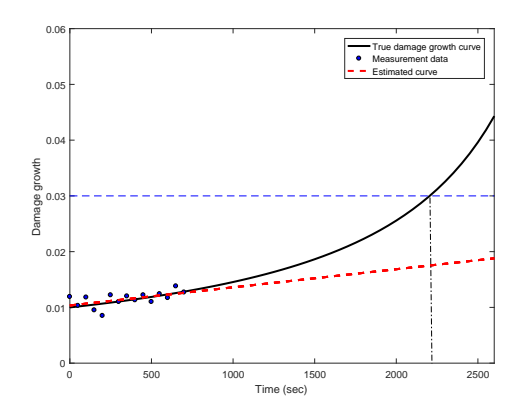


Figure 6.4: Illustration of damage path prognosis and RUL prediction [8]

reaches a predefined failure threshold. Failure threshold is usually decided as the value of HI when the system is expected to crash or fail and is generally obtained from domain experts in the specific application field/ industry.

$$RUL = \hat{\tau} - k \tag{6.5}$$

At a first glance, damage prognosis may seem like a trivial problem of polynomial fitting on the measurement data and then extending the fitted curve upto the threshold to calculate the RUL. However, this may not be a feasible approach in most practical cases. Figure 6.5 illustrates the reason why RUL prediction using a simple curve fitting solution may not always lead to the correct solution. In many cases the damage propagation is a complex and dynamic phenomenon which not only depends on the material and dimensions of the structure but also on external characteristics such as pressure, temperature or other environmental conditions etc. In such cases, a damage propagation curve generated from first few measurements is very different from the true damage growth path. Wrong estimation of RUL can be dangerous especially if it is over-estimated (illustrated in Figure 6.5 (a)). A first order polynomial fit is applied on the measurement data acquired upto 750 hours and the damage growth curve is estimated. If damage size of 0.03 mm is considered as the failure threshold, then the optimum time at which the system should be stopped is at 2200 hours. However, the estimated damage growth line reaches the threshold of 0.03 much beyond 2200 hours and therefore the equipment will continue operation beyond its safety limit which may be fatal.



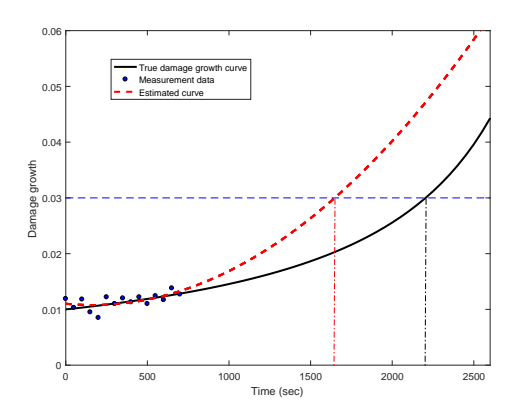


Figure 6.5: (a) 1 degree polynomial fitting on measurement data leading to under estimation of RUL (b)2 degree polynomial fitting on measurement data leading to over estimation of RUL

On the other hand, under-estimation of RUL leads to suboptimal performance of the equipment as the system is stopped too early, as shown in Figure 6.5 (b). A 2nd order polynomial curve is fitted on the same measurement data which reaches the failure threshold of 0.03 mm at 1630 hours (much earlier than 2200 hours). As a result, the system is stopped earlier than its safety limit(2200-1630=570 hours before expected failure). Both these cases should be avoided and therefore statistical methods are adopted for accurate RUL estimation. Prognostic approaches should ideally be able to incorporate underlying uncertainties involved in the damage propagation process in order to provide accurate prediction results. A review of current state-of the art in this topic is provided in the following section.

6.3 Literature Review on RUL Prognosis

6.3.1 Model-based methods

Existing prognosis methods can be roughly classified into model-based (or physics-based) and data-driven methods. Model-based methods predict the equipment health condition using component physical models, such as finite element (FE) models, and damage propagation models based on damage mechanics. Such methods use fixed model parameters depending on material properties and generally do not use condition monitoring data for prediction of damage evolution. Several model-based systems has been studied over the past years. Kacprzynski et al. [75] presented a prognosis tool using 3D gear FE modeling to study damage inititation and propagation in helicopter gears. Li and Lee [76] proposed a gear prognosis approach based on FE modeling where an embedded model was proposed to estimate Fourier coefficients of the meshing stiffness expansion. The strip-yield model included in the NASGRO software developed in [77] is widely used to simulate crack growth under variable amplitude loading. If accurate models can be developed for every mechanical structure and damage type, model-based prognosis can provide prediction results with high precision. However, building authentic physical models for describing the equipment dynamic response and damage propagation is a challenging task in itself which requires a thorough understanding of the system. If any important physical phenomenon is missed, the prediction of degradation will be erroneous resulting in catastrophic consequences..

6.3.2 Data-based methods

On the other hand, data-driven prognostic methods models the relationship between equipment age and condition monitoring data by training the prognostic system on historical data. Gebraeel et al. [78] used Artificial Neural Network (ANN) for monitoring rolling bearing elements and predicting fatigue crack propagation from vibration-based degradation signals. Bayesian updating methods have been investigated in equipment prognostics for utilizing the real-time condition monitoring data [79]. Data-driven methods do not rely on physical models, and only utilize the collected condition monitoring data for health prediction. Accuracy of these methods strongly rely upon the training data characteristics. As a result, they may fail to produce accurate prediction if insufficient or under-representative training data is used. Results from these methods may sometimes be counter-intuitive as they do not consider underlying physics of the system and therefore may be erroneous at times.

6.3.3 Integrated methods

By incorporating benefits of both model-based and data-based prognostic approaches, integrated or hybrid methods have gained a lot of popularity in recent years [80]. Under these methods, physics based degradation models are considered but the parameters of the physical model underlying the damage growth process are not fixed. Instead they are estimated utilizing the data from CBM of the structure. Bayesian inference [81] is a common technique implemented in several studies wherein the model parameters are updated at every instant a new inspection data is reported, thereby increasing the accuracy of estimated physical model. Another crucial benefit of integrated methods is their ability to incorporate uncertainty due to model as well as measurements into their algorithm which makes them a better representative of practical systems. Bayesian inference has been used by Shankar et al. [82] to estimate parameters of finite element model, surrogate model and crack growth model in cylindrical structures subjected to fatigue. Another hybrid approach is the particle filter

based framework developed by Orchard and Vachtsevanos [83] for the failure prognosis of planetary carrier plates.

A literature review and mathematical theories of a few broad categories of prognostic approaches are discussed below for understanding the state-of-art methodologies in this area.

6.3.3.1 Regression based models

Regression-based methods are have gained popularity in industries and academic fields for estimation of equipment life due to the simplicity of these models.[84, 85]. They fall into the category of data-based prognosis. The fundamental principle of these methods is that the health of the systems under study can be mapped by some key features obtained from condition monitoring (CM) of systems and RUL can be estimated by trending, and predicting these CM features upto a predefined threshold. Lu and Meeker [84] were the first authors to present a general nonlinear regression model to characterize the degradation path of a population of units. According to the general degradation model, the observed sample degradation Y(t) at time t can be represented as $Y(t) = D(t; \Psi, \theta) + \epsilon(t)$, where $D(t; \Psi, \theta)$ is the actual path at time t, Ψ is the fixed effect regression coefficients common for all units, θ is the random effect representing individual unit characteristics, and $\epsilon(t)$ is the random error term described by $\mathcal{N}(0, \sigma_{\epsilon})$. Here, θ and $\epsilon(t)$ are assumed to be independent of each other. Using this model, the RUL at sampling time t_i can be defined as:

$$X_{t_i} = x_{t_i} : D(t_i + x_{t_i}; \Psi, \theta) \ge w | D(t_i; \Psi, \theta) < w$$

$$\tag{6.6}$$

Similar to the work by Lu and Meeker, many extensions and applications have appeared in literature, such as machine condition monitoring using regression trees [86, 87], updating

prognosis in biliary cirrhosis using Cox regression models [88], degradation assessment using logistic regression [89]. Based on critical analysis of previous methods and case studies involved, the underlying assumptions of the regression model can be summarized as follows: (i) the condition of the device deteriorates with operating time and the level of deterioration can be observed at any time; (ii) the device being monitored comes from a population of devices, each of which exhibits the same degradation form; and (iii) the distribution of the random term across the population of devices is known with the error in degradation signal being independent and identically distributed across the population of devices.

Although regression is a relatively simpler technique for prognosis, it is not very well suited for dynamic systems in which damage growth rate changes at different stages of degradation. All data which has been observed upto the current time is considered as a collective dataset and regression is performed instead of capturing the temporal characteristics of the measurements. Assumption of independence and identically distribution of measurements may not be valid for all applications as a result of which the final RUL computation may be inaccurate.

6.3.3.2 Markovian based models

Temporal characteristics or the observed data is incorporated into Markovian models where it is assumed that the future degradation state of a system depends only on its current degradation state, which is often termed as being memoryless. In general, the degradation process $Y_n, n \geq 0$ evolves on a finite state space $\phi = 0, 1, ..., N$ with 0 corresponding to the perfect healthy state and N representing the failed state of the monitored system. The RUL

at time instant n can be defined as

$$X_n = \inf x_n : Y_{n+x_n} = N | Y_n \neq N \tag{6.7}$$

The transition probability matrix of such Markov models can be written as:

$$P = \begin{pmatrix} \tilde{P} & P_0 \\ 0 & 1 \end{pmatrix} \tag{6.8}$$

with $P_0 = (I - \tilde{P})e$, where \tilde{P} is the transition matrix for transient states $\phi \backslash N$, I is the identity matrix and $e = (1, ..., 1)^T$ is a column vector with dimensions N - 1. In principle, RUL estimation using Markovian-based models can be captured by computing amount of time the process will take to transit from the current state to the absorbing state N for the first time, referred to as FPT.

Based on this framework, several authors have developed their prognosis methods suited to respective applications. Kharoufeh [90] considered the reliability of a single-unit system whose cumulative damage over time was a continuous wear process that depended on an external environment process. The external process was characterized as a time homogeneous Markovian environment with continuous time. Later, Kharoufeh and Mixon [91] proved several limit theorems related to a time-scaled version of the degradation process and a space-scaled version of the unit's random lifetime. Although their models were mathematically appealing and easy to implement, they lacked the flexibility to account for the environment state sojourn times or shock inter-arrival times which may not be exponentially distributed. Additionally, Lee et al. [92] incorporated the Markov property into a regression model and presented a new model for the survival analysis called Markov threshold regression, in which

the subject's health followed a stochastic process and failure occurred when the process first reached a failure state.

Despite their strong mathematical background, RUL estimation based on Markov models faces a few limitations. Firstly, the underlying assumption of independence and memoryless property is difficult to achieve in real measurements. Also, the transition probability among the system states in Markov models is often determined by empirical knowledge or by a large number of samples, which is not always available. These limitations have been addressed to an extent by studies based on semi-Markov or Hidden Markov Models with indirectly observed state processes. Several papers can be found in literature showing their application to structural prognosis [93, 94, 95, 96].

6.3.3.3 Stochastic Filtering

In lieu of a deterministic RUL calculated by the above two approaches, the RUL is treated as a random variable by stochastic filtering models. This broad category of methods allows system uncertainties incorporated into the estimation of damage propagation path which makes them suitable for structural monitoring systems. Batzel and Swanson [97] presented a RUL estimation method based on the Kalman filter for aircraft power generators. In their work, it was assumed that the relationship between the RUL and the estimated state followed a time-dependent function. Hence, the RUL estimation was achieved by minimizing the difference between the value of such function and a pre-determined state threshold. If, for an observation state y_t , x_t is defined as the RUL at time t or the current monitoring check point, then

$$x_t = x_{t-k} - (t-k) \text{ if } x_{t-k} > (t-k)$$
 (6.9)

and

$$y_t = g(x_t, \theta) \tag{6.10}$$

where g is a function to be determined, θ is a noise term, k is the time of the last monitoring checkpoint and (t-k) is the interval between the current and the last checkpoint. In addition, Luo et al. [98] used a multiple-model filter to estimate the mean and variance of the RUL without considering the distribution of RUL explicitly.

Among all stochastic filtering techniques, the most commonly used process is the Bayesian updating based on the philosophy that one can incorporate prior knowledge about the degradation phenomenon in the model and update the model as more measurements are collected. One of the ways of achieving Bayesian updating process is the particle filtering approach investigated by Orchard and Vachtsevanos [83]. They used a non-linear state-space model (with unknown time-varying parameters) and a particle filtering algorithm that can update the current state estimate. In this thesis, this approach was used to compute the damage growth curve in composite materials and therefore this algorithm will be described in more detail in the following sections.

6.4 Theory of Bayesian Updating

According to the Bayesian point of view, observation data X is considered a random variable generated from an underlying pdf $f(x, \boldsymbol{\theta}), \boldsymbol{\theta} \in \Theta$. $\boldsymbol{\theta}$ is also defined by a random variable with density $f_{\Theta}(\boldsymbol{\theta})$ which describes the probability of occurrence of a parameter value from Θ , before any observation is made. Hence $f_{\Theta}(\boldsymbol{\theta})$ is called the prior density of Θ . The objective of Bayes updating is to obtain $\hat{\boldsymbol{\theta}}$, the estimated value of $\boldsymbol{\theta}$ that characterizes the underlying pdf generating the observation data.

With this interpretation, joint density of X and Θ , $f_{X,\Theta}(x,\boldsymbol{\theta})$, is given by:

$$f_{X,\Theta}(x,\boldsymbol{\theta}) = f_{X|\Theta}(x|\boldsymbol{\theta}).f_{\Theta}(\boldsymbol{\theta})$$
 (6.11)

The marginal density of X is,

$$f_X(x) = \int_{\Omega} f_{X,\Theta}(x, \boldsymbol{\theta}) d\boldsymbol{\theta} = \int_{\Omega} f_{X|\Theta}(x|\boldsymbol{\theta}) f_{\Theta}(\boldsymbol{\theta}) d\boldsymbol{\theta}$$
 (6.12)

Hence, the conditional density of Θ given X = x becomes,

$$f_{\Theta|X}(\boldsymbol{\theta}|x) = \frac{f_{X,\Theta}(x,\boldsymbol{\theta})}{f_{X}(x)} = \frac{f_{X|\Theta}(x|\boldsymbol{\theta})f_{\Theta}(\boldsymbol{\theta})}{f_{X}(x)}$$
(6.13)

 $f_{\Theta|X}(\boldsymbol{\theta}|x)$ expresses the probability distribution of Θ after having observed X=x, and $f_{\Theta|X}(\boldsymbol{\theta}|x)$ is therefore called the posterior density of Θ . It should be noted that when X is observed, $f_X(x)$ occurs in Equation 6.13 as a constant. Hence $f_{\Theta|X}(\boldsymbol{\theta}|x)$ is always proportional to f $f_{X|\Theta}(x|\boldsymbol{\theta})f_{\Theta}(\boldsymbol{\theta})$:

$$f_{\Theta|X}(\boldsymbol{\theta}|x) \propto f_{X|\Theta}(x|\boldsymbol{\theta})f_{\Theta}(\boldsymbol{\theta})$$
 (6.14)

The Bayesian approach is used for updating information about the parameter Θ . First, an initial probability density for Θ is assigned before observations of X=x is collected. When the first measurement in X is available, the prior distribution of Θ is updated to the posteriori distribution of Θ , given X=x. This process is repeated and in the next iteration the posterior distribution of Θ , given X=x, is chosen as the new prior distribution. When another measurement in X is observed, it leads to a second posterior distribution, and so

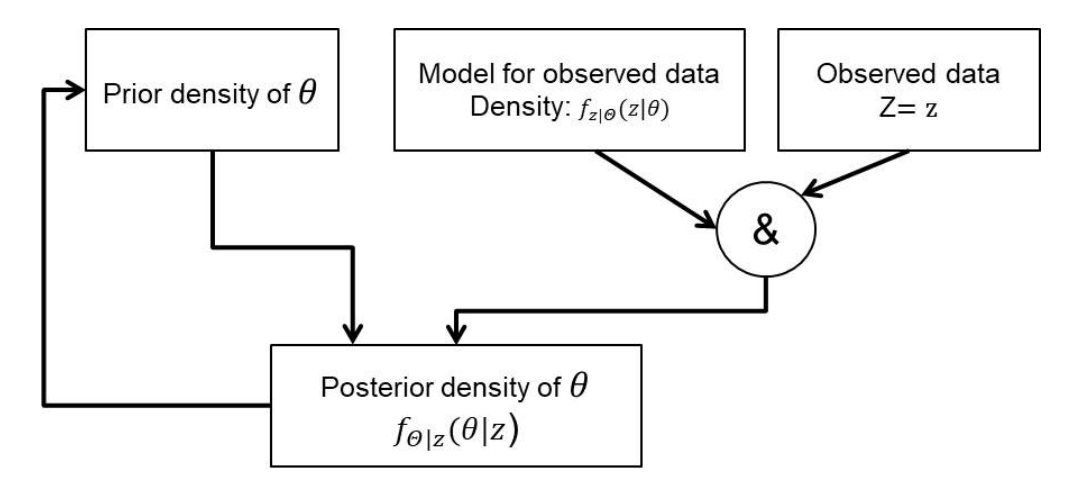


Figure 6.6: Bayes Updating Process

on. This updating process is illustrated in Figure 6.6.

The final task of the Bayes updating process is to estimate the value θ of Θ that generates an observed value x of X. We denote this estimate by $\widehat{\theta}(x)$. The optimum estimate is the one that minimizes the expectation of mean squared error (MSE): $E[(\widehat{\theta}(x) - \Theta)^2]$.

$$E[(\widehat{\theta}(x) - \Theta)^2] = \int_{-\infty}^{\infty} \int_{\Omega} (\widehat{\theta}(x) - \Theta)^2 f_{X,\Theta}(x,\theta) dx d\theta$$
 (6.15)

By using equation 6.14,

$$E[(\widehat{\theta}(x) - \Theta)^2] = \int_{-\infty}^{\infty} f_X(x) \left[\int_{\Omega} (\widehat{\theta}(x) - \Theta)^2 f_{\Theta|X}(\theta|x) d\theta \right] dx$$
 (6.16)

 $E[(\widehat{\theta}(x)-\Theta)^2] \text{ is minimized when for each } x, \theta(x) \text{ is chosen to minimize } [\int_{\Omega} (\widehat{\theta}(x)-\Theta)^2 f_{\Theta|X}(\theta|x) d\theta]$ whose solution is $E(\Theta|X)$.

Hence, according to Bayes inference or updating process, the estimate of θ is the mean of the posterior distribution of Θ .

$$\widehat{\boldsymbol{\theta}} = E(\Theta|X) \tag{6.17}$$

6.4.1 Bayes update of model parameters using synthetic data

For prognostics application, the primary goal is to estimate the damage growth path based on measurement data, as illustrated in Figure 6.4. If data based method is adopted in such applications, no damage model needs to be defined; but data driven models may not always yield accurate results as discussed earlier. Hence integrated methods are a better alternative where a damage propagation model is defined whose parameters are estimated using the measurement data by Bayes updating process. It should be noted that in this thesis, damage growth model for degradation in composites is defined based on experimental measurements acquired from periodic NDE inspections. Although measurements were assumed to imply the underlying model, physics based relation between damage level and loading cycles have not been studied in this research. Physics-based relationships for a specific geometry and loading conditions depend entirely on the structural mechanics of a component and will be incorporated in future extensions of this research.

A synthetic measurement dataset is considered to demonstrate the implementation of Bayes updating procedure using a simple exponential damage model defined as:

$$k = Ct^m (6.18)$$

where, k represents the crack length propagating over time t. C and m are the model parameters. In this example, the value of C is kept fixed at 9.12×10^{-3} and m is estimated using the Bayes updating. 6 synthetic measurements are selected by adding random noise to the true crack length values at time 1, 10, 20, 30, 40 and 50 seconds. These replicate the observations that are obtained from experiments where the crack length is measured after fixed intervals of time or loading cycles. Figure 6.7 (b) shows the true crack growth curve

(by using true value of m = 1.48) along with the measurements selected. Only these 6 measurement data were used to estimate the unknown parameter m of the damage model to eventually predict the crack propagation path.

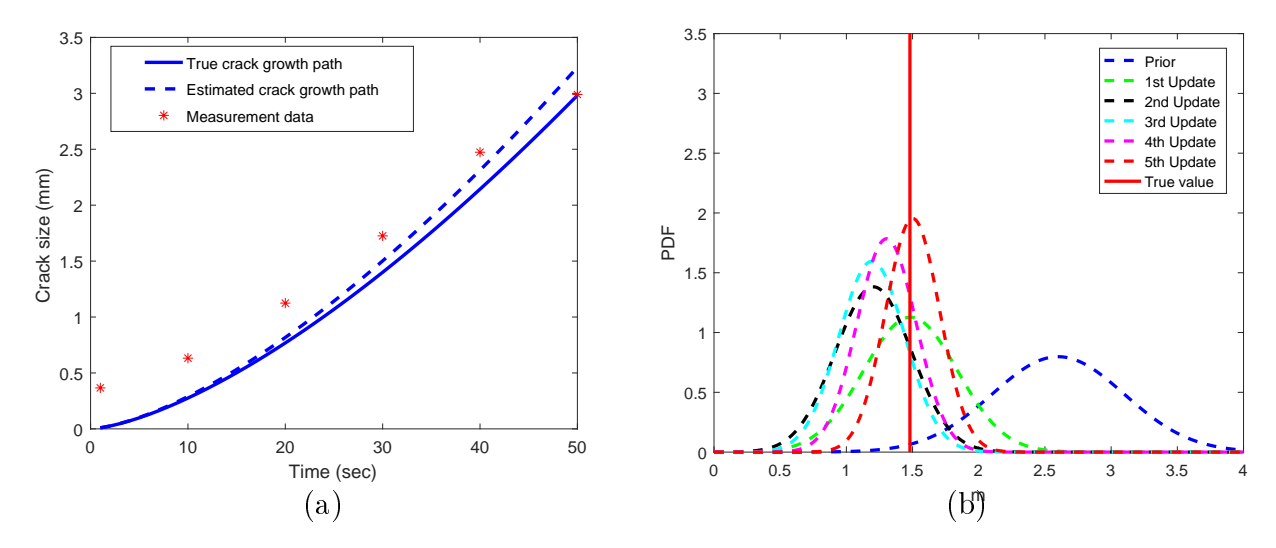


Figure 6.7: (a)Bayes Updating of parameter m (b) Crack growth example for synthetic dataset with estimated crack growth path.

The prior distribution of m is chosen as:

$$f_{prior}(m) \sim \mathcal{N}(2.6, 0.5^2)$$
 (6.19)

At each inspection time instant, the posterior distribution of the current iteration becomes the prior distribution for the next updating time. The updating history for the crack growth parameters is shown in Table 6.1. Thus it can be concluded that by repeating the recursive process as new measured data becomes available, the estimated parameters converges to their true values [99].

Inspection time (sec)	Crack length (mm)	Mean of m	Standard Deviation of m
1	0.296	2.6	0.5
10	0.645	1.45	0.35
20	1.086	1.19	0.29
30	1.695	1.17	0.25
40	2.17	1.27	0.22
50	3.10	1.43	0.2

Table 6.1: Bayes Updating history of parameter m for synthetic crack growth path.

6.5 Bayesian Updating based on Particle Filtering(PF) Approach

In recent years, recursive Bayesian framework has been used extensively in fault diagnostics and prognostics applications [100, 101]. In this approach, observed data is incorporated into the a-priori state estimation by considering the likelihood of measured values. Particularly, sequential Monte Carlo (SMC) technique, also referred to as particle filtering(PF) has gained popularity in engineering domain owing to their consistent theoretical foundation to handle model non-linearities or non-Gaussian observation noise [83, 102]. In this approach, the conditional probability is approximated by a 'swarm' of points, known as 'particles'. The particles constitute discrete samples with associated weights representing the discrete probability masses. Particles can be generated and recursively updated given a non-linear process model, a measurement model, a set of available measurements $Z = \{z_k, k \in N\}$ and an initial estimation for the state probability density function (pdf) $p(x_0)$. Using this idea Orchard and Vachtsevanos [83] presented a failure prognostic model to predict the evolution in time of the fault indicator and compute the RUL pdf of the faulty subsystem.

Under PF framework, the Bayesian update is processed in a sequential way with particles having probability information of unknown parameters. It is based on a state-transition

function or the damage propagation model f and measurement function h [103].

$$a_k = (f, \theta_k, \nu_k) \tag{6.20}$$

$$z_k = h\left(a_k, \omega_k\right) \tag{6.21}$$

where k is the time step index or index of loading cycle at which sample is scanned, a_k is damage state, θ_k is parameter vector and z_k is the measurement data. ν_k and ω_k are the model and measurement noise respectively. In prognostic applications, the measurement is assumed to be affected by white Gaussian noise $\omega_k \sim N(0,\sigma)$. Therefore, the unknown parameters are $\Theta = \{a, \theta, \sigma\}$, including the damage state a which is obtained based on the model parameters θ .

Figure 6.8 illustrates the process of Bayes updation using particle filtering technique.

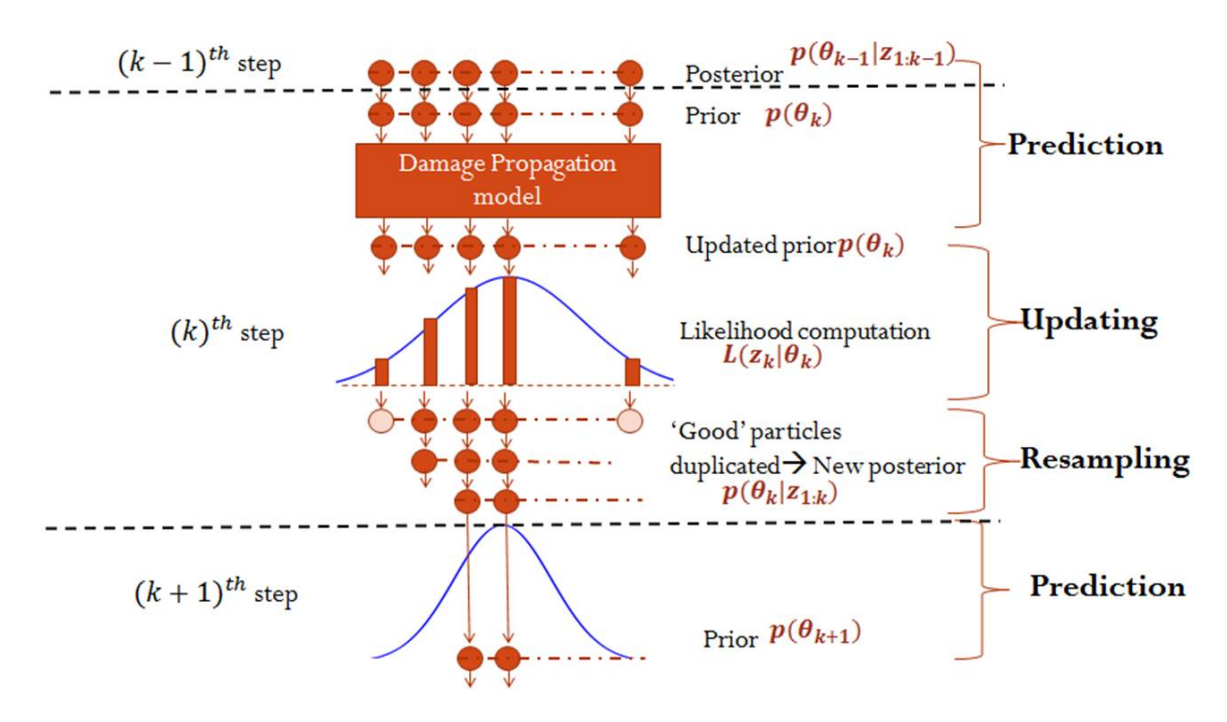


Figure 6.8: Illustration of Bayes estimation using particle filtering technique.

Next, a synthetic dataset is used as an example to demonstrate the PF algorithm for

estimation of damage growth path and remaining useful life (RUL).

6.5.1 PF estimate of model parameters using synthetic data

A simple exponential damage propagation model is defined where the crack grows exponentially with time (8.4). The true values of the parameters are selected as C = -22.62 and m = 3.8 and the true crack growth path is shown in Figure 6.10.

$$a = Ct^m (6.22)$$

For applying PF algorithm, both parameters C and m are considered unknown and represented by a set of n = 5000 particles. For the sake of simplicity, measurement noise is modelled as white Gaussian density with standard deviation (σ) of 0.01. A synthetic dataset of 25 points are chosen, also denoted in Figure 6.10, which form the measurements used in Bayes updating by particle filtering. The particle filtering approach can be described in the following steps.

(a) Initialization: At k = 1 step, n samples of all parameters are drawn from initial (prior) distribution. The prior distribution parameters are slected either based on domain knowledge or intelligent data processing from available measurements. Most often, experiments are conducted multiple times and the first inspection observations are used as the prior. In this example, the prior distributions for the unknown parameters are set as:

$$a_0 \sim \mathcal{N}(0.01, (5 \times 10^{-4})^2)$$

$$m_0 \sim \mathcal{N}(4, (0.02)^2),$$

$$\log C_0 \sim \mathcal{N}(-22.33, (1.12)^2)$$

In this example, the parameter C and m follow log-normal and normal distribution respectively.

(b) **Prediction**: Posterior distributions of the model parameters evaluated at the previous $(k-1)^{th}$ step are used as prior distributions at the current step (k^{th}) in the form of particles.

Also, damage state at the current time step is transmitted from the samples at the previous step according to the damage propagation model (8.4).

$$a_k = C_k (\Delta t_k)^{m_k} + a_{k-1} (6.23)$$

where Δt_k is the time gap between $(k-1)^{th}$ and k^{th} inspection step.

(c) Updating: In this step, the likelihood is calculated such that Bayes inference can be evaluated according to Equation 6.11. Given that measurement noise ω_k follows normal distribution, the likelihood can be computed as:

$$L(z_k|a_k^i, m_k^i, C_k^i) = \frac{1}{z_k \sqrt{2\pi} \xi_k^i} exp \left[-\frac{1}{2} \left(\frac{\ln z_k - \lambda_k^i}{\xi_k^i} \right)^2 \right], i = 1, ...n$$
 (6.24)

where,

$$\xi_k^i = \sqrt{\ln\left[1 + \left(\frac{\sigma}{a_k^i(m_k^i, C_k^i)}\right)^2\right]}$$
 (6.25)

and

$$\lambda_k^i = \ln\left[a_k^i(m_k^i, C_k^i)\right] - \frac{1}{2}(\xi_k^i)^2 \tag{6.26}$$

(d) Resampling: Resampling is the step in which an existing set of particles is replaced

by a new set. It is particularly essential in PF in order to avoid degeneracy of weights [104] in which a few particles dominate the rest, after the first few iterations. This often leads to inaccurate estimates with large variances.

Several resampling techniques are discussed in literature such as single distribution sampling [105] thresholds/grouping-based resampling [106] or variable size resampling [107]. In our application, a sequential importance resampling technique, specifically the inverse CDF method is applied to achieve the resampling process [102] whereby a particle of the parameter having the CDF value generated randomly is chosen and the process is repeated n times in order to obtain n resampled particles at the end of k^{th} iteration.

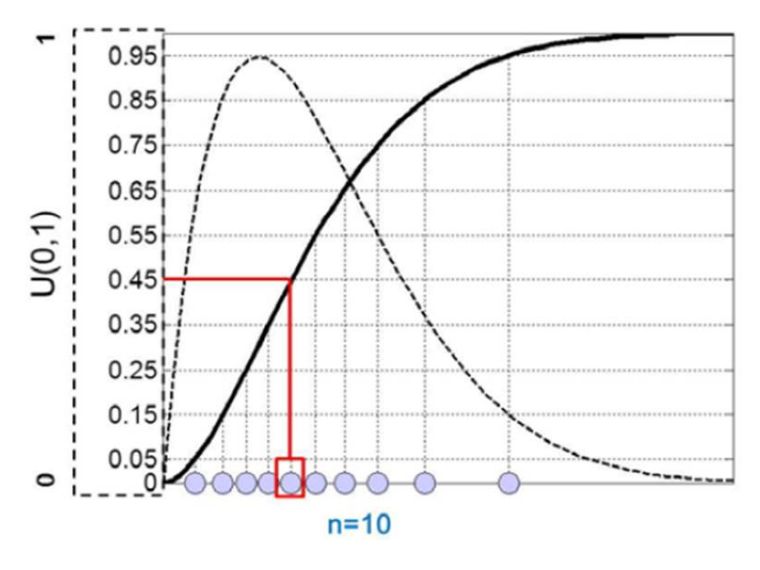


Figure 6.9: Illustration of resampling by inverse CDF method [8].

Figure 6.9 illustrates the above process. Here a random value is generated from U(0,1) which becomes a particular CDF value (e.g., 0.45 in the figure). Finally, a sample of the parameter having the CDF value is found, which is marked by a rectangle in the figure. By repeating this process n times, n samples are obtained. Note that since samples exist in a discrete form, the sample having the closest value to the CDF value

is selected.

The PDF constituted from these resampled particles forms the posterior distribution of the current iteration or the prior distribution of the next iteration.

(e) Prognosis: Once the model parameters are estimated, the damage state is propagated from the current state upto the threshold value. The PDF of the particles in current state is subtracted from those at the threshold value in order to evaluate the PDF of the RUL. The median RUL along with its confidence intervals are calculated from the PDF of the RUL.

Figure 6.10 demonstrates the results of applying particle filtering on the synthetic dataset. The true values of parameters were known a-priori and served as a reference to compare the accuracy of estimated values using the synthetic data. The estimated crack growth path with its confidence bounds matches closely to the true path as seen in Figure 6.10(a). Also, the estimated RUL histogram is plotted in Figure 6.10(b) using a failure thresold at crack length = 0.03 units. The median RUL at 1200 cycles is computed as 950 cycles with its 95% confidence bounds at 750 and 1200 cycles. This means that if the current inspection is done at 1200 cycles, after 950 cycles the crack length is predicted to reach its failure thresold of 0.03 mm. The results show close alignment of predicted RUL with its true value which is 1000 cycles.

It is important to note that in statistical prognosis, observed condition monitoring (CM) data from periodic NDE can be classified into direct and indirect CM [108, 109]. Data from direct CM describes the underlying damage state directly such as crack length or damage area extracted from NDE imaging techniques or stiffness data obtained from strain gauge. For direct CM, prediction of RUL is equivalent to prediction of the CM data to reach a

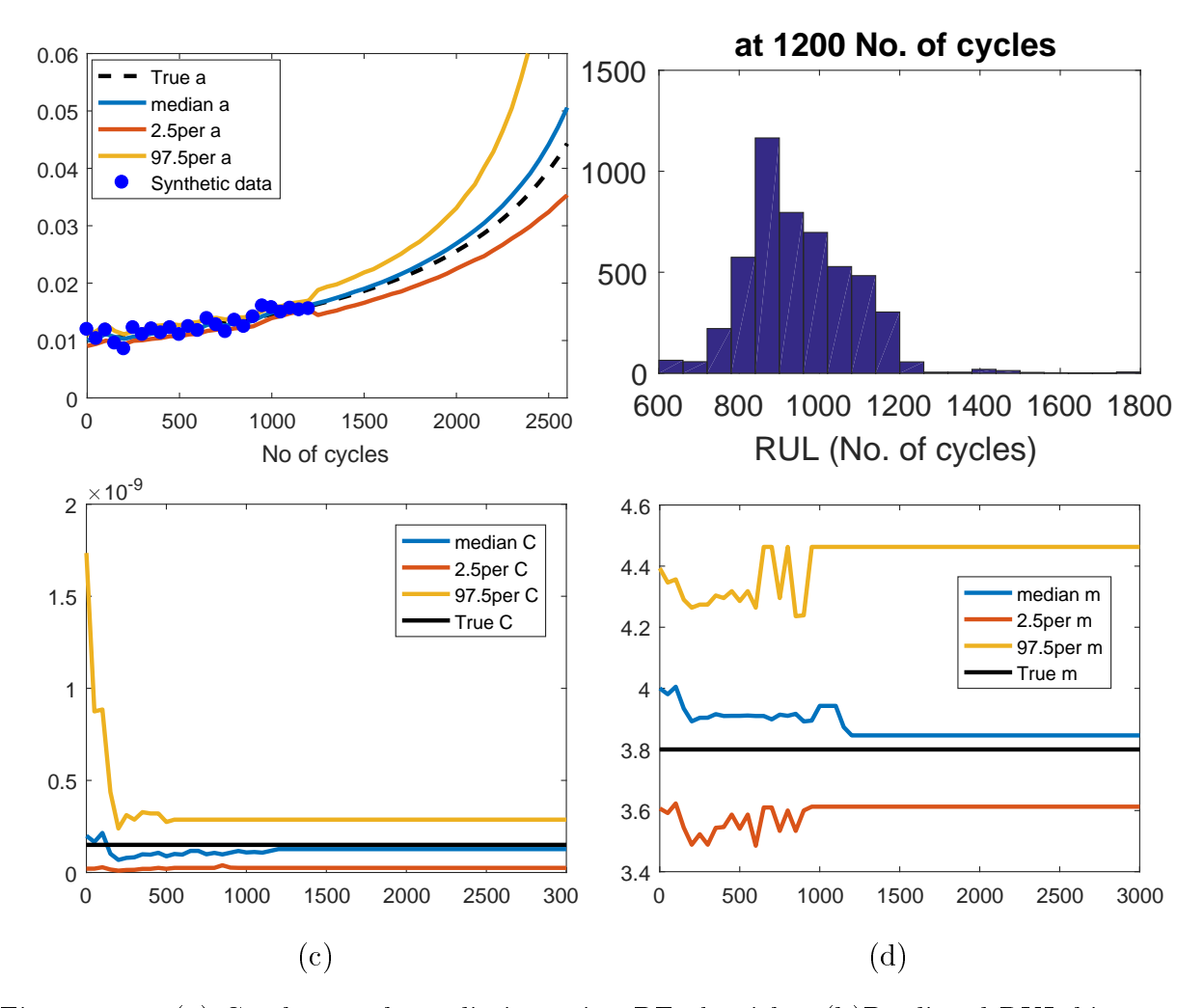


Figure 6.10: (a) Crack growth prediction using PF algorithm (b)Predicted RUL histogram (c) Trace of updating of parameter C (d) Trace of updating of parameter m

predefined failure threshold level. On the other hand, indirect CM provides data which can indirectly or partially indicate the health status of a structure. In these cases, failure event data may be needed in addition to CM data for RUL estimation. Examples of indirect CM are time-of-flight data obtained from ultrasonic waves, amplitude data from eddy current signals or features from other NDE techniques from which structural health can be deduced indirectly. Chapter 7 focuses on prognosis using direct CM whereas applications on indirect CM are discussed in chapters 8 and 9.

Chapter 7

Single Sensor Prognosis in Composites

by Direct Condition Monitoring

7.1 Introduction

In last few decades, composite materials have gained immense popularity and replaced metals or alloys in several industries namely aviation, automotive, space and construction owing to their salient properties of light-weightness, high specific stiffness and strength. Despite their high environmental and fatigue resistance, laminated fibre-reinforced polymers (FRP) are often vulnerable to flaws during fabrication and service such as fatigue cracks or disbonds in adhesive metal-composite joints. Hence there is a need for NDE experts to develop methodologies for inspecting composite materials. Also, industrial components made of composite materials are subjected to a wide range of stresses during their service life. Dynamic loading is common especially in aircraft components such as dropping of tools during maintenance or hailstorms while in service which pose serious threat to the remaining usability and reliability of such components. If a composite laminate is subjected to repeated low-velocity impact of sufficient energy, it may create damage internally in the form of delaminations which may remain invisible but can significantly compromise the structure's integrity. Hence, several analytical and experimental investigations [110, 111, 112, 113,

114] have been conducted on the initiation and evolution of impact damages in composite materials which demonstrated that the extent and rate of growth of such damage depend on the material, manufacturing process, hybridization, energy levels and geometry of the impactor. Vulnerability of composite materials propels the need for robust prognostics and health monitoring techniques. In this chapter we focus on prognosis of damage accumulation in GFRP samples due to repeated low velocity impacts.

Accurate health prognostics is critical for condition-based-maintenanace (CBM) and for reducing overall life-cycle costs. Under CBM, data is collected from various non-destructive evaluation (NDE) techniques such as vibration, acoustic emission, X-ray imaging etc. are utilized for structural health inspection and prediction of RUL. Several NDE techniques are discussed in literature for inspecting impact damage in composite laminates. Meola et al. [115] demonstrated the use of infrared thermography to image delaminations in the sample. X-ray computed tomography has been popular as well to inspect delaminations in GFRP [116, 117]. In this work, optical transmission scanning (OTS) was used to detect and locate damage introduced in a GFRP composite plate by successive low velocity impacts. OTS has been recently proposed by Khomenko et al. [118] as a novel optical method for quantitative NDE of GFRP structures. The technique can be used when access to both the top and bottom surfaces of the test sample are available. In addition to being non-contact, rapid, cost-efficient and safe, it provides high-resolution optical transmittance (OT) scans of a GFRP sample. Details of this method has been described in section 2.

This chapter presents two crucial contributions to research in prognosis of composite materials by direct CM utilizing experimental data from OTS of GFRP samples. Firstly, an optimized damage propagation model is described using improved Paris' law for delamination growth in the sample. Lack of robust models capable of describing the critical transition

from a healthy to a progressively damaged sample up to the complete collapse of the material makes estimation of failure thresholds more challenging for composite structures. Although crack propagation models in metals has been studied extensively, damage propagation in GFRP specifically the growth of delaminations introduced by low-velocity impacts have not been addressed yet. Secondly, an integrated prognosis method is implemented to estimate damage area growth in GFRP wherein data from OTS forms the CBM data to be used for estimation of the future damage area under the framework of particle-filtering. With growing demand of GFRP in industries, prognostic studies on such materials have become imperative and are addressed in this study.

7.2 Condition based Maintenance of GFRP

7.2.1 Impact Damage in GFRP

One of the most common degradation mechanisms encountered in composite samples is delamination formed by low velocity impacts. Impact damage in composites occur in the transverse direction where they lack through-thickness reinforcement and the transverse damage resistance is poor. As a result, the impact force tends to break the fibres in the polymer and eventually leads to formation of air gaps or delaminations inside the material which may or may not be visibly detected [119]. Delamination in a composite plate is caused due to interlaminar stresses which are dependent on specimen geometry and loading parameters such as dimensions of specimen, type of boundary conditions, shape of impactor, impact energy, etc. Interlaminar strength is strongly related to the material properties, i.e., fracture toughness of matrix and bonding strength between fiber and matrix. Effect of impact damage on residual compressive strength of GFRP laminates have been studied

previously by several researchers [113, 114].

Figure 7.1 shows a healthy sample of GFRP laminate and after being subjected to an impact of 20 J. As delamination area increases, the strength of the structure reduces which eventually leads to failure.

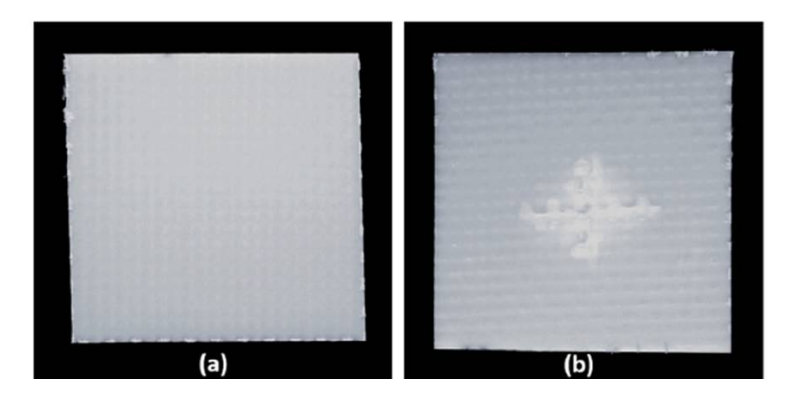


Figure 7.1: (a) Healthy GFRP sample (no damage),(b) Delaminated GFRP sample after E=20J impact.

7.2.2 Optical Transmission Scanning (OTS)

In this paper, experimental data from Optical Transmission Scanning (OTS) system [120] is used for assessing and predicting delamination growth in GFRP due to repeated impacts. Optical transmission scanning (OTS) has emerged as a viable technique for rapid and non-contact nondestructive evaluation (NDE) of glass fiber reinforced polymer (GFRP) composites [118]. Earlier works [121, 120] highlighted the capabilities of OTS in quantifying low velocity impact damage in multilayer GFRP samples, which, in combination with advanced image processing, allowed for accurate characterization of multiple delaminations and their contours. The results obtained demonstrated excellent agreement with well-established NDE techniques.

Figure 7.2 shows the image of the OTS setup. It comprises a translation stage, a laser

source that illuminates the GFRP samples, and a downstream photodetector placed underneath the sample. The photodetector records the power transmitted through the sample
after it is illuminated by the laser source. Consequently the output power depends on the
transmission properties of the sample being tested. Hence, presence of delamination (airgap)
inside the sample alters the transmitted radiation received by the photodetectors which is
captured by the OTS system. Images from inspection of a healthy and impacted sample by
the OTS is presented in Figure 7.3.

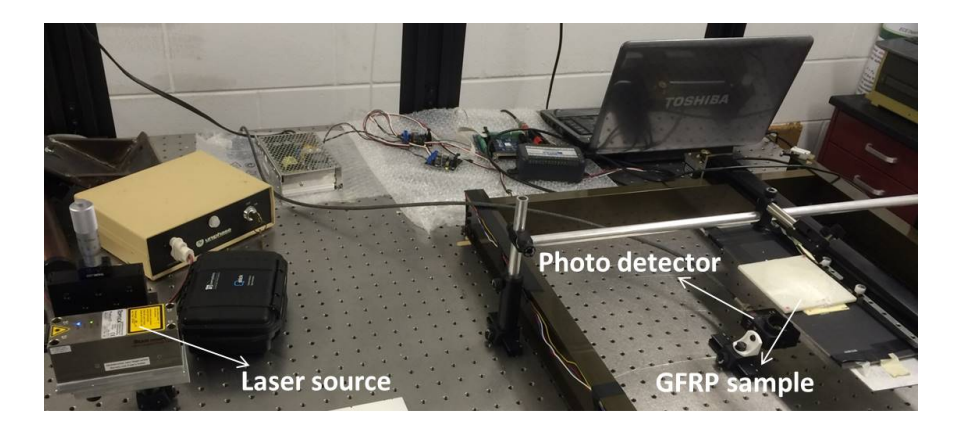


Figure 7.2: Experimental setup of optical transmission scanning system with impacted sample under test.

OTS has been demonstrated as a successful fast and non-contact technique to detect delaminations in GFRP and validated using a digital camera image of the cross-section of the GFRP sample[118]. The authors further applied advanced signal processing on the OT images in order to determine the delamination contours as a function of the number of fiber layers that have been affected by impact. As denoted in figure 7.3 (c), the OTS image of impacted GFRP is segmented into four sets of delaminations, ranging from 1 to 4+, quantifying the extent and severity of damage. A detailed description of the OTS operating principle, image processing procedure for determining the segments of delaminations in GFRP and computation of the area of each delmaination segment is illustrated in [118]. The

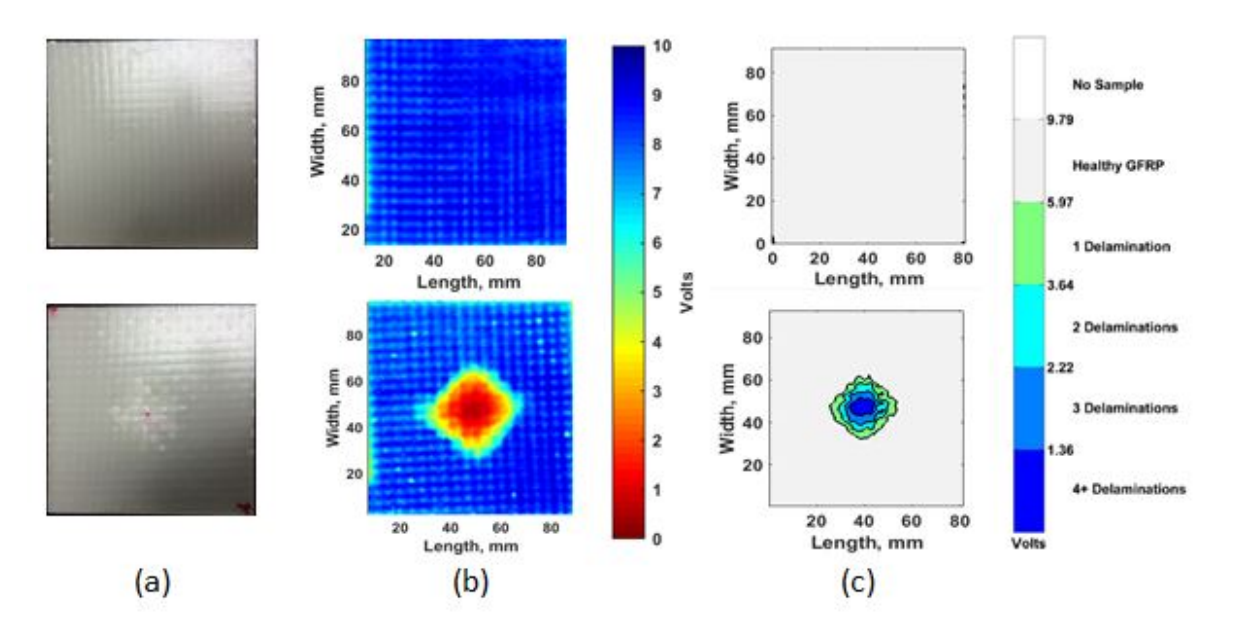


Figure 7.3: (a)(top)Healthy (no impact) GFRP sample; (bottom)GFRP sample after E=30J impact (b) OT Scan of (top)healthy; (bottom) impacted sample (c) Segmentation of delaminations in (top)healthy; (bottom) impacted sample.

results obtained demonstrated excellent agreement with other well-established NDE techniques. Ongoing work of the authors is focused on extending the capabilities of OTS to 3D imaging such that they can be tailored towards scanning the GFRP structure under loading conditions in industrial applications.

7.3 Proposed Prognostic framework for delamination growth model

7.3.1 Damage Propagation Model

In this application, damage propagation model used for describing propagation of delamination area inside a GFRP sample due to repeated low-velocity impacts is based on Paris Law which defines the relationship between crack growth rate and stress state of the structure, as given by equation 1.

$$\frac{da}{dN} = C \left(\Delta K\right)^m \tag{7.1}$$

where a is the crack length, $\frac{da}{dN}$ is the crack growth rate per cycle, N is the total number of load/ impact cycles, ΔK is the range of the stress intensity factor and C and m are the Paris law parameters. ΔK can be further interpreted as:

$$\Delta K = Y\sqrt{\pi a} \tag{7.2}$$

where, Y is a dimensionless constant depending on the crack shape and geometry of the specimen for a given stress range in fatigue crack growth models.

From material structures theory, it can be inferred that most of existing crack growth models are based on the empirical Paris' law [122] to define the relationship between crack growth rate and stress state of the structure. There are several prognostic studies in literature which adheres to Paris law to predict crack growth in metallic structures such as analysis of axial crack growth in UH-60 planetary carrier plate [83], aluminium alloy specimens [123] or fatigue cracks in SAE1045 steel [124]. However, unlike crack growth in metals, delamination in GFRP samples due to repeated impacts behave differently. In particular, the fibre/matrix interphase properties, which are affected by fibre surface treatment, play an important role in determining the failure mechanisms, the extent of damage and the threshold energy of the composite [125]. Many researchers have studied impact damages in composite materials [112, 119] and monitored the relationship between delamination area and impact energy. A typical damage propagation curve is presented in Figure 7.4. The damage area is found

to increase rapidly in the first few impacts and then slow down beyond a threshold. Such behaviour of delamination area growth has been studied before by Wu et al.[112] where he reported that the area extends at a slower rate after the first few impacts due to constraints from the four-fixed end boundaries in $(0^{\circ}, 90^{\circ})$ cross-ply laminates.

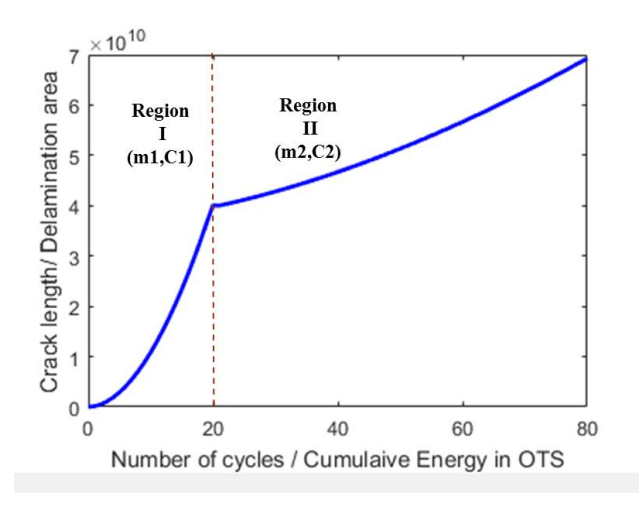


Figure 7.4: Delamination area propagation with respect to increase in cumulative impact energy.

Applying Paris Law directly was not suitable for modeling and predicting degradation processes in GFRP samples and hence a modified version referred as the Paris-Paris model based on Piecewise-deterministic Markov processes (PDMPS) is proposed. The mathematical details are described in [123] where the authors presented fatigue crack growth (FCG) prediction approach using "Paris model with one jump". In this paper, the damage propagation plot is divided into two regions- Region I and Region II. Instead of considering a single exponential model, two different exponential models are considered before and after the threshold or 'jump' in damage propagation curve. Paris law is used in both the regions but defined by different set of parameters. Overall, the five parameters in the Paris-Paris model to be estimated are : $\{m_1, C_1, m_2, C_2, E^*\}$ where m_1, C_1 and m_2, C_2 are the parameters of Paris model before and after the loading cycle E^* . It should be noted that the PDMPs

may use other crack propagation laws such as Paris-Forman law [126] or Paris-Erdogan law [122] for other applications and the number of 'jumps' may not be restricted to one. More 'jumps' will lead to more regions and more parameters to be estimated, without changing the underlying theory. In our study, the Paris-Paris model was used for modelling the growth of delamination area in GFRP samples with one 'jump' in the damage growth curve.

7.3.2 Particle Filtering based Prognosis of Delamination Area in GFRP

The particle filtering approach, described in chapter 6, has been implemented in this study for the prognosis of delamination area in a GFRP sample. The overall algorithm is modified to estimate unknown parameter vector $\boldsymbol{\theta}$ of the Paris-Paris model where $\boldsymbol{\theta} = \{m_1, C_1, m_2, C_2, E*\}$ (Note: T* is replaced by E* since we measure delamination area after fixed intervals of impact energy instead of time or loading cycle).

Damage area obtained from OTS measurement (z_k) at k_{th} observation is assumed to be equivalent to the true damage area (a_k) with additive noise, as described in equation 7.3, where $\omega_k \sim \mathcal{N}(0, \sigma^2)$.

$$z_k = a_k + \omega_k \tag{7.3}$$

The assumption of additive normal measurement noises is backed by experimental evidence. Measurement noise in the OTS system is essentially generated due to vibrations in the equipment gantry, noise in photodetector and external lights (eg: from computer screens in the optical laboratory). Noise from external lights contribute to majority of the experimental noise whereas the other factors can be neglected. In order to quantify the noise distribution, OTS system was used to scan a $40mm \times 50mm$ area without specimen in absence of

laser source. The output image captured by OTS photodetectors in depicted in Figure 7.5 (a). It can be further concluded that the measurement noise follows a normal distribution with mean at 0.2535 and standard deviation of 0.0091. Similar observations were found for repeated OTS scans without specimen.

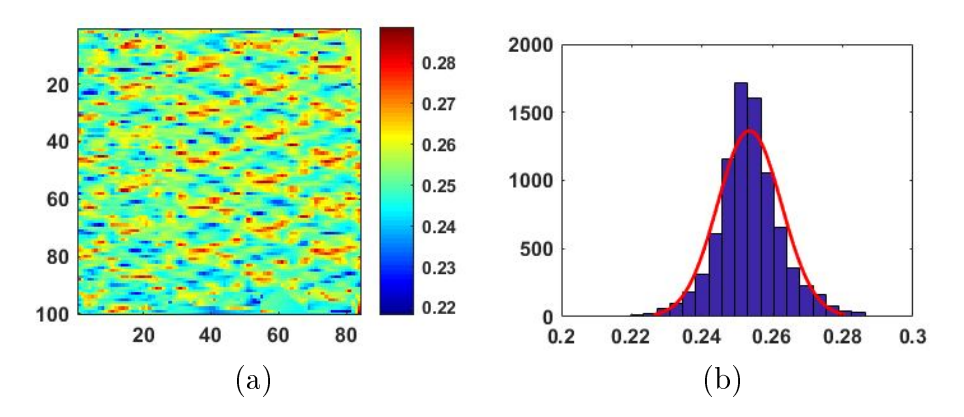


Figure 7.5: (a) Measurement noise collected by photodetector without specimen in absence of laser source (b) Measurement noise histogram : $\mathcal{N}(\mu = 0.2535, \sigma = 0.0091)$.

Therefore, the unknown parameters to be estimated are $\Theta = \{a, \theta, \sigma\}$, including the damage state a that depends on the model parameters θ . The particle filtering approach tailored towards this application is summarized in the following steps.

- (a) Initialization: At k = 1 step, n samples of all parameters are drawn from initial (prior) distribution.
- (b) **Prediction**: Posterior distributions of the model parameters evaluated at the previous $(k-1)^{th}$ step are used as prior distributions at the current step (k).

Using equation 7.1,damage state at the current time step is predicted from the parameters estimated at the previous step according to equation 7.4.

$$da = C \left(Y \sqrt{\pi a} \right)^m dN \tag{7.4}$$

The Paris model is re-written in the form of state-transition function in equation 7.5. It should be noted, loading cycle interval dN of Paris law for crack propagation in metals is replaced by ΔE or the interval of impact energy between two consecutive impacts on GFRP.

$$a_k - a_{k-1} = C \left(Y \sqrt{\pi a_{k-1}} \right)^m dN$$
 (7.5)

When the cumulative energy of the impacts is lower than the unknown 'jump' energy E^* , the damage update follows the Paris law with parameters $\{C_1, m_1\}$. Beyond E^* , the model shifts to Region II (in Fig.2) wherein the damage propagates according to Paris Law with parameters $\{C_2, m_2\}$.

$$a_{k} = \begin{cases} C_{1}^{k} \left(Y \sqrt{\pi a_{k-1}} \right)^{m_{1}^{k}} \Delta E + a_{k-1}, & \text{if } E_{k} \leq E^{*} \\ C_{2}^{k} \left(Y \sqrt{\pi a_{k-1}} \right)^{m_{2}^{k}} \Delta E + a_{k-1}, & \text{if } E_{k} \geq E^{*} \end{cases}$$

$$(7.6)$$

(c) Updating: In this step, the likelihood is calculated according to Bayes inference denoted in Equation 3. Assuming that measurement noise ω_k follows normal distribution, the likelihood is computed as:

$$L(z_k|a_k^i, m_k^i, C_k^i) = \frac{1}{z_k \sqrt{2\pi} \xi_k^i} exp\left[-\frac{1}{2} \left(\frac{\ln z_k - \lambda_k^i}{\xi_k^i} \right)^2 \right], i = 1, ...n$$
 (7.7)

where,

$$\xi_k^i = \sqrt{\ln\left[1 + \left(\frac{\sigma}{a_k^i(m_k^i, C_k^i)}\right)^2\right]}$$
 (7.8)

and

$$\lambda_k^i = \ln\left[a_k^i(m_k^i, C_k^i)\right] - \frac{1}{2}(\xi_k^i)^2 \tag{7.9}$$

The *n* particles for each parameter in Θ at k^{th} iteration are associated with weights that correspond to the PDF value of the i^{th} particle in measurement z_k as calculated by Equation 8. Paris law parameters $\{m,C\}$ are chosen differently before and after the cumulative impact energy E_k crosses the 'jump' energy E^* .

- (d) Resampling: Samples with higher likelihood are duplicated whereas the ones with lower likelihood are eliminated. This step captures the essence of optimization by particle filtering such that the 'good' particles are transmitted to the next iteration, thereby refining the estimation of model parameters.
- (e) Remaining-Useful-Life (RUL) computation: Once the model parameters are estimated, the damage state is propagated from the current state upto the threshold value or end-of-life EOL. After every measurement state, every particle which crosses the failure threshold are identified and its RUL is computed as $RUL_n = EOL n$, n being the current observation time instant. PDF of RUL is generated by computing the RUL of all the particles. The median and mean value of the RUL along with its confidence intervals are calculated from the RUL PDF.

7.4 Experimental Setup and Results

7.4.1 GFRP Specimen and Experimental Setup

Three eight-layered S2-glass reinforced laminates S1, S2 and S3 of dimensions $100 \times 100 \times 4.7mm$ were subjected to a sequence of low-velocity impacts by drop-weight tests with fixed mass of 17Kg with different energies (or different velocities) and scanned at every interval using the OTS technique. S1 and S2 were subjected to 15 impacts with energies stated in Table 7.1, whereas S3 was impacted with 14 impacts of different energies upto 89J, as denoted in Table 7.1. The velocity of the impact varied depending on the impact energy such that for a 10J impact, the velocity of drop-weight tests was recorded as 1 m/s, whereas for 50J and 100J, the measured velocity was around 2.41 m/s and 3.39 m/s respectively.

Impacts	1	2	3	4	5	6	7	8	9	10	11	12	13	14	15
Cumulative Energy (J)	2.5	5	10	12.5	15	17.5	20	30	40	50	60	70	80	90	100

Table 7.1: Cumulative energies of consequtive low velocity imapacts on GFRP sample 1 and 2.

Impact	1	2	3	4	5	6	7	8	9	10	11	12	13	14
Cumulative	1.5	3	4.5	6	7.5	11	15.5	21.5	29	38	48.5	60.5	74	89
energy (J)														ĺ

Table 7.2: Cumulative energies of consequtive low velocity imagacts on GFRP sample 3

The OTS setup used in this experiment consisted of an iBeam-smart-640s laser diode with 640nm fundamental wavelength used as the light source. It had 1.5mm beam diameter and up to 150mW output power. The transmitted radiation was registered using a DET36A Si detector with 350 - 1100nm wavelength range, 14ns rise time and $13 mm^2$ active area. The voltage on the output of the photodetector was directly proportional to registered radiation power. The XY-coordinate stage with stepper motors allowed for rapid inspection of the

GFRP samples with a lateral resolution of 0.25mm.

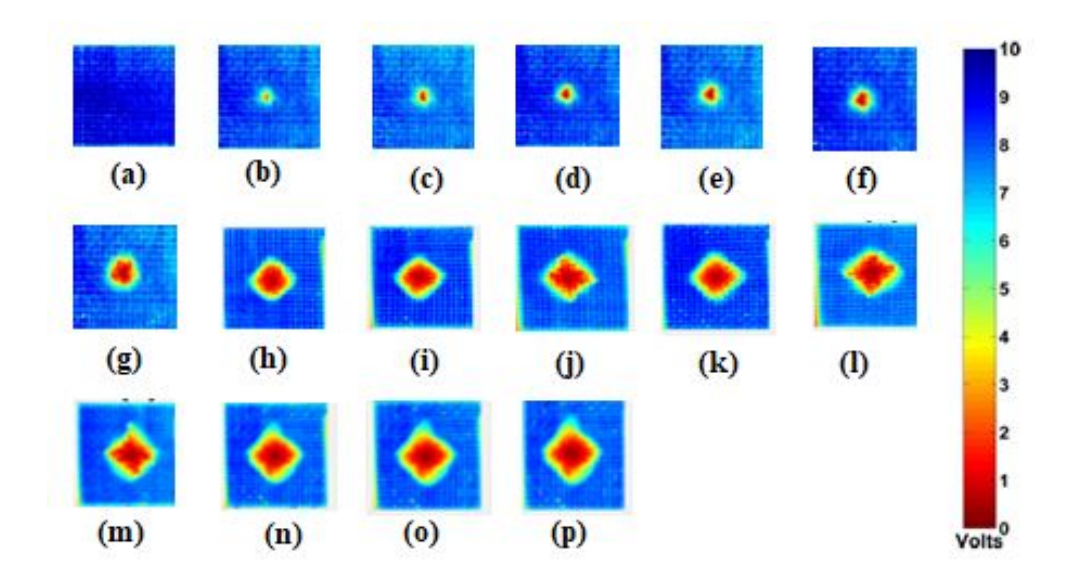
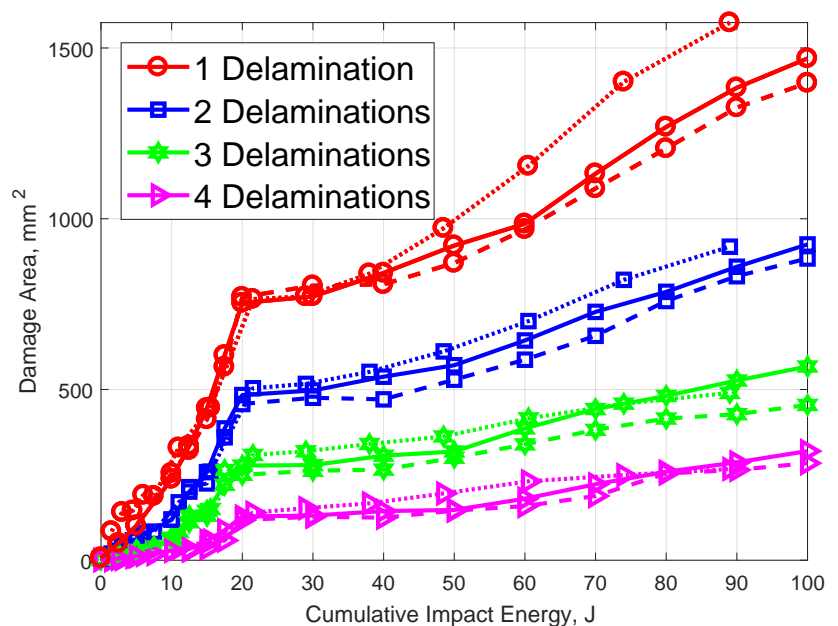


Figure 7.6: OTS scans of GFRP sample (a) healthy (b)-(p) after each consequtive impact from 1 to 15 as mentioned in Table 7.1.

At the end of each impact, the GFRP sample was inspected by OTS thereby producing 15 scans for S1 and S2 and 14 scans for S3. The OTS images for S1 after 15 repeated impacts are presented in Figure 7.6. Based on the image segmentation as shown in Figure 7.3 (c), delamination area for 1,2,3,4+ delminations were calculated from each OTS scan for the three samples. The damage area growth curve with respect to cumulative impact energies is plotted in Figure 7.7 which verifies the damage growth behaviour caused by repeated impacts in the three samples. These curves are considered as the ground truth for our application and estimation of damage growth parameters using our proposed method is validated against them. It is observed that the 'knee' of the health index curve or the 'jump' energy correspond to an approximate value of 20J for all three samples, even when the sample were impacted with different intervals of impact energy (or velocity) due to the same geometry of specimens and the location of impact.



Cumulative Impact Energy, J Figure 7.7: Growth of delamination area for three samples with increased cumulative impact energies (Solid curve- S1, Dashed curve- S2, Dotted curve- S3).

7.4.2 Prognosis Results

In order to implement particle filtering algorithm to predict damage growth curve from initial measurements, initial distribution for the parameters were set as:

$$a_0 \sim \mathcal{N}(20, (0.01)^2)$$

 $m_{10} \sim \mathcal{N}(4, (0.02)^2), \log C_{10} \sim \mathcal{N}(-22.33, (1.2)^2)$
 $m_{20} \sim \mathcal{N}(2.87, (0.1)^2), \log C_{20} \sim \mathcal{N}(-22.2, (0.1)^2)$
 $E_0^* \sim \mathcal{N}(20.02, (0.45)^2)$

The prior distibution of E^* where the Paris law parameters 'jump' from Region I to Reguion II is highly sensitive to the OTS measurements for individual GFRP specimens. Slope difference at every measurement cycle with respect to its last two predicted delamination areas was calculated according to equation (7.10) and $E_0^*(i) = E_{k-1}$ if $S_{diff}(k) = max(S_{diff})$. This process was repeated for damage growth curves in the three GFRP sam-

ples (i=1 to 3) and the mean and sample variance were used to define the prior PDF of E_0^* .

$$S_{diff}(k) = \frac{a_k - a_{k-1}}{E_k - E_{k-1}} - \frac{a_{k-1} - a_{k-2}}{E_{k-1} - E_{k-2}}$$

$$(7.10)$$

To verify the particle filtering prognostics approach, parameters of the Paris-Paris model were estimated with varying number of available measurements from 9 to 12 and the estimated curves are presented in Figure 7.8.

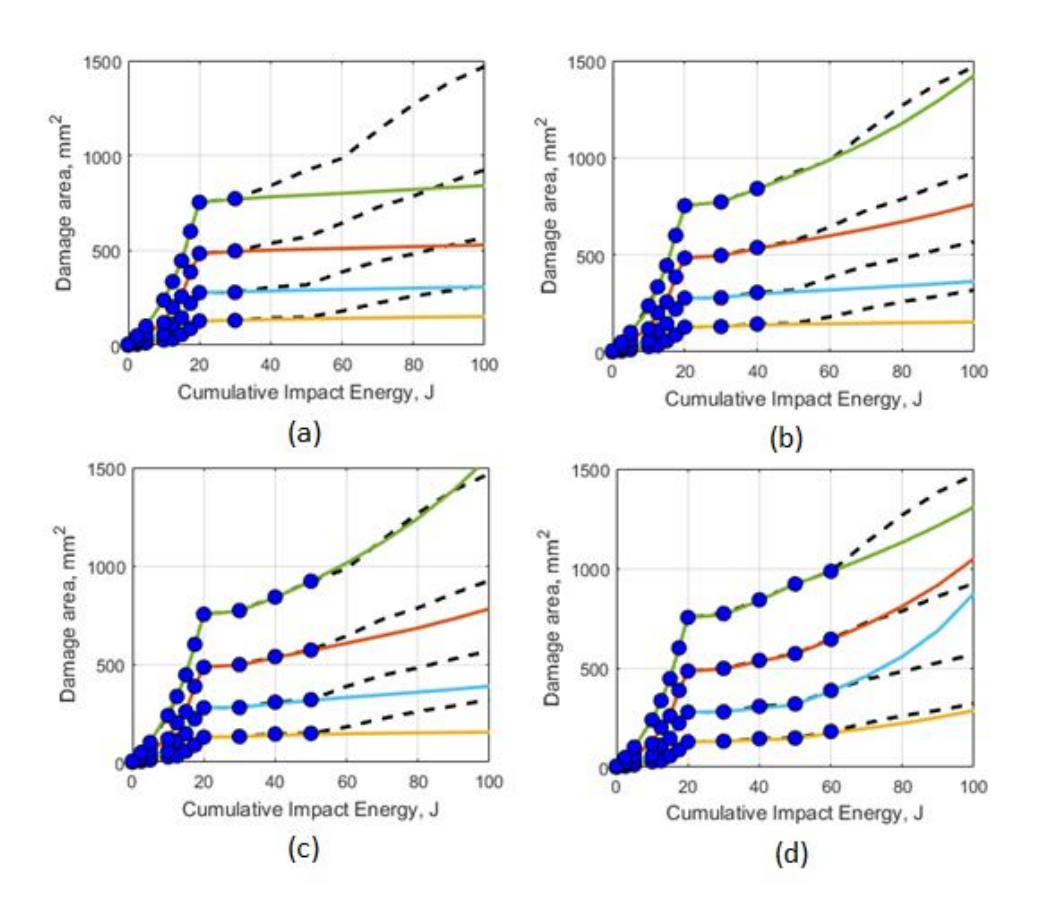


Figure 7.8: Prediction of delamination area curves based on different number of available measurements (a) n=9, (b) n=10, (c) n=11, (d) n=12. The true measured delamination area curve is plotted in dashed lines.

It is observed that the prediction became more accurate with number of observations Figure 7.8. The RMSE of estimated vaues compared to the OTS measurements was computed according to equation 7.11 and plotted in Figure 7.9 which shows a decreasing trend with increasing number of observations.

$$RMSE = \sqrt{\frac{1}{n} \sum_{i=1}^{n} (a_i - \hat{a_i})^2}$$
 (7.11)

To further demonstrate the benefit of an optimized Paris-Paris model over a regular Paris model, RMSE was computed for number of available measurements increasing from 10 to 13 and plotted in Figure 7.9. Although RMSE is less than 0.15 for both the models when more than 10 measurements were considered, prediction is more accurate with Paris-Paris model since it has lower RMSE in general than the regular Paris model.

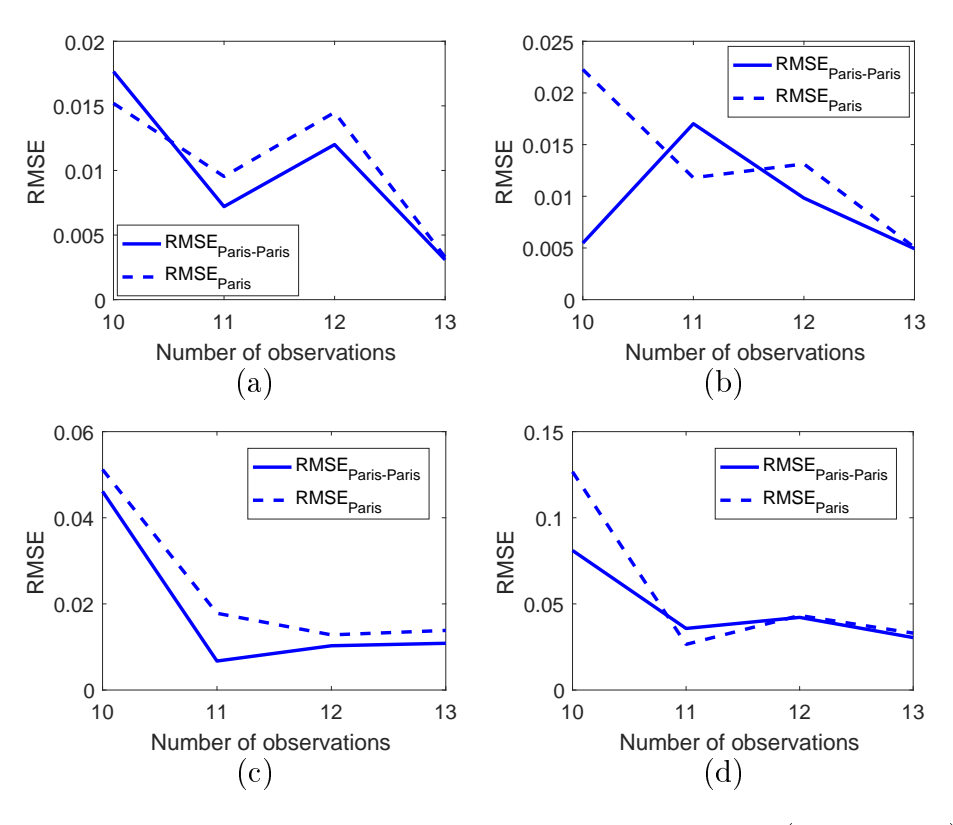


Figure 7.9: Comparison of damage area prognosis by Paris model (dashed line) and Paris-Paris model (solid line) for (a) 1 delamination (b) 2 delaminations (c) 3 delaminations (d) 4+ delaminations.

An interesting thing to note is that when number of available measurements of delamina-

tion area were more than 8 or when the cumulative impact energy was higher than the 'jump' energy ($E^* = 20J$), the predicted damage growth curves matched the true measured growth accurately, with maximum RMSE of 0.07. However when the number of measurements was either 8 or 7 i.e before the damage growth curve changed its growth rate, estimation becomes more challenging as the impending 'jump' energy needs to be predicted accurately even before it is reached. This is where an optimized Paris-Paris model outperforms a regular Paris model.

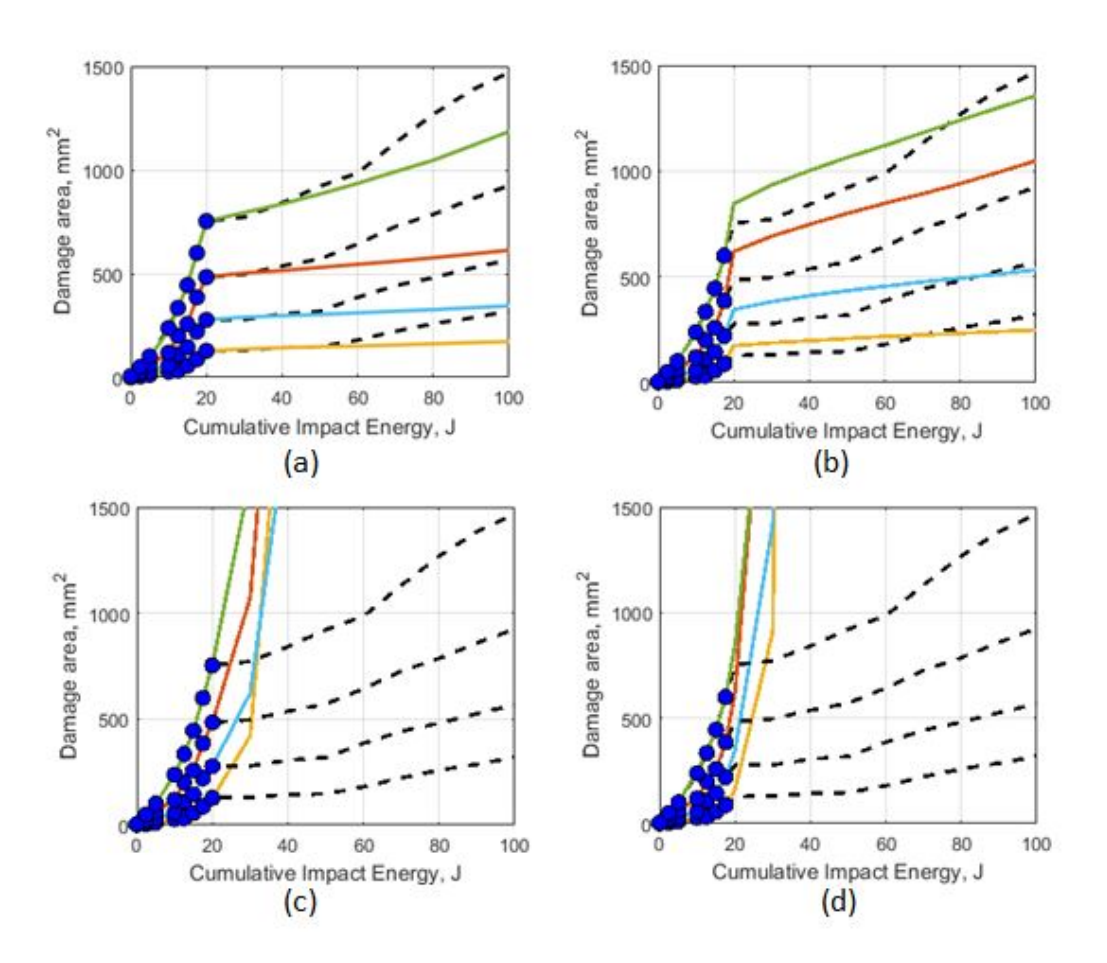


Figure 7.10: Prediction of delamination area curves based on different number of available measurements (a) n=8, Paris model (b) n=7, Paris model (c) n=8, Paris -Paris model (d) n=7, Paris -Paris model. The true measured delamination area curve is plotted in dashed lines.

Results are presented in Figure 7.10(a) and (b) for estimation of damage growth curve

wth 8 and 7 measurements using Paris-Paris model. The maximum RMSE is calculated to be 0.1. On the other hand, when same measurements were used to predict the damage growth curve using regular Paris model with one set of parameters $\{m_1, C_1\}$, the estimation failed, as shown in figure 7.10 (a) and (b). Clearly for these cases, the Paris model could not capture the 'jump' in the damage growth curve, therefore resulting in wrong prediction of its future values. If 6 or less measurements were chosen, both the models failed to accurately predict the 'jump' in the damage growth curve due to lack of sufficient information.

In order to compute the remaining-useful-life of the GFRP sample from the initial OTS measurements, sample S1 was subjected to more number of impacts with higher energy intervals, as stated in Table 7.3. At the end of 450 J, OTS image of the GFRP specimen in Figure 7.11 (g-h) shows that delamination had reached to one of its edges leading to breakage of fibres at that end, hence denoting its end-of-life (EOL) as further usage of the specimen could not be continued. The net delamination area after 450 J was calculated as $7803.8 \ mm^2$ or 78.03% of total area of the sample. Figure 7.12 presents the damage growth curve upto EOL for sample 1.

Impacts	16	17	18	19	20	21
Cumulative Energy (J)	150	200	250	300	350	450

Table 7.3: Cumulative energies of more number of impacts on GFRP sample S1 from 150J to 450J

A set of damage thresholds was set τ_d ; d=1,2,3,4 for every delaminations corresponding to the 21^{st} impact or total energy of 450J: $\tau_1=955$ sq mm, $\tau_2=1362$ sq mm, $\tau_3=2065$ sq mm, $\tau_4=3422$ sq mm. RUL was calculated on the Paris-Paris model for different number of observations ranging from 14 to 21 and the corresponding result is illustrated in

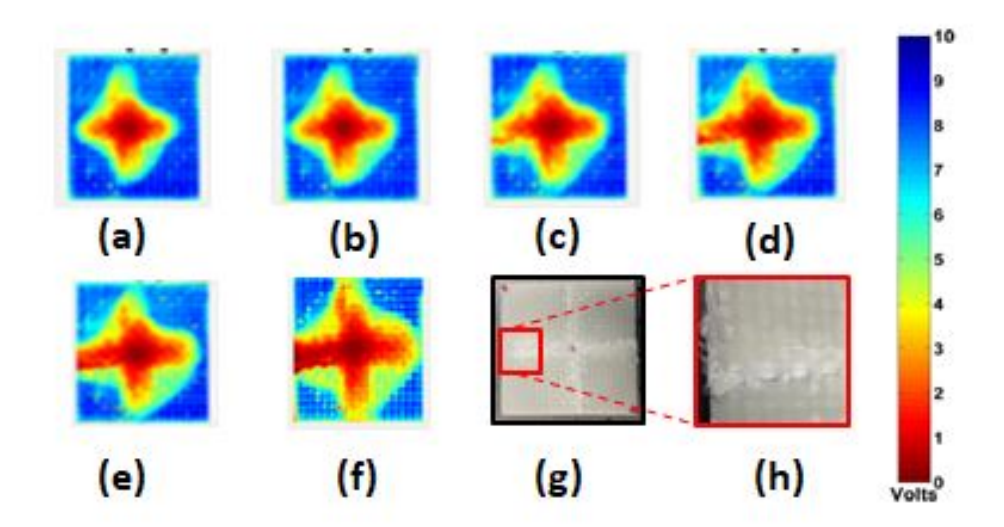


Figure 7.11: OTS scans of GFRP sample (a)-(f) after each consequtive impact from 16 to 21 as mentioned in Table 7.3,(g) Camera image of sample 1 after 450 J impact (H) Enlarged image of delamination reaching the edges and breakage of fibers denoting its end-of-life.

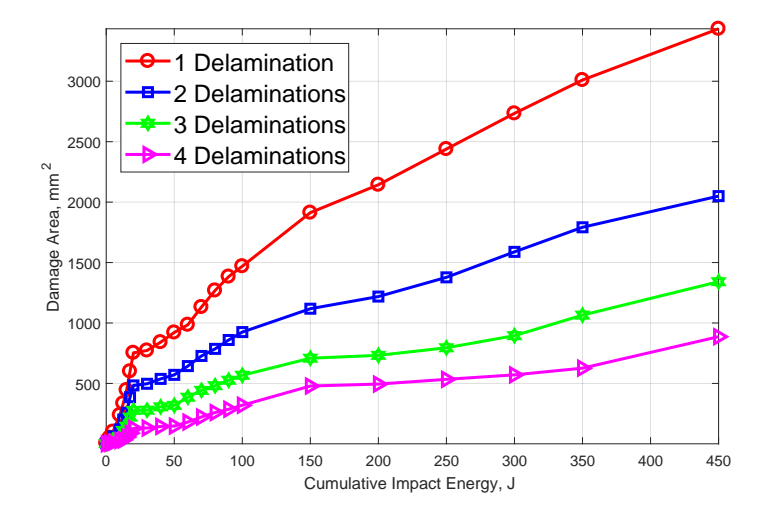


Figure 7.12: Growth of delamination area for sample 1 with increased cumulative impact energies upto end-of-life.

Figure 7.13. At 14^{th} observation, the cumulative impact energy was 90J, hence true RUL is 450J - 90J = 360J whereas at 21^{st} observation, the cumulative impact energy was 450J, hence true value of RUL is 0.

The mean and median of estimated RUL values along with their 90% confidence bounds is shown in Figure 7.13. The two shaded cones of accuracy at 20% and 30% of true RUL enable

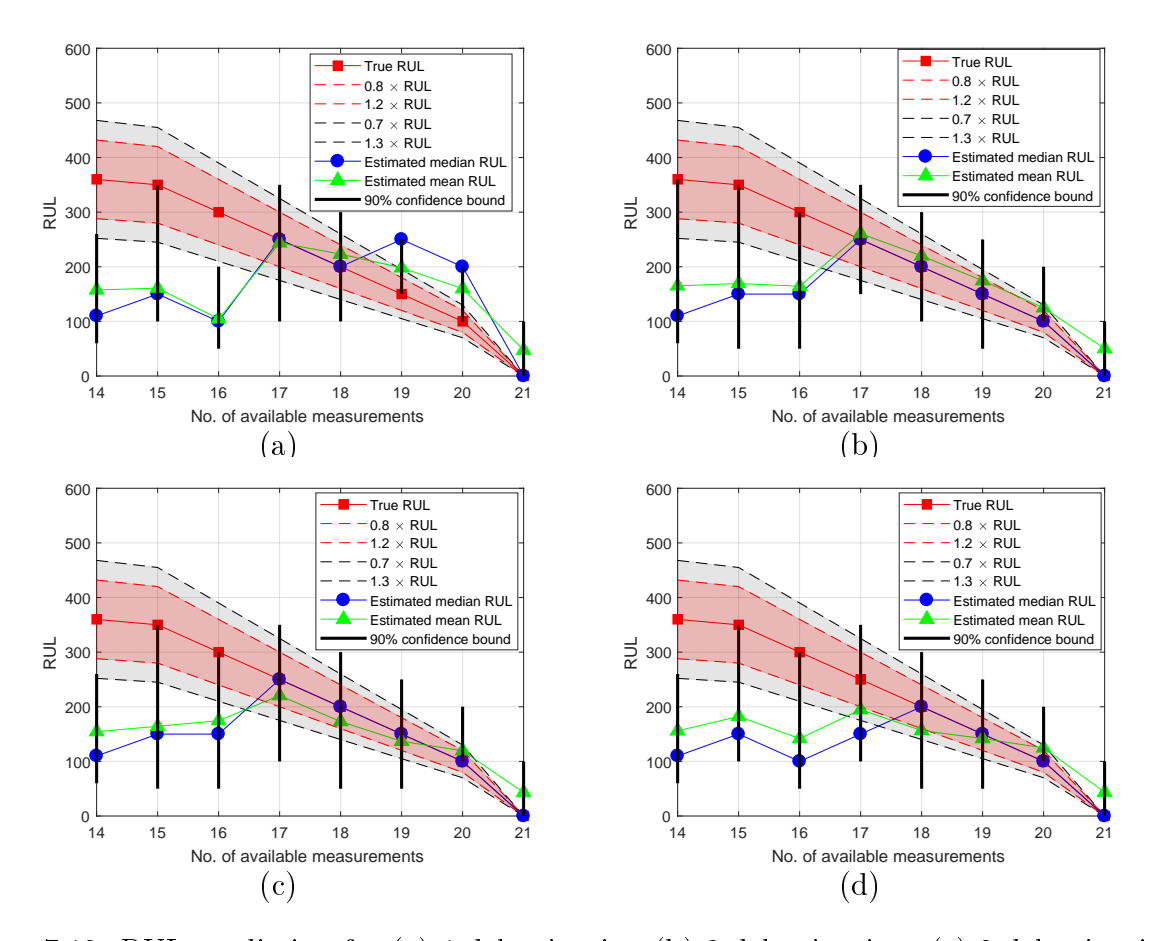


Figure 7.13: RUL prediction for (a) 1 delamination (b) 2 delaminations (c) 2 delaminations and (d) 4 delaminations.

comparison of prediction accuracy and precision. Prediction precision clearly improves with time as the 90 % confidence interval of estimated RUL decreases with addition of more measurements. The true RUL lies within the confidence intervals for most of the cases. In fact for delamination 2,3 and 4, the mean of estimated RUL exactly matches the true RUL when 18 or more measurements are used for prediction. However, it can be seen that RUL estimation error is high (50%) when 16 or fewer measurements are used (true value lies within 90% CI) which indicates that the model and its variance structure do not fully capture the damage dynamics at the earlier stages of delamination growth. In order to improve RUL prediction with lesser measurements, a more accurate damage growth model should be investigated.

Chapter 8

Single Sensor Prognosis in Composites

by Indirect Condition Monitoring

8.1 Introduction

Prediction of future damage state using NDE data from direct condition monitoring (CM) of a composite specimen is discussed in chapter 7. Accurate estimation of delamination area could be achieved with high-resolution optical transmission scanning (OTS) system, particularly suitable for transparent GFRPs. However, often industries demand in-situ monitoring of slow-growing defects in structures such as fatigue-induced delamination in composites. Airplane wings or automobile parts made of composites are frequently subjected to a wide spectrum of loading patterns during their service resulting in slow progression of cracks caused by fatigue. Fatigue-induced delamination in composite joints poses serious threat to their remaining usability [127, 128] propeling several analytical and experimental investigations on the initiation and evolution of fatigue cracks in composites [129, 130]. Fatigue behavior often results in formation of air-gaps in between the matrix layers known as delamination which may be hidden in internal layers and not visible on outer surfaces. Therefore, complex damage mechanisms in composites demand the use of NDE and SHM techniques not only to detect damages at the initial stages of fatigue but also to provide indirect CM

data for future health prognosis.

Although some NDE techniques such as pulse-echo ultrasonics [131], far-field microwave imaging [132] and sonic infrared imaging technique [133] are capable of diagnosing delamination in composites, accurate prognosis of fatigue damage in composites using NDE data remains a challenging task. Firstly in the case of most NDE techniques, no known physicsbased models are available for describing fatigue-damage progression in composite joints [134]. As discussed before, unlike metals, composites are heterogenous in nature where a slight change in the material or geometry can result into an entirely different and complex damage mechanism resulting in uncertain NDE inspection results. Crack or delamination growth behavior in composites strongly depend on the manufacturing process, mechanical properties of material(s), presence of impurities or inclusions in resin and other complex micro-level phenomenon which are difficult to be incorporated into known electromagnetic, acoustic or optical measurements, particularly for composites cured from multiple and newer materials. As a result in most practical applications, prognosis is solely dependent on indirect CM data from periodic NDE / SHM of the composite structures. Secondly, most of in-situ monitoring systems cannot provide accurate estimation of the slow-growing defect in adhesive joints especially in the early stages of fatigue. Prognosis based on noisy estimates collected under uncertain environment inherently leads to overfitting on the training data and wrong prediction of future damage states.

This chapter presents the prognostic capabilities of two methods using indirect CM data: regression based prediction[85] and stochastic filtering based on Bayes inference[81] in a sequential Monte Carlo framework, such as Kalman filter and particle filter. Delamination area is predicted for a GFRP specimen subjected to mode I fracture mechanism under cyclic loading. Indirect CM data is provided by guided wave(GW)[135] signals which are generated

through surface-mounted piezo electric transducers, therefore facilitating on-line monitoring of composite structures while they are in service. Delamination area computed from periodic OTS measurements are considered as the ground truth. Prediction results of both approaches are compared to demonstrate the benefit of dynamic parameter update in NDE prognosis applications.

8.2 Experimental Setup

8.2.1 Specimen Geometry and Material

GFRP composite samples, used in the mode I fatigue experiment, were manufactured using vacuum assisted liquid molding process. The reinforcement was S2-glass plain weave fabric with areal weight of $818g/m^2$, namely Shield-Strand S, provided by Owens Corning. The GFRP samples comprised six layers of such fabrics stacked at the same angle. The distribution medium was Resinflow 60 LDPE/HDPE blend fabric from Airtech Advanced Materials Group and the resin, SC - 15, was a two part toughened epoxy obtained from Applied Poleramic. GFRP plate of size $300 \times 150 mm^2$ was manufactured in a 914.4×10^{-2} $609.6mm^2$ aluminum mold with point injection and point venting. Two teflon sheets of dimensions $50 \times 150 mm^2$ with density $2.16q/cm^3$ and tensile strength of 3900psi were inserted in between third and fourth layer of GFRP fabrics at the two edges of the plate. After the materials were placed, the mold was sealed using a vacuum bag and sealant tape, and it was then infused under vacuum at 29 in Hg. The resin-infused panel was cured in a convection oven at $60^{\circ}C$ for two hours and post-cured at $94^{\circ}C$ for four hours. Finally, double-cantilever beam (DCB) samples with dimensions of L = 150mm, b = 25mm and h = 2mm were cut from the manufactured GFRP plate using a diamond saw and piano hinges were attached

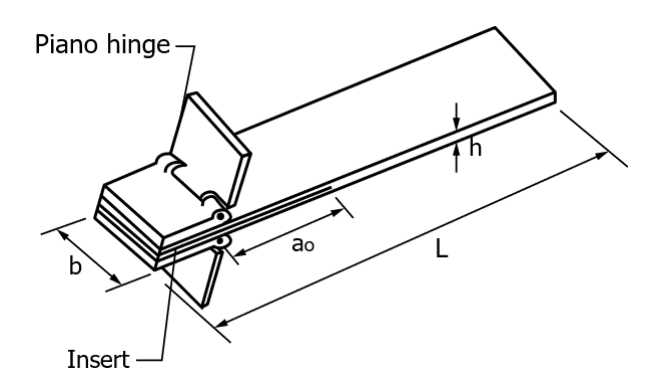


Figure 8.1: Double-cantilever beam (DCB) specimen for Mode I fatigue tests, according to ASTMD5528.

using high-strength cyanoacrylate glue. The design of the sample adheres to ASTMD5528 standard for mode 1 fatigue testing, as shown in figure 8.1. Figure 8.3(a) shows a DCB sample used in our experiments which is made of 6 layers with a teflon sheet of length 50mm inserted from the edge in between second and third layer of the plate. As the teflon inserts are ultra-thin, they have no mechanical contribution to the sample but are used solely to create initial delamination in the specimen. Each DCB specimen is characterized with Young's modulus of 26GPa, density $1907Kg/cm^3$ and the poison's ratio of 0.17 (material is assumed to be quasi-isotropic).

8.2.2 Fatigue testing of GFRP under Mode I failure

According to ASTM standard E 1823, fatigue in mechanical systems is defined as: "The process of progressive localized permanent structural changes occurring in a material subjected to conditions that produce fluctuating stresses at some point or points and that may culminate in cracks or complete fracture after a sufficient number of fluctuations". When a structure is subjected to cyclic loading, the applied stress is not constant but changes with time leading to fatigue failure. Striking characteristic of fatigue is that due to repeated

variable loading, localized stress concentration points are created at which crack is initiated and the system fails at stress values below the yield strength of the material. Hence, fatigue poses serious threat in the overall reliability of materials and requires accurate prognosis. Practical mechanical systems undergo variable loading in several scenarios such as;

- 1. Change in the magnitude of applied load Example: punching or shearing operations.
- 2. Change in direction of load application Example: a connecting rod.
- 3. Change in point of load application Example: a rotating shaft.

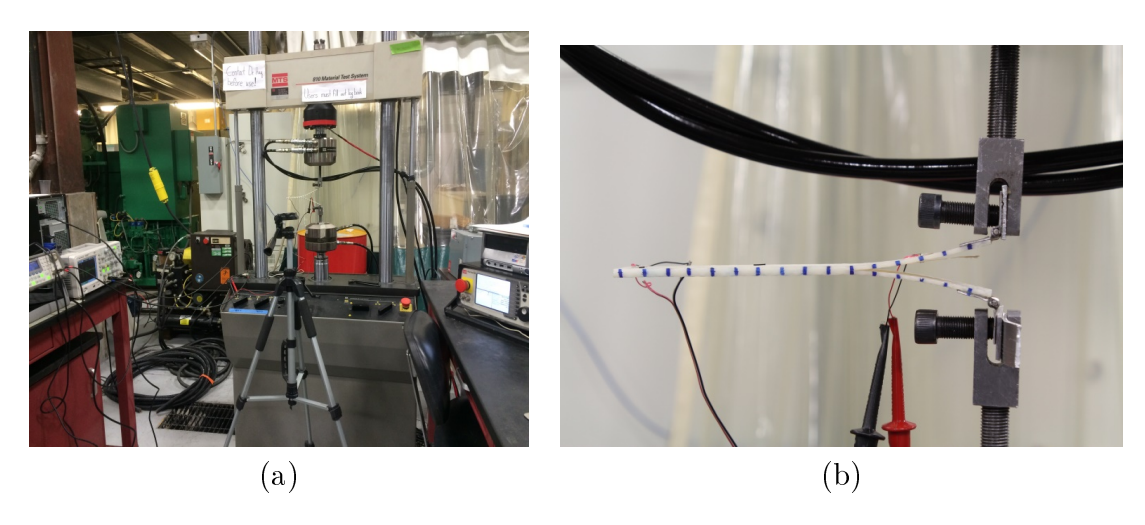


Figure 8.2: (a) Experimental setup for Mode I GFRP sample subjected to cyclic loading in MTS machine, (b) Enlarged image of GFRP sample under Mode I test.

Susceptibility to delamination is one of the major weaknesses of many advanced laminated composite structures. Although progressing at a lower rate, fatigue can induce local matrix cracking in composites leading to delaminations in adhesive joints or matrix laminates, which significantly compromises structure's health and can be catastrophic. Owing to its industrial importance, fatigue mechanisms have been studied extensively with regards to composite materials [136, 137, 138]. In this paper, effect of fatigue loading is studied on reliability of a DCB GFRP sample under Mode I cyclic loading. The GFRP specimen is subjected to

tension-tension fatigue testing in 810 Material Test System (MTS) machine with 50kN load cell. At first, critical displacement where the specimen cracks is recorded by introducing monotonic loading. The process is repeated on 5 similar specimens and the average critical displacement is computed. Fatigue loading is then conducted on a new sample under constant displacement at 5 Hz with displacement ratio of 0.1 and maximum stress equal to 70% of critical displacement. The experimental setup for DCB GFRP sample subjected to cyclic loading in MTS machine follows ASTM Standard D6115 and is illustrated in Figure 9.4.

8.3 NDE of Fatigue Damage in Composites

For reliability analysis, interrupted fatigue tests are performed on the DCB sample. Starting from its pristine condition, cyclic loading is paused after every 20,000 cycles and the specimen is inspected using two NDE methods. This process was continued up to 120,000 cycles. NDE measurements along with features indicating the structural damage growth is described in this section.

8.3.1 Delamination detection using OTS

A detailed description of the OTS operating principle for detection of impact damages in GFRP is discussed in chapter 7. Similar experimental setup is used for inspection of the DCB GFRP specimen subjected to Mode I failure under cyclic loading. A GFRP sample with delamination shown in Figure 8.3 (a) is inspected by OTS imaging system and the resulting image data is presented in Figure 8.3 (b). Light is obstructed by the teflon sheet inserted within the DCB specimen resulting in no power transmitted through that region. Detailed profile of delamination starting from the edge of teflon sheet is visble from the OT

scan, shown in Figure 8.3 (b).

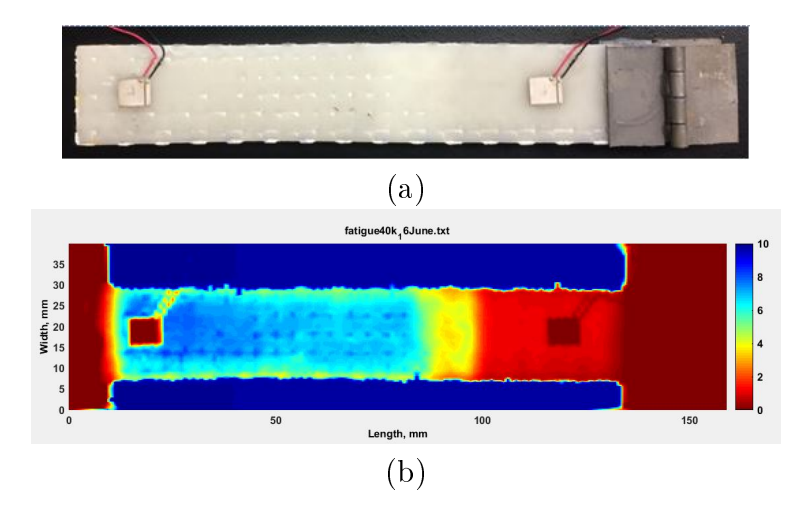


Figure 8.3: (a)GFRP sample under Mode I fatigue tests after 160K load cycles (b) OTS image of GFRP sample with delamination indications.

OTS images of the DCB GFRP sample obtained after every 20K cycles of fatigue loading up to 160K load cycles is presented in Figure 8.4. An iBeam-smart-640s laser diode with 640 nm fundamental wavelength, 1.5 mm beam diameter and 3.1 mW output power was used as the light source. The OTS system was placed on an active vibration isolation table and optical scans were acquired in dark ambience with a 1 mm step size.

From the OTS images, extent of delamination can be observed as the region between end of teflon and the beginning of healthy part of the sample. As expected, delamination grows inside the sample with increase in number of load cycles. Area of delamination from the scanned image is computed using image processing algorithm implemented in MATLAB, as depicted in Figure 8.5. The delaminated area is identified using segmentation via fast marching method [139] to generate the gray scale image shown in Figure 8.5 (b). The total number of pixels that are 'turned on' provides the area of delamination in terms of pixels (d_{pix}) .

The piezoelectric sensors attached to the GFRP sample mark as reference points and are

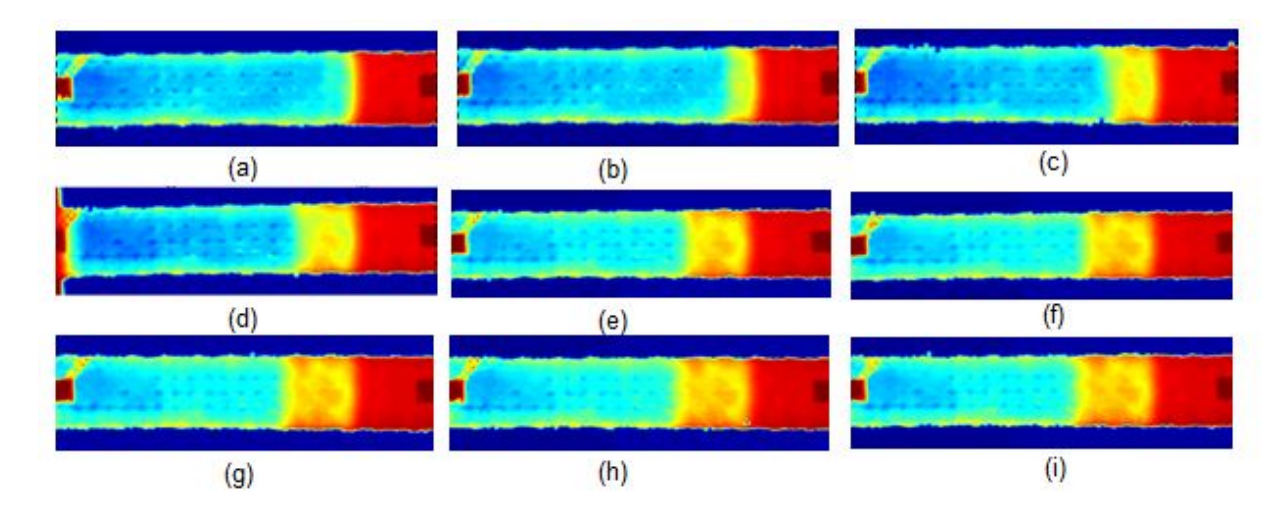


Figure 8.4: OTS images of a GFRP sample (a) Healthy sample and on being subjected to Mode 1 cyclic loading after (b) 20K cycles (c) 40K cycles (d) 60K cycles (e) 80K cycles (f) 100K cycles (g) 120K cycles (h) 140K cycles (i) 160 cycles.

used to calculate the physical area of delamination from d_{pix} . Specific use of the sensors are described in the following section. Using cluster-based-segmentation followed by connected components [19], location of the two pzt sensors are identified and the pixel distance between their inner edges is recorded as l_{pix} . Additionally, edge detection algorithm is implemented to determine the upper and lower edges of the sample and its pixel width is recorded as w_{pix} . Measuring the physical distance between two PZT sensors (L_{phy}) and width of the sample (W_{phy}) , the delamination area (D_{phy}) is calculated according to equation 8.1. In this paper, $L_{phy} = 10cm$ and $(W_{phy}) = 2.5cm$.

$$D_{phy} = \frac{(d_{pix})}{(l_{pix} \times w_{pix})} (L_{phy} \times W_{phy}) cm^2$$
(8.1)

Area of delamination is computed for each of the OTS images depicted in Figure 8.4, after every interval 20K load cycles. Plot of delamination area against number of load cycles is shown in Figure 8.6. The initial damage area computed from the healthy sample is deducted from all successive area measurements. Khomenko et al. [120] successfully demonstrated

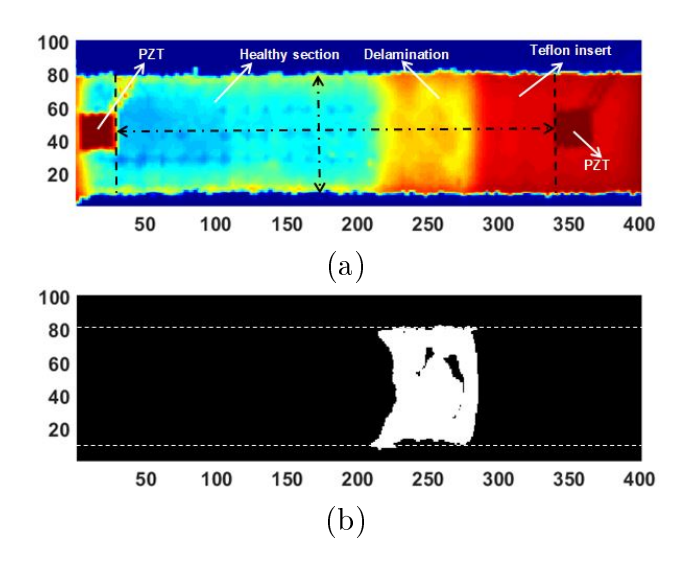


Figure 8.5: (a) Fatigued GFRP sample after 160K load cycles (b) OTS image of delaminated sample (c) Binary image denoting delamination area identified after image processing.

OTS as a valid technique to detect delamination in GFRP induced by repeated low-velocity impacts and validated scanned results by observing damage in a cross-section of the impacted samples after being cut by diamond-saw. Similar to crack length in fatigue-crack-growth (FCG) prediction, delamination area served as a suitable health indicator of the DCB GFRP sample subjected to Mode I fatigue testing.

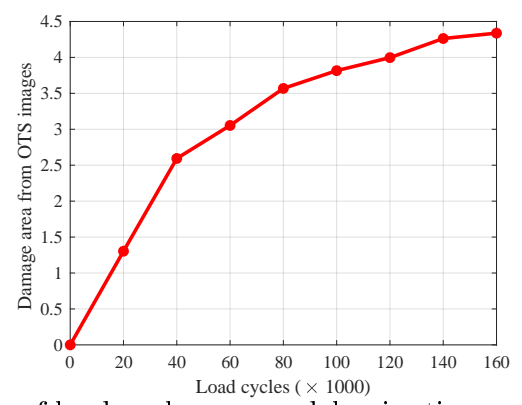


Figure 8.6: Plot of number of load cycles versus delamination area from OTS measurements.

8.3.2 Delamination detection using GW

One of the in-situ NDE/SHM techniques which has been used for real-time monitoring of aerospace and automobile components is guided wave (GW) sensing [140, 141]. Delamination detection using GW technique can be achieved using PZT sensors mounted on the surface of composite laminates which can transmit and receive guided wave signals in pitch-catch configuration [135]. The excitation frequency is identified by studying dispersion curves for selected materials such that complex wave modes are avoided and the anti-symmetric A_0 and symmetric S_0 modes are excited. PZTs with resonant frequency close to excitation frequency are mounted on both ends of the specimen (see Fig 8.3 (a)). Waveform generator excites the transducer and generates the guided wave, which propagates through the specimen and picked up by a second transducer. The received signals can be observed via an oscilloscope. Schematic of the experimental setup for GW inspection of GFRP specimen is depited in figure 8.7 (a).

According to GW theory [142], geometrical properties of the waveguide, especially specimen thickness, determine the mode content of the GW signal at the receiver PZT sensor. In Mode I fracture tests, growth of delamination results in change of thickness of the waveguide at the crack tip which modifies the dispersion curves or leads to mode conversion [143]. Earlier works [144] confirm that the group velocity of the GW signal is reduced as delamination grows and therefore, analyzing the time of flight (TOF) from the received GW signal, as depicted in Figure 8.7 (b), provides information about presence of internal air-gaps (or damage) in the composite laminate.

The same 6-layered GFRP sample is monitored using GW setup in addition to OTS, after every 20K fatigue cycles. As delamination area increases, time of flight between received and

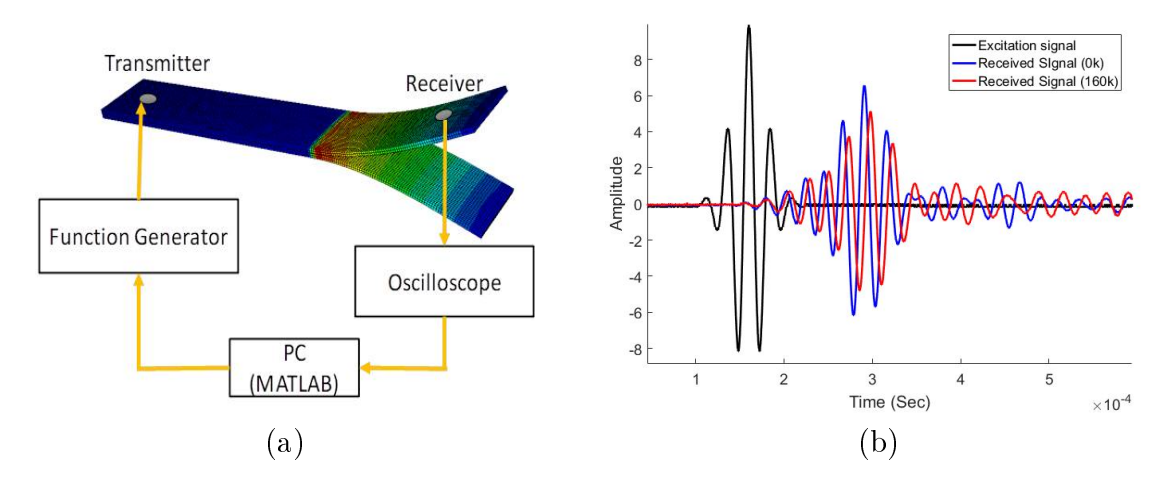


Figure 8.7: (a) Schematic of GW experimental setup (b)Excited and received signals in healthy sample.

transmitted signal increases. The incremental change in TOF of received GW signal is computed for 9 rounds of tension-tension loading of the sample. Figure 8.8(a) shows the phase shift in received GW signal as the sample progresses from healthy to delaminated layers after every 20K cycles. Figure 8.8(b) illustrates the ΔTOF from healthy to 160K fatigue cycles at an interval of 20K cycles. A steady growth in ΔTOF is noticed which can be correlated to the increase in delamination inside the specimen.

In order to quantify effect of delamination growth in the GW measurements, difference of TOF of received GW signals between the delaminated and healthy specimen is computed.

$$\Delta TOF_k = TOF_k - TOF_1 \forall k = 1, 2, ..., 9$$
 (8.2)

 ΔTOF of GW signals were compared with the delamination area extracted from OTS images of fatigue-induced samples. A positive correlation between the two parameters, as shown in Figure 8.9, demonstrates that monitoring TOF of received GW signals can be used to estimate the area of delamination in GFRP specimens. A 2nd degree polynomial curve,

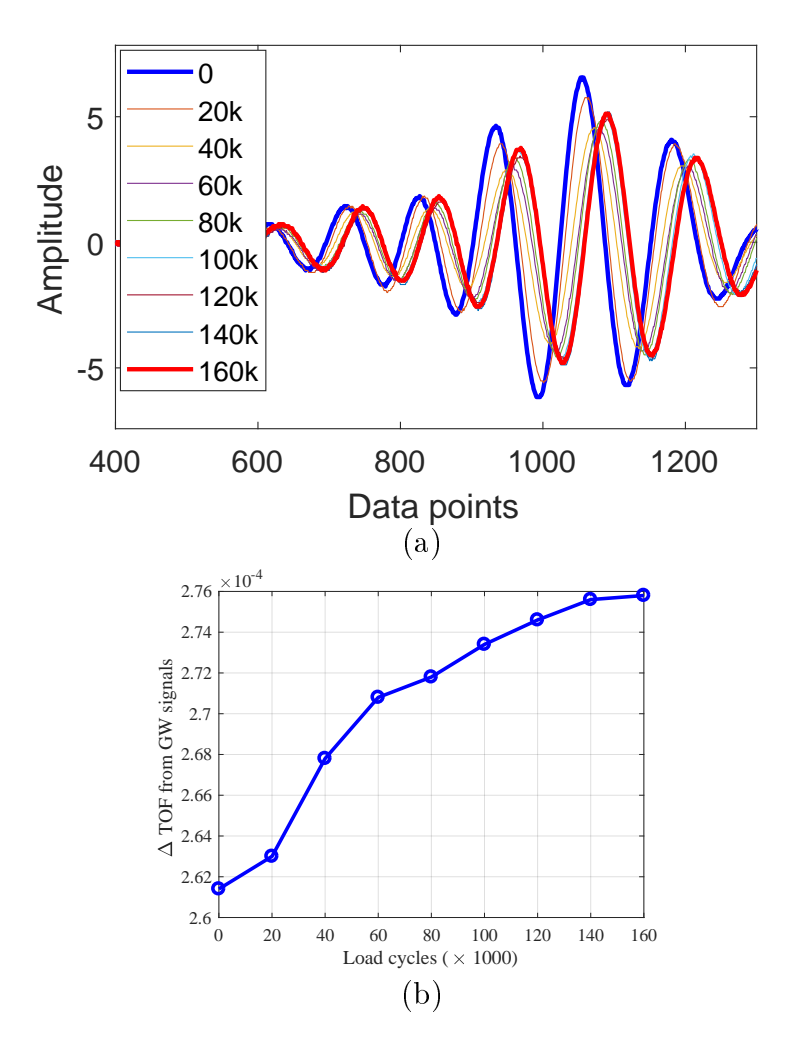


Figure 8.8: (a) Received signal for a healthy sample and sample after 20K-160K cycle (b) TOF between received and excited signal with increase in number of fatigue cycles.

according to equation 8.3, was estimated based on the measurements and then used to predict the delamination area from guided wave signals recorded at the receiver PZT sensor. From the experimental dataset, the coefficients were computed as $p_1 = -9.1005 \times 10^9$, $p_2 = 0.4 \times 10^6$ and $p_3 = 0.297$.

$$\hat{Area} = p_1(\Delta TOF)^2 + p_2(\Delta TOF) + p_3 \tag{8.3}$$

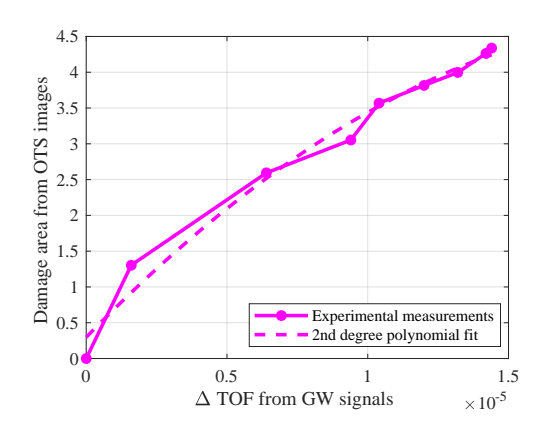


Figure 8.9: Correlation between TOF from guided wave signals and delamination area from OTS images.

8.3.3 Overall Framework of Damage Prognosis

In our application, damage area in the adhesive joint was derived from sensor measurements obtained at regular intervals of fatigue progression. Fatigue tests were intermediately
stopped on the training specimens to extract the guided wave (GW) data from attached PZT
sensors and imaged using OTS technique. Features determining degradation of structural
health were extracted from the GW signals and compared with the delamination area computed from OTS images. Finally, features from test specimen, extracted after intermediate
fatigue cycles, were implemented via regression and stochastic filtering approaches to predict
future feature values from which the future delamination area was computed. Predicted area
was then compared with OTS image data to assess the performance of the damage prognosis
algorithm. The entire approach is described in the flowchart of figure 8.10.

Measurements from OTS and GW sensors on a GFRP specimen subjected to interrupted fatigue loading is recorded in table 8.1.

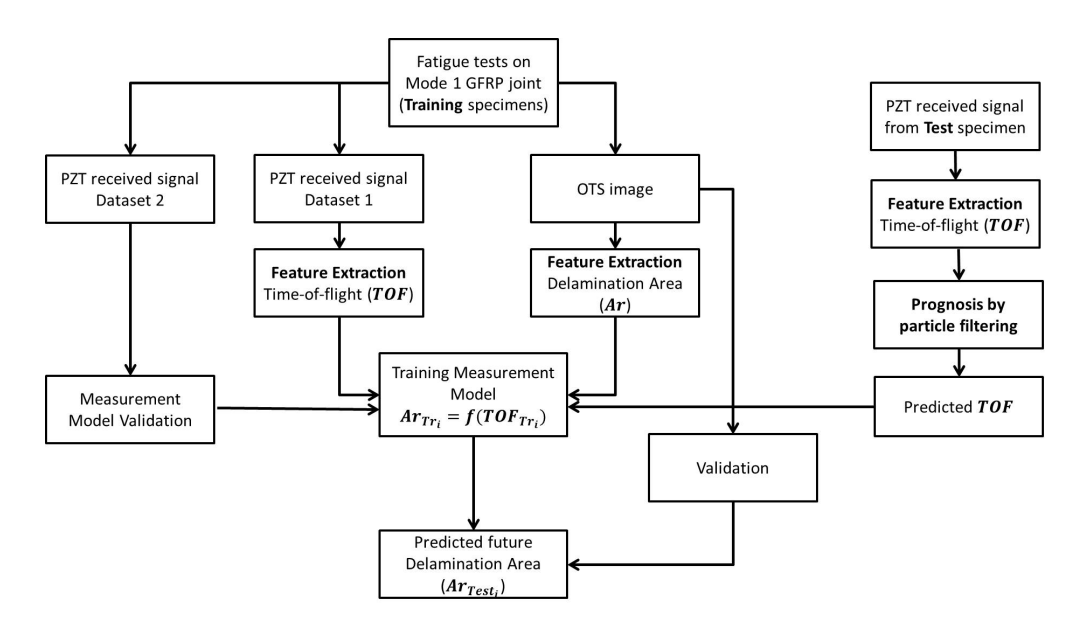


Figure 8.10: Damage prognosis flowchart using guided wave and optical transmission data.

Obs. (k)	1	2	3	4	5	6	7	8	9
Load cycles (T_k) × 1000	0	20	40	60	80	100	120	140	160
$TOF_k \times 10^{-4} (sec)$	2.61	2.63	2.67	2.70	2.71	2.73	2.74	2.75	2.76
$\begin{array}{c} \Delta TOF_k \times 10^{-5} \\ (TOF_k - TOF_1) \ (sec) \end{array}$	0	0.16	0.64	0.94	1.04	1.21	1.32	1.42	1.44
$Ar_k (sq.mm)$	0	1.31	2.59	3.05	3.56	3.81	3.99	4.26	4.33
Displacement control: Maxi Failure Strain.	Displacement ratio =0.1 Frequency= 5								

Table 8.1: OTS and GW measurements from Mode I fatigue testing of GFRP at intermediate load cycles.

8.4 Damage Prognosis Results

Prediction of future delamination area in a GFRP specimen based on initial GW measurements is performed using two dynamic data-driven prediction approaches, namely kalman filter and particle filter. The prediction accuracy for each of these methods are compared with regression based static estimation approach. Starting with the first 3 GW measurements $(T_{1:3} = 0, 20K, 40K \text{ cycles})$, ΔTOF is computed for the next measurement time-point which is at 60K load cyces. All measurements upto k^{th} observation are utilized to predict the

 ΔTOF for $(k+1)^{th}$ observation. Delamination area Ar_{k+1} is then computed from predicted ΔTOF using the correlation expression given by equation 8.3. This process is repeated upto 160K cycles.

8.4.1 Prediction of Delamination Area by Logarithmic Regression

Based on damage-propagation curve depicted in Figure 8.8(b), a simple logarithmic function, as described in equation 8.4, is implemented to model change in TOF measurements in DCB composite sample over time (number of loading cycles). Logarithmic regression is achieved by fitting a function of the form 8.4 on the measurements $TOF_{1:k}$ to estimate model parameter m and hence, TOF_{k+1} .

$$\Delta TOF = mlog(T) \tag{8.4}$$

Results of delamination area prediction under static approach using logarithmic regression is presented in Figure 8.11(a). Updated values of parameter m at every k^{th} observation time is plotted in figure 8.11(b).

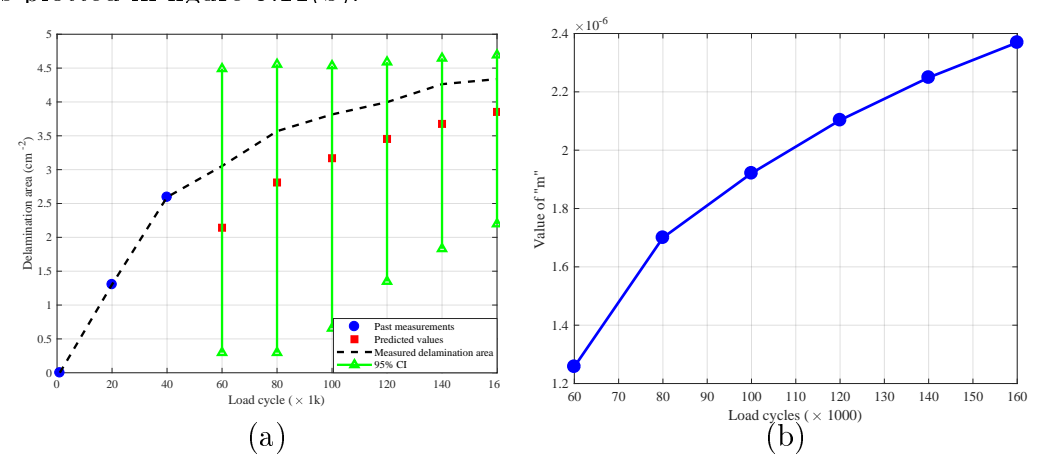


Figure 8.11: (a) Predicted delamination area from predcited GW measurements using correlation curve(b) Updation of logarithmic rate 'm'' at every estimation step.

It can be observed that estimates of future damage area from predicted ΔTOF values do not match the true damage area obtained from OTS measurements. Besides, the predicted values have high variances that translate to large confidence intervals which makes these results unacceptable. Primary reason for the high prediction error in regression based prognosis is the lack of large number of NDE measurements. Regression can achieve accurate estimation only when a large amount of data is available which is seldom the case in industrial applications. Hence, other prognosis techniques such as stochastic filtering is explored for prediction of damage area from fewer GW measurements.

It should be noted that in this thesis, logarithmic function is selected to model propagation of GW measurements with increasing fatigue cycles, due to lack of known physics-based-models that can define ΔTOF of GW signals in DCB woven composites under cyclic load. If underlying physics of guided wave propagation in GFRP plates can be modeled accurately, improved model-based-prediction of damage growth may be achieved.

8.4.2 Prediction of Delamination Area by Kalman filtering

As discussed in chapter 6, Bayes inference [145] is a widely used approach for parameter estimation $\hat{\theta}$. This approach derives the posterior distribution of parameters by updating an initial prior estimate multiplied with likelihood function obtained from measurements, according to equation 6.14. Particularly in fatigue damage prognosis, Bayesian inference has been implemented by Peng et al. [146] for probabilistic prognosis in fatigue test of lap joints, Enrico et al. [102] for fault prognosis in non-linear components and An et al. [81] for crack growth modeling under Mode I fracture tests.

Apart from particle filtering, approximate solution of Bayes inference can be achieved by another stochastic filtering approach known as Kalman filtering [147], specifically suitable

for linear systems with Gaussian noise. Since, the logarithmic model for ΔTOF adheres to a linear system, Kalman filter was explored for this prognosis application.

Christer et al. [148] applied Kalman filter for estimating refractory thickness in an inductor furnace from a series of measurements, containing measurement noise and model uncertainties. Kalman filter is a typical tool used for optimal estimation of unknown parameters in linear systems, with Gaussian measurement and process noise. In this paper, an empirical relationship is established between fatigue cycle and change in TOF of received GW signals from damaged GFRP specimens, as stated in equation (8.4). It is important to note that this empirical model is valid only for the given specimen geometry, material and Mode I loading conditions.

This logarithmic relationship is represented in a state space model, which is derived in equations (8.5) - (8.9),

$$x_{k+1} = \mathbf{A}x_k \tag{8.5}$$

$$y_{k+1} = \mathbf{C}x_{k+1} \tag{8.6}$$

where, x is the state vector, \mathbf{A} is the state-transition matrix and \mathbf{C} is the observation matrix.

$$x_k = \begin{bmatrix} \Delta T O F_k \\ m_k \end{bmatrix} \tag{8.7}$$

$$\mathbf{A} = \begin{bmatrix} 1 & log(\Delta T) \\ 0 & 1 \end{bmatrix} \tag{8.8}$$

$$\boldsymbol{C} = \begin{bmatrix} 1 \\ 0 \end{bmatrix} \tag{8.9}$$

The developed damage evolution state space model can be used in Kalman filter (KF) algorithm for prognosis. In general, KF algorithm follows two steps i.e. prediction and measurement update. In prediction step, the states x, error covariance $P_{-}(k|k-1)$ and output $y_{-}(k|k-1)$ for the k^{th} fatigue interval is predicted with the information available from $k-1^{th}$ fatigue interval as shown in equation (8.5). The prediction step of Kalman filter computes change in TOF x_k for next iteration from the experimental GW data z_k according to equations (8.11)-(8.13).

$$x_{(k|k-1)} = \mathbf{A}x_{(k-1)} \tag{8.10}$$

$$P_{(k|k-1)} = \mathbf{A}P_{(k-1)}\mathbf{A}^{T}$$
(8.11)

$$y_{(k|k-1)} = Cx_{(k|k-1)}$$
(8.12)

(8.13)

When a new measurement is obtained, estimated parameters (x_k) are updated according to equations (8.15)-(8.16) where K_k is the kalman gain, P_k is the error covariance and R = 0.025 is the measurement noise. The future damage area is hence predicted from estimated x_k which is updated once a new GW measurement is available.

$$K_k = P_{(k|k-1)} \mathbf{C}^T (\mathbf{C} P_{(k|k-1)} + R)^{-1}$$
(8.14)

$$x_k = x_{(k|k-1)} + K_k(z_k - Cx_{(k|k-1)})$$
(8.15)

$$P_k = (1 - K_k \mathbf{C}) P_{(k|k-1)} \tag{8.16}$$

Implementing Kalman filter on the same dataset generated prediction results depicted in Figure 8.12. The initial distribution of parameters are computed using the first two GW observations, as denoted in equation 8.18.

$$a = \Delta T O F_1 \tag{8.17}$$

$$m = \frac{(\Delta T O F_2 - \Delta T O F_1)}{\log(\Delta T)} \tag{8.18}$$

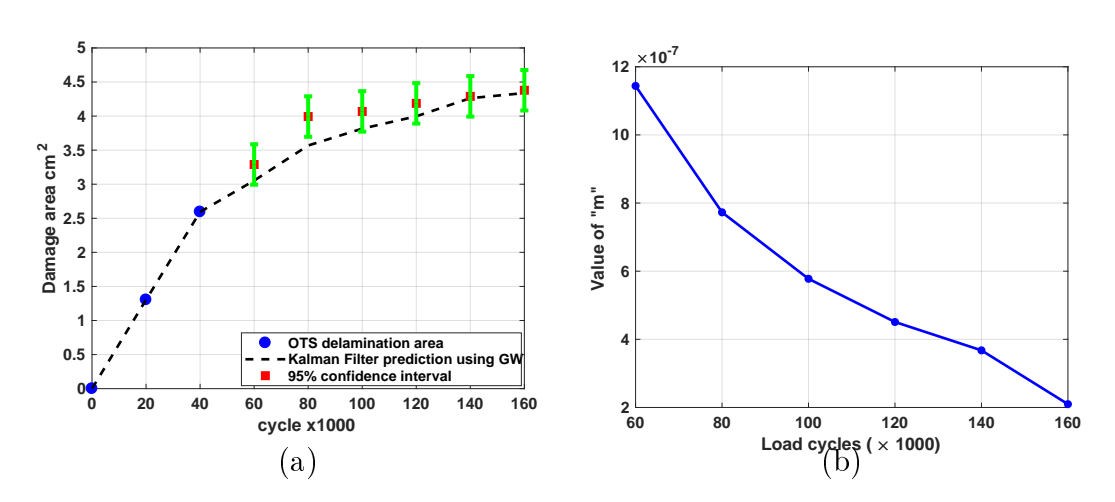


Figure 8.12: (a) Predicted delamination area from predcited GW measurements using correlation curve(b) Updation of logarithmic rate 'm'' at every estimation step.

8.4.3 Prediction of Delamination Area by Particle filtering

As explained in chapters 6 and 7, under particle filtering framework, Bayes inference is processed in sequential manner with particles associated with probability weights [103, 149]. Prediction of delamination area in composite laminates under Mode I fatigue testing is based on the damage propagation model given by the logarithmic function in equation (8.19) where ΔT_k is the time gap between $(k-1)^{th}$ and k^{th} inspection step.

$$a_k = m_k \log(\Delta T_k) + a_{k-1} \tag{8.19}$$

Unlike the case of Kalman filtering, in this case noise variance is treated as an unknown parameter which is estimated by the particle filtering algorithm. Assuming zero model noise, the conditional probability of the NDE measurements can be deduced as,

$$L(z_k|a_k^i) = \frac{1}{z_k\sqrt{2\pi}\sigma_k^i}exp\left[-\frac{1}{2}\left(\frac{z_k - a_k^i}{\sigma_k^i}\right)^2\right]$$
(8.20)

Starting with uniform initial distributions for all the parameters in equation 8.21 and n = 5000 particles, the estimated damage area curve along with updating path of 'm' are denoted in Figure 8.13.

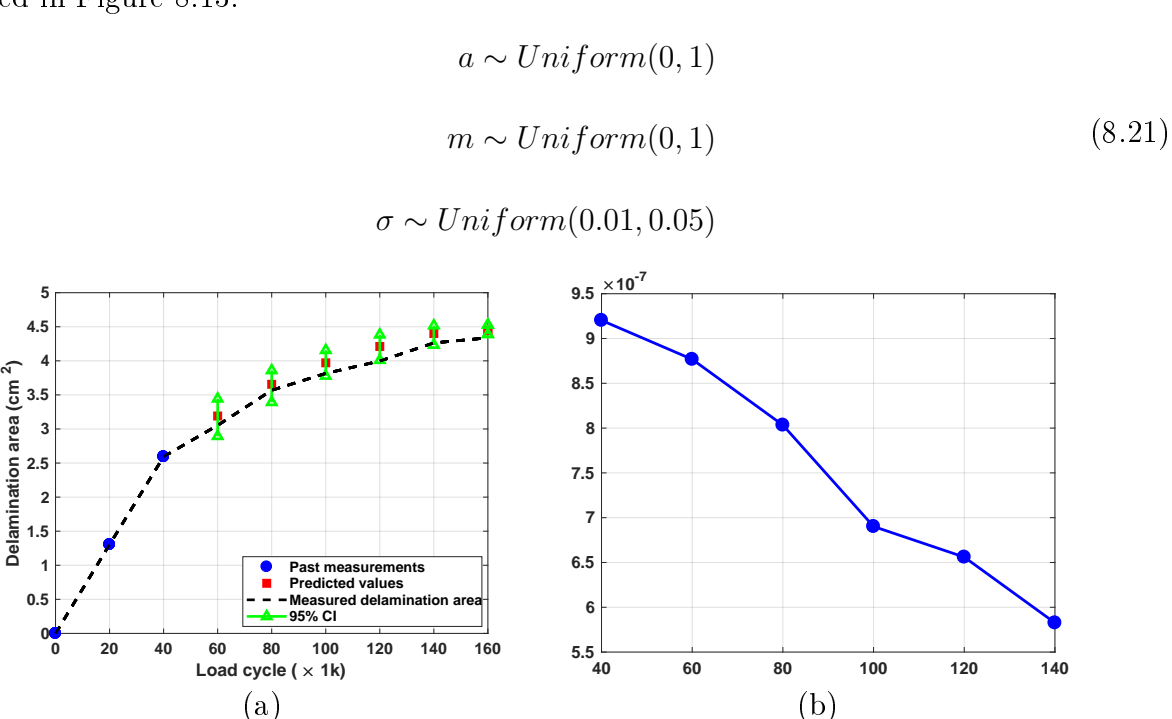
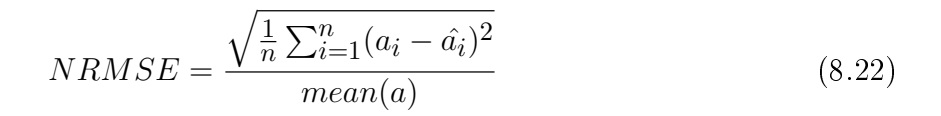


Figure 8.13: (a) Predicted delamination area from predcited GW measurements using correlation curve (b) Updation of logarithmic rate 'm'' at every estimation step.

In order to compare prediction performance of the three methods, the normalized root mean squared error (RMSE) is computed according to equation 8.22, for variable number of observations and plotted in Figure 8.14. The prediction error is lower in the dynamic data-driven approaches by approximately 10 - 15%, especially at the earlier stages of damage

progression when fewer measurements are considered. Therefore, it can be concluded that both the dynamic data-driven techniques via Kalman and particle filtering outperforms the static regression based approach owing to capability of sequential update of function parameters by incorporating uncertainties of non-linear model and measurement noise. Moreover, resampling based on likelihood computation within particle filtering technique drives the estimation towards the optimum parameter value even when fewer measurements are available. Hence the prediction error is lower than Kalman filtering at the earlier stages of damage area growth. With additional measurements after 120K load cycles, prediction results from both the filters become comparable.



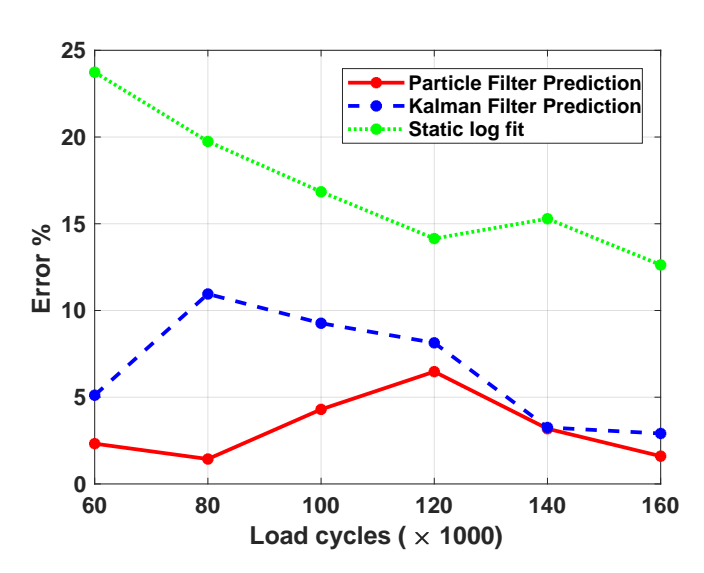


Figure 8.14: Error comparison of prognosis methods for prediction of delamination area from guided wave measurements.

Chapter 9

Multi-sensor Prognosis in Composites

9.1 Introduction

One of the recent extensions of NDE is the use of more than one sensing technique for inspection of structures. Traditional NDE prognostics focuses on analyzing a single sensor signal when a unit runs under a single operational condition [150, 151]. In most practical situations, a stochastic model is first developed at the training stage based on historical results. Inspection data from a test unit is then applied onto the model to predict its future health state. These approaches are effective under the assumption that single sensor data is able to capture the entire stochastic nature of the degradation process. Unfortunately, as system becomes more complex, several uncertainty factors come into play during damage propagation wherein measurements from one sensor may suffer from noise, outliers or biases [152, 153]. In such cases, relying on single sensor data becomes insufficient to accurately predict the growth of underlying degradation mechanism, leading to inaccurate and unreliable remaining-useful-life (RUL) prediction.

Assessing fatigue behaviour of any structure is an important aspect of its reliability analysis. Fatigue in mechanical systems occurs when a structure is subjected to continuous cyclic loading resulting in progressive, localized and permanent structural changes. Repeated variable loading creates localized stress concentration points in a specimen at which crack

is initiated and the system fails at stress values below the yield strength of the material. Hence, fatigue poses serious threat in the overall reliability of materials and demands accurate prognosis, especially at its initial stages. Although progressing at a lower rate, fatigue induces local matrix cracking in composites leading to global damages, which significantly compromises structure's overall health. Owing to its industrial importance, fatigue mechanisms have been studied extensively with regards to composite materials. In [154, 138], Bayesian model is discussed for parameter estimation of fatigue damage propagation based on modified Paris law. Owen [155] presented an exponential cumulative damage model for estimation of strength of carbon fiber polymers. Kruger et al. [156] studied an energy based approach for fatigue damage model in FRP under plane loading.

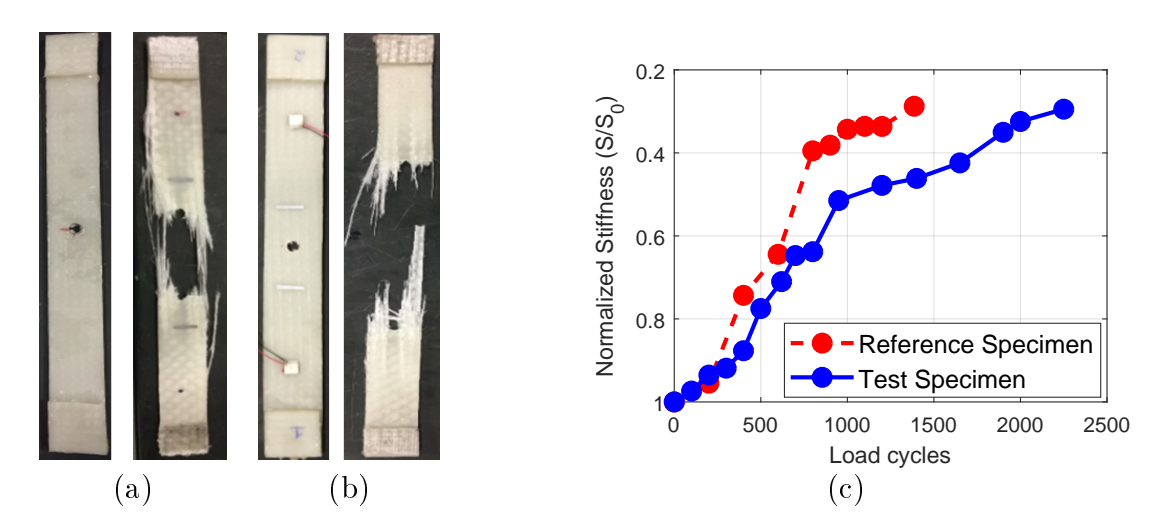


Figure 9.1: (a) Reference GFRP specimen failing after 1386 cycles while subjected tension-tension fatigue test under constant load (Max load= 70% of failure load, Stress ratio=0.1,Frequency =3Hz), (b) Test GFRP specimen (identical manufacturing conditions) failing after 2250 cycles subjected to identical fatigue testing conditions (c) Normalized stiffness degradation of reference and test specimen from MTS measurements.

Reliability assessment of fatigue behavior is more challenging in composite materials, compared to metals, owing to poorly understood nature of damage propagation. Unlike metals, cyclic loading in composites results in simultaenous formation of complex damages

consisting of matrix cracking, fiber breakage and delamination, which do not follow known crack propagation models such as Paris-Forman[157] or Paris-Erdogan law [122]. Most importantly, variations in composite manufacturing such as improper resin mixing proportions or presence of impurities results in large differences of tensile stiffness from one specimen to another, even when subjected to exact same loading conditions. As shown in figure 9.1 (a) and (b), two glass fiber-reinforced polymers (GFRP) specimens manufactured under identical conditions and subjected to same fatigue load may fail at significantly different time instants. Normalized stiffness degradation curves for the reference and the test specimen under identical loading conditions, computed from mechanical testing system (MTS), are plotted in figure 9.1 (c). Although belonging to the same GFRP plate, minor variations in number of fibers or fiber orientation responsible for specimen's tensile strength lead to significant difference in failure time of the two specimens. Therefore, life-cycle studies inferred from mechanical testing on a reference specimen may no longer remain valid for a test sample which poses serious issue on RUL prediction in composite structures.

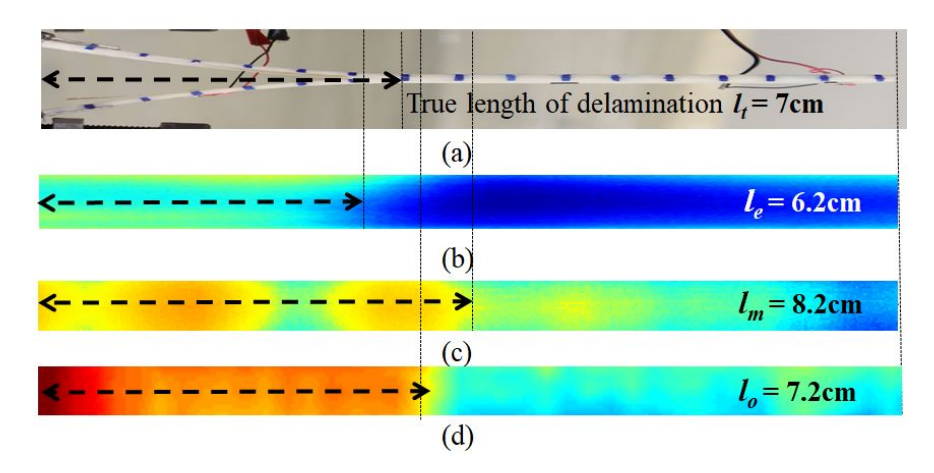


Figure 9.2: (a) Digital camera image of GFRP sample with delamination, under Mode I fracture test (b) Low-frequency eddy current inspection usng TR coil at 10MHz(c) Near-field microwave scan at 7.5GHz (d)Optical transmission scan at 2.5mW.

One possible way to overcome these issues is to use multiple NDE sensors for tracking

defects in a composite structure [158]. Different sensitivity of individual NDE techniques can provide distinct inferences of the damage mechanism, which if judiciously combined can precisely describe the overall stiffness degradation of the structure. However, individual sensor information may be incoherent, uncertain, fuzzy or even in conflict which demands development of robust data fusion methods to estimate the true damage status of the specimen. Figure 9.2 shows a GFRP delaminated sample inspected using three NDE techniques: (a) low-frequency eddy current inspection using TR coil at 10MHz, (b) near-field microwave scan at 7.5GHz and (c) optical transmission scan at 2.5mW. The length of delamination inferred from each of these techniques are not equal to the true delamination length ($l_0 = 7cm$) and even varies from each other. Therefore, using only one technique is not ideal for accurate prognosis since incorrect evaluation of damage length at an observation time leads to incorrect prediction of length at a future time instant. In such cases, fusion of information gathered from multiple NDE sensors is a possible solution for reducing prediction errors.

Despite several multi-sensor fusion processes been reported in literature [159, 160, 161], implementation of effective data fusion systems for prediction of composite stiffness is non-trivial. In practice, if individual NDE data are biased and their underlying uncertainty or variance is not taken into account, prognosis based on fused data may produce worse results than what could be obtained from the 'best' sensor [1]. Moreover, some of the existing data fusion techniques such as the cluster based fusion [162] assumes measurements at consecutive time instants to be statistically independent which is specifically not applicable in damage prognostics. In the case of composites where the structure deteriorates from its pristine state to total failure, correlation exists between NDE observations at consecutive time instants which needs to be incorporated into the fusion methodology. Besides, cluster based fusion approaches [162, 163] are able to provide accurate prediction results only when data from a

large number of sensors are available since number of clusters is usually selected as $N_s/3$, N_s being the number of sensors. Since NDE of composites in automotive or aviation structures is usually an expensive and time-consuming process, most industrial applications rely on inspection from 1 or 2 NDE systems and therefore demand a data fusion technique for fewer sensor data.

Using multiple sensors for NDE inspection raises two main challenges. Firstly, sensors may have different sensitivity at different stages of the degradation. For example, thermal camera is often incapable of imaging small cracks in metals at their initial stage but can sense them once the crack is of a substantial size [164]. Thus, contribution of measurements from different sensors to the fused path should change with time. This brings in the notion of associating dynamic and non-uniform weights to individual sensors while generating the fused path. Secondly, signals collected from multiple sensors are often correlated and each signal only contains partial information of the degraded unit. A good example for such scenarios is the one where a sample is inspected using optical and acoustic technique. Regular optical methods do not provide information regarding the depth of volumetric defects in samples which can be obtained from the acoustic methods. In such cases, data fusion methods should be designed for effective combination of information from multiple sensors to achieve better characterization of system health. Besides, since all sensors measure the same degradation process, their measurements are highly correlated and hence should be treated jointly.

In this chapter, a multi-sensor prognosis methodology is proposed based on joint likelihood computation in particle filtering framework to predict residual stiffness of a GFRP specimen subjected to fatigue. Three major contributions in reliability assessment of composite materials are demonstrated through this study- 1) a paris-paris model is discussed for potential modeling of normalized stiffness degradation of GFRP tensile coupon under cyclic loading conditions, which have not been reported before, 2) improvement in prediction results using two independent NDE sensors over single-sensor prognosis is established, both in RUL computation as well as prediction error domain and 3) possible reduction in number of particles used in particle filters is achieved by implementing multi-sensor prognosis based on joint likelihood computation which may result in significant benefit in lowering the computation time and cost.

9.2 Literature Review of Data Fusion Techniques

Historically, data fusion techniques were primarily developed for military applications (stated in Table 9.1) such as automated target recognition, remote sensing, battlefield surveillance, and automated threat recognition systems. Later the techniques were adopted in several civilian applications as summarized in Table 9.2. For our study, we focus on the application of data fusion for condition based maintenance of structures as an extension to existing NDE technology.

Specific Applications	Inferences Sought by DF Process	Primary Observable Data	Surveillance Volume	Sensor Platforms - Ships - Aircraft - Submarines - Ground-based - Ocean-based		
Ocean Surveillance	Detection, tracking, identification of targets/events	EM signal Acoustic signals Nuclear related Derived observations (wake)	Hundreds of nautical miles Air/surface/sub-surface			
Air-to-Air and Surface-to- Air Defense	Detection, tracking, identification of aircraft	EM radiation	Hundreds of miles (strategic) Miles (tactical)	Ground-based Aircraft Ships		
Battlefield Intelligence, Surveillance, and Target Acquisition	Detection and identification of potential ground target	EM radiation	Tens to hundreds of miles about a battlefield	Ground-based Aircraft		
Strategic Warning and Defense	Detection of indications of impending strategic actions Detection/tracking of ballistic missiles and warheads	EM radiation Nuclear related	Global	Satellit is Aircraft Ground-based		

Table 9.1: Military applications of data fusion, from [1].

Measurement data can be combined or fused at multiple stages resulting in data level

Specific Applications	Inferences Sought by DF Process	Primary Observable Data	Surveillance Volume	Sensor Platforms		
Condition-Based Maintenance	Detection, characterization of system faults Recommendations for maintenance corrective actions	EM signal Acoustic signals Magnetic Temperature X-rays Vibration	Microscopic inspection to hundreds of feet	Ships Aircraft Ground-based (e.g., factory)		
Robotics	Location, identifica- tion of obstacles, and objects to be manipulated	TV Acoustic signals EM signals X-rays	Microscopic to tens of feet about the robot	Robot body		
Medical Diagnostics	Location, identifica- tion of tumors, abnormalities, and disease	X-rays NMR Temperature IR Visual inspection Chemical/biological data	Human body volume	Labora.ory		
Environmental Monitoring	Identification, location of natural phenomena (earthquakes, weather)	SAR Seismic EM radiation Core samples Chemical/biological data	Hundreds of miles Miles (site monitoring)	Satellites Aircraft Ground-based Underground samples		

Table 9.2: Non-military applications of data fusion, from [1].

fusion, feature level fusion or decision level fusion [165, 166]. Data level fusion combines the raw data measured by individual sensors to form an unified indicator [159, 160]. Data level fusion can be implemented when the sensors are commensurate, i.e they have similar output measurements such as combining data from two acoustic sensors or two eddy current sensors acquiring data at different frequencies. Feature level fusion is combination of representative features from sensor data and concatenating them to form a new feature vector which is then fed to pattern recognition approaches such as neural network, clustering etc [161, 167]. The most common example of feature level fusion is the human cognitive system. Finally, decision level fusion is obtained by combining inferences from individual sensors after each sensor has made a preliminary decision in order to extract more comprehensive information [168]. In the case of condition based maintenance by NDE techniques, decision level fusion combines damage propagation path predicted by multiple NDE sensors and then computes the final residual life using the fused path.

Several statistical tools and signal processing techniques have been incorporated in the past for the objective of data fusion. Typical decision level fusion include evidential reason-

ing [169], Bayesian inference [170], and Dempster-Shafer's method[171]. Besides, pattern recognition approaches have been incorporated in decision level fusion such as artificial neural network based fusion [172] and cluster based fusion [162]. A detailed review of popular data fusion techniques can be found in [1].

Despite these qualitative notions and quantitative calculations of improved system operation by using multiple sensors and fusion processes, actual implementation of effective data fusion systems is not trivial at all. In practice, fusion of sensor data may produce worse results than what could be obtained from the 'best' sensor. This can happen especially when individual sensor data are biased and their underlying uncertainty or variance is not taken into account while fusing their decisions. Moreover, some of the existing data fusion techniques such as the cluster based fusion only considers the measurements at a particular time instant which is specifically not applicable in prognostics. Correlations exist between observations from sensors at consecutive time instants which needs to be incorporated into the fusion methodology. In this chapter, all the above challenges are addressed by developing a data fusion framework based on weighted combination of sensor data depending on its consistency and quality of inspection signal. The methodology will be implemented for prognosis and reliability analysis of delamination growth in glass fiber reinforced polymer(GFRP) composites subjected to fatigue testing.

9.3 Joint Likelihood Computation in Particle Filtering

In this study, integrated prognostics under particle filtering framework is implemented for prediction of stiffness degradation in composites. Similar to prediction of impact damage area in GFRP described in chapter 7 [149], stiffness (s) degradation in GFRP tensile coupons

caused by fatigue is modeled according to the Paris-Paris model [123]. When composites are subjected to tensile loading, different damages occur in sequential phases; the matrix begins to crack at the initial stages of fatigue followed by delamination growth during mid-life and fiber breakage towards the end-of-life (EOL)[138]. Since matrix stiffness is relatively lower than fiber strength in composites, overall structural stiffness drops rapidly in the first few load cycles and then decreases at a lower rate until failure. Such a stiffness degradation curve can therefore be described by the Paris-Paris model based on Piecewise-deterministic Markov processes (PDMPS) where Paris law is described by two sets of parameters (m_1, C_1, m_2, C_2) before and after a transition time N^* , denoted by equation 9.1.

$$\frac{ds}{dN} = \begin{cases}
C_1 \left(Y \sqrt{\pi s} \right)^{m_1}, & \text{if } N \leq N^* \\
C_2 \left(Y \sqrt{\pi s} \right)^{m_2}, & \text{if } N \geq N^*
\end{cases}$$
(9.1)

Periodic stiffness values obtained from NDE measurements, denoted by z_k , are incorporated for updation of model parameters where z_k is considered as noisy estimate of true stiffness value s_k of the composite specimen at time instant T_k .

$$z_k = s_k + \omega_k \tag{9.2}$$

$$\omega_k \sim \mathcal{N}(0, \sigma^2)$$
 (9.3)

In existing PF algorithm, distribution of i^{th} particle is updated based on its likelihood given the evidence or the measurement data z_k , as denoted in equation 9.4. It is important to note that different Paris law parameters $\{m_1, C_1\}$ and $\{m_2, C_2\}$ are selected before and after the loading cycle N_k crosses the 'jump' cycle N^* .

$$L(z_k|s_k^i) = \frac{1}{z_k \sqrt{2\pi} \xi_k^i} exp \left[-\frac{1}{2} \left(\frac{\ln z_k - \lambda_k^i}{\xi_k^i} \right)^2 \right]$$
 (9.4)

where,

$$\xi_k^i = \sqrt{\ln\left[1 + \left(\frac{\sigma}{s_k^i}\right)^2\right]} \tag{9.5}$$

$$\lambda_k^i = \ln\left[s_k^i\right] - \frac{1}{2}(\xi_k^i)^2 \tag{9.6}$$

In order to incorporate data from multiple NDE sources, likelihood of particles are computed according to the principle of Bayesian network (see Appendix A.), as depicted in figure 9.3. For multi-sensor NDE systems, if true stiffness parameter s_k^i of a structure is known, evidence from individual NDE techniques $\{z_k^1, z_k^2, ..., z_k^M\}$ can be considered to be statistically independent. For example, a structure with a particular stiffness can be imaged using NDE sensor 1 as well as NDE sensor 2. Owing to difference in physics of the NDE methods, features extracted from individual NDE signals can be different, yet both can be used to characterize the same structural stiffness. Any change in the stiffness value extracted from one sensor image does not affect stiffness measurement from second sensor. Therefore, according to the theory of conditional independence, the joint likelihood for i^{th} particle can be computed from M measurements using equation 9.7, where individual likelihoods are obtained using equation 9.4–9.6. Additional advantage of this approach lies in the fact that single sensor likelihood is computed incorporating the model and measurement noise of the corresponding NDE sensor which facilitates dynamic updating of weights from individual

sensors on the resultant stiffness estimation.

$$L(z_k^1, z_k^2, ..., z_k^M | s_k^i) = \prod_{j=1}^M L(z_k^j | s_k^i)$$
(9.7)

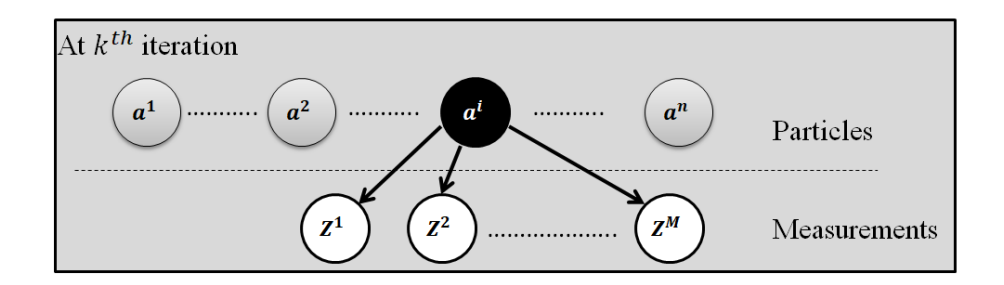


Figure 9.3: Bayesian network in multi-sensor particle filtering framework.

It should be noted that the assumption of conditional independence remains valid only when different NDE sensors are used for inspection of same structural stiffness. If multiple features are extracted from the same NDE result (eg: eddy current measurements obtained at more than one frequencies) and implemented into the multi-sensor framework, conditional independence between measurements will not be applicable. In such cases, correlation between each measurement has to be considered while computing the joint likelihood of each particle.

As described in chapter 6, resampling in PF algorithm is achieved through inverse CDF method such that particles with likelihood greater than a random number generated from U(0,1) are duplicated and others are discarded [102]. In this study, it is assumed that the end-of-life (EOL) of the composite structure is known a-priori from previous experiments for a specific geometry and material. Under fatigue tests, GFRP specimens failed at 30% of initial stiffness obtained at pristine condition. The stiffness model parameters θ_k are updated upto k = L iterations, where L is the total number of observed measurements.

After L iterations, future stiffness is predicted using equations 7.6 until it reaches 30% of initial stiffness. RUL after L iterations is hence computed as $RUL_L = (L_{EOL} - L)$ cycles where L_{EOL} is the load cycle at EOL. PDF of RUL is generated by computing the RUL of all the particles and the RUL median and mean along with its confidence intervals are calculated from the RUL's PDF.

9.4 Experimental set-up

9.4.1 Specimen Geometry and Material

For our experiment, four-layered (0/90) GFRP specimens were fabricated using Vacuum Assisted Resin Transfer Molding (VARTM) technique. The reinforcement consisted of S2-glass plain weave fabric with areal weight of $818g/m^2$ provided by Owens Corning and distribution medium comprising Resinflow 60 LDPE/HDPE blend fabric obtained from Airtech Advanced Materials Group. A two part toughened epoxy resin ,SC-15, was used from Applied Poleramic . The GFRP plate $(150\times300mm^2)$ was manufactured in a $609.6\times914.4mm^2$ aluminum mold with point injection and point venting. After the glass fabric with resin transfer medium were placed on the mold and sealed using a vacuum bag and sealant tape, the reinforcement was infused under vacuum at 29 in-Hg following by curing in a convection oven at 60^o C for two hours and post-curing at 94^o C for four hours. Finally, open-hole tensile coupons with dimensions of $250mm\times25mm\times2mm$ and center hole diameter of 6mm were cut from the manufactured GFRP plate using a water-cooled diamond saw, according to ASTMD7615/D7615M standard, as depicted in Figure 9.6 (a).

9.4.2 Fatigue testing of GFRP under tensile loading

In this chapter, effect of fatigue loading on stiffness degradation is studied on an open-hole GFRP sample under tension-tension cyclic load on a 810 Material Test System (MTS) machine with 50kN load cell, according to ASTMD3479/D3479Mstandard. The experimental setup for open-hole GFRP sample subjected to cyclic loading in MTS machine is illustrated in Figure 9.4 with a laser extensometer to track the axial displacement while the sample is under load. At first, average failure load (F_L) where the specimen breaks was recorded by introducing monotonic loading to five similar samples. Then a test sample was subjected to cyclic loading at constant load equal to 70% of F_L , frequency of 3 Hz and stress ratio of 0.1. Axial load (F) and axial displacement (ΔL) was continuously recorded by the MTS measurement and laser extensometer respectively.

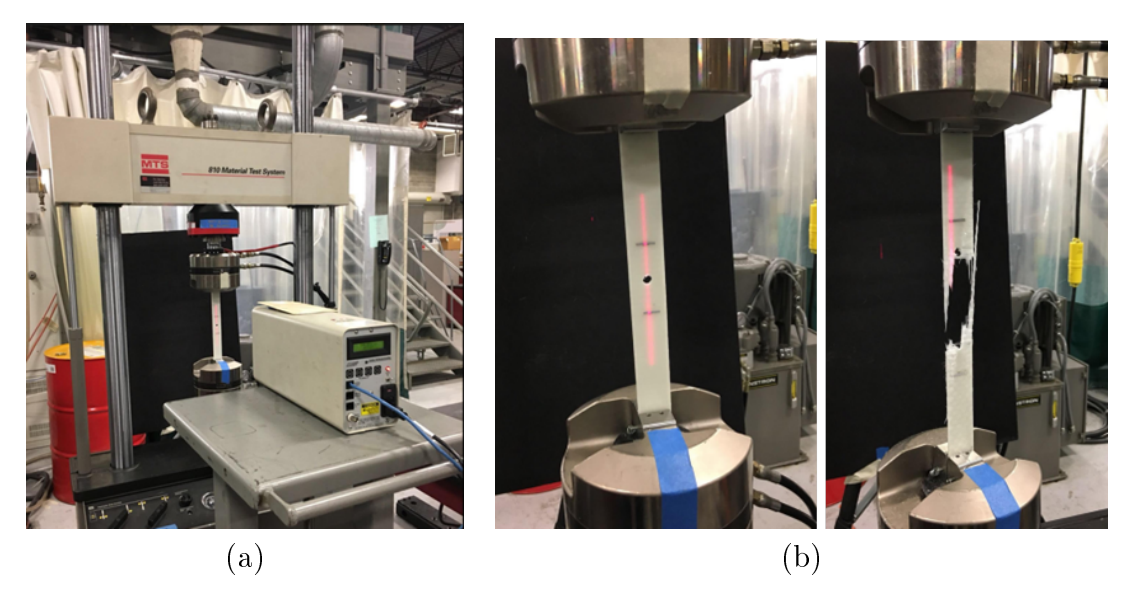


Figure 9.4: (a) Experimental setup for tensile open-hole GFRP coupon subjected to cyclic loading in MTS machine, (b) Healthy and broken GFRP coupons subjecte to fatigue.

Tensile stiffness of any material is given by its Young's modulus (E), as defined by equation 9.8, where ϵ is the axial strain undergone by the specimen subjected to axial stress σ , F is the constant load applied to the specimen in axial direction, A is the cross-sectional

area of sample perpendicular to the direction of applied force, L is the original length of the sample and ΔL denotes the change in specimen length caused by loading. Cross-sectional area (A) and original length (L) of the specimen are constant, therefore the stiffness is directly proportional to the ratio of the axial load and change in length of the specimen under cyclic loading.

$$E = \frac{\sigma}{\epsilon} = \frac{F/A}{\Delta L/L} \propto \frac{F}{\Delta L} \tag{9.8}$$

For a composite specimen under cyclic loading, stiffness modulus S is computed as the slope of the load – displacement (or stress – strain) hysteresis loop ,i.e., the slope of the line connecting the maximum stress and minimum stress point[173, 174]. As depicted in figure 9.5 (a), the slope of hysteresis loop reduces with increasing load cycles. Stiffness computed from this slope, versus number of loading cycles for a training GFRP specimen is plotted in Figure 9.5 (b). The stiffness modulus was normalized with respect to the maximum stiffness modulus (S_0) computed in its pristine condition. Details of computing tensile strength of composite material is derived in Appendix B.

9.5 NDE data acquisition

9.5.1 Fatigue damage detection by OTS)

One of the NDE sensors used in this study is based on an optical transmission scanning (OTS) system developed by Khomenko et al. [118]. Formation of air gaps inside GFRP material introduces changes in its optical properties such as radiation absorption and scattering, which are captured by the OTS system. Earlier works have demonstrated the capability of OTS to image impact damages in GFRP specimens and allowed for accurate characterization

of multiple delaminations and their contours [120, 149]. The results obtained demonstrated excellent agreement with camera images using dye penetrant. Besides, OTS showed great potential for quality control (QC) and other crucial NDE applications such as characterization of thickness variations, improper resin proportions and mixing and inclusions of foreign objects.

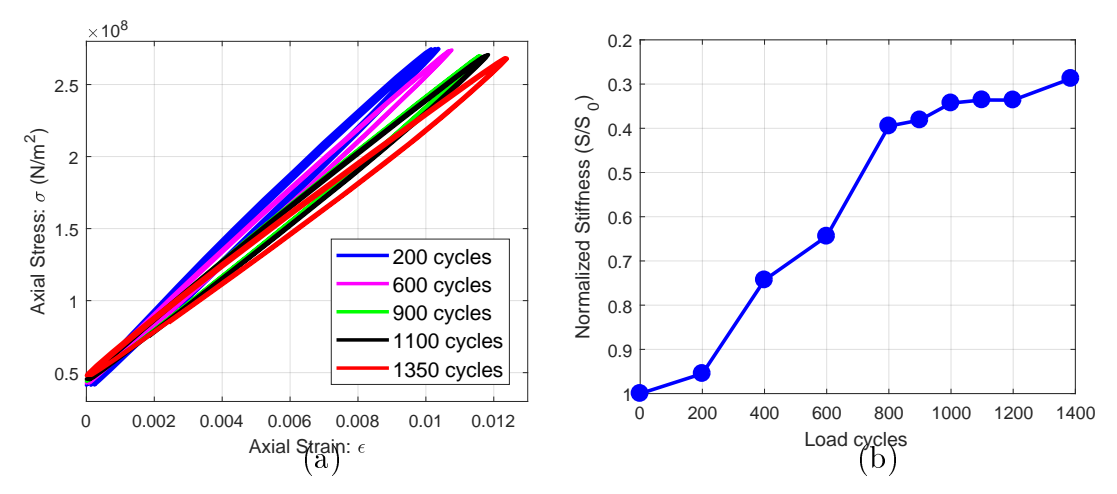


Figure 9.5: (a) Stress-strain hysteresis loop of GFRP specimen at different intervals of fatigue cycles (b) Stress-strain slope or stiffness modulus (S) as a function of number of load cycles.

In this study, the experimental setup used for NDE data acquisition consisted of an iBeam-smart-640s laser diode source emitting light of wavelength 640nm, 1.5mm beam diameter and maximum output power of 150mW. A photodetector underneath the GFRP specimen recorded the through-transmission power and mapped to 0-10V value such that direct transmission in air without specimen corresponded to 10V. The laser power was fixed at 1.9mW in order to obtain highest signal-to-noise ratio and to fix transmission voltage close to 9.8V at the healthy sections of the sample. These specifications provided high contrast images of damaged or delaminated regions in the specimen, as shown in Figure 9.6.

The goal of NDE prognosis is to infer stiffness of the structure from multi-modal NDE techniques including OTS and GW collected at periodic intervals of fatigue loading, starting

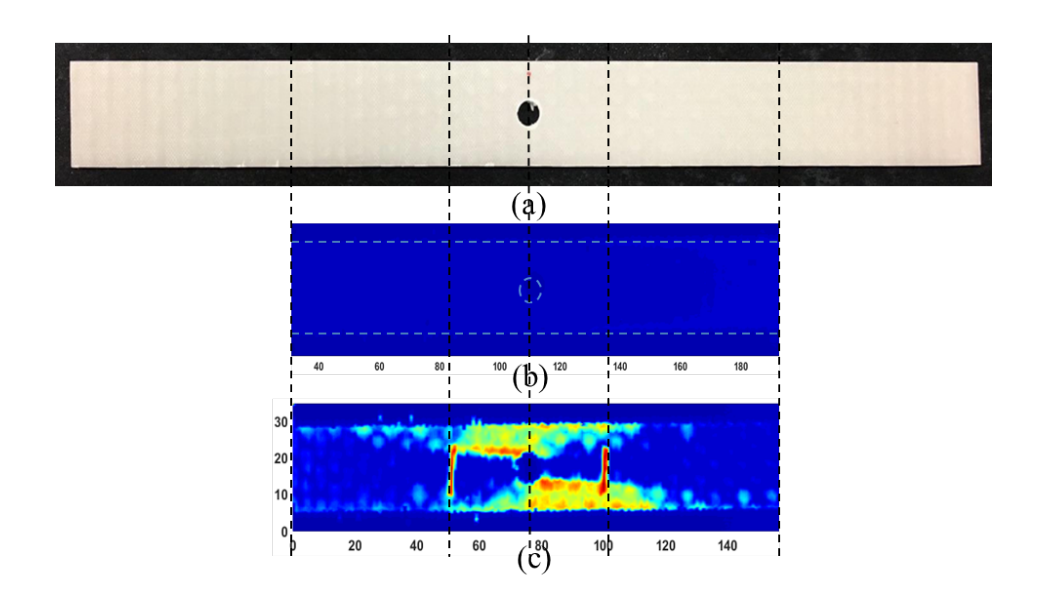


Figure 9.6: (a) Healthy open-hole GFRP coupon (b) OTS image of healthy GFRP coupon (c) OTS image of GFRP coupon after 900 fatigue cycles at 70% of failure load and stress ratio of 0.1.

from its pristine condition up to end-of-life. OTS images for an open-hole GFRP coupon (training specimen) subjected to fatigue test in the MTS machine, are presented in figure 9.7. At cyclic loading of 70% of failure load and load ratio of 0.1, the specimen failed after 1386 cycles.

Strong indications on the OTS images reflect the presence of air gap hidden inside the composite layers caused by continuos cyclic loading, which eventally leads to loss of stiffness in the composite matrix. Pixels associated with damage were extracted from the OTS images via histogram thresholding [175]. It is known from structural mechanics theory, the open hole in a tensile coupon results in stress concentration zone around the hole and the material starts to crack (or delaminate in case of composites) surrounding the hole. The OTS images supports the above theory and therefore a 100mm length of the sample is considered for damage area computation, keeping the hole at the center. Damage area computed for each of the OTS images in figure 9.7 is plotted in Figure 9.8 (a).

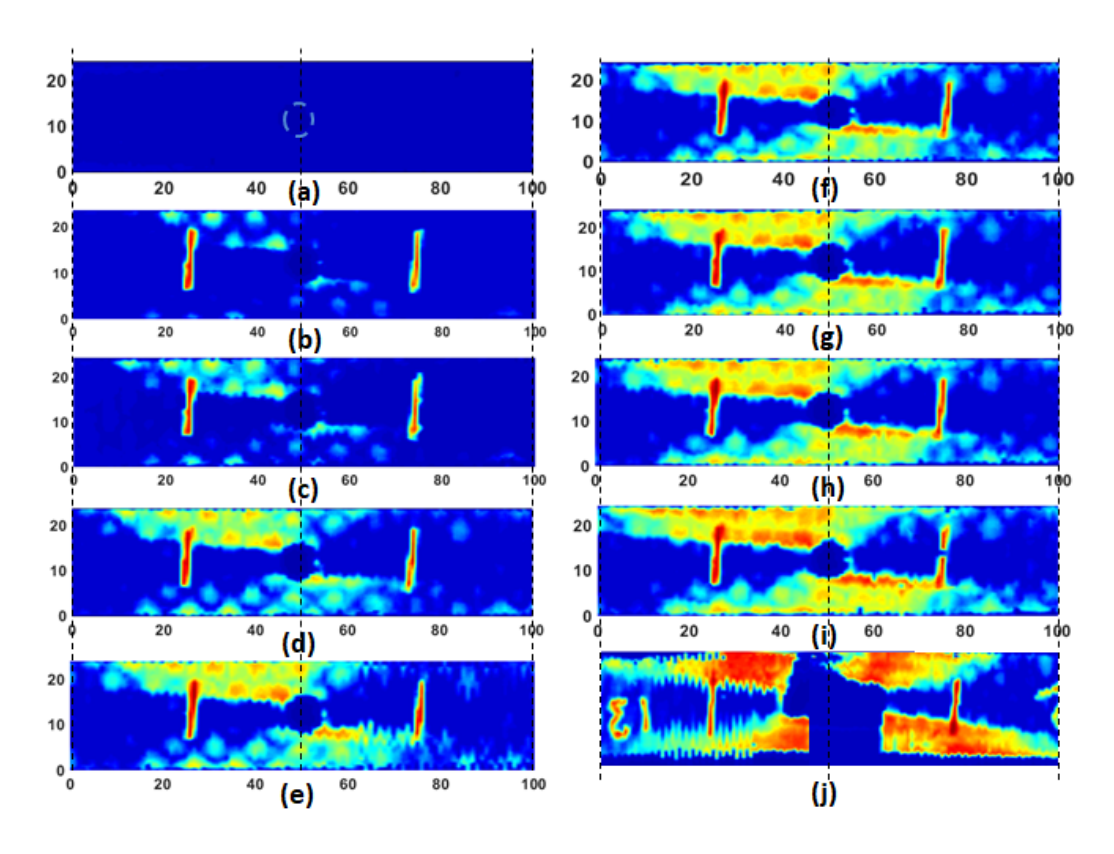


Figure 9.7: OTS images of an open-holed GFRP coupon under fatigue loading :(a) Healthy (0 cycles) (b)200 cycles (c)400 cycles (d) 600 cycles (e) 800 cycles (f) 900 cycles (g) 1000 cycles (h) 1100 cycles (i) 1200 cycles (j) Total failure at 1386 cycles.

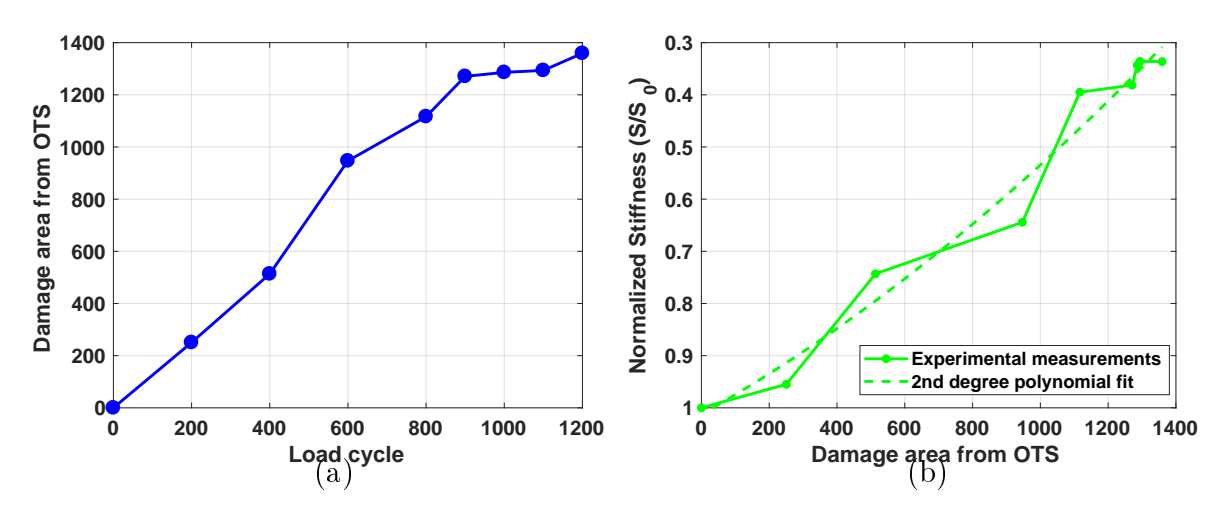


Figure 9.8: (a) Increase in delamination area in open-holed GFRP coupon under fatigue loading, from OTS measurements (b)Correlation between normalized stiffness from MTS measurements and delamination area from OTS images.

Normalized stiffness can be interpreted from the damage area in an OTS image using calibration curve obtained from training specimen, depicted in Figure 9.8 (b). It is important

to repeat the experiments on multiple specimens in order to assess the reproducibility of the NDE method as well as calculate underlying model uncertainty and measurement noise variance. A second order polynomial curve, given by equation 9.9, is implemented to define the relationship between normalized stiffness (\hat{S}) and damage area (Ar_{OTS}) from OTS image. For the set of GFRP specimens used in our study, the parameters of the polynomial curve were computed as $p_1 = -1.12 \times 10^{-7}$, $p_2 = -3.66 \times 10^{-4}$ and $p_3 = 1.014$.

$$\hat{S} = p_1 (Ar_{OTS})^2 + p_2 (Ar_{OTS}) + p_3 \tag{9.9}$$

9.5.2 Fatigue damage detection by GW

Guided wave (GW) sensing technique is an in-situ NDE method which captures the change in acoustic waves propagating through structures in presence of an anomaly [140, 141, 121]. Capability of GW sensing for detection of fatigue damage in GFRP adhesive joints via surface mounted PZT sensors have been successfully established in chapter 8. In this study, GW sensing is implemented via a sensing skin with pressure sensitive adhesive. In stead of mounting PZT sensors on the specimen, the transducers are embedded on a sensing skin with pressure sensitive adhesive for repeated bonding and debonding as shown in Fig. 9.9. The experimental setup used for GW inspection of GFRP specimen is shown in figure 9.9 (a). Gaussian pulse with 50 KHz central frequency was generated using function generator to excite the transmitter PZT.

In comparison to permanently bonded transducers, these sensing skins are reusable. Besides, distance between the two transducers are held constant irrespective of any plastic (permanent) strain in the specimen. Neglecting plastic strain in the material, the observed time of flight (TOF) change in guided wave signals can be solely accounted to the speci-

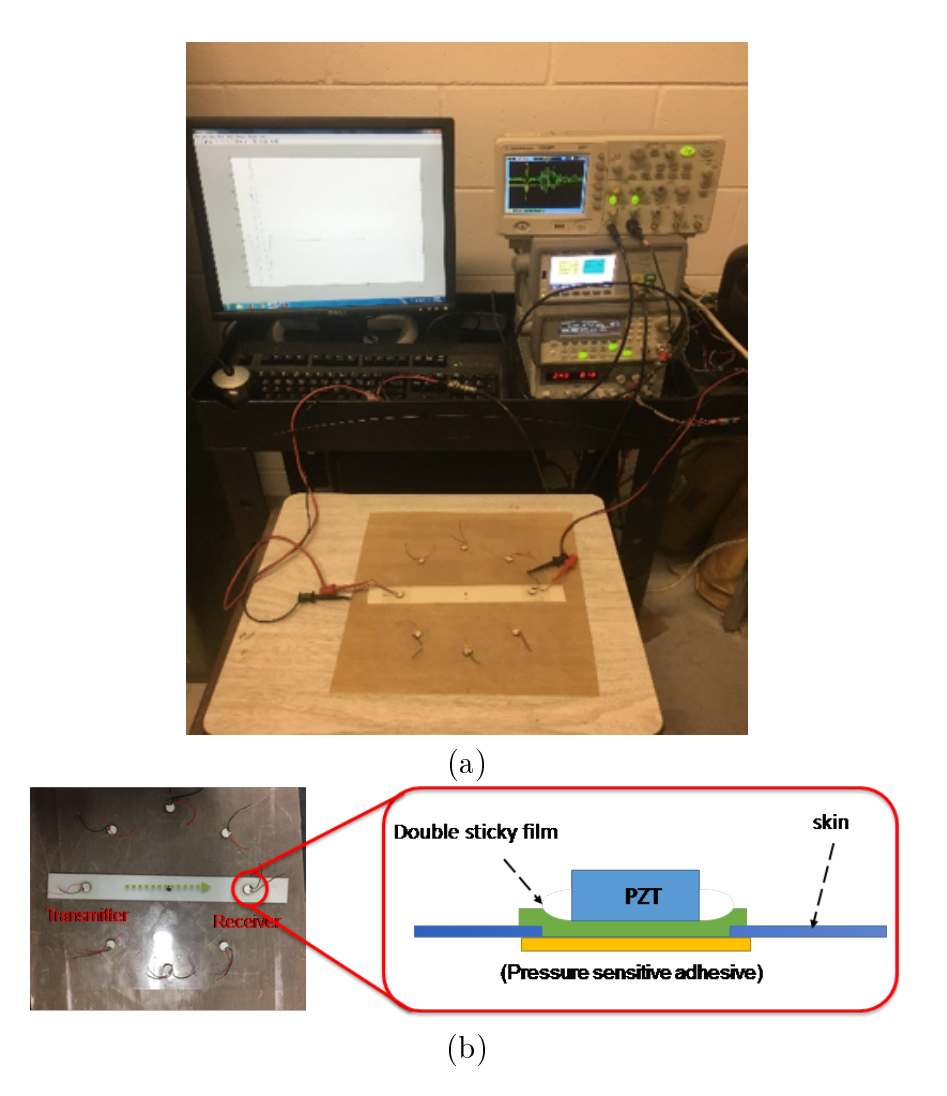


Figure 9.9: Guided Wave inspection of GFRP specimen (a) Experimental setup (b) Schematic of pressure sensitive skin.

men stiffness degradation which arises from various source of damage such as fiber breakage, matrix cracking, delamination etc. Group velocity of acoustic wave (c) traversing through specimen depends on its stiffness along longitudinal direction given by its Young's modulus E_1 according to equation 9.10. ν is Poisson's ratio, ρ is density, ω is angular frequency and d is the thickness of the plate. Assuming the change in Poisson's ratio to be nominal, for a fixed frequency and specimen geometry, the velocity of acoustic waves decreases with reduction of its stiffness modulus. Given the distance between PZT transducers do not change in the sensing skin, time taken by the GW signal to reach the receiver PZT sensor is more in a

damaged GFRP specimen. Hence, change in TOF of GW signals serve as suitable indicator of stiffness degradation.

$$c = 2\sqrt{\frac{E_1}{3\rho(1-\nu^2)}}\sqrt{\omega d} \tag{9.10}$$

GW data was collected from the open-hole GFRP coupon in intermediate load cycles as it gradually progressed from healthy to total failure, with the help of the GW sensing skin. Raw ultrasonic signals were averaged 64 times prior to plotting and were filtered with a bandpass filter with cut off frequencies of 5 kHz and 400 kHz. As the composite specimen underwent matrix cracking followed by formation of delamination and fiber breakage, structural stiffness reduced which caused a phase-shift in the group S_0 mode of the GW signals. A time-shift was observed in the GW signal at the receiver PZT, as depicted in figure 9.10 . ΔTOF was hence computed at every load cycle interval and plotted in figure 9.11 (a).

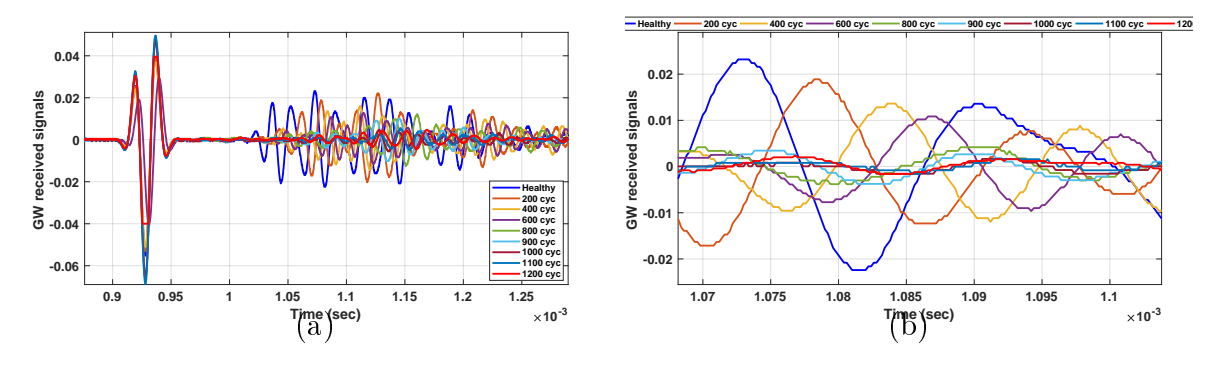


Figure 9.10: (a) Time shift in GW signals in progressively damaged GFRP specimen under fatigue cycles (b) Enlarged region in S_0 mode of received GW signals.

Similar to OTS sensing, normalized stiffness obtained from MTS measurements could be correlated with the GW signal features. On contrary to OTS, GW signal propagation through the damaged region of composite plate provids a more global assessment of damage in composites including effect of matrix cracking, delamination and fibre breakage on the overall stiffness reduction. A 2nd order polynomial curve is fitted on the correlation curves,

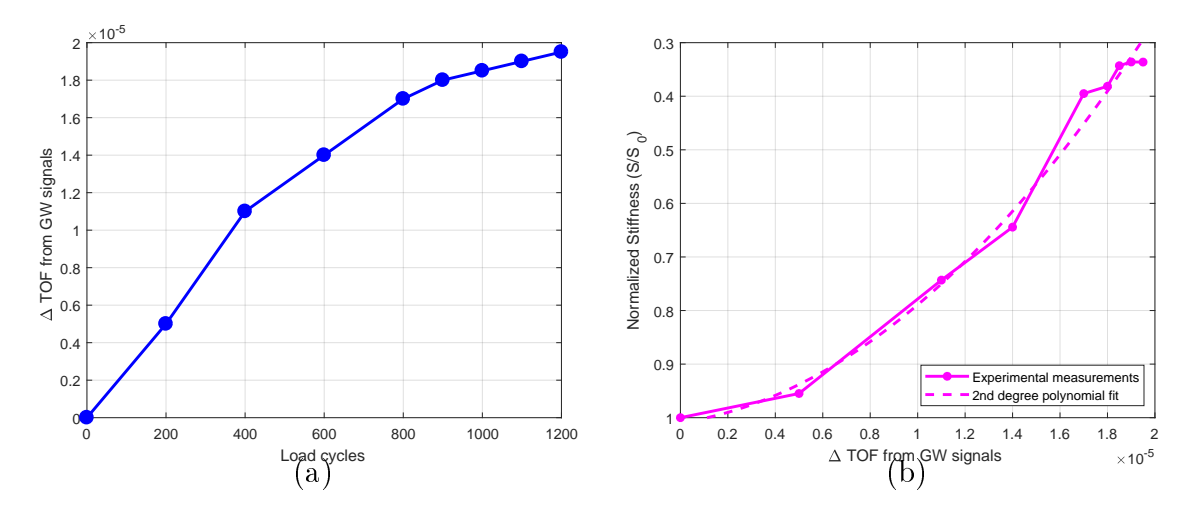


Figure 9.11: (a) Increase in ΔTOF in open-holed GFRP coupon under fatigue loading, from GW measurements (b) Correlation between normalized stiffness from MTS measurements and delamination area from GW images.

as depicted in figure 9.11 (b) and the calibration coefficients are obtained from the training specimens as $p_1 = -1.5 \times 10^9$, $p_2 = -6.5 \times 10^3$ and $p_3 = 1.009$.

$$\hat{S} = p_1(\Delta TOF)^2 + p_2\Delta TOF) + p_3 \tag{9.11}$$

9.6 Prognosis Results

Particle filtering based prognosis was applied to the OTS and GW data collected from GFRP specimens subjected to fatigue testing and the prediction results are reported in this section. Initial distribution of unknown parameters (θ) and correlation coefficients(p_1, p_2, p_3) of NDE data and stiffness measured from MTS system were obtained from training sample. PF algorithm with the estimated parameters was then implemented in an identical test where GFRP specimen was subjected to fatigue loading with conditions as recorded in table 9.3.

Starting from its pristine condition, the test specimen was subjected to progressive fatigue degradation until it failed after 2250 cycles. Stiffness computed from measurements

	1	2	3	4	5	6	7	8	9	10	11	12	13	14	15	16
Load cycles (T_k)	0	100	200	300	400	500	600	700	800	950	1200	1400	1650	1900	2000	2250
Norm. MTS meas. (s_k)	1	0.97	0.93	0.91	0.87	0.77	0.71	0.64	0.63	0.51	0.47	0.46	0.42	0.35	0.32	0.29
Norm. OTS meas. (z_k^{OTS})	1	0.98	0.92	0.87	0.80	0.78	0.70	0.65	0.62	0.58	0.52	0.50	0.41	0.323	0.30	0.27
Norm. GW meas. (z_k^{GW})	1	0.99	0.90	0.87	0.82	0.80	0.72	0.67	0.60	0.57	0.50	0.46	0.39	0.35	0.30	0.28
Failure Load = 25.5 kN Maximum stress= 70% of Failure Stress						Stress ratio =0.1			Frequency = 3Hz							

Table 9.3: Loading cycles for intermediate OTS and GW inspections on test GFRP specimen.

from the MTS and laser extensometer were considered as the ground truth in this study.

Benefit of using two NDE sensor data over single sensor prognosis is assessed and results from implementing the proposed joint likelihood computation approach is compared with prediction on average of sensor measurements.

9.6.1 PF prognosis on OTS data

Stiffness computed from OTS measurements $\{z^{OTS}\}$ using equation 9.9 were used to predict unknown parameters in Paris-Paris model describing the stiffness degradation in fatigue-induced GFRP test specimen. Initial distribution of parameters were obtained from training dataset and set as:

$$s_0 \sim \mathcal{N}(0.01, (0.001)^2)$$

$$m_{10} \sim \mathcal{N}(4, (0.6)^{0.01}), \log C_{10} \sim \mathcal{N}(-10, (0.1)^2)$$

$$m_{20} \sim \mathcal{N}(0.3, (0.01)^2), \log C_{20} \sim \mathcal{N}(-10, (0.1)^2)$$

$$T_0^* \sim \mathcal{N}(750, (10)^2)$$

$$\omega \sim \mathcal{N}(0.09, (0.001))$$

$$(9.12)$$

Initial distribution of noise was characterized based on experimental evidence of NDE measurements on training specimens. Prediction results with different number of OTS observations are presented in figure 9.12. The likelihood of each particle in the PF algorithm is updated according to the single-sensor prognosis framework, as given in equation 9.13. With increasing number of available OTS measurements, the predicted stiffness curve converges to the true stiffness calculated from MTS measurements along with decreasing 95% confidence intervals.

$$L(z_k^{OTS}|s_k^i) = \frac{1}{z_k^{OTS}\sqrt{2\pi}\xi_k^i} exp \left[-\frac{1}{2} \left(\frac{\ln z_k^{OTS} - \lambda_k^i}{\xi_k^i} \right)^2 \right]$$
 (9.13)

Similar to training specimen, stiffness prediction of the test specimen was continued up till the composite stiffness reduced to less than 30% of its initial stiffness in pristine condition. The estimated RUL values at all fatigue stages along with their 95% confidence intervals are illustrated in figure 9.13. When 2 OTS observations were available, the specimen had already been subjected to 100 cycles, therefore the true RUL was computed as 2250 - 1000 = 2150 cycles whereas true RUL at the end of 2250 cycles was 0 since it reached its EOL. Prediction accuracy of RUL in terms of normalized mean squared error (NRMSE), according to equation 9.14, was 0.1761 where O is the number of observations. Since RUL predicted from OTS measurements is lower than its true value for most of the cases, it does not lead to usage of GFRP structure beyond its safety limit. However, portion of its residual life may remain unexploited due to underestimation of RUL by single sensor NDE.

$$NRMSE = \frac{\sqrt{\frac{1}{O-1} \sum_{i=2}^{O} (RUL_i - R\hat{U}L_i)}}{mean(RUL_i)}$$
(9.14)

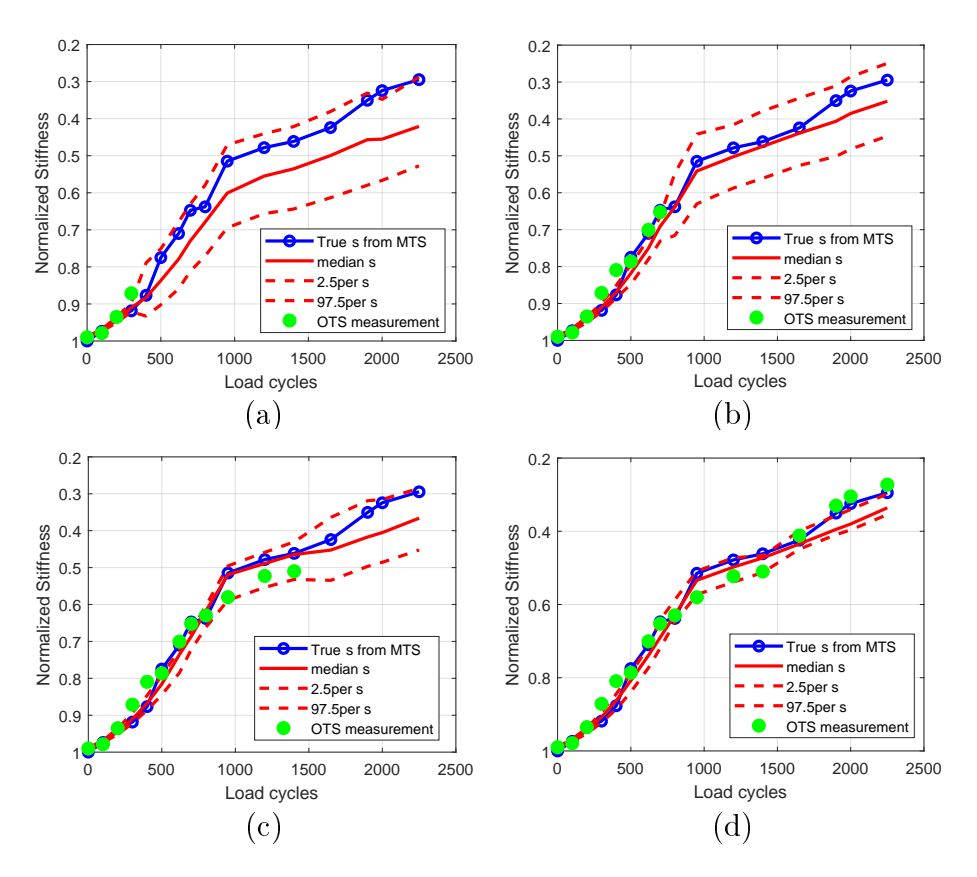


Figure 9.12: Prediction of stiffness degradation curve based on different number of available OTS measurements in Paris-Paris model (a) n=4, (b) n=8 (c) n=12(d) n=16.

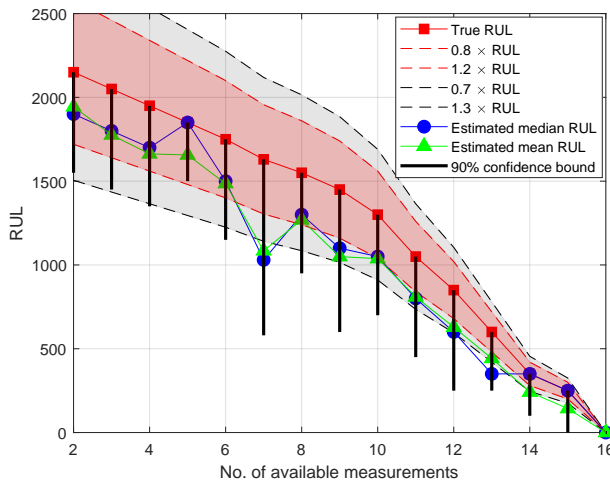


Figure 9.13: RUL prediction for varying number of available OTS measurements (NRMSE=0.1761).

9.6.2 PF prognosis on GW data

Prediction results of stiffness reduction in GFRP specimen via implementation of PF based prognosis on GW sensing data is presented in this section. Normalized stiffness is computed from the ΔTOF of GW received signals using the calibration coefficients in equation 9.11. Particles were updated in the PF approach by resampling according to their likelihood values computed by equation 9.13, with $\{z^{OTS}\}$ being replaced by $\{z^{GW}\}$ or the stiffness values of the specimen at different stages of fatigue inferred from GW measurements. Prediction results of future stiffness values using the Paris-Paris model are denoted in figure 9.14. Similar to OTS data, initial noise distribution was characterized from GW experiments on training specimens. Initial distribution of other parameters in PF algorithm were kept unchanged, in order to compare the prediction capability of the two NDE techniques.

It is obvious from figure 9.14 that as number of available measurements increases, the predicted stiffness curve becomes more representative of the true stiffness values. the confidence interval reduces. Similar to OTS measurement results, the RUL is computed for different number of available GW measurements assuming that the specimen's EOL occurs at 2250 cycles. Figure 9.15 presents the accuracy of RUL estimation compared to the true values at every intermediate stage of fatigue testing. NRMSE for RUL prediction using GW measurements was obtained as 0.1441. Comparing figures 9.13 and 9.15, it can be concluded that GW measurements can describe the damage growth progression more accurately than OTS data, the reason being that GW data provide global assessment of damage status including matrix cracks, fiber breakage and delamination whereas, OTS system captures effect of delamination on stiffness degradation. Diagnosis of stiffness from OTS measurements lacks the contribution from matrix cracking and fiber breakage, thereby leading to higher

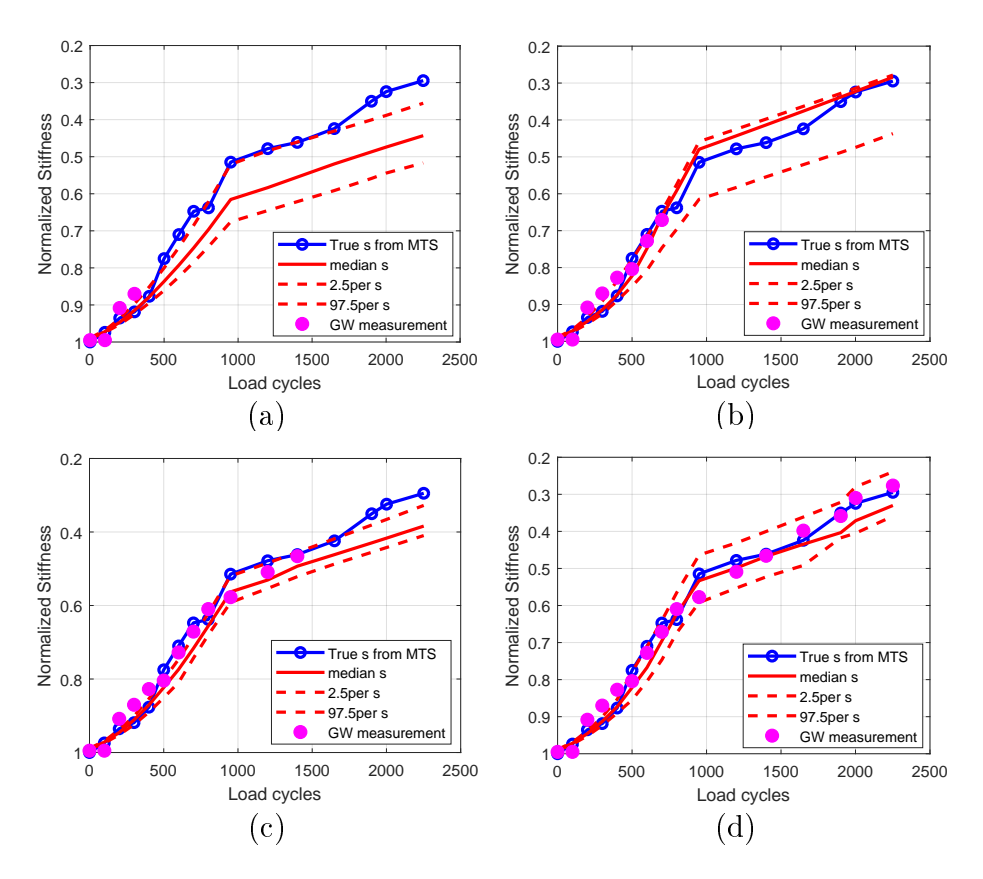


Figure 9.14: Prediction of stiffness degradation curve based on different number of available GW measurements in Paris-Paris model (a) n=4, (b) n=8 (c) n=712 (d) n=16.

error in its prognosis results.

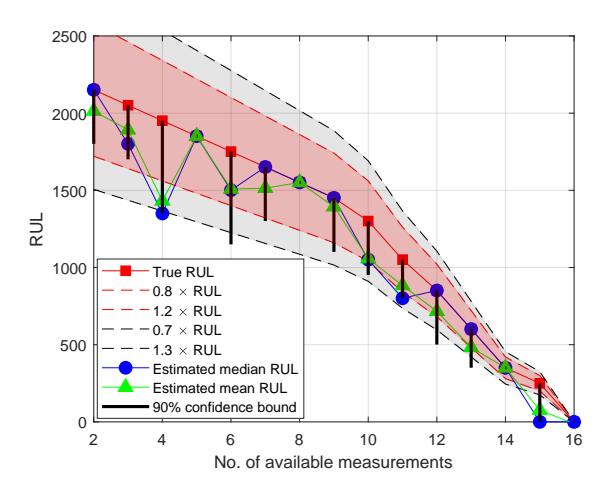


Figure 9.15: RUL prediction for varying number of available GW measurements (NRMSE=0.1441).

9.6.3 PF prognosis on Average of Two Sensors data

With an aim to exploit the benefits of both NDE sensors, PF based prognosis was implemented on a dataset obtained by averaging OTS and GW measurements at every time-step. The likelihood for each particle in the PF framework was computed according to equation 9.13 with $\{z^{OTS}\}$ being replaced by $\{z^{AVG}\}$, where $\{z^{AVG}\}$ is:

$$\{z^{AVG}\} = \frac{\{z^{OTS}\} + \{z^{GW}\}}{2} \tag{9.15}$$

Keeping all other parameters of the Paris-Paris model unchanged, future stiffness values were predicted, given varying number of known measurements and the corresponding estimated stiffness curves are denoted in Figure 9.16. As expected, the predicted curve was closer to the true stiffness computed from MTS measurements with increasing number of observations. The corresponding RUL prediction for different observed measurements using average data is presented in Figure 9.17. NRMSE of predicted RUL was computed as 0.1507 which shows that a simple averaging of two sensor data does not provide higher accuracy in its prognosis results. Stiffness degradation in a composite material is inherently a dynamic process which cannot be captured by static weighted combination of the two sensor data. Accuracy of OTS and GW measurements varies at different load cycles which require dynamic updating of weights on the final prediction result. On the contrary, averaging lead to higher NRMSE of RUL prediction compared to that of GW measurements.

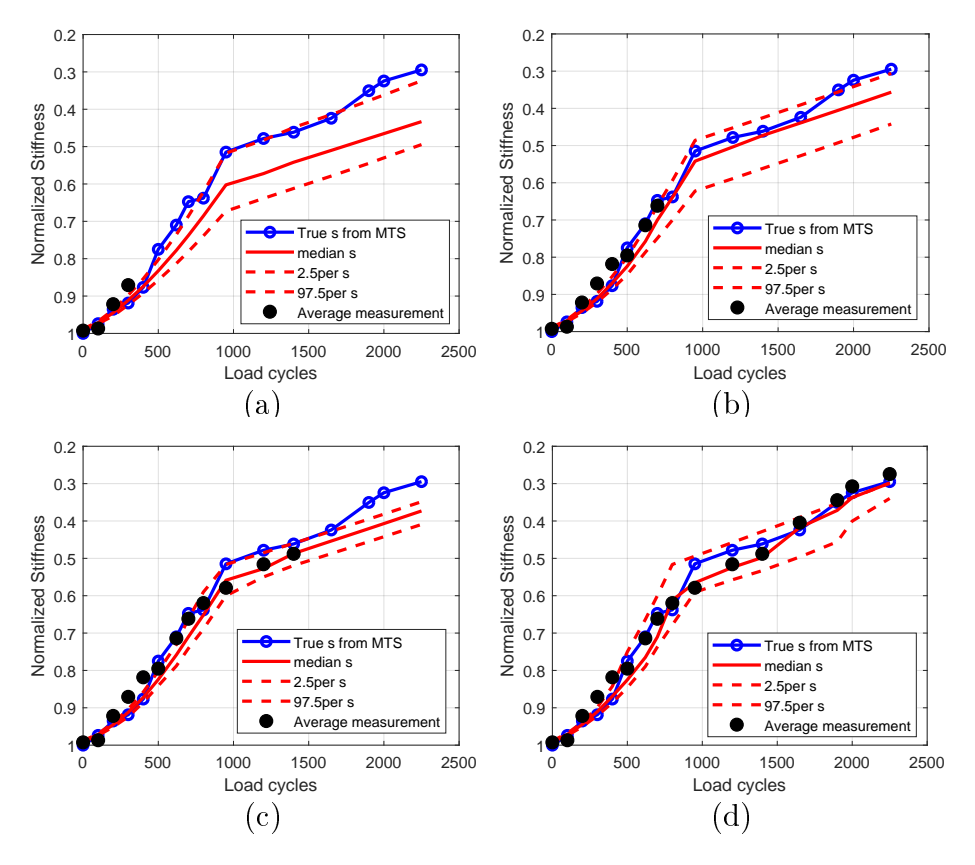


Figure 9.16: Prediction of stiffness degradation curve based on different number of available AVG measurements n=16.

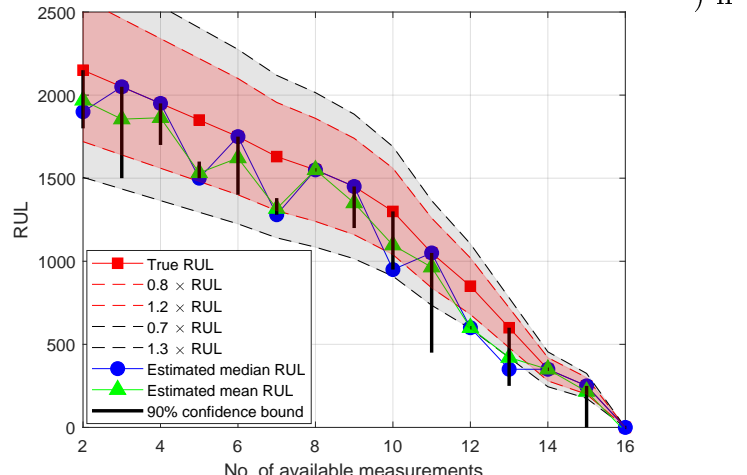


Figure 9.17: RUL prediction for varying number of available AVG measurements (NRMSE=0.1507).

9.6.4 PF Prognosis on Two Sensor Data by Joint Likelihood Computation

In a GFRP specimen with a open-hole at the center undergoing fatigue test, overall stiffness reduction can be accredited to the damage growth around the hole. Particularly

for composites, damage includes multiple structural phenomenon occuring simultaneously. However analysing OTS and GW data, it was observed that the individual sensors only provided partial representation of damage status inside a GFRP specimen subjected to fatigue. On one hand, stiffness inferred from OTS measurements accounted for the increase in delamination area around the hole, whereas on the other hand, stiffness computed from GW measurements captured overall damage mechanism throughout the specimen length and not limited to the region around hole. Besides, measurements from individual NDE sensors were affected by variable noise at every inspection. Since different sensor data provides different contribution to the stiffness reduction, it is crucial to implement joint likelihood in Bayesian network within the PF algorithm, for this application.

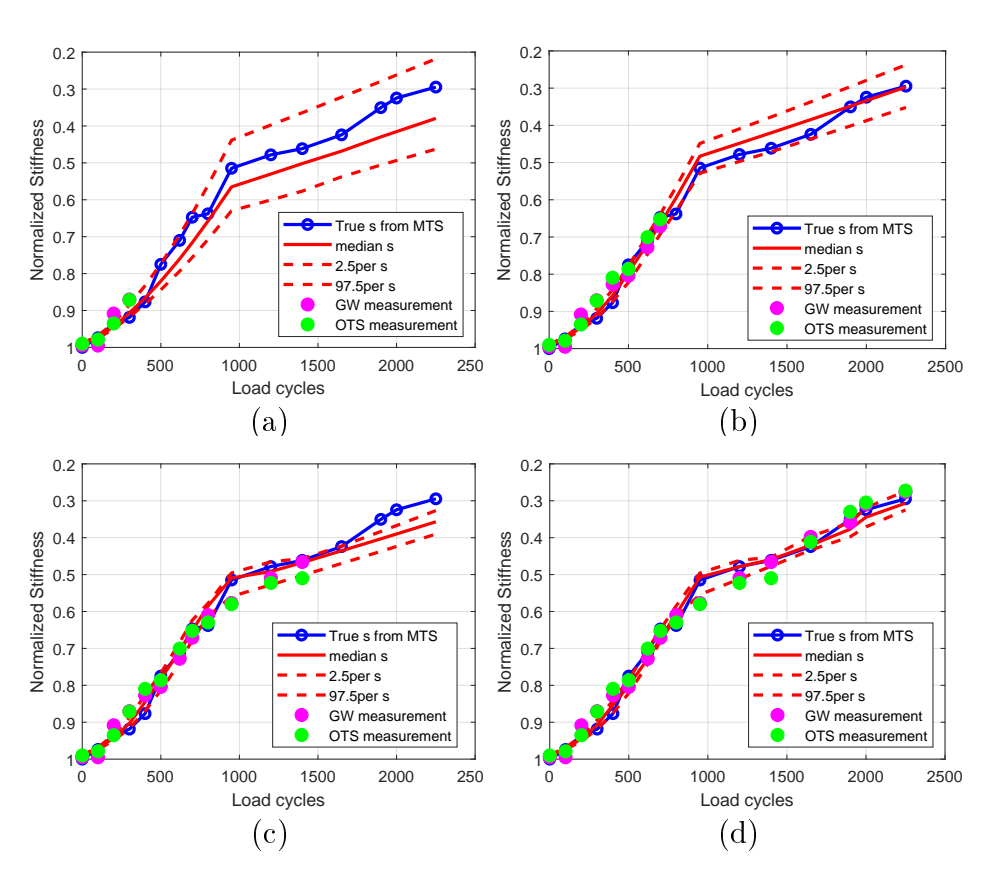


Figure 9.18: Prediction of stiffness degradation curve based on different number of available measurements using joint likelihood computation in Paris-Paris model (a) n=4, (b) n=8 (c) n=12 (d) n=16.

Using same parameters as before, joint likelihood particles at every iteration is calculated by equation 9.13, replacing $\{z^{OTS}\}$ with $\{z^{JL}\}$ where $L\{z^{JL}\}$ is computed according to conditional independence of OTS and GW measurements in Bayesian networks.

$$L\{z^{JL}\} = L\{z^{OTS}\} \times L\{z^{GW}\}$$
 (9.16)

As shown in figure 9.18, predicted stiffness by joint likelihood converges closer to the ground truth with increasing number of observed measurements. Moreover, compared to the previous results, the most accurate RUL prognosis is achieved, with NRMSEof 0.065 when joint likelihood is taken into account, as denoted in figure 9.19. The mean of RUL distribution lied within 20% error bound from true values with exact matching of median RUL at most observation cycles. The primary reason for higher accuracy of RUL prognosis by joint likelihood computation of two sensor data is due to the fact that this approach allowed dynamic update of weights contributing to the true stiffness value unlike simple averaging of two data. Especially at earlier stages of fatigue when fewer measurements were available, decision fusion from both sensors with unequal weights based on their stiffness model uncertainty and measurement noise lead to more accurate prediction of stiffness degradation in GFRP specimen.

For additional comparison between the prognosis approaches, NRMSE is calculated for every predicted stiffness curve using different number of observed measurements and plotted in figure 9.20. Benefit of proposed joint likelihood based PF algorithm over other approaches is evident from Fig. 9.20 (a) especially in the earlier stages of fatigue. Further, the final error after 16 measurements reaches 3%, thereby reinforcing the proposed method as a valid prediction technique.

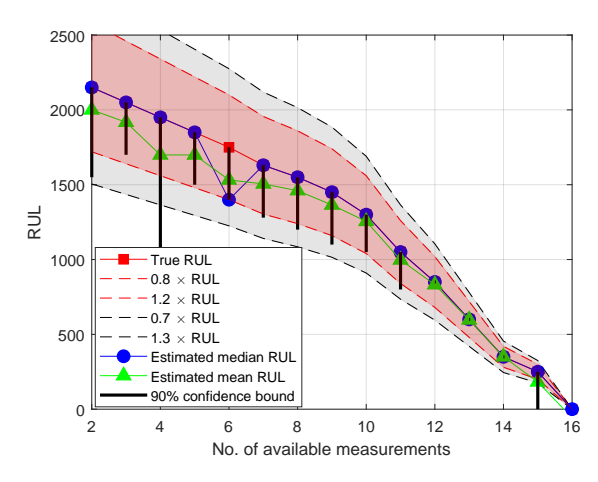


Figure 9.19: RUL prediction for varying number of available OTS and GW measurements using joint likelihood computation (NRMSE=0.065).

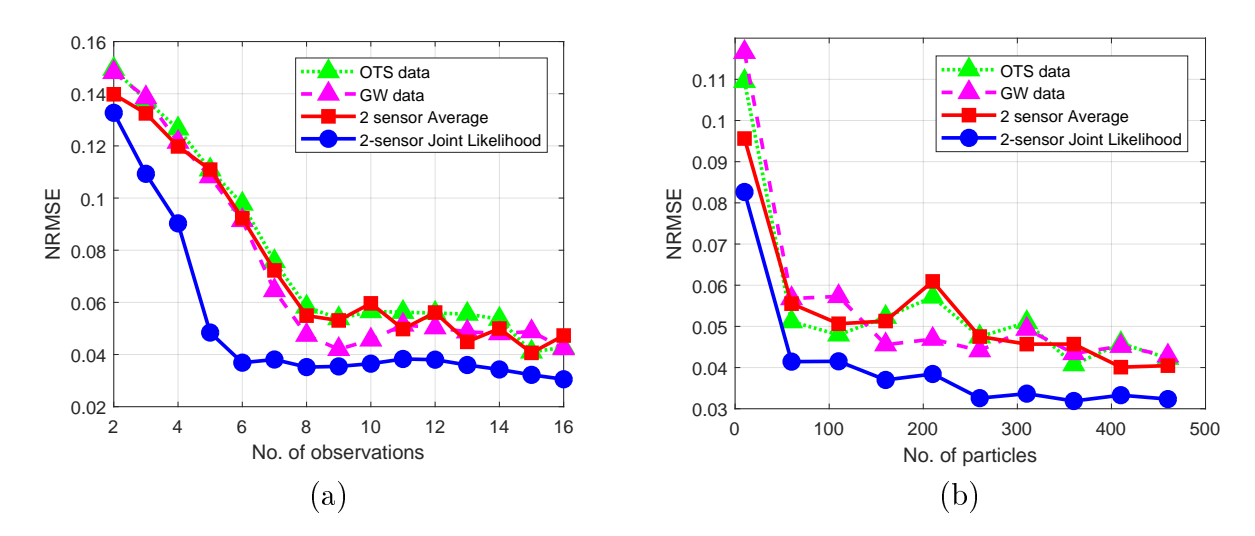


Figure 9.20: (a) Error comparison for varying number of available OTS and GW measurements, (b) Error comparison for varying number of particles in PF algorithm.

It is important to note that increasing number of particles in PF algorithm reduces the estimation error, but leads to higher computation time [176]. Advantage of joint likelihood in PF algorithm in producing accurate prediction results at lower particle count compared to the other single-sensor prognosis is depicted in figure 9.20 (b). Implementing the joint likelihood approach on 16 observations, NRMSE reaches to 0.04 using 50 particles whereas it takes almost 500 particles for single sensor or average data prognosis. Computation time is doubled when 500 particles are used compared to 50 particles. Besides, averaging of

two measurements does not guarantee higher estimation accuracy compared to the single sensor data. However, joint likelihood computation ensures the lowest error for all particle counts. Therefore, the proposed method of computing joint likelihood of measurements from multi-modal NDE system demonstrates an added advantage of reducing particle count in PF algorithm. Reduction of particles have significant impact in reducing overall computation time and resources, thereby achieving real-time prognosis of industrial structures.

Chapter 10

Conclusion

In this study, the importance of self evaluation in existing automated NDE signal analysis system has been discussed. Sources of uncertainties in a typical NDE signal classification system and their effects on classification confidence have been identified. Benefits of Bayes posterior probability as a strong measure of reliability has been implemented which captures the effect of interclass distance and intra-class variance in the feature space. In addition to that, effect of inspection noise has been incorporated into confidence calculation. It has been shown that bootstrapping and weighting Bayes posterior probability with the noise statistics of the test data achieves a more comprehensive confidence metric associated with classification of noisy NDE data. Further, implementation of the proposed approach on steam generator tube inspection data shows possible application of the method.

In future, other factors of reliability in NDE analysis such as effect of a-priori information about the mechanical structure and historical inspection results can be studied. Another highly important problem to be addressed is the effect of ill-fitting of statistical model on the data. If data does not follow normal distribution, the proposed confidence metric will fail to capture the reliability of classification results accurately. In such cases, a more adaptive reliability measure based on non-parametric statistical model is necessary. The challenging task of evaluating classification confidence with limited data, missing data or presence of outliers should be investigated.

The second part of the thesis presents an NDE approach for condition based maintenance and reliability analysis of structures under operation. Prediction of delamination growth in GFRP samples subjected to low velocity impacts is discussed. Images from optical transmission scanning system were used for extracting delamination area from impacted samples which is a rapid and non contact scanning technique in addition to being cost effective and easy to be implemented in industries. Results from implementation of particle filtering approach to estimate delamination propagation path and remaining useful lifetime of a GFRP sample are promising. Due to unique characteristic of GFRP resin, the delamination area growth had a sudden 'jump' at the transition impact energy which made the prediction all the more challenging. Applying two Paris models with different parameters for capturing the 'jump' instead of a single Paris model enhances the prognosis performance of the approach and refined estimation of the delamination propagation path and RUL.

Despite striking benefits of the Paris-Paris model, one of the limitations of this model is that it strongly depends on the initial distribution of the 'jump' energy. If the 'jump' energy is highly different from the true value, the model fails to correctly estimate the transition and yields a sub-optimal result and hence predicted delamination curve is inaccurate. Moreover the delamination path could not be estimated when fewer measurements were available due to lack of enough information to predict the 'jump' energy. In future, the proposed algorithm should be investigated on other composite samples by incorporating additional factors affecting inter-laminar delamination such as complex damage growth due to vibration following impacts or complicated specimen geometry. In such cases, the damage growth model has to be modified without changing the overall framework of the prediction approach.

An obvious extension to the NDE prognostics is the use of multi-sensor information to refine the prediction of residual life of a system under operation. It is evident from prognosis results hat OTS and GW measurements complement each other for estimating composite's stiffness from NDE methods. OTS can image delamination accurately but cannot detect matrix cracking which occurs at the initial stages of fatigue. On the other hand, overall effect of matrix crack and delamination is captured within change in TOF of GW signals. Judicious usage of both measurements enables higher prediction accuracy, even for earlier stages of fatigue. OTS-stiffness model error is higher than GW-stiffness model error, which can be fed into the PF model, thereby automatically adjusting fusion weights during joint likelihood computation. PF prognosis by joint likelihood achieves highest RUL prediction and lowest prediction error (NRMSE), thereby validating the proposed prognosis approach based on joint likelihood computation.

Results are encouraging and can be implemented using more than 2 sensors, without changing the Bayesian Network framework since the assumption of conditional independence stays valid in multiple sensor framework. In future, prediction results can be further refined by replacing empirical correlation curves between NDE features and structural stiffness with physics-based models. Besides, Paris-Paris model should be investigated for more specimens under varying load conditions. Overall, the proposed prognosis method can be used for reliability assessment of any multi-sensory network across various application fields.

APPENDICES

Appendix A

Bayesian Networks for multi-sensor

fusion

Bayesian networks, also known as belief networks is a popular method for modeling uncertain and complex domains such as environmental modelling [177], fault diagnosis [178] and forensic science [179]. Bayesian networks are a type of probabilistic graphical model that represents a set of variables (nodes), and their conditional dependencies (arrows) via a directed acyclic graph (DAG), as shown in figure A.1.In this example, there are M children nodes $(X_1, X_2, ..., X_M)$ from the parent variable P.

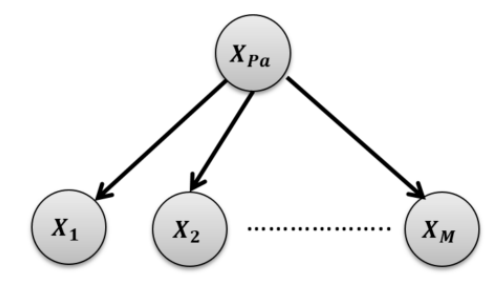


Figure A.1: Example of Bayesian Network with children nodes $(X_1, X_2, ..., X_M)$ and their parent node (P).

The primary advantage of Bayes network is to decompose the joint distributions of all variables by exploiting local Markov property of variables, thereby reducing dimensionality of the model to make it computationally feasible. Local Markov property of variables dictates that the joint probability density function can be written as a product of the individual

density functions, conditional on their parent variables [180].

$$p(x) = \prod_{v \in V} p(x_v | x_{pa(v)}) \tag{A.1}$$

Now, for any set of random variables, the probability of any member of a joint distribution can be calculated from conditional probabilities using the chain rule (given a topological ordering of X) as follows:

$$P(X_1 = x_1, ..., X_M = x_m) = \prod_{v \in V}^M P(X_v = x_v | X_{v+1} = x_{v+1}, ..., X_M = x_m)$$
 (A.2)

By conditional independence of variables, for each X_j which is a parent of X_v the joint likelihood can therefore be computed as:

$$P(X_1 = x_1, ..., X_M = x_m) = \prod_{v \in V}^M P(X_v = x_v | X_j = x_j)$$
(A.3)

Bayesian networks are particularly suitable for decision fusion in practical applications owing to their favorable features such as:

- They facilitate learning about causal relationships between variables [180].
- They provide a method for avoiding overfitting of data [181]
- They can show good prediction accuracy even with rather small sample sizes [182]

Appendix B

Stiffness of Composite Materials

Tensile load applied to any specimen stretches its material. The change in length of the specimen with respect to its original length is termed as the strain. Now, for isotropic materials such as metals, the relationship between stress (σ) and strain (ε) is independent of the direction of applied force. Hence, stiffness in isotropic materials can be defined by a single parameter called Young's modulus (E) which relates the stress and strain according to equation B.1.

$$\sigma = E\varepsilon \tag{B.1}$$

Materials in which their mechanical properties differ in different directions are known to be anisotropic. Composite materials belong to this category and therefore stiffness computation is more complicated in polymers compared to metals. For anisotropic materials, the stress-strain behavior is given by the generalized Hooke's law, given by equation B.2. Apart from the Youngs modulii, material properties are also given by the Poisson's ratio (ν) which is the ratio of the strain perpendicular to a given loading direction, to the strain parallel to the given loading direction. Eg: $\nu_{12} = \frac{-\varepsilon_2}{\varepsilon_1}$ for unixial load in direction 1.

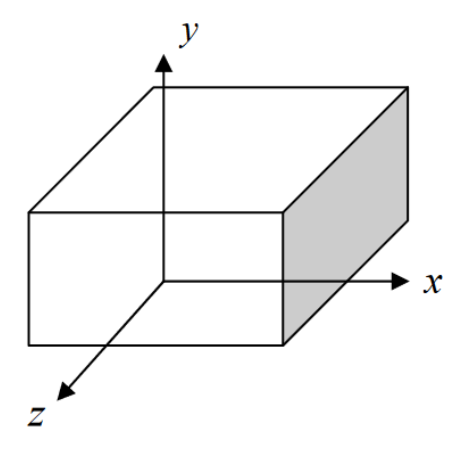


Figure B.1: Material directions in a specimen $x \equiv 1; y \equiv 2; z \equiv 3$.

$$\begin{bmatrix} \sigma_{1} = \sigma_{xx} \\ \sigma_{2} = \sigma_{yy} \\ \sigma_{3} = \sigma_{zz} \\ \sigma_{4} = \sigma_{yz} \\ \sigma_{5} = \sigma_{xz} \\ \sigma_{6} = \sigma_{xy} \end{bmatrix} = \begin{bmatrix} C_{11} & C_{12} & C_{13} & C_{14} & C_{15} & C_{16} \\ C_{21} & C_{22} & C_{23} & C_{24} & C_{25} & C_{26} \\ C_{31} & C_{32} & C_{33} & C_{34} & C_{35} & C_{36} \\ C_{41} & C_{42} & C_{43} & C_{44} & C_{45} & C_{46} \\ C_{51} & C_{52} & C_{53} & C_{54} & C_{55} & C_{56} \\ C_{61} & C_{62} & C_{63} & C_{64} & C_{65} & C_{66} \end{bmatrix} \begin{bmatrix} \varepsilon_{1} = \varepsilon_{xx} \\ \varepsilon_{2} = \varepsilon_{xx} \\ \varepsilon_{2} = \varepsilon_{yy} \\ \varepsilon_{3} = \varepsilon_{zz} \\ \varepsilon_{4} = \varepsilon_{yz} \\ \varepsilon_{5} = \varepsilon_{xz} \\ \varepsilon_{6} = \varepsilon_{xy} \end{bmatrix}$$

$$(B.2)$$

The C matrix consisting of 36 constants is known as the generalized **stiffness matrix** in which the subscripts 1 to 6 denote the six possible directions of stiffness change in the matrix subjected to external load. 1,2 and 3 refer to the longitudinal (x) and transverse directions (y, z) as shown in figure B.1, whereas $\varepsilon_4, \varepsilon_5$ and ε_6 denotes the strain along xz, yz and xy directions.

A composite with unidirectional fiber orientation can be considered as an orthotropic material is one which has three orthogonal planes of microstructural symmetry. As explained in [183], material symmetry (equal normal stresses $\sigma_1 = \sigma_1^i$, $\sigma_2 = \sigma_2^i$, opposite shear stresses $\sigma_6 = -\sigma_6^i$) inherent in the orthotropic material reduces the number of independent elastic constants. As a result, the stiffness matrix is reduced to nine independent elastic constants, according to equation B.3.

$$\begin{bmatrix} \sigma_{1} \\ \sigma_{2} \\ \sigma_{3} \\ \sigma_{4} \\ \sigma_{5} \\ \sigma_{6} \end{bmatrix} = \begin{bmatrix} C_{11} & C_{12} & C_{13} & 0 & 0 & 0 \\ & C_{22} & C_{23} & 0 & 0 & 0 \\ & & C_{33} & 0 & 0 & 0 \\ & & & C_{44} & 0 & 0 \\ & & & & C_{55} & 0 \\ & & & & & C_{66} \end{bmatrix} \begin{bmatrix} \varepsilon_{1} \\ \varepsilon_{2} \\ \varepsilon_{3} \\ \varepsilon_{4} \\ \varepsilon_{5} \\ \varepsilon_{6} \end{bmatrix}$$
(B.3)

Expanding the elastic constants in terms of Youngs modulus (E), Poisson's ratio (ν) and shear modulus (G), equation B.4 is obtained.

$$\begin{bmatrix} \mathcal{E}_{1} \\ \mathcal{E}_{2} \\ \mathcal{E}_{3} \\ \mathcal{E}_{4} \\ \mathcal{E}_{5} \\ \mathcal{E}_{6} \end{bmatrix} = \begin{bmatrix} \frac{1}{E_{1}} & -\frac{v_{21}}{E_{2}} & -\frac{v_{31}}{E_{3}} & 0 & 0 & 0 \\ -\frac{v_{12}}{E_{1}} & \frac{1}{E_{2}} & -\frac{v_{32}}{E_{3}} & 0 & 0 & 0 \\ -\frac{v_{13}}{E_{1}} & -\frac{v_{23}}{E_{2}} & \frac{1}{E_{3}} & 0 & 0 & 0 \\ 0 & 0 & 0 & \frac{1}{2G_{23}} & 0 & 0 \\ 0 & 0 & 0 & 0 & \frac{1}{2G_{13}} & 0 \\ 0 & 0 & 0 & 0 & \frac{1}{2G_{13}} & 0 \end{bmatrix} \begin{bmatrix} \sigma_{1} \\ \sigma_{2} \\ \sigma_{3} \\ \sigma_{4} \\ \sigma_{5} \\ \sigma_{6} \end{bmatrix}$$

$$(B.4)$$

In our application of tensile loading, only axial stress along the direction of fibers (σ_1) is present. Further, in tensile coupons, the width of the specimen being very small, strains in z direction can be neglected. Besides, in orthotropic material there is no shear coupling with respect to the material axes, i.e., normal stresses result in normal strains only and shear stresses result in shear strains only. Hence, by retaining only the x, y components of normal strains and inverting the compliance matrix of equation B.4, the stiffness matrix can

be generated as equation B.5.

$$\begin{bmatrix} \sigma_1 \\ \sigma_2 \\ \sigma_6 \end{bmatrix} = \begin{bmatrix} S_{11} & S_{12} & 0 \\ S_{21} & S_{22} & 0 \\ 0 & 0 & S_{66} \end{bmatrix} \begin{bmatrix} \varepsilon_1 \\ \varepsilon_2 \\ \varepsilon_6 \end{bmatrix}$$
(B.5)

where,
$$S_{11} = \frac{E_1}{1 - \nu_{12}\nu_{21}}, S_{22} = \frac{E_2}{1 - \nu_{12}\nu_{21}}, S_{12} = \frac{\nu_{12}E_2}{1 - \nu_{12}\nu_{21}} = \frac{\nu_{21}E_1}{1 - \nu_{12}\nu_{21}}$$
 and $S_{66} = G_{12}$.

For axial loading of a tensile GFRP specimen, its has been assumed that majority of deformation in the specimen is contributed by material strain in the axial direction. The Poisson's ratio along the direction perpendicular to applied load is considered to be negligible $(\nu_{12} = \nu_{21} = 0; \nu_{13} = \nu_{31} = 0)$. Therefore, approximate stiffness of the specimen in axial direction or S_{11} is calculated by the ratio of axial stress and strain, as given by the hysteresis loop for a specimen undergoing tensile fatigue tests.

$$S_{11} = E_1 = \frac{\sigma_1}{\varepsilon_1} \tag{B.6}$$

BIBLIOGRAPHY

BIBLIOGRAPHY

- [1] David L Hall and James Llinas. An introduction to multisensor data fusion. *Proceedings* of the IEEE, 85(1):6–23, 1997.
- [2] Charles Annis, John C Aldrin, and Harold A Sabbagh. What is missing in nondestructive testing capability evaluation? *Materials Evaluation*, 73(1), 2015.
- [3] Bryan D Olin and William Q Meeker. Applications of statistical methods to nondestructive evaluation. *Technometrics*, 38(2):95–112, 1996.
- [4] Jeremy S Knopp and Li Zeng. Statistical analysis of hit/miss data. *Materials Evaluation*, 71(3), 2013.
- [5] P Xiang, S Ramakrishnan, X Cai, P Ramuhalli, R Polikar, SS Udpa, and L Udpa. Automated analysis of rotating probe multi-frequency eddy current data from steam generator tubes. *International Journal of Applied Electromagnetics and Mechanics*, 12(3, 4):151–164, 2000.
- [6] L Udpa, P Ramuhalli, J Benson, and S Udpa. Automated analysis of eddy current signals in steam generator tube inspection. *Proceedings of the 16th WCNDT*, 2004.
- [7] Marvin Rausand, HOYLAND Arnljot, et al. System reliability theory: models, statistical methods, and applications, volume 396. John Wiley & Sons, 2004.
- [8] Dawn An, Joo-Ho Choi, and Nam Ho Kim. A tutorial for model-based prognostics algorithms based on matlab code. In *Annual Conference of Prognostics and Health Management Society*, volume 3, 2012.
- [9] Jaejoon Kim, Guang Yang, Lalita Udpa, and Satish Udpa. Classification of pulsed eddy current gmr data on aircraft structures. *NDT & E International*, 43(2):141–144, 2010.
- [10] Zheng Liu, David S Forsyth, Jerzy P Komorowski, Koichi Hanasaki, and Thia Kirubarajan. Survey: State of the art in nde data fusion techniques. *Instrumentation and Measurement, IEEE Transactions on*, 56(6):2435–2451, 2007.
- [11] L Obrutsky, J Renaud, and R Lakhan. Overview of steam generator tube-inspection technology. CINDE J, 35(2):5–13, 2009.
- [12] V Oppenheim Alan, W Schafer Ronald, and RB John. Discrete-time signal processing. New Jersey, Printice Hall Inc, 1989.

- [13] David L Donoho. Nonlinear wavelet methods for recovery of signals, densities, and spectra from indirect and noisy data. In *In Proceedings of Symposia in Applied Mathematics*. Citeseer, 1993.
- [14] John A Hartigan and Manchek A Wong. Algorithm as 136: A k-means clustering algorithm. *Applied statistics*, pages 100–108, 1979.
- [15] L Udpa and SS Udpa. Neural networks for the classification of nondestructive evaluation signals. In *IEE Proceedings F (Radar and Signal Processing)*, volume 138, pages 41–45. IET, 1991.
- [16] Alan P Berens. Nde reliability data analysis. ASM Handbook., 17:689-701, 1989.
- [17] Zhiwei Zeng. Applications of pod studies and robust design to electromagnetic nde. 2003.
- [18] Jeremy S Knopp, JC Aldrin, E Lindgren, and C Annis. Investigation of a model-assisted approach to probability of detection evaluation. In *Review of Progress in Quantitative Nondestructive Evaluation*, volume 894, pages 1775–1782. AIP Publishing, 2007.
- [19] SN Rajesh, L Udpa, and SS Udpa. Numerical model based approach for estimating probability of detection in nde applications. *IEEE transactions on magnetics*, 29(2):1857–1860, 1993.
- [20] Muhammad Dawood and Ram M Narayanan. Receiver operating characteristics for the coherent uwb random noise radar. *IEEE Transactions on Aerospace and Electronic Systems*, 37(2):586–594, 2001.
- [21] Dirk Grunwald, Artur Klauser, Srilatha Manne, and Andrew Pleszkun. Confidence estimation for speculation control. *ACM SIGARCH Computer Architecture News*, 26(3):122–131, 1998.
- [22] Trevor C Bailey, Richard M Everson, Jonathan E Fieldsend, Wojtek J Krzanowski, Derek Partridge, and Vitaly Schetinin. Representing classifier confidence in the safety critical domain: an illustration from mortality prediction in trauma cases. *Neural Computing and Applications*, 16(1):1–10, 2007.
- [23] Wojtek J Krzanowski, Trevor C Bailey, Derek Partridge, Jonathan E Fieldsend, Richard M Everson, and Vitaly Schetinin. Confidence in classification: a bayesian approach. *Journal of Classification*, 23(2):199–220, 2006.
- [24] Erik Jacobsen, Eric Rotenberg, and James E Smith. Assigning confidence to conditional branch predictions. In *Proceedings of the 29th annual ACM/IEEE international symposium on Microarchitecture*, pages 142–152. IEEE Computer Society, 1996.

- [25] Sarah Jane Delany, Pádraig Cunningham, Dónal Doyle, and Anton Zamolotskikh. Generating estimates of classification confidence for a case-based spam filter. In Case-Based Reasoning Research and Development, pages 177–190. Springer, 2005.
- [26] P Ramuhalli, L Udpa, and SS Udpa. An automatic signal classification system for ultrasonic weld inspection signals. *Materials evaluation*, 58(1):65–69, 2000.
- [27] Juan Ignacio Arribas and Jesús Cid-Sueiro. A model selection algorithm for a posteriori probability estimation with neural networks. *Neural Networks, IEEE Transactions on*, 16(4):799–809, 2005.
- [28] Ian Lane, Tatsuya Kawahara, Tomoko Matsui, and Satoshi Nakamura. Out-of-domain utterance detection using classification confidences of multiple topics. *Audio, Speech, and Language Processing, IEEE Transactions on*, 15(1):150–161, 2007.
- [29] Mitch Weintraub, Francoise Beaufays, Ze'ev Rivlin, Yochai Konig, and Andreas Stolcke. Neural-network based measures of confidence for word recognition. In *icassp*, page 887. IEEE, 1997.
- [30] Richard O Duda, Peter E Hart, and David G Stork. *Pattern classification*. John Wiley & Sons, 1999.
- [31] DAS Fraser. Confidence, posterior probability, and the buehler example. *The Annals of Statistics*, pages 892–898, 1977.
- [32] John A Richards, Wallace J Bow Jr, and Brian K Bray. An informative confidence metric for atr. In *AeroSense 2003*, pages 336–348. International Society for Optics and Photonics, 2003.
- [33] Robi Polikar, Lalita Udpa, Satish S Udpa, and Tom Taylor. Frequency invariant classification of ultrasonic weld inspection signals. *Ultrasonics, Ferroelectrics, and Frequency Control, IEEE Transactions on*, 45(3):614–625, 1998.
- [34] AA Anastassopoulos, VN Nikolaidis, and TP Philippidis. A comparative study of pattern recognition algorithms for classification of ultrasonic signals. *Neural Computing & Applications*, 8(1):53–66, 1999.
- [35] Kai F Goebel, Weizhong Yan, Neil HW Eklund, Xiao Hu, Viswanath Avasarala, and Jose Celaya. Defect classification of highly noisy nde data using classifier ensembles. In *Smart structures and materials*, pages 616710–616710. International Society for Optics and Photonics, 2006.
- [36] John C Aldrin and Jeremy S Knopp. Crack characterization method with invariance to noise features for eddy current inspection of fasterner sites. *Journal of Nondestructive Evaluation*, 25(4):165–181, 2006.

- [37] Robi Polikar, Lalita Udpa, Satish Udpa, and Vasant Honavar. An incremental learning algorithm with confidence estimation for automated identification of nde signals. *Ultrasonics, Ferroelectrics, and Frequency Control, IEEE Transactions on*, 51(8):990–1001, 2004.
- [38] Bradley Efron and Robert J Tibshirani. An introduction to the bootstrap, volume 57. CRC press, 1994.
- [39] Javier García-Martín, Jaime Gómez-Gil, and Ernesto Vázquez-Sánchez. Non-destructive techniques based on eddy current testing. Sensors, 11(3):2525–2565, 2011.
- [40] Gangzhu Chen, Atsunori Yamaguchi, and Kenzo Miya. A novel signal processing technique for eddy-current testing of steam generator tubes. *Magnetics, IEEE Transactions on*, 34(3):642–648, 1998.
- [41] Matteo Cacciola, A Gasparics, Francesco Carlo Morabito, Mario Versaci, and Vincenzo Barrile. Advances in signal processing to reduce lift-off noise in eddy current tests. *Piers Online*, 3(4):517–521, 2007.
- [42] Nathan J Leap and Kenneth W Bauer. A confidence paradigm for classification systems. Naval Research Logistics (NRL), 58(3):236–254, 2011.
- [43] Donald H Foley. Considerations of sample and feature size. *Information Theory*, *IEEE Transactions on*, 18(5):618–626, 1972.
- [44] Rong Hu, Sarahjane Delany, and Brian MacNamee. Sampling with confidence: Using k-nn confidence measures in active learning. In *UKDS Workshop at International Conference on Case-based Reasoning*, pages 181–192, 2009.
- [45] M Das, H Shekhar, X Liu, R Polikar, P Ramuhalli, L Udpa, and S Udpa. A generalized likelihood ratio technique for automated analysis of bobbin coil eddy current data. NDT & E International, 35(5):329–336, 2002.
- [46] Portia Banerjee, Seyed Safdarnejad, Lalita Udpa, and Satish Udpa. Investigation of a comprehensive confidence measure in nde. In Donald O Thompson and Dale E Chimenti, editors, 41st Annual Review of Progress in Quantitative Nondestructive Evaluation, volume 34, pages 1948–1957. American Institute of Physics 1650, Melville, NY, 2015.
- [47] Michael E Mann and Jonathan M Lees. Robust estimation of background noise and signal detection in climatic time series. *Climatic change*, 33(3):409–445, 1996.
- [48] Portia Banerjee, Lalita Udpa, Satish Udpa, and James Benson. Confidence metric for signal classification in non destructive evaluation. *NDT & E International*, 91:88–96, 2017.

- [49] Junjun Xin, Naiguang Lei, Lalita Udpa, and Satish S Udpa. Rotating field eddy current probe with bobbin pickup coil for steam generator tubes inspection. Ndt & E International, 54:45–55, 2013.
- [50] Junjun Xin, Naiguang Lei, Lalita Udpa, and Satish S Udpa. Nondestructive inspection using rotating magnetic field eddy-current probe. *IEEE Transactions on Magnetics*, 47(5):1070–1073, 2011.
- [51] Naiguang Lei, Lalita Udpa, Satish Udpa, and Zhiwei Zeng. Rotating field eddy current (rofec)-probe for steam generator inspection. *International Journal of Applied Electromagnetics and Mechanics*, 33(3, 4):1279–1285, 2010.
- [52] Pradeep Ramuhalli, Jamie Coble, Ryan M Meyer, and Leonard J Bond. Prognostics health management and life beyond 60 for nuclear power plants. In *Future of Instrumentation International Workshop (FIIW)*, 2012, pages 1–4. IEEE, 2012.
- [53] K Arunchalam, P Ramuhalli, L Udpa, S Udpa, Donald O Thompson, Dale E Chimenti, Linda Poore, Connie Nessa, and Sarah Kallsen. Nonlinear mixing algorithm for suppression of tsp signals in bobbin coil eddy current data. In *AIP Conference Proceedings*, volume 615, pages 631–638. AIP, 2002.
- [54] F Koiimn et al. Wavelet basis function neural network for eddy current signal characterization. *Electromagnetic Nondestructive Evaluation (VI)*, 6:245, 2002.
- [55] Simone Fiori and Pietro Burrascano. Ect-data fusion by the independent component analysis for non-destructive evaluation of metallic slabs. In *Third International Conference on Independent Component Analysis and Signal Separation*, pages 323–327, 2001.
- [56] Carlo Francesco Morabito. Independent component analysis and feature extraction techniques for ndt data. *Materials Evaluation*, 58(1):85–92, 2000.
- [57] Raimond Grimberg, Adriana Savin, Sorin Leitoiu, Alina Bruma, Rozina Steigmann, Lalita Udpa, and Satish S Udpa. Automated eddy current data analysis. *International Journal of Materials and Product Technology*, 41(1-4):75–88, 2011.
- [58] Raimond Grimberg, Lalita Udpa, Adriana Savin, Rozina Steigmann, Valerian Palihovici, and Satish S Udpa. 2d eddy current sensor array. Ndt & E International, 39(4):264–271, 2006.
- [59] SS Upda and W Lord. A fourier descriptor classification scheme for differential probe signals. *Materials Evaluation*, 42(9):1136–1141, 1984.

- [60] Ali Sophian, Gui Yun Tian, David Taylor, and John Rudlin. A feature extraction technique based on principal component analysis for pulsed eddy current ndt. NDT & e International, 36(1):37–41, 2003.
- [61] Paulo G Normando, Elineudo P Moura, José A Souza, Sérgio SM Tavares, and Linilson R Padovese. Ultrasound, eddy current and magnetic barkhausen noise as tools for sigma phase detection on a uns s31803 duplex stainless steel. *Materials Science and Engineering:* A, 527(12):2886–2891, 2010.
- [62] Yoshiaki Nagaya, Toshiyuki Takagi, Tetsuya Uchimoto, and Haoyu Huang. Identification of multiple cracks from eddy-current testing signals with noise sources by image processing and inverse analysis. *IEEE transactions on magnetics*, 40(2):1112–1115, 2004.
- [63] S Safdarnejad, L Udpa, SS Udpa, C Buynak, G Steffes, E Lindgren, and J Knopp. Statistical algorithms for eddy current signal and noise analysis. In 40TH ANNUAL REVIEW OF PROGRESS IN QUANTITATIVE NONDESTRUCTIVE EVALUATION: Incorporating the 10th International Conference on Barkhausen Noise and Micromagnetic Testing, volume 1581, pages 1328–1335. AIP Publishing, 2014.
- [64] Robert E Schapire. The strength of weak learnability. *Machine learning*, 5(2):197–227, 1990.
- [65] Yoav Freund. Boosting a weak learning algorithm by majority. *Information and computation*, 121(2):256–285, 1995.
- [66] Yoav Freund. An adaptive version of the boost by majority algorithm. *Machine learning*, 43(3):293–318, 2001.
- [67] Robert A Jacobs, Michael I Jordan, Steven J Nowlan, and Geoffrey E Hinton. Adaptive mixtures of local experts. *Neural computation*, 3(1):79–87, 1991.
- [68] Michael I Jordan and Robert A Jacobs. Hierarchical mixtures of experts and the em algorithm. *Neural computation*, 6(2):181–214, 1994.
- [69] Ludmila I Kuncheva, James C Bezdek, and Robert PW Duin. Decision templates for multiple classifier fusion: an experimental comparison. *Pattern recognition*, 34(2):299–314, 2001.
- [70] Harris Drucker, Corinna Cortes, Lawrence D Jackel, Yann LeCun, and Vladimir Vapnik. Boosting and other ensemble methods. *Neural Computation*, 6(6):1289–1301, 1994.
- [71] Robi Polikar, Lalita Upda, Satish S Upda, and Vasant Honavar. Learn++: An incremental learning algorithm for supervised neural networks. Systems, Man, and Cy-

- bernetics, Part C: Applications and Reviews, IEEE Transactions on, 31(4):497–508, 2001.
- [72] Yoav Freund and Robert E Schapire. A decision-theoretic generalization of on-line learning and an application to boosting. *Journal of computer and system sciences*, 55(1):119–139, 1997.
- [73] Robert E Schapire and Yoram Singer. Improved boosting algorithms using confidence-rated predictions. *Machine learning*, 37(3):297–336, 1999.
- [74] Charles R Farrar and Nick AJ Lieven. Damage prognosis: the future of structural health monitoring. *Philosophical Transactions of the Royal Society of London A: Mathematical, Physical and Engineering Sciences*, 365(1851):623–632, 2007.
- [75] GJ Kacprzynski, A Sarlashkar, MJ Roemer, A Hess, and B Hardman. Predicting remaining life by fusing the physics of failure modeling with diagnostics. *JOM Journal of the Minerals, Metals and Materials Society*, 56(3):29–35, 2004.
- [76] C James Li and Hyungdae Lee. Gear fatigue crack prognosis using embedded model, gear dynamic model and fracture mechanics. *Mechanical systems and signal processing*, 19(4):836–846, 2005.
- [77] M Sander and HA Richard. Lifetime predictions for real loading situations—concepts and experimental results of fatigue crack growth. *International journal of fatigue*, 25(9):999–1005, 2003.
- [78] Nagi Gebraeel, Mark Lawley, Richard Liu, and Vijay Parmeshwaran. Residual life predictions from vibration-based degradation signals: a neural network approach. *IEEE Transactions on industrial electronics*, 51(3):694–700, 2004.
- [79] Haitao Liao and Zhigang Tian. A framework for predicting the remaining useful life of a single unit under time-varying operating conditions. *IIE Transactions*, 45(9):964–980, 2013.
- [80] Jay Lee, Fangji Wu, Wenyu Zhao, Masoud Ghaffari, Linxia Liao, and David Siegel. Prognostics and health management design for rotary machinery systems—reviews, methodology and applications. *Mechanical systems and signal processing*, 42(1):314–334, 2014.
- [81] Dawn An, Joo-Ho Choi, and Nam H Kim. Identification of correlated damage parameters under noise and bias using bayesian inference. *Structural Health Monitoring*, page 1475921711424520, 2011.

- [82] Shankar Sankararaman, You Ling, and Sankaran Mahadevan. Confidence assessment in fatigue damage prognosis. In *Annual Conference of the Prognostics and Health Management Society*, pages 10–16, 2010.
- [83] Marcos E Orchard and George J Vachtsevanos. A particle-filtering approach for on-line fault diagnosis and failure prognosis. *Transactions of the Institute of Measurement and Control*, 31(3-4):221–246, 2009.
- [84] William Q Meeker and Luis A Escobar. Statistical methods for reliability data. John Wiley & Sons, 2014.
- [85] YG Li and P Nilkitsaranont. Gas turbine performance prognostic for condition-based maintenance. *Applied energy*, 86(10):2152–2161, 2009.
- [86] Bo-Suk Yang, Myung-Suck Oh, Andy Chit Chiow Tan, et al. Machine condition prognosis based on regression trees and one-step-ahead prediction. *Mechanical Systems and Signal Processing*, 22(5):1179–1193, 2008.
- [87] Bo-Suk Yang, Andy Chit Chiow Tan, et al. Multi-step ahead direct prediction for the machine condition prognosis using regression trees and neuro-fuzzy systems. *Expert Systems with Applications*, 36(5):9378–9387, 2009.
- [88] Erik Christensen, Douglas G Altman, James Neuberger, Bianca L De Stavola, Niels Tygstrup, Roger Williams, PBC The, and PBC2 Trial Groups. Updating prognosis in primary biliary cirrhosis using a time-dependent cox regression model. *Gastroenterology*, 105(6):1865–1876, 1993.
- [89] Jihong Yan and Jay Lee. Degradation assessment and fault modes classification using logistic regression. *Journal of manufacturing Science and Engineering*, 127(4):912–914, 2005.
- [90] Jeffrey P Kharoufeh. Explicit results for wear processes in a markovian environment. Operations Research Letters, 31(3):237–244, 2003.
- [91] Jeffrey P Kharoufeh and Dustin G Mixon. On a markov-modulated shock and wear process. Naval Research Logistics (NRL), 56(6):563-576, 2009.
- [92] Mei-Ling Ting Lee, GA Whitmore, and Bernard A Rosner. Threshold regression for survival data with time-varying covariates. *Statistics in medicine*, 29(7-8):896–905, 2010.
- [93] Ming Dong and David He. Hidden semi-markov model-based methodology for multi-sensor equipment health diagnosis and prognosis. *European Journal of Operational Research*, 178(3):858–878, 2007.

- [94] Zhi-Jie Zhou, Chang-Hua Hu, Dong-Ling Xu, Mao-Yin Chen, and Dong-Hua Zhou. A model for real-time failure prognosis based on hidden markov model and belief rule base. *European Journal of Operational Research*, 207(1):269–283, 2010.
- [95] Carey Bunks, Dan McCarthy, and Tarik Al-Ani. Condition-based maintenance of machines using hidden markov models. *Mechanical Systems and Signal Processing*, 14(4):597–612, 2000.
- [96] Jie Ying, Thia Kirubarajan, Krishna R Pattipati, and Ann Patterson-Hine. A hidden markov model-based algorithm for fault diagnosis with partial and imperfect tests. *IEEE Transactions on Systems, Man, and Cybernetics, Part C (Applications and Reviews)*, 30(4):463-473, 2000.
- [97] Todd D Batzel and David C Swanson. Prognostic health management of aircraft power generators. *IEEE Transactions on Aerospace and Electronic Systems*, 45(2), 2009.
- [98] Jianhui Luo, Krishna R Pattipati, Liu Qiao, and Shunsuke Chigusa. Model-based prognostic techniques applied to a suspension system. *IEEE Transactions on Systems, Man, and Cybernetics-Part A: Systems and Humans*, 38(5):1156–1168, 2008.
- [99] Th Bayes. An essay towards solving a problem in the doctrine of chances. 1763. MD computing: computers in medical practice, 8(3):157, 1991.
- [100] Fuqiong Zhao, Zhigang Tian, and Yong Zeng. Uncertainty quantification in gear remaining useful life prediction through an integrated prognostics method. *IEEE Transactions on Reliability*, 62(1):146–159, 2013.
- [101] James L Beck and Siu-Kui Au. Bayesian updating of structural models and reliability using markov chain monte carlo simulation. *Journal of Engineering Mechanics*, 128(4):380–391, 2002.
- [102] Enrico Zio and Giovanni Peloni. Particle filtering prognostic estimation of the remaining useful life of nonlinear components. Reliability Engineering & System Safety, 96(3):403–409, 2011.
- [103] Ping Li, Roger Goodall, and Visakan Kadirkamanathan. Parameter estimation of railway vehicle dynamic model using rao-blackwellised particle filter. In *European Control Conference (ECC)*, 2003, pages 2384–2389. IEEE, 2003.
- [104] Tiancheng Li, Miodrag Bolic, and Petar M Djuric. Resampling methods for particle filtering: classification, implementation, and strategies. *IEEE Signal Processing Magazine*, 32(3):70–86, 2015.

- [105] Neil J Gordon, David J Salmond, and Adrian FM Smith. Novel approach to nonlinear/non-gaussian bayesian state estimation. In *IEE Proceedings F (Radar and Signal Processing)*, volume 140, pages 107–113. IET, 1993.
- [106] Paul Fearnhead and Peter Clifford. On-line inference for hidden markov models via particle filters. Journal of the Royal Statistical Society: Series B (Statistical Methodology), 65(4):887–899, 2003.
- [107] Tiancheng Li, Shudong Sun, and Tariq Pervez Sattar. Adapting sample size in particle filters through kld-resampling. *Electronics Letters*, 49(12):740–742, 2013.
- [108] Wenbin Wang and AH Christer. Towards a general condition based maintenance model for a stochastic dynamic system. *Journal of the operational research society*, 51(2):145–155, 2000.
- [109] Xiao-Sheng Si, Wenbin Wang, Chang-Hua Hu, and Dong-Hua Zhou. Remaining useful life estimation—a review on the statistical data driven approaches. *European journal of operational research*, 213(1):1–14, 2011.
- [110] Giovanni Belingardi and Roberto Vadori. Low velocity impact tests of laminate glass-fiber-epoxy matrix composite material plates. *International Journal of Impact Engineering*, 27(2):213–229, 2002.
- [111] Dahsin Liu. Delamination resistance in stitched and unstitched composite plates subjected to impact loading. *Journal of Reinforced Plastics and Composites*, 9(1):59–69, 1990.
- [112] Enboa Wu and Kae Shyu. Response of composite laminates to contact loads and relationship to low-velocity impact. *Journal of composite materials*, 27(15):1443–1464, 1993.
- [113] G Zhou. Effect of impact damage on residual compressive strength of glass-fibre reinforced polyester (gfrp) laminates. Composite Structures, 35(2):171–181, 1996.
- [114] C Hiel, D Dittman, and O Ishai. Composite sandwich construction with syntactic foam core: a practical assessment of post-impact damage and residual strength. *Composites*, 24(5):447–450, 1993.
- [115] Carosena Meola and Giovanni M Carlomagno. Impact damage in gfrp: new insights with infrared thermography. Composites Part A: Applied Science and Manufacturing, 41(12):1839–1847, 2010.
- [116] Ahmed Arabi Hassen, Hossein Taheri, and Uday K Vaidya. Non-destructive investigation of thermoplastic reinforced composites. *Composites Part B: Engineering*, 97:244–254, 2016.

- [117] Joy P Dunkers, Daniel P Sanders, Donald L Hunston, Matthew J Everett, and William H Green. Comparison of optical coherence tomography, x-ray computed tomography, and confocal microscopy results from an impact damaged epoxy/e-glass composite. The Journal of Adhesion, 78(2):129–154, 2002.
- [118] Anton Khomenko, Oleksii Karpenko, Ermias Koricho, Mahmoodul Haq, Gary L Cloud, and Lalita Udpa. Theory and validation of optical transmission scanning for quantitative nde of impact damage in gfrp composites. *Composites Part B: Engineering*, 107:182–191, 2016.
- [119] MOW Richardson and MJ Wisheart. Review of low-velocity impact properties of composite materials. Composites Part A: Applied Science and Manufacturing, 27(12):1123–1131, 1996.
- [120] Anton Khomenko, Oleksii Karpenko, Ermias G Koricho, Mahmoodul Haq, Gary L Cloud, and Lalita Udpa. Optical transmission scanning for damage quantification in impacted gfrp composites. In SPIE Smart Structures and Materials+ Nondestructive Evaluation and Health Monitoring, pages 98040R-98040R. International Society for Optics and Photonics, 2016.
- [121] Oleksii Karpenko, Anton Khomenko, Ermias Koricho, Mahmoodul Haq, Gary Cloud, and Lalita Udpa. Monitoring of impact damage accumulation in gfrp composites using guided waves and optical transmission scannings. In *CAMX 2016 Conference Proceedings*, pages TP16–0122:1081–1093. CAMX The Composites and Advanced Materials Expo, 2016.
- [122] PC Paris and Fazil Erdogan. A critical analysis of crack propagation laws. *Journal of basic engineering*, 85(4):528–533, 1963.
- [123] Anis Ben Abdessalem, Romain Azaïs, Marie Touzet-Cortina, Anne Gégout-Petit, and Monique Puiggali. Stochastic modelling and prediction of fatigue crack propagation using piecewise-deterministic markov processes. *Proceedings of the Institution of Mechanical Engineers*, Part O: Journal of Risk and Reliability, 230(4):405–416, 2016.
- [124] Nicola Pugno, M Ciavarella, Pietro Cornetti, and Alberto Carpinteri. A generalized paris' law for fatigue crack growth. *Journal of the Mechanics and Physics of Solids*, 54(7):1333–1349, 2006.
- [125] Yasunobu Hirai, Hiroyuki Hamada, and Jang-Kyo Kim. Impact response of woven glass-fabric composites—i.: Effect of fibre surface treatment. Composites Science and Technology, 58(1):91–104, 1998.
- [126] RG Forman, VE Kearney, and RM Engle. Numerical analysis of crack propagation in cyclic-loaded structures. 1997.

- [127] HT Hahn and R Yo Kim. Fatigue behavior of composite laminate. *Journal of Composite Materials*, 10(2):156–180, 1976.
- [128] Ramesh Talreja. Fatigue of composite materials: damage mechanisms and fatigue-life diagrams. In *Proceedings of the Royal Society of London A: Mathematical, Physical and Engineering Sciences*, volume 378, pages 461–475. The Royal Society, 1981.
- [129] Yasushi Miyano, Masayuki Nakada, and Naoyuki Sekine. Accelerated testing for long-term durability of frp laminates for marine use. *Journal of composite materials*, 39(1):5–20, 2005.
- [130] Bryan Harris. Fatigue in composites: science and technology of the fatigue response of fibre-reinforced plastics. Woodhead Publishing, 2003.
- [131] AP Mouritz, C Townsend, and MZ Shah Khan. Non-destructive detection of fatigue damage in thick composites by pulse-echo ultrasonics. *Composites Science and Technology*, 60(1):23–32, 2000.
- [132] Saptarshi Mukherjee, Antonello Tamburrino, Mahmoodul Haq, Satish Udpa, and Lalita Udpa. Far field microwave nde of composite structures using time reversal mirror. NDT & E International, 93:7–17, 2018.
- [133] Ahsan Mian, Xiaoyan Han, Sarwar Islam, and Golam Newaz. Fatigue damage detection in graphite/epoxy composites using sonic infrared imaging technique. *Composites Science and Technology*, 64(5):657–666, 2004.
- [134] M Corbetta, C Sbarufatti, A Saxena, M Giglio, and K Goebel. Model-based fatigue prognosis of fiber-reinforced laminates exhibiting concurrent damage mechanisms. 2016.
- [135] Dong Wang, Lin Ye, Youhong Tang, and Ye Lu. Monitoring of delamination onset and growth during mode i and mode ii interlaminar fracture tests using guided waves. *Composites science and technology*, 72(2):145–151, 2012.
- [136] Juan Chiachio, Manuel Chiachio, Abhinav Saxena, Guillermo Rus, and Kai Goebel. A model-based prognostics framework to predict fatigue damage evolution and reliability in composites. *Prognostics and Health Management Society, Nantes, France2014. EPHM*, pages 732–742, 2014.
- [137] Tishun Peng, Abhinav Saxena, Kai Goebel, Shankar Sankararaman, Yibing Xiang, and Yongming Liu. Probabilistic delamination diagnosis of composite materials using a novel bayesian imaging method. In 2013 Annual Conference of the Prognostics and Health Management Society, PHM 2013. Prognostics and Health Management Society, 2013.

- [138] Tishun Peng, Yongming Liu, Abhinav Saxena, and Kai Goebel. In-situ fatigue life prognosis for composite laminates based on stiffness degradation. *Composite Structures*, 132:155–165, 2015.
- [139] James Albert Sethian. Level set methods and fast marching methods: evolving interfaces in computational geometry, fluid mechanics, computer vision, and materials science, volume 3. Cambridge university press, 1999.
- [140] Victor Giurgiutiu, Andrei Zagrai, and Jing Jing Bao. Piezoelectric wafer embedded active sensors for aging aircraft structural health monitoring. Structural Health Monitoring, 1(1):41–61, 2002.
- [141] DA Van den Ende, HJ Van de Wiel, WA Groen, and S Van der Zwaag. Direct strain energy harvesting in automobile tires using piezoelectric pzt-polymer composites. *Smart materials and structures*, 21(1):015011, 2012.
- [142] Lei Wang and FG Yuan. Group velocity and characteristic wave curves of lamb waves in composites: Modeling and experiments. *Composites science and technology*, 67(7-8):1370–1384, 2007.
- [143] Younho Cho and Joseph L Rose. A boundary element solution for a mode conversion study on the edge reflection of lamb waves. The Journal of the Acoustical Society of America, 99(4):2097–2109, 1996.
- [144] Oleksii Y Karpenko, Mahmoodul Haq, Anton Khomenko, Lalita Udpa, and Satish Udpa. Lamb wave based monitoring of delamination growth in mode i and mode ii fracture tests. In *Fracture and Fatigue*, *Volume* 7, pages 33–43. Springer, 2014.
- [145] Carl N Morris. Parametric empirical bayes inference: theory and applications. *Journal* of the American Statistical Association, 78(381):47–55, 1983.
- [146] Tishun Peng, Jingjing He, Yibing Xiang, Yongming Liu, Abhinav Saxena, Jose Celaya, and Kai Goebel. Probabilistic fatigue damage prognosis of lap joint using bayesian updating. *Journal of Intelligent Material Systems and Structures*, 26(8):965–979, 2015.
- [147] Rudolph Emil Kalman et al. A new approach to linear filtering and prediction problems. *Journal of basic Engineering*, 82(1):35–45, 1960.
- [148] AH Christer, Wenbin Wang, and JmM Sharp. A state space condition monitoring model for furnace erosion prediction and replacement. *European Journal of Operational Research*, 101(1):1–14, 1997.
- [149] Portia Banerjee, Oleksii Karpenko, Lalita Udpa, Mahmood Haq, and Yiming Deng. Prediction of impact-damage growth in gfrp plates using particle filtering algorithm. *Composite Structures*, 2018.

- [150] Maurizio Gobbato, Joel P Conte, John B Kosmatka, and Charles R Farrar. A reliability-based framework for fatigue damage prognosis of composite aircraft structures. *Probabilistic Engineering Mechanics*, 29:176–188, 2012.
- [151] Tushar Salunkhe, NI Jamadar, and SB Kivade. Prediction of remaining useful life of mechanical components-a review. *International Journal of Engineering Science and Innovative Technology (IJESIT)*, 3(6):125–135, 2014.
- [152] Gongsheng Huang, Shengwei Wang, Fu Xiao, and Yongjun Sun. A data fusion scheme for building automation systems of building central chilling plants. *Automation in Construction*, 18(3):302–309, 2009.
- [153] John E Seem. Using intelligent data analysis to detect abnormal energy consumption in buildings. *Energy and buildings*, 39(1):52–58, 2007.
- [154] Juan Chiachío, Manuel Chiachío, Abhinav Saxena, Shankar Sankararaman, Guillermo Rus, and Kai Goebel. Bayesian model selection and parameter estimation for fatigue damage progression models in composites. *International Journal of Fatigue*, 70:361–373, 2015.
- [155] William J Owen. An exponential damage model for strength of fibrous composite materials. *IEEE Transactions on Reliability*, 56(3):459–463, 2007.
- [156] Heiko Krüger and Raimund Rolfes. A physically based fatigue damage model for fibre-reinforced plastics under plane loading. *International Journal of Fatigue*, 70:241–251, 2015.
- [157] Royce G Forman, VE Kearney, and RM Engle. Numerical analysis of crack propagation in cyclic-loaded structures. *Journal of basic Engineering*, 89(3):459–463, 1967.
- [158] Belur V Dasarathy. Industrial applications of multi-sensor multi-source information fusion. In *Industrial Technology 2000. Proceedings of IEEE International Conference on*, volume 2, pages 5–11. IEEE, 2000.
- [159] Kaibo Liu and Shuai Huang. Integration of data fusion methodology and degradation modeling process to improve prognostics. *IEEE Transactions on Automation Science and Engineering*, 13(1):344–354, 2016.
- [160] Kaibo Liu, Abdallah Chehade, and Changyue Song. Optimize the signal quality of the composite health index via data fusion for degradation modeling and prognostic analysis. *IEEE Transactions on Automation Science and Engineering*, 2015.
- [161] Sasi Balakrishnan, Matteo Cacciola, Lalita Udpa, Bhagi Purnachandra Rao, Tammana Jayakumar, and Baldev Raj. Development of image fusion methodology using discrete wavelet transform for eddy current images. NDT & E International, 51:51–57, 2012.

- [162] Mohammad M Alyannezhadi, Ali A Pouyan, and Vahid Abolghasemi. An efficient algorithm for multisensory data fusion under uncertainty condition. *Journal of Electrical Systems and Information Technology*, 2016.
- [163] Changxi Wang, EA Elsayed, Kang Li, and Javier Cabrera. Multisensor degradation data fusion and remaining life prediction. In ASME 2017 Pressure Vessels and Piping Conference, pages V005T10A003-V005T10A003. American Society of Mechanical Engineers, 2017.
- [164] Kang L Cabrera J Wang C, Elsayed A. Multi sensor degradation data fusion and remaining life prediction. In ASME 2017 Pressure Vessels and Piping Conference, 2017.
- [165] Lawrence A Klein. Sensor and data fusion concepts and applications. Society of Photo-Optical Instrumentation Engineers (SPIE), 1993.
- [166] Alan N Steinberg and Christopher L Bowman. Revisions to the jdl data fusion model. In *Handbook of Multisensor Data Fusion: Theory and Practice, Second Edition*, pages 45–67. CRC Press, 2008.
- [167] Gonzalo Pajares and Jesus Manuel De La Cruz. A wavelet-based image fusion tutorial. Pattern recognition, 37(9):1855–1872, 2004.
- [168] Qiao Sun. Sensor fusion for vehicle health monitoring and degradation detection. In *Information Fusion*, 2002. Proceedings of the Fifth International Conference on, volume 2, pages 1422–1427. IEEE, 2002.
- [169] Xiukuan Zhao, Ruolin Wang, Haichang Gu, Gangbing Song, and YL Mo. Innovative data fusion enabled structural health monitoring approach. *Mathematical Problems in Engineering*, 2014, 2014.
- [170] Harvey B Mitchell. Multi-sensor data fusion: an introduction. Springer Science & Business Media, 2007.
- [171] Ronald R Yager and Liping Liu. Classic works of the Dempster-Shafer theory of belief functions, volume 219. Springer, 2008.
- [172] Youzhu Ling, Xiaoguang Xu, Lina Shen, and Jingmeng Liu. Multi sensor data fusion method based on fuzzy neural network. In *Industrial Informatics*, 2008. INDIN 2008. 6th IEEE International Conference on, pages 153–158. IEEE, 2008.
- [173] Anastasios P Vassilopoulos and Thomas Keller. Fatigue of fiber-reinforced composites. Springer Science & Business Media, 2011.
- [174] StephenW Tsai. Introduction to composite materials. Routledge, 2018.

- [175] Orlando José Tobias and Rui Seara. Image segmentation by histogram thresholding using fuzzy sets. *IEEE transactions on Image Processing*, 11(12):1457–1465, 2002.
- [176] Randal Douc and Olivier Cappé. Comparison of resampling schemes for particle filtering. In *Image and Signal Processing and Analysis*, 2005. ISPA 2005. Proceedings of the 4th International Symposium on, pages 64–69. IEEE, 2005.
- [177] Laura Uusitalo. Advantages and challenges of bayesian networks in environmental modelling. *Ecological modelling*, 203(3-4):312–318, 2007.
- [178] Baoping Cai, Lei Huang, and Min Xie. Bayesian networks in fault diagnosis. *IEEE Transactions on Industrial Informatics*, 13(5):2227–2240, 2017.
- [179] Franco Taroni, Colin GG Aitken, Paolo Garbolino, and Alex Biedermann. *Bayesian networks and probabilistic inference in forensic science*. Wiley Online Library, 2006.
- [180] Katrina M Groth and Ali Mosleh. Deriving causal bayesian networks from human reliability analysis data: A methodology and example model. *Proceedings of the Institution of Mechanical Engineers, Part O: Journal of Risk and Reliability*, 226(4):361–379, 2012.
- [181] David Heckerman. A tutorial on learning with bayesian networks. microsoft research. 1995.
- [182] Petri Kontkanen, Petri Myllymäki, Tomi Silander, Henry Tirri, and Peter Grunwald. Comparing predictive inference methods for discrete domains. In *In Proceedings of the sixth international workshop on artificial intelligence and statistics*. Citeseer, 1997.
- [183] Kelly P. Solid Mechanics Part I: An Introduction to Solid Mechanics. The University of Auckland., 2018.